

# Identification of the mechanical properties of nodular graphite cast iron via multiaxial tests

---

**Tomičević, Zvonimir**

**Doctoral thesis / Disertacija**

**2015**

*Degree Grantor / Ustanova koja je dodijelila akademski / stručni stupanj:* **University of Zagreb, Faculty of Mechanical Engineering and Naval Architecture / Sveučilište u Zagrebu, Fakultet strojarstva i brodogradnje**

*Permanent link / Trajna poveznica:* <https://urn.nsk.hr/urn:nbn:hr:235:459809>

*Rights / Prava:* [In copyright](#)/[Zaštićeno autorskim pravom.](#)

*Download date / Datum preuzimanja:* **2024-07-30**

*Repository / Repozitorij:*

[Repository of Faculty of Mechanical Engineering and Naval Architecture University of Zagreb](#)





University of Zagreb  
FACULTY OF MECHANICAL  
ENGINEERING AND NAVAL  
ARCHITECTURE



<sup>C</sup> <sup>A</sup> <sup>C</sup> <sup>H</sup> <sup>A</sup> <sup>N</sup>  
LABORATOIRE DE  
MÉCANIQUE  
ET TECHNOLOGIE

Zvonimir Tomičević

**IDENTIFICATION OF THE MECHANICAL  
PROPERTIES OF NODULAR GRAPHITE CAST IRON  
VIA MULTIAXIAL TESTS**

INTERNATIONAL DUAL DOCTORATE

ZAGREB, 2015.



University of Zagreb  
FACULTY OF MECHANICAL  
ENGINEERING AND NAVAL  
ARCHITECTURE



Zvonimir Tomičević

**IDENTIFICATION OF THE MECHANICAL  
PROPERTIES OF NODULAR GRAPHITE CAST IRON  
VIA MULTIAXIAL TESTS**

INTERNATIONAL DUAL DOCTORATE

Supervisors:  
Prof. dr. sc. Janoš Kodvanj  
François Hild, Directeur de Recherche

ZAGREB, 2015.



University of Zagreb  
FACULTY OF MECHANICAL  
ENGINEERING AND NAVAL  
ARCHITECTURE

**CVS**  
C A C H A N  
LABORATOIRE DE  
MÉCANIQUE  
ET TECHNOLOGIE

Zvonimir Tomičević

IDENTIFIKACIJA MEHANIČKIH SVOJSTAVA  
NODULARNOG LIJEVA KOD VIŠEOSNIH  
OPTEREĆENJA

MEĐUNARODNI DVOJNI DOKTORAT ZNANOSTI

Mentori:  
Prof. dr. sc. Janoš Kodvanj  
François Hild, Directeur de Recherche

ZAGREB, 2015.

**THÈSE DE DOCTORAT  
DE L'ÉCOLE NORMALE SUPÉRIEURE DE CACHAN**

Présentée par

**Zvonimir Tomičević**

pour obtenir le grade de

**DOCTEUR DE L'ÉCOLE NORMALE SUPÉRIEURE DE CACHAN**

Domaine

**MÉCANIQUE - GÉNIE MÉCANIQUE - GÉNIE CIVIL**

Sujet de la thèse

**Identification of the mechanical properties of nodular  
graphite cast iron via multiaxial tests**

Soutenue à Zagreb le 2015 devant le jury composé de :

Michel Grédiac	Professeur, Institut Pascal. Université Blaise Pascal	Rapporteur
Zdenko Tonković	Professeur, Université de Zagreb, Croatie	Rapporteur, Président
Ante Bakić	Ingénieur (HDR,) INETEC	Examineur
François Hild	Directeur de Recherche, CNRS, LMT	Co-directeur de thèse
Janoš Kodvanj	Professeur, Université de Zagreb, Croatie	Co-directeur de thèse

**LMT-Cachan**

ENS Cachan / CNRS / UPMC / PRES UniverSud Paris  
61 avenue du Président Wilson, F-94235 Cachan cedex, France

*To my parents:  
Štefica and Mirko.*

## BIBLIOGRAPHY DATA

UDC 620.17:539.5

Keywords: nonlinear material behaviour, full-field measurement, identification, nodular graphite cast iron, multiaxial loading, crack networks, regularization, tomography

Scientific area: Technical sciences

Scientific field: Mechanical engineering

Institution: Faculty of Mechanical Engineering and Naval Architecture (FMENA), University of Zagreb

Supervisors: Dr. sc. Janoš Kodvanj, Professor  
Dr. sc. François Hild, Directeur de Recherche

Number of pages: 239

Number of figures: 131

Number of tables: 23

Number of references: 150

Date of oral examination: 13. 02. 2015.

Jury members: Dr. sc. Zdenko Tonković, Professor  
Dr. sc. Michel Grédiac, Professor  
Dr. sc. Ante Bakić, R&D Engineer  
Dr. sc. Janoš Kodvanj, Professor  
Dr. sc. François Hild, Directeur de Recherche

Archive: FMENA, University of Zagreb  
ENS Cachan,  
CNRS / UPMC / PRES UniverSud Paris





# Acknowledgement

*“Where you come from is  
much less important than  
where you are going.”*

Selected quote is the motto that I try to follow in life since my goal is to look towards the future and not dwell on the past. Life is unpredictable and it is necessary to accept all the challenges that are set in front of us because latter actually make our life more interesting. In this way I experienced my PhD thesis.

I would like to thank all the people who contributed in some way to the work described in this thesis. First and foremost, I thank my academic supervisors, Professor Janoš Kodvanj and Research Professor François Hild. I would like to express my gratitude to Janoš for being an outstanding advisor and excellent professor. His constant encouragement, support, and invaluable suggestions made this work successful. He has been everything that one could want in an advisor. Thank you for believing in me and standing up for me when it was the most necessary. I am also deeply grateful to my second advisor François Hild. To work with you has been a real pleasure to me, with heaps of fun and excitement. You have been a steady influence throughout my PhD career; you have oriented and supported me with promptness and care, and have always been patient and encouraging in times of new ideas and difficulties; you have listened to my ideas and discussions with you frequently led to key insights. Your ability to select and to approach compelling research problems, your high scientific standards, and your hard work set an example. I admire your ability to balance research interests and personal pursuits. Above all, you made me feel a friend, which I appreciate from my heart. P.S. I will miss our long meetings on Tuesday evening.

Besides my advisor, I would like to thank Research Professor Stéphane Roux for his enthusiasm and unique advices on many challenges that occurred during the PhD. Collaboration with you raised my scientific research on a higher level.

I am also very thankful to the jury members, Professor Zdenko Tonković, Professor Michel Grédiac (Université Blaise Pascal), and dr.sc. Ante Bakić (Institute for Nuclear

Technology - INETEC), for finding time during Christmas holidays to review my thesis, and for giving valuable comments and encouragement needed for completing this work.

This thesis was supported by the Ministry of Science, Education and Sports of the Republic of Croatia, Laboratoire de mécanique et technologie (LMT-Cachan) and scholarships from the Campus France (Eiffel scholarship in 2012/2013), ENS Cachan (SRI scholarship in 2012/2013 and 2014/2015). This support is gratefully acknowledged.

I would like to thank my colleagues from both FAMENA UniZg, and from ENS-Cachan for the given help, advices and simply for listening during the period I have spent at these institutions. Among them, my special appreciation goes to all those great people working at LEM and LMT.

One of the most interesting and instructive interaction I had was with the members of Stéphane's and François's research group. I want to thank all Eikologie "gang" members (present and past) for their support and for providing a pleasant and productive working atmosphere. In addition, I have been very privileged to get to know and to collaborate with many other great people who became friends over the last several years. I learned a lot from you about life, research, how to tackle new problems and how to develop techniques to solve them. Special gratitude goes to Bumedijen Boubou Raka for his technical support in conducting biaxial experiments on Astree but also for helping me survive in my everyday life in Paris. Without Boubou this "journey" would not be the same.

I would like to thank my fiancée Marina for her love and encouragement. We met in the most delicate time of the thesis and spend a lot of time separated but I never doubted in our love. Thank you for all your support when I have needed it the most. You really let me feel like a 'Dancing Bear'. Thank you with all my heart!

Finally, I would like to acknowledge friends and family who supported me during my PhD. First and foremost, my deepest gratitude goes to my mom, dad and brother for their unflagging love and unconditional support throughout my life and my studies. The most important thing they learned me is to work with a smile. From you I gained the work habits that helped me to overcome successfully all the challenges that were in front of me. You made me live the most unique, magic and carefree childhood that has made me who I am now!

# Contents

<b>Contents</b>	<b>i</b>
<b>Abstract</b>	<b>v</b>
<b>Prošireni sažetak</b>	<b>vii</b>
<b>List of Figures</b>	<b>xv</b>
<b>List of Tables</b>	<b>xxv</b>
<b>Introduction</b>	<b>1</b>
<b>I State of the art</b>	<b>7</b>
<b>1 Material, models and methodology</b>	<b>9</b>
1 Preface . . . . .	11
2 Studied material: SG cast iron . . . . .	11
2.1 Introduction . . . . .	11
2.2 Microstructure . . . . .	12
2.3 Mechanical properties . . . . .	16
2.4 Application of cast iron . . . . .	19
2.5 SG cast iron produced with sandwich technique . . . . .	21
3 Constitutive equations describing elastoplasticity and damage . . . . .	22
3.1 Introduction . . . . .	22
3.2 Elastoplastic models . . . . .	23
3.3 Damage law . . . . .	27
4 Advanced identification procedures for elastoplastic and damage models .	31
4.1 Intoduction . . . . .	31
4.2 Identification of elastoplastic and damage behaviour . . . . .	31
4.3 Finite Element Model Updating . . . . .	32
5 Conclusion . . . . .	34

<b>2</b>	<b>Digital Image Correlation</b>	<b>37</b>
1	Preface . . . . .	39
2	Introduction . . . . .	39
3	Digital Image Correlation . . . . .	40
	3.1 Local DIC approach . . . . .	41
	3.2 Global DIC approach . . . . .	43
	3.3 Comparison between local and global DIC . . . . .	44
4	Regularized DIC . . . . .	47
	4.1 Introduction . . . . .	47
	4.2 Regularized correlation principle . . . . .	48
	4.3 Validation of R-DIC . . . . .	49
5	Integrated DIC . . . . .	57
	5.1 Introduction . . . . .	57
	5.2 I-DIC principle . . . . .	57
6	Digital Volume Correlation - DVC . . . . .	58
7	Conclusion . . . . .	59

**II Identification of nonlinear material behaviour via uniaxial experiments 61**

<b>3</b>	<b>Identification of elastoplastic and damage parameters under uniaxial loading regimes</b>	<b>63</b>
1	Preface . . . . .	65
2	Monotonic loading history . . . . .	65
	2.1 Experimental setup of monotonic tensile test . . . . .	65
	2.2 Parametric analysis of measurement resolution . . . . .	66
	2.3 Conventional determination of material parameters . . . . .	71
	2.4 Identification of material parameters via FEMU . . . . .	76
3	Cyclic loading history . . . . .	84
	3.1 Experimental setup . . . . .	84
	3.2 Standard displacement resolution . . . . .	87
	3.3 Identification of elastic properties . . . . .	91
	3.4 Identification of Johnson-Cook parameters . . . . .	93
	3.5 Identification of Armstrong-Frederick parameters . . . . .	94
	3.6 Identification of isotropic hardening coupled with damage . . . . .	96
4	Uniaxial cyclic experiment monitored via X-ray tomography . . . . .	99
	4.1 Experimental procedure . . . . .	100
	4.2 A priori analysis . . . . .	100
	4.3 Analysis of the results . . . . .	103
5	Conclusion . . . . .	107

<b>III</b>	<b>Identification of nonlinear material behaviour via biaxial experiments</b>	<b>111</b>
<b>4</b>	<b>Analysis of the elastoplastic behaviour under biaxial loading regimes</b>	<b>113</b>
1	Preface . . . . .	115
2	Experimental setup . . . . .	116
2.1	ASTREE: Triaxial testing machine . . . . .	116
2.2	In-plane cruciform specimen . . . . .	117
2.3	Two scale optical setup . . . . .	117
2.4	Applied loading histories . . . . .	120
3	Displacement resolution on macro- and mesoscales . . . . .	124
3.1	Macroscale analysis . . . . .	124
3.2	Mesoscale analysis . . . . .	125
4	Equibiaxial loading history . . . . .	130
4.1	Two scale strain analysis . . . . .	130
4.2	Implementation of 3D FEMU procedure using 2D-DIC measurements . . . . .	133
4.3	Identification of elastic parameters . . . . .	135
4.4	Identification of parameters describing isotropic and kinematic hardening . . . . .	137
5	“Snail” loading history . . . . .	140
5.1	Two-scale measurements . . . . .	140
5.2	Validation of elastic parameters . . . . .	141
5.3	Identification of plastic parameters . . . . .	148
6	Conclusion . . . . .	151
<b>5</b>	<b>Biaxial fatigue experiments</b>	<b>153</b>
1	Preface . . . . .	155
2	Equibiaxial fatigue experiments . . . . .	156
2.1	Analysis of experiment EBE-1 . . . . .	156
2.2	Microcrack initiation for EBE-5 test . . . . .	164
2.3	Results of equibiaxial fatigue campaign . . . . .	167
3	“Snail” fatigue experiments . . . . .	170
3.1	Validation of the kinematic hardening law . . . . .	170
3.2	Analysis of experiment SBE-2 . . . . .	174
3.3	Microcrack initiation in SBE-5 test . . . . .	180
3.4	Results of “snail” fatigue campaign . . . . .	185
4	Conclusion . . . . .	185
	<b>Conclusions and perspectives</b>	<b>191</b>
<b>A</b>	<b>Design of samples used for standard tensile tests</b>	<b>195</b>
<b>B</b>	<b>Design of uniaxial sample used for in situ tests</b>	<b>197</b>

<b>C Design of in-plane biaxial specimen</b>	<b>199</b>
<b>D Article 1</b>	<b>201</b>
<b>E Hybrid snail test data</b>	<b>217</b>
<b>Bibliography</b>	<b>223</b>
<b>F Životopis</b>	<b>237</b>
<b>G Biography</b>	<b>239</b>

# Abstract

The majority of engineering structures is subjected to various and complex in-service loading regimes. In order to satisfy the construction demands and increase the reliability of structures resulted in the development of new engineering elements. Furthermore, new technologies and materials are also introduced. This trend has stimulated in the last few decades scientists to describe the material behaviour with more reliable and complex constitutive laws. The latter ones require advanced methods for the identification and validation of material parameters.

The material response was initially observed with contact measurement techniques (*e.g.*, strain gauges, extensometers ) yielding data locally at just few points on the loaded specimen/structure. Measurements performed with classical methods give a global overview of the material behaviour. Hence, localised phenomena (*e.g.*, cracks, heterogeneous strain fields, shear bands) are not captured due to the lack of measured degrees of freedom. These limitations are successfully overcome with the development of non-contact full-field measurement techniques. Among different principles Digital Image Correlation (DIC) is the most widely used in the experimental mechanics community. Over the years DIC surpassed the initial application of measuring displacement/strain fields to become a powerful tool for identification of mechanical properties, verification of numerical simulations, detection and monitoring of local phenomena (*e.g.*, onset of plasticity, crack initiation and propagation). Originally the applied principle of DIC was a local approach based on successive correlations over small zones of interest (ZOIs) where displacements are calculated independently from each other. Detached ZOIs are favourable regarding the time cost since the computations may be run in parallel. However, it is necessary to emphasize that the assumption of field continuity defined by a global DIC approach, outperforms the local ones in terms of displacement resolution. As opposed to local approach, global DIC considers the whole region of interest (ROI) using a large number of Degrees of Freedom (DOFs) and minimizes the difference between reference and deformed configurations. Hence, global DIC was chosen as a full-field measurement technique since lower displacement resolution is possible. Furthermore, coupling the latter with Finite Element analyses is straightforward for identification and validation purposes.

Within this thesis, the identification and validation of nonlinear models describing the behaviour of nodular graphite cast iron is carried out. In general the material parameters are obtained by iterative or direct identification procedures. Finite Element Model Updating (FEMU) procedures are used herein as the identification tool. The aim is to

analyse the damage law coupled with the elastoplastic behaviour of graphite cast iron in the identification process for simple and complex loading regimes.

First, the identification is performed on uniaxial experiments with two different loading histories, namely monotonic and cyclic. A FEMU-UF procedure is used to determine parameters of isotropic and kinematic hardening laws. Furthermore, the parameters describing damage coupled with isotropic hardening are obtained. The identification results of the same constitutive model for different uniaxial loading histories yield different parameters. Force residuals as the criterion for estimation of the most reliable behaviour lead to the lowest values when coupled elastoplastic and damage law is used to model cyclic loading regime. In order to determine microdamage mechanisms an in-situ uniaxial cyclic experiment is monitored via X-ray tomography. For the investigated SG cast iron it is detected via digital volume correlation that debonding between the matrix and the nodules causes damage phenomena.

Second, in-plane biaxial experiments are conducted. Cruciform samples are subjected to two different loading regimes, namely proportional (*i.e.*, equibiaxial) and non-proportional (referred to as “snail”). Since the microstructure of cast iron is well suited to correlation techniques, experiments are monitored on two scales (*i.e.*, macro- and mesoscales). The challenge related with mesoscale observations implies that conventional or even standard global DIC approaches fail to accurately capture the displacement fields. In order to overcome such issues a regularized DIC algorithm is introduced and validated. The results observed on the two scales show a very good agreement when two opposite sides of the sample are simultaneously analysed. The identification of isotropic and kinematic hardening parameters is performed for the three tests. The constitutive behaviour is better captured with kinematic hardening since the sample was subjected to cyclic loading histories. Higher force residuals are obtained in the “snail” experiments when compared with the equibiaxial tests. This shows that non-proportional loading regimes are more damaging and complex to analyse, and that even more advanced models need to be considered.

Last, two series of fatigue experiments are presented. A first series of five experiments is performed with an equibiaxial history, and a second series of five “snail” loadings. The goal is to evaluate the fatigue lifetime for the two loading paths in order to evaluate the more damaging one. Two-scale DIC is performed to measure displacement fields of both sample sides. From the mesoscale measurements, the crack networks are detected and quantified with respect to the number of cycles. Correlation and mechanical residuals are used to monitor the crack network initiation and growth since the strain data could not be directly used. The analysed fatigue results show that lower lifetimes are to be expected from more complex loading histories.

**Keywords:** nonlinear material behaviour, full-field measurement, identification, cast iron, multiaxial loading, crack networks, regularization, tomography



# Prošireni sažetak

Ova disertacija izrađena je u okviru dvojnog doktorata. Prema Ugovoru o dvojnog doktoratu potpisanom između Sveučilišta u Zagrebu i École Normale Supérieure de Cachan, Francuska, disertacija je pisana na engleskom jeziku. Stoga je cilj ovog proširenog sažetka dati kratki pregled disertacije s naglaskom na terminologiju koja je nova u hrvatskom jeziku.

## Uvod

Ubrzani razvoj industrije zahtijeva proizvodnju sve složenijih mehaničkih komponenti i konstrukcija. Oni moraju ispuniti projektne zahtjeve kao što su korištenje pri većim opterećenjima te eksploatacija u ekstremnim uvjetima rada, dok u isto vrijeme moraju biti pouzdani i imati zadovoljavajući radni vijek. Ovakav trend potiče razvoj naprednih metoda analize konstrukcija te opisivanja ponašanja materijala pri različitim složenim opterećenjima. Posljednjih nekoliko godina posebna pažnja je posvećena istraživanju utjecaja mikrostrukture materijala na njegovo mehaničko ponašanje. Klasična mehanika kontinuuma na makro razini ne uzima u obzir mikrostrukturna svojstva materijala, a to zahtijeva korištenje modela temeljenih na mehanizmima koji opisuju nelinearne pojave u mikrostrukтури materijala poput raspodjele, orijentacije i veličine oštećenja. U takvim slučajevima heterogenost materijala igra vrlo važnu ulogu.

Razvoj novih konstrukcijskih elemenata povećao je primjenu novih tehnologija proizvodnje i materijala. Tijekom eksploatacije većina mehaničkih komponenti je izložena složenim režimima opterećenja (npr. zrakoplovna, automobilska, kemijska, naftna i transportna industrija). Zbog široke primjene mehaničkih konstrukcija proučavanje ponašanja materijala i njegova izdržljivost uslijed promijenjivih višeosnih opterećenja postaje područje istraživanja mnogih znanstvenika. Naime, inženjersko područje interesa u okviru mehaničkog ponašanja uključuje čvrstoću materijala uslijed višeosnih uvjeta opterećenja, višeosnu deformaciju i zamor materijala, te razvoj višeosnih eksperimenata kojima bi se promatralo ponašanje materijala pri kontroliranim uvjetima prototipskih opterećenja. Kako bi se što pouzdanije opisala navedena opterećenja i odziv materijala započinju se provoditi višeosni testovi. S razvojem višeosnih ispitnih uređaja (npr. dvoosnih, trosnih i višeosnih kao što je npr. heksapod) započinje nova era provedbe eksperimenata s obzirom da je moguće propisati različite složene režime opterećenja. Rezultati višeosnih testova su posebno važni u određivanju mehaničkih karakteristika ma-

terijala te pri razvoju novih materijalnih modela koji se mogu koristiti u svrhu predviđanja zamornog ponašanja materijala. U znanosti o materijalima zamor je progresivno i lokalizirano strukturno oštećenje koje nastaje kada se materijal podvrgne cikličkom opterećenju, odnosno kada je materijal kontinuirano izložen opterećenju i rasterećenju. Ukoliko su opterećenja iznad određenih vrijednosti na površini nastaju mikroskopske pukotine. S vremenom pukotina će dostići kritičnu veličinu i nastupit će lom konstrukcije. Fenomen zatvaranja pukotine tijekom zamornog opterećenja prvi je opisao Elber prije više od 40 godina. Iako se kritična veličina za predviđanje vijeka trajanja neke konstrukcije procijenjuje Parisovim zakonom (korištenjem efektivnog faktora intenzivnosti naprezanja), još uvijek ne postoji jedinstvena metoda mjerenja oko koje je postignut konsenzus.

U ovom radu je razmatrano ponašanje nodularnog lijeva koji se smatra jednim od značajnih željeznih lijevova u inženjerskoj praksi. Nodularni lijev je familija željeznih lijevova koja ima široki spektar svojstava primjenjiv u različitim inženjerskim eksploatacijskim uvjetima. Iako razlog raspodjele grafitnih nodula nije u potpunosti poznat, nodularni lijev ima široki spektar svojstava koji su postignuti kontroliranim proizvodnim procesima. Kontinuiranim razvojem tijekom mnogih godina nodularni lijev je postao pouzdan materijal i opravdao je svoju sve veću primjenu za proizvodnju visokoopterećenih konstrukcija. Budući da se obično koristi za složeno opterećene mehaničke komponente, neophodno je istražiti njegova zamorna svojstva kod niskocikličkog i visokocikličkog zamora. Mikrostrukturu nodularnog lijeva čini željezna matrica i grafit u obliku kuglica. Željezna matrica u kojoj su nodule raspršene značajno utječe na mehanička svojstva. Kontrolom svojstava matrice mogu se dobiti različite vrste nodularnog lijeva, na što utječe kemijski sastav i dodatna toplinska obrada. Najvažnija mikrostrukturalna značajka nodularnog lijeva je prisutnost grafita u obliku nodula koji sprječavaju širenje pukotina, dajući nodularnom lijevu veću duktilnost i žilavost.

Konvencionalne metode korištene za mjerenje eksperimentalnih podataka nisu zabilježavale sve pojave koje nastaju u materijalu kada je na njega narinuto određeno opterećenje. Navedena činjenica potakla je u posljednjih nekoliko desetljeća znanstvenike da razvijaju napredne metode u svrhu identifikacije/validacije parametara materijala koji opisuju ponašanje materijala kroz pouzdanije, a ujedno i složenije konstitutivne zakone. Štoviše, razvijene su nove identifikacijske procedure koje su izričito u spregu s cijelim mjerenim poljem pomaka. Najčešće korištena metoda mjerenja cijelog polja pomaka u domeni eksperimentalne mehanike je korelacija digitalne slike (Digital Image Correlation (DIC)). Zajedno s algoritmima konačnih elemenata izvrsno je prilagođena identifikaciji materijalnih parametara. U dosadašnjim istraživanjima korištene su različite identifikacijske procedure u spregu s mjerenim cijelim poljem pomaka kako bi se odredili traženi elastoplastični parametri te parametri oštećenja materijala.

Tijekom opterećenja mehaničkih konstrukcija izrađenih iz nodularnog lijeva moguće su pojave različitih mehanizama oštećenja koji su uzrokovani heterogenom mikrostrukturom nodularnog lijeva. Dosadašnje spoznaje vezane su uz promatranje površine ispitnog uzorka te pokazuju kako oštećenje može nastati unutar grafitnih nodula, uslijed greške u procesu lijevanja (šupljina uslijed mikrostezanja materijala), odvajanjem željezne matrice

---

i grafitne nodule. Razvojem uređaja za računalnu tomografiju otvaraju se mogućnosti promatranja ponašanja materijala unutar uzorka a ne samo na površini. Zbog svoje heterogene mikrostrukture nodularni lijev je zanimljivo promatrati na mikro razini pošto njegova prirodna tekstura podsjeća na onu potrebnu za DIC mjerenje. Stoga, X-ray računalna tomografija zajedno s korelacijom digitalnog volumena (Digital Volume Correlation) omogućuje prepoznavanje mehanizma oštećenja te unaprijeđenje materijalnog modela.

## Ciljevi i hipoteze istraživanja

Istraživanje u sklopu ovog rada obuhvaća identifikaciju elastoplastičnih parametara i parametara oštećenja nodularnog lijeva pri različitim režimima opterećenja. Eksperimentalna ispitivanja će biti provedena s jednostavnim (tj. jednoosnim) i složenim (tj. ravninskim dvoosnim) programima opterećenja. Pretpostavka je da parametri materijala određeni na jednostavnim mehaničkim testovima nisu nužno prikladni za opisivanje složenijih režima opterećenja. Cilj predložene metodologije je određivanje pouzdanih nelinearnih materijalnih parametara za svaki program opterećenja povezivanjem mjerenja cijelog polja pomaka i numeričkih simulacija metodom konačnih elemenata. Globalni pristup korelacije digitalne slike kao metoda mjerenja cijelog polja pomaka povezan s metodom konačnih elemenata je prikladan u identifikacijske i validacijske svrhe pošto se temelji na formulaciji konačnih elemenata (FE). Prednost koju ima u usporedbi sa lokalnim DIC pristupom je niža standardna rezolucija. Metoda ažuriranja modela konačnih elemenata (Finite Element Model Update (FEMU)) primijenit će se u svrhu identifikacije materijalnih parametara nodularnog lijeva koji karakteriziraju nelinearne konstitutivne modele.

Sljedeći cilj je određivanje materijalnih parametara koji opisuju zakon rasta oštećenja kod cikličkog opterećenja nodularnog lijeva. Glavni izazov će biti odrediti elastoplastično ponašanje materijala u sprezi s predloženim zakonom oštećenja u zajedničkoj identifikacijskoj proceduri. Mehanički eksperimenti s kompleksnim režimom opterećenja biti će promatrani na dvije razine, makro i mezo razini, kako bi se bolje uočilo/zabilježilo oštećenje materijala, a dobiveni rezultati na dvije razine će se usporediti. Na mezo razini koristiti će se prirodna tekstura nodularnog lijeva za DIC analizu. U slučaju da se na mezo razini pojavi siromašna prirodna tekstura s obzirom na razinu sive skale boja, konvencionalni pa čak i standardni globalni DIC pristupi neće uspjeti precizno odrediti polje pomaka sa zadovoljavajućom točnošću. Zbog povećanje mjerne nesigurnosti, vrlo je vjerojatno da će biti potrebno koristiti regularizacijske tehnike kako bi se eliminirao navedeni problem. Osim toga, da bi se odredio mehanizam oštećenja kod ispitivanog nodularnog lijeva vlačni in-situ eksperiment će se provoditi na laboratorijskom tomografu. Globalni (C8-DVC) i/ili regularizirani RC8-DVC će se koristiti kako bi se odredilo polje pomaka unutar ispitnog uzorka.

## Metoda ažuriranja modela konačnih elemenata

Novorazvijene identifikacijske metode koriste mjerenje cijelog polja pomaka za određivanje parametara materijala. Prilikom identifikacije karakterističnih vrijednosti materijalnog modela moguće je koristiti dvije različite procedure. Parametre materijala moguće je odrediti direktnim identifikacijskim postupkom (tj. ne iterativnom metodom) kao što su metoda virtualnih polja pomaka (Virtual Fields Method (VFM)) i metoda ravnotežnih razlika (Equilibrium Gap Method (EGM)). Drugi način određivanja parametara je iterativnim identifikacijskim procedurama (tj. ažuriranjem modela konačnih elemenata). U tu grupu spadaju FEMU, metoda razlike materijalnog modela (Constitutive Equation Gap Method (CEGM)), metoda reciprocitetne razlike (Reciprocity Gap Method (RGM)) koje koriste polja pomaka i/ili naprezanja izračunata metodom konačnih elemenata. Kod iterativnih metoda potrebne su početne vrijednosti parametara materijal za provedbu numeričkih simulacija. Traženi materijalni parametri su identificirani minimiziranjem funkcije cilja (cost function) u kojoj se uspoređuje dostupno izmjereno polje pomaka s izračunatim. Funkcije cilja uobičajeno su definirane kao kvadratna greška između mjerenih i izračunatih vrijednosti. Prednost direktnih metoda s obzirom na iterativne metode je kraće vrijeme trajanja identifikacijske procedure pošto nije potrebna serija numeričkih simulacija da bi se dosegnuo minimum funkcije cilja. S druge strane iterativnim metodama je moguće identificirati/validirati parametre materijala složenijih konstitutivnih zakona na složenijim geometrijskim modelima.

Pregledom dosadašnjih istraživanja rijetki su radovi koji se odnose na određivanje parametara materijala koji opisuju elastoplastično ponašanje i oštećenje materijala u jednoj proceduri. No međutim, iterativne i direktne identifikacijske metode su korištene za određivanje elastoplastičnih parametara materijala. FEMU identifikacijska procedura je odabrana za određivanje traženih parametara materijala pošto je cilj ovoga rada identificirati elastoplastično ponašanje nodularnog lijeva u sprezi s pojavom oštećenja. Drugi razlog odabira iterativne metode je složena geometrija ispitnog uzorka koja će se koristiti prilikom primjene složenih režima opterećenja. Funkcija cilja FEMU metode može se zasnivati na razlici između mjerenih i računatih polja deformacija ili pomaka. Iz radova u kojima su korištena polja deformacija za identifikaciju parametara materijala nije jasno kako su propisani rubni uvjeti na modelu konačnih elemenata. Za slučaj primjene polja pomaka, sve identifikacijske metode uspoređuju mjereno i izračunato polje pomaka za odgovarajuću razinu opterećenja. Numeričke simulacije i mjerenja cijelog polja pomaka (za lokalni DIC pristup) su provedena u različitim programskim paketima koji se ne zasnivaju na istoj formulaciji. Kao posljedica toga referentne točke kod mjerenih i izračunatih podataka ne nalaze se na istoj poziciji. Da bi se minimizacija funkcije cilja provela korektno, potrebno je potpuno preklapanje svih točaka dobivenih DIC-om i FE algoritmima. Stoga je potrebno provesti dodatnu prilagodbu (interpolaciju) kako bi se oba polja mogla usporediti. Dodatne interpolacije unose nove greške i time se povećava nesigurnost identifikacijske procedure. Korištenjem DIC algoritma koji se temelji na FE formulaciji (globalni DIC pristup) spomenuti problem se ne javlja pošto mreža može biti prenesena na sliku iz FE algoritma, ili obrnuto mreža kreirana u DIC kodu može

---

definirati FE model. Ovime je osigurano da mreža koja se koristi u numeričkim simulacijama odgovara mreži korištenoj za dobivanje mjerenog polja pomaka. Veza između simulacija i eksperimentalnih podataka također može biti limitirana uobičajenom pretpostavkom da su uvjeti opterećenja u simulacijama definirani idealnim rubnim uvjetima koji ne odgovaraju inherentnim nesavršenostima mehaničkog testa. Umjesto propisivanja rubnih uvjeta idealnim opterećenjem mogu se primijeniti stvarni rubni uvjeti dobiveni eksperimentom (npr. izmjereni pomaci ili informacija statičkog opterećenja).

U predloženom istraživanju FEMU identifikacijska procedura zasniva se na istim principima u eksperimentalnom i numeričkom dijelu metode. Koristi se na jednostavnijim (2D) i složenijim (3D) geometrijskim modelima. Rubni uvjeti propisani na FE model su preuzeti iz polja pomaka mjerenih DIC metodom za različite faze opterećenja. Potrebno je naglasiti kako mnogo čimbenika može utjecati na krajnji ishod eksperimenta. Kod provedbe, čak ni jednostavni mehanički testovi (npr. jednoosni vlačni eksperiment) nisu provedeni u idealnim uvjetima te odziv materijala uključuje i neke anomalije eksperimentalnog postava kao što je rotacija uzorka u poprečnom smjeru uslijed prihvatnog mehanizma koji nije savršen. Primjenom mjerenih pomaka na rubovima FE modela uzimaju se u obzir sve nesavršenosti zabilježene kod eksperimenata. Između spomenutih suvremenih identifikacijskih procedura, logičan je odabir FEMU metode pošto je moguće identificirati elastoplastično ponašanje i oštećenje materijala u jednoj identifikacijskoj proceduri koristeći UMAT rutinu u FE programskom paketu Abaqus. Polja pomaka i suma reakcijskih sila na rubovima modela je preuzeta pomoću Python koda a minimizacija funkcije cilja je izvedena u programu Matlab.

## Zaključak i doprinos rada

Numeričke simulacije provode se u svrhu procjene cjelovitosti mehaničkih konstrukcija. Kako bi se što pouzdanije opisalo ponašanje materijala uslijed narinutog opterećenja potrebno je što točnije odrediti parametre materijala koji opisuju odabrani konstitutivni zakon. Stoga je u ovom radu predložena primjena novih identifikacijskih procedura kako bi se što pouzdanije opisalo nelinearno mehaničko ponašanje nodularnog lijeva. U radu su, pregledom dosadašnjih istraživanja, pokazane napredne identifikacijske metode i tehnike korelacije digitalne slike. S obzirom na pretpostavljenu problematiku i moguće izazove u istraživanju objašnjeni su razlozi korištenja odabranih procedura. Identifikacija nelinearnog ponašanja provedena je na različitim materijalnim modelima. Uzeti su u obzir konstitutivni zakoni koji opisuju izotropno i kinematičko očvršćenje te model oštećenja materijala. Za opisivanje izotropnog očvršćenja korišten je Johnson-Cook-ov materijalni model dok je kinematsko očvršćenje opisano Armstrong-Frederick-ovim modelom. Predloženi zakoni su odabrani iz razloga što su implementirani u FE program Abaqus te je njihova upotreba bila intuitivni izbor. Oštećenje materijala u sprezi s izotropnim očvršćenjem opisano je UMAT procedurom. Lemaitre-ov model oštećenja i Ludwik-ov zakon su predloženi u spomenutoj proceduri. Provedeno istraživanje obuhvaćalo je interakciju između eksperimentalnih rezultata i modeliranja u svrhu točnijeg opisivanja

ponašanja materijala. U nastavku su istaknuti najvažniji doprinosi koji se odnose na: 1. regulariziranu korelaciju digitalne slike, odnosno dobivanje polja pomaka s većom točnošću, 2. identifikaciju materijalnih parametara pri jednoosnim eksperimentima, 3. identifikaciju materijalnih parametara pri ravninskim dvoosnim opterećenjima, te 4. sveobuhvatni doprinos.

### 1. Regularizirana korelacija digitalne slike

- Za uspješnu provedbu predloženog istraživanja razvijena je nova varijanta globalnog DIC pristupa koja se zasniva na dodavanju mehaničkog funkcionala u svrhu analize samo pojava mehaničke prirode. Primjenom regularizacije pronađen je kompromis između standardne rezolucije pomaka te prostorne rezolucije. Kao rezultat regularizirane korelacije digitalne slike smanjena je mjerna nesigurnost polja pomaka/deformacija u usporedbi s lokalnim i standardnim globalnim DIC pristupom.
- Osim što je potvrđena činjenica da je moguće smanjiti mjernu nesigurnost dobivenog polja pomaka korištenim RT3-DIC algoritmom, izazov analize siromašne teksture nodularnog lijeva uspješno je savladan što nije bilo moguće standardnim korelacijskim pristupima. Razvoj regulariziranih procedura izuzetno je bitan za primjenu tehnika mjerenja cijelog polja pomaka na 3D volumene (tj. skenove) gdje se mnogo češće susreće siromašna struktura materijala.
- Derivati regularizacijske metode, naime, korelacijski i mehanički reziduali dobiveni kao rezultat korelacije digitalne slike pokazuju veću osjetljivost prilikom detekcije diskontinuiteta (mikropukotina) koji se pojavljuju tijekom opterećenja u materijalu za razliku od izmjerenog polja deformacija. Ova činjenica dozvoljava preciznije određivanje trenutka inicijacije mikropukotine te propagaciju makro pukotine.

### 2. Identifikacija materijalnih parametara pri jednoosnim eksperimentima

- Izazov određivanja elastoplastičnih parametara i parametara oštećenja materijala u jednoj identifikacijskoj proceduri je riješen primjenom FEMU metode. Razlika između mjerenih i izračunatih pomaka te mjerene sile i sume reakcijskih sila iz FE analize korišteni su kao kriterij procjene pouzdanosti vrijednosti identificiranih parametara. Važno je naglasiti kako je vidljiva razlika između parametara identificiranih klasičnim putem poklapanja eksperimentalnih podataka s predloženim materijalnim modelom i rezultata dobivenih FEMU procedurom.
- Na cikličkom jednoosnom vlačnom testu pokazano je da ponašanje materijala opisano kinematskim očvršćenjem bolje odgovara eksperimentalnim rezultatima u usporedbi s modelom izotropnog očvršćenja. Pošto spomenuti modeli ne uključuju efekte oštećenja materijala korištena je subrutina koja opisuje

---

izotropno očvršćenje i Lemaitr-ov model oštećenja. Identificirani parametri materijala navedene rutine rezultiraju najmanjim rezidualima između eksperimentalnih podataka te onih dobivenih numeričkim simulacijama. Stoga se može zaključiti kako predloženi model najpouzdanije opisuje ponašanje materijala pri cikličkom opterećenju.

- Provedbom in-situ vlačnog cikličkog eksperimenta promatranog s X-ray računalnom tomografijom detektiran je mehanizam oštećenja kod odabranog tipa nodularnog lijeva. Odvajanje željezne matrice i grafitnih nodula u ranoj fazi opterećenja (tj. elastičnosti) uzrokuje oštećenje u materijalu. Bez provedbe ovakvog ispitivanja nemoguće bi bilo objasniti ponašanje materijala kod eksperimenata provedenih u ovom radu.

### 3. Identifikacija materijalnih parametara pri ravninskim dvoosnim opterećenjima

- Ispitni uzorci korišteni za provedbu dvoosnih testova geometrijski su složeni te je potrebno koristiti 3D FE model. U sklopu ovog istraživanja po prvi put je primijenjeno 2D DIC mjerenje za identifikaciju parametara materijala na prostornom 3D modelu. Pokazano je kako su za geometriju križne epruvete s kalotom uspješno identificirani elastoplastični parametri materijala.
- Model korišten za opisivanje kinematskog očvršćenja i u slučaju dvoosnih ravninskih eksperimenata bolje opisuje ponašanje materijala u usporedbi s predloženim modelom izotropnog očvršćenja u slučaju proporcionalnog i neproporcionalnog tipa opterećenja.
- Dva različita režima dvoosnog ravninskog opterećenja su korištena u ovom istraživanju, proporcionalno opterećenje (equibiaxial) i neproporcionalno (snail). Identifikacijom elastoplastičnih parametara potvrđena je pretpostavka kako se parametri razlikuju od onih određenih jednostavnijim testovima. Vrlo je važno naglasiti kako su s obzirom na narinuti program opterećenja identificirane različite vrijednosti parametara materijala.
- Niz dvoosnih ispitivanja na zamor materijala je provedeno s predloženim programima opterećenja. Rezultati DIC analize zabilježili su formiranje i rast mreže mikropukotina. Veličina mreže mikropukotina je veća kod neproporcionalnog opterećenja te je njezin razvoj također brži nego kod proporcionalnog. Stoga, uz spomenute efekte, istovremeno manji potrebni broj ciklusa do loma epruvete potvrđuje hipotezu kako neproporcionalno dvoosno opterećenje rezultira većim oštećenjem u materijalu.

### 4. Sveobuhvatni doprinos

- Cjelokupni doprinos ovog doktorskog rada odnosi se na bolje razumijevanje nelinearnog mehaničkog ponašanja promatranog nodularnog lijeva. U okviru ovog istraživanja razvijeni su generički algoritmi za identifikaciju parametara materijala te je njihova primjena moguća i na drugim materijalima koji mogu

uključivati raznovrsne režime opterećenja. Predložena su i moguća daljnja istraživanja koja bi trebala rezultirati još pouzdanijim opisivanjem ponašanja materijala.

**Ključne riječi:** nelinearno mehaničko ponašanje materijala, mjerenje cijelog polja pomaka, identifikacija, nodularni lijev, višeosno opterećenje, mreža mikropukotina, regularizacija, tomografija



# List of Figures

1.1	(a) Končar wind turbine. (b) Main parts of the wind turbine . . . . .	13
1.2	Metallography of flotret - type 200 SG cast iron [Čanžar et al., 2012] . . . . .	14
1.3	Influence of graphite shape on stress concentration . . . . .	16
1.4	Crack propagating around nodules . . . . .	17
1.5	True stress-strain curves for four different types of EN-GJS-400-18LT cast irons . . . . .	18
1.6	DVC results on SG cast iron [Rannou et al., 2010] . . . . .	20
1.7	Metallography of sandwich SG cast iron . . . . .	21
1.8	True stress-strain curve of sandwich cast iron . . . . .	22
1.9	Cast shapes . . . . .	23
1.10	Change of stress with respect to plastic equivalent strain. The curve 1 is a fit of the reference stress-strain curve when the points are equally spaced with 1 % plastic strain increments. For curve 2 the points are spaced more densely from 0 to 1 % with 0.1 % increments . . . . .	30
2.1	Three possible situations between neighbouring ZOIs . . . . .	41
2.2	Principle of local approach that registers the ZOI in the reference configuration with that in the deformed configuration . . . . .	42
2.3	Principle of global approach where the whole ROI is taken into account and discretized with Q4 elements in the reference and deformed configurations . . . . .	43
2.4	Standard displacement uncertainty as functions of the ZOI or element size $\ell$ . The results are obtained by Q4-DIC and compared with FFT-DIC. The dashed lines correspond to power-law fits [Besnard et al., 2006] . . . . .	45
2.5	Comparison of local and global approach when discontinuities appear in the image. Cracked CT sample (a) analysed with local (b) and global (c) DIC approaches . . . . .	46
2.6	Reference image of the two artificial cases (a) and the T3 unstructured mesh with the element size of 10 pixels (b) . . . . .	50
2.7	Prescribed displacement field in the sine wave test case in (a) vertical and (b) horizontal directions. The displacements are expressed in pixels . . . . .	51

2.8	Change of standard displacement error for different regularization lengths and different $\ell_b/\ell_m$ ratios in the vertical (left) and horizontal (right) directions. Three initial regularization lengths $\ell_m$ are considered: (a) & (b) 32, (c) & (d) 256, and (e) & (f) 1024 pixels . . . . .	52
2.9	Sine wave test case. Change of the standard displacement error for different regularization lengths and different $\ell_m$ initialization lengths (in pixels) indicated in the legend: (a) error in vertical and (b) in horizontal directions	53
2.10	Residual fields when $\ell_m = 1$ pixel with an initial length of 128 (a) and 1024 pixels (b). The fields are expressed in grey levels . . . . .	54
2.11	Sine wave test case. Change of (a) the dimensionless correlation residuals and (b) equilibrium residuals for different regularization lengths and different initialization lengths $\ell_m$ (in pixels) indicated in the legend . . . .	54
2.12	Prescribed displacement field in the mechanical test case in (a) vertical and (b) horizontal directions. The displacements are expressed in pixels .	55
2.13	Mechanical test case. Change of the standard displacement error for different regularization lengths and different $\ell_m$ initialization lengths (in pixels) indicated in the legend. (a) Standard error in vertical and (b) in horizontal direction . . . . .	56
2.14	Mechanical test case. Change of (a) the dimensionless correlation residuals and (b) equilibrium residuals for different regularization lengths and different initialization lengths $\ell_m$ (in pixels) indicated in the legend . . . .	56
3.1	Uniaxial setup on an <i>MTS</i> servo-hydraulic machine with the optical equipment . . . . .	66
3.2	Dog-bone sample for uniaxial tensile tests. (a) One side has a black and white texture used for DIC measurements, and (b) the other one has a rosette measuring strains in the longitudinal and transverse directions . .	67
3.3	Reference image with no applied load (a) and T3 mesh with an element size of 14 (b) and 25 (c) pixels . . . . .	68
3.4	Change of the standard displacement resolution in (left) transverse and (right) longitudinal directions for different regularisation lengths $\ell_m$ and the two meshes. The legend indicates the initial length $\ell_m$ (in pixels) . . .	69
3.5	Change of (left) the dimensionless correlation residuals and (right) equilibrium residuals for different regularisation lengths and different initialisations for (a) & (b) 14-pixel, and (c) & (d) 25-pixel element size. Note the narrow range of variation of $\hat{\Phi}_c$ . . . . .	70
3.6	Two analyses performed in the elastic regime where longitudinal (a) and transverse (b) strains were measured with the rosette. (c) Poisson's ratio evaluated via Equation (3.1) . . . . .	72

## List of Figures

---

3.7	Reference picture of monotonic uniaxial experiment used for a DIC analysis with 25-pixel elements. The blue rectangle depicts the zone where the DIC gauge was measuring the mean strain. Edge regularisation was applied on the green nodes while all the others were treated as inner nodes. In the FEMU procedure, boundary conditions measured with DIC were prescribed on the edge nodes labelled with green circles . . . . .	73
3.8	Comparison of measured (a) longitudinal ( $\epsilon_L$ ) and (b) transverse ( $\epsilon_T$ ) strains with rosette and DIC gauge. (c) Poisson's ratio is calculated with Equation (3.1) . . . . .	74
3.9	Stress-strain curve for the tensile test. The curve is divided in two parts (back line) elastic, and (red line) plastic part. The marker denotes the yield point while the blue line fits the slope of Young's modulus. . . . .	75
3.10	Measured displacement fields via RT3-DIC in (a) transverse and (b) longitudinal directions for a load level corresponding to 18 kN . . . . .	76
3.11	Change of the three identified Johnson-Cook parameters with the number of iterations. Three variants (-U, -F, -UF) of FEMU are compared . . . . .	79
3.12	Change of displacement ( $\chi_u$ ) and force ( $\chi_F$ ) residuals with the number of iterations when identifying Johnson-Cook's parameters. Three variants (-U, -F, -UF) of FEMU are compared . . . . .	80
3.13	(a) Comparison of measured force and sum of the reaction forces for the three FEMU variants. (b) Comparison of measured force and sum of reaction forces computed with initial and identified Johnson-Cook's parameters via FEMU-UF . . . . .	80
3.14	Sensitivity of the displacement field with respect to each sought parameter. The maps correspond to differences of displacements (expressed in pixel) when the sought parameter is changed by 1 % . . . . .	82
3.15	Sensitivity of the load level ( <i>i.e.</i> , sum of reaction forces) with respect to each sought parameter of Johnson-Cook's law for a 1 % variation . . . . .	83
3.16	Comparison of measured force and sum of reaction forces computed with the initial and identified parameters for Armstrong-Frederick's law . . . . .	84
3.17	Sensitivity of the displacement field with respect to each sought parameter. The maps correspond to differences of displacements (expressed in pixel) when the sought parameter is changed by 1 % . . . . .	85
3.18	Sensitivity of the load level ( <i>i.e.</i> , sum of reaction forces) with respect to each sought parameter of Armstrong-Frederick's law for a 1 % variation . . . . .	86
3.19	Experimental setup on an <i>Instron</i> electro-mechanical machine . . . . .	86
3.20	Loading history for the uniaxial cyclic experiment. The image acquisition rate was 1 frame/s . . . . .	87
3.21	Reference image without applied load (a) and T3 mesh with an element sizes of 14 (b) and 25 (c) pixels . . . . .	88
3.22	Change of standard displacement resolution in (left) transverse and (right) longitudinal directions for different regularisation lengths $\ell_m$ with two meshes. The legend indicates the initial length $\ell_m$ (in pixels) . . . . .	89

3.23	Change of (left) the dimensionless correlation residuals and (right) equilibrium residuals for different regularisation lengths and different initialisations for two element sizes. Note the narrow range of variation of $\hat{\Phi}_c$ . . . . .	90
3.24	Comparison of measured $\varepsilon_L$ (a) and $\varepsilon_T$ (b) with strain gauge and DIC gauge. (c) Instantaneous Poisson's ratio calculated with Equation (3.1) . . . . .	92
3.25	Stress-strain curve for monotonic and cyclic tensile tests . . . . .	93
3.26	Sensitivity of the displacement field with respect to a change of 1% of Poisson's ratio $\nu$ (in pixel). (a) Cut in the middle of the longitudinal direction and (b) in the middle of the transverse direction of the ROI . . . . .	94
3.27	Comparison of measured force and sum of reaction forces computed with initial and identified material parameters for Johnson-Cook's law . . . . .	95
3.28	Comparison of measured force and sum of reaction forces computed with the initial and identified parameters for Armstrong-Frederick's constitutive law . . . . .	95
3.29	RVE used to get a first estimate of the damage parameters. Displacement distribution of the last loading level of the cyclic experiment corresponding to 22 kN . . . . .	97
3.30	Change of Young's modulus with cumulative plastic strain . . . . .	97
3.31	Comparison of the measured force and sum of reaction forces computed with the initial and identified material parameters of an elastoplastic law coupled with damage for the RVE . . . . .	98
3.32	Comparison of measured force and sum of reaction forces computed with the initial and identified parameters of the elastoplastic and damage law . . . . .	99
3.33	X50+ Computed Tomography System (a) and corresponding custom made uniaxial tensile machine for in situ tomography experiments (b) . . . . .	101
3.34	Loading history of the in situ experiment on X50+ CT system . . . . .	101
3.35	(a) Dog-bone sample used for tomography. The red zone inside the sample denotes the investigated ROI ( $160 \times 196 \times 608$ voxels). (b) Reference volume ( $F = 200$ N) . . . . .	102
3.36	Standard displacement resolution with C8 and RC8-DVC for different regularisation lengths $\ell_m$ (RC8-DVC) or element size $\ell$ (C8-DVC, circle). 16-voxel elements are used in RC8-DVC . . . . .	104
3.37	Measured displacement fields in (a) & (b) $x$ , (b) & (c) $y$ and (c) & (d) $z$ -directions corresponding to load levels 560 N (left) and 750 N (right). . . . .	105
3.38	Von Mises' equivalent strain fields (a) & (b), and gray level residual fields (c) & (d) for load levels 560 N (left) and 750 N (right) . . . . .	106
3.39	Residual maps corresponding to the plane normal to the $y$ -axis for the 12 scans . . . . .	108
3.40	SEM analysis of the broken tomographic sample . . . . .	109
4.1	Triaxial testing machine ASTREE (LMT-Cachan) . . . . .	116
4.2	Maltese cross-shaped specimen designed for in-plane biaxial experiments . . . . .	118

## List of Figures

---

4.3	Two-scale experimental setup. (a) Mesoscale optical setup, (b) macroscale optical setup, (c) CCD camera <i>Dalsa</i> with telecentric lens (magnification $\times 4$ ), (d) macroscale image, (e) beam-splitter, (f) CCD camera <i>Pixelfly</i> with telecentric lens (magnification $\times 1$ ), (g) DedoCool light source, (h) mesoscale image . . . . .	119
4.4	The two prepared sides of the cross-shaped specimen for two-scale observations. (a) Artificial texture for macro- and (b) polished surface for mesoscale observations . . . . .	120
4.5	One cycle for (a) equibiaxial and (b) “snail” loading histories. Equibiaxial loading consists of two ( <i>i.e.</i> , (1)-(2)) characteristic points while “snail” history has four ( <i>i.e.</i> , (1)-(2)-(3)-(4)) . . . . .	121
4.6	FE model used to estimate the (un)loading path of equibiaxial and “snail” regimes . . . . .	122
4.7	Equibiaxial loading regime. Applied load level with respect to number of pictures . . . . .	123
4.8	“Snail” loading paths. Applied load level with respect to number of images	123
4.9	Reference image at the macroscale (a) and corresponding T3 unstructured mesh with an element size of 10 pixels (b) . . . . .	124
4.10	Change of the standard displacement resolutions for different regularization lengths $\ell_m$ and different initialization lengths (in pixels) indicated in the legend. (a) Displacement resolution in vertical and (b) in horizontal directions . . . . .	125
4.11	Change of (a) the dimensionless correlation residuals and (b) equilibrium residuals for different regularization lengths and different initializations. Note the narrow range of variation of $\hat{\Phi}_c$ . . . . .	126
4.12	Reference image of the mesoscale resolution analysis (a) and corresponding T3 unstructured mesh with an element size of 10 pixels . . . . .	126
4.13	Standard displacement errors in (a) the vertical and (b) horizontal directions for different regularization lengths $\ell_m$ when $\ell_b/\ell_m = 1/2$ . The legend indicates the initial regularization length $\ell_m$ (in pixels) . . . . .	128
4.14	Change of (a) the dimensionless correlation residuals and (b) equilibrium residuals for different regularization lengths and different initializations. Note the narrow range of variation of $\hat{\Phi}_c$ . . . . .	128
4.15	Standard displacement resolution in (a) the vertical and (b) horizontal directions for different regularization lengths $\ell_m$ , ZOI (dashed blue line) or element (solid blue line) sizes $\ell$ when $\ell_b/\ell_m = 1/2$ . The legend indicates the initial length $\ell_m$ (in pixels) . . . . .	129
4.16	Change of (a) the dimensionless correlation residuals and (b) equilibrium residuals for different regularization lengths and different initializations. Note the narrow range of variation of $\hat{\Phi}_c$ . . . . .	130
4.17	Measured displacement fields at the macroscale in the horizontal (a) and vertical (b) directions for a load level equal to 30 kN. The displacements are expressed in pixels. The physical size of one pixels is equal to $48 \mu\text{m}$ .	131

4.18	Measured displacement fields at the mesoscale in the horizontal (a) and vertical (b) directions for a load level corresponding to 30 kN. The displacements are expressed in pixels. The physical size of one pixels is equal to $6.7 \mu\text{m}$ . . . . .	131
4.19	DIC gauges at the two scales. (a) Macroscale and (b) mesoscale DIC gauges depicted as square (blue) zones over the T3 unstructured mesh with 10 pixel elements (red) . . . . .	132
4.20	Change of (a) $\epsilon_{11}$ , (b) $\epsilon_{22}$ , (c) $\epsilon_{12}$ during the equibiaxial test on macro- and mesoscales . . . . .	133
4.21	(a) Change of mean eigen strain components on the macroscale with time. (b) Dependence of mean eigen strains ( <i>i.e.</i> , $\epsilon_1$ vs. $\epsilon_2$ ) . . . . .	134
4.22	(a) Image at mesoscale corresponding to a load level of 55 kN, (b) correlation residuals (expressed in gray levels) revealing the crack network . .	134
4.23	Implementation of boundary conditions obtained from 2D-DIC measurement onto the 3D FE model. (a) 3D FE model created in Abaqus, (b) nodes (red circles) extracted from the 3D model to create a 2D mesh for RT3-DIC, (c) model nodes (red circles) used to prescribe the measured displacements from DIC analyses, (d) T3 mesh fitted and scaled onto the reference image, (e) DIC displacements prescribed as boundary conditions of the FE model, (f) symmetry boundary condition . . . . .	136
4.24	Comparison of measured force and sum of reaction forces computed with initial and identified elastic parameters . . . . .	137
4.25	Comparison of measured force and sum of reaction forces computed with initial and identified material parameters for Johnson-Cook's constitutive law . . . . .	139
4.26	Comparison of measured force and sum of reaction forces computed with initial and identified parameters for Armstrong-Frederick' constitutive law	140
4.27	Measured displacement fields at the macroscale in the horizontal (left) and vertical (right) directions for a maximum loading level of 30 kN. (a) and (b) correspond to loading point 1 (FIG. 4.5(b)), (c) and (d) correspond to loading point 2 (see FIG. 4.5(b)), (e) and (f) correspond to loading point 3 (see FIG. 4.5(b)) . . . . .	142
4.28	Measured displacement fields at the mesoscale in the horizontal (left) and vertical (right) directions for a maximum load level of 30 kN. (a) and (b) correspond to loading point 1 (see FIG. 4.5(b)), (c) and (d) correspond to loading point 2 (see FIG. 4.5(b)), (e) and (f) correspond to loading point 3 (see FIG. 4.5(b)). . . . .	143
4.29	Change of (a) $\epsilon_{11}$ , (b) $\epsilon_{22}$ , (c) $\epsilon_{12}$ during the fully load-controlled "snail" test at the macro- and mesoscales . . . . .	144
4.30	(a) Change of the mean eigen strains on the macroscale with respect to time. (b) Dependence of mean eigen strains ( <i>i.e.</i> , $\epsilon_1$ vs. $\epsilon_2$ ) . . . . .	145
4.31	Measured loading history for the "snail" test . . . . .	145

## List of Figures

---

4.32	Comparison of measured force and sum of reaction forces computed with the initial and identified elastic parameters for (a-c) loading direction 1, and (b-d) loading direction 2 of the load-controlled (a-b) and hybrid (c-d) “snail” tests . . . . .	147
4.33	Comparison of measured force and sum of reaction forces computed with the initial and identified material parameters for Johnson-Cook’s law for (a-c) loading direction 1, and (b-d) loading direction 2 of the load-controlled (a-b) and hybrid (c-d) “snail” tests . . . . .	149
4.34	Comparison of measured force and sum of reaction forces computed with the initial and identified material parameters for Armstrong-Frederick’s law for (a-c) loading direction 1, and (b-d) loading direction 2 of the load-controlled (a-b) and hybrid (c-d) “snail” tests . . . . .	151
5.1	Strain histories describing the first cycle of equibiaxial experiment 1 ( $F_{max} = 50$ kN). (a) Normal strains in the loading directions of the sample. (b) Mean eigen strains. Blue, green and yellow circles correspond to the three characteristic points of equibiaxial experiments (see FIG. 4.5(b)) . . . . .	157
5.2	EBE-1: (a) Displacement and (b) mechanical residual maps corresponding to maximum imposed load level ( <i>i.e.</i> , $F_1 = F_2 = 50$ kN) at first cycle. . . . .	158
5.3	Comparison of measured force and sum of reaction forces computed with the initial and identified parameters for Armstrong-Frederick’ constitutive law . . . . .	159
5.4	Measured (a) $\epsilon_1$ and (b) $\epsilon_2$ histories with respect to the number of cycles. The maximum peak values are denoted by yellow circle and minimum with green circles . . . . .	161
5.5	Measured amplitudes for (a) $\epsilon_1$ and (b) $\epsilon_2$ at macro and mesoscales . . . . .	162
5.6	(a) Change of mesoscale mechanical $\tilde{\Phi}_m$ and normalized correlation residuals $\hat{\Phi}_c$ with the number of cycles. (b) Corresponding change of $\tilde{\Phi}_m$ and $\hat{\Phi}_c$ with respect to the strain amplitude $\Delta\epsilon_1/2$ . . . . .	163
5.7	Mesoscale gray level (left) and mechanical (right) residual maps corresponding to the maximum applied load level . . . . .	165
5.8	Mean eigen strains for the first cycle of equibiaxial experiment 5 ( <i>i.e.</i> , $F_{max} = 20$ kN). Blue, green and yellow circles correspond to the three characteristic points of equibiaxial experiments (FIG. 4.5(a)) . . . . .	166
5.9	(a) Gray level and (b) mechanical residual maps corresponding to a maximum applied load $F_1 = F_2 = 20$ kN) for the first cycle . . . . .	166
5.10	Correlation between mechanical ( $\tilde{\Phi}_m$ ) and normalised correlation ( $\hat{\Phi}_c$ ) residuals from whole series of images acquired in experiment EBE-5 . . . . .	167
5.11	(a) Change of mesoscale mechanical $\tilde{\Phi}_m$ and normalized correlation residuals $\hat{\Phi}_c$ with the number of cycles. For comparison purposes $\Delta\epsilon_1/2$ are reported at macro and mesoscales. (b) Change of $\tilde{\Phi}_m$ and $\hat{\Phi}_c$ with the strain amplitude $\Delta\epsilon_1/2$ at the mesoscale . . . . .	168
5.12	Correlation residual maps for different cycle number . . . . .	169

5.13	History of (a) maximum mean eigen and (b) minimum mean eigen strain amplitudes observed at the macroscale . . . . .	171
5.14	History of (a) maximum mean eigen and (b) minimum mean eigen strain amplitudes observed at the mesoscale . . . . .	172
5.15	Comparison of measured force and sum of reaction forces computed with initial and identified parameters for Armstrong-Frederick' constitutive law	173
5.16	Strain histories describing the first cycle of "snail" experiment 2 ( $F_{max} = 40$ kN). (a) Normal strain for the two loading directions. (b) Mean eigen strains. Blue, green, yellow, black and red circles correspond to five characteristic points of "snail" experiment (see FIG. 4.5(b)) . . . . .	175
5.17	(a) Gray level and (b) mechanical residual maps corresponding to the maximum applied load level ( <i>i.e.</i> , $F_1 = F_2 = 40$ kN) . . . . .	176
5.18	Measured (a) $\epsilon_1$ and (b) $\epsilon_2$ history. The maximum peak values are depicted with yellow circles and minimum with green circles . . . . .	177
5.19	Measured strain amplitudes (a) $\epsilon_1$ and (b) $\epsilon_2$ at macro and mesoscales . .	178
5.20	(a) Change of mechanical $\tilde{\Phi}_m$ and normalized correlation residuals $\hat{\Phi}_c$ with the number of cycles. (b) Change of $\tilde{\Phi}_m$ and $\hat{\Phi}_c$ with respect to the strain amplitude $\Delta\epsilon_1/2$ at the mesoscale . . . . .	179
5.21	Gray level (left) and mechanical (right) residual maps corresponding to the maximum applied load level for different cycle numbers . . . . .	181
5.22	Mean eigen strains for the first cycle of "snail" experiment 5 ( $F_{max} = 20$ kN). Five characteristic points (FIG. 4.5(b)) of "snail" experiment depicted	182
5.23	(a) Gray level and (b) mechanical residual maps corresponding to the load level when the maximum value of $\epsilon_1$ is reached ( <i>i.e.</i> , $F_1 = 0, F_2 = 20$ kN) for the first cycle . . . . .	182
5.24	(a) Change of mesoscale mechanical $\tilde{\Phi}_m$ and normalized correlation residuals $\hat{\Phi}_c$ with the number of cycles. For comparison purposes $\Delta\epsilon_1/2$ are reported at macro and mesoscales. (b) Change of $\tilde{\Phi}_m$ and $\hat{\Phi}_c$ with respect to the strain amplitude $\Delta\epsilon_1/2$ at the meso scale . . . . .	183
5.25	Correlation residual maps for different cycle number . . . . .	184
5.26	History of the (a) maximum mean eigen and (b) minimum mean eigen strain amplitudes on macroscale . . . . .	186
5.27	History of the (a) maximum mean eigen and (b) minimum mean eigen strain amplitudes on mesoscale . . . . .	187
5.28	Comparison of equibiaxial and snail tests. Applied load versus number of cycles to failure. Load levels for first cycle correspond to biaxial experiments presented in CHAP. 4 . . . . .	189
E.1	Measured displacement fields at macroscale in the horizontal (left) and vertical (right) directions for the loading step corresponding to 30 kN. (a) and (b) correspond to point 1 (see FIG. 4.5(b)), (c) and (d) correspond to point 2 (see FIG. 4.5(b)), (e) and (f) correspond to point 3 (see FIG. 4.5(b))	218



## List of Figures

---

E.2	Measured displacement fields at mesoscale in the horizontal (left) and vertical (right) directions for the loading level corresponding to 30 kN. (a) and (b) correspond to point 1 (see FIG. 4.5(b)), (c) and (d) correspond to point 2 (see FIG. 4.5(b)), (e) and (f) correspond to point 3 (see FIG. 4.5(b))	219
E.3	Changes of (a) $\epsilon_{11}$ , (b) $\epsilon_{22}$ , (c) $\epsilon_{12}$ during the hybrid “snail” loading history on macro and mesoscales . . . . .	220
E.4	(a) Change of mean eigen strains on macroscale with the picture number. (b) Dependence of mean eigen strains ( <i>i.e.</i> , $\epsilon_1$ vs. $\epsilon_2$ ) . . . . .	221
E.5	Measured loads in the hybrid “snail” path . . . . .	222



# List of Tables

1.1	Chemical compositions in mass% of different SG cast irons. . . . .	14
1.2	Chemical compositions in mass% of SG cast iron produced by the sandwich technique . . . . .	21
3.1	Identified elastoplastic parameters . . . . .	75
3.2	Elastic parameters identified with FEMU. The reference values denote conventionally determined data. The FEMU-U procedure is carried out with fixed $E$ , and FEMU-F with fixed $\nu$ . In FEMU-UF both parameters are identified at the same time . . . . .	77
3.3	Identified Johnson-Cook parameters with the three different variants of FEMU . . . . .	78
3.4	Identified Armstrong-Frederick's parameters with three different variants of FEMU . . . . .	83
3.5	Initial and identified elastic parameters for cyclic uniaxial tension . . . .	91
3.6	Identified Johnson-Cook parameters via FEMU-UF . . . . .	94
3.7	Identified Armstrong-Frederick's parameters with the FEMU-UF variant .	96
3.8	Identified elastoplastic and damage parameters on an RVE via FEMU-UF	98
3.9	Identified elastoplastic and damage parameters with an FE model . . . . .	99
4.1	Initial and identified elastic material parameter for equibiaxial experiment	137
4.2	Initial and identified Johnson-Cook parameters by FEMU-UF for an equibiaxial loading path . . . . .	138
4.3	Initial and identified Armstrong-Frederick's parameters via FEMU-UF for an equibiaxial loading path . . . . .	139
4.4	Measurement displacement resolution calculated for fully load-controlled and hybrid "snail" tests . . . . .	146
4.5	Initial and identified elastic parameters for "snail" tests . . . . .	146
4.6	Identified Johnson-Cook material parameters on "snail" test cases. . . . .	150
4.7	Identified Armstrong-Frederick's parameters for the two "snail" tests . . .	150
5.1	Definition of the equibiaxial and "snail" loading paths. The acronym EBE refers to the <i>equibiaxial experiment</i> and SBE to the <i>"snail" biaxial experiment</i> . . . . .	155

5.2	Initial and identified Armstrong-Frederick's parameters via FEMU-UF for an equibiaxial loading path . . . . .	159
5.3	Number of cycles to failure for the equibiaxial tests . . . . .	170
5.4	Initial and identified Armstrong-Frederick's parameters via FEMU-UF for a snail loading path . . . . .	174
5.5	Number of cycles to failure for the "snail" experiments . . . . .	185

# Introduction

## Background and motivation

The rapid development of industry requires the production of new engineering structures. They must meet the requirements of the latter ones, namely, use at higher workloads and exploitation at extreme working conditions while at the same time having longer lifetime and reliability. This trend stimulates the development of advanced methods of design and description of the material behaviour. In recent years, particular attention was given to exploring the influence of the material microstructure on its mechanical behaviour [Hübner et al., 2007, Costa et al., 2008, Costa et al., 2010]. Classical (macro)mechanics does not consider microstructural features of the material, and this calls for mechanism-based models to describe the nonlinear phenomena in the microstructure of materials such as distribution, orientation and size of damage. In such cases the material heterogeneity plays an important role.

The development of new engineering elements has increased the application of new technologies and materials. During the exploitation the majority of engineering structures is subjected to complex loading regimes (*e.g.*, aeronautical, astronautical, automotive, chemical, power generation, petroleum, and transportation industries). The extensive use of engineering structures over such a wide range of applications has generated extraordinary interest in the material behavior and fatigue durability of these materials under multiaxial loading conditions. Specifically, the technical areas of interest include strength of the materials under multiaxial loading conditions, multiaxial deformation and fatigue of materials, and development of multiaxial experimental capabilities to test materials under controlled prototypical loading conditions. To describe these loading regimes in more reliable manners multiaxial experiments started to be conducted at LMT [Batisse et al., 1996, Doudard et al., 2007, Poncelet et al., 2010, Fremy et al., 2014]. With the development of multiaxial testing machines (biaxial, triaxial, multiaxial (hexapod)) a new era of experiments was opened thanks to the possibility of prescribing a wide range of loading histories [Poncelet et al., 2010, Fremy et al., 2014]. The results of multiaxial tests are important, in particular, for the characterization of the material properties and the development of constitutive laws that can be used for predictive purposes (*i.e.*, fatigue).

In materials science, fatigue is the progressive and localized structural damage that occurs when a material is subjected to cyclic loading. If the load levels are above a certain threshold, microscopic cracks will begin to form on the surface. Eventually a crack will

reach a critical size, and the structure will suddenly fail. Fatigue crack closure was first described by Elber more than 30 years ago. Although it is a critical issue for lifetime predictions through Paris' law [Paris et al., 1961, Paris and Erdogan, 1963] (with the use of effective stress intensity factor ranges), there is still no unified method of measurement that reaches general consensus.

The work presented herein is a continuation of the “*Development of Fatigue Analysis Procedure for Wind Turbine Components*” project. Wind turbines as a complex product are made out of many different materials (*e.g.*, ductile cast iron, gray cast iron, steels) depending on the construction demands and loading regimes during exploitation. During their lifetime they are subjected to variable cyclically loading regimes. To satisfy the latter demands ductile cast iron is used as the material for cyclic loaded parts of the windmill. Due to low production costs and good material properties in cyclic loaded constructions SG cast iron is suitable to be considered in such working conditions. Within the latter project four different types of ductile cast iron were investigated under uniaxial cyclic loading [Čanžar et al., 2012]. The aim was to observe from a macroscopic point of view the influence of matrix phases, distribution, size, density of nodules on the cyclic and fracture behaviour in order to define the microstructure of nodular cast iron with optimal mechanical properties.

One of the significant cast irons used in engineering applications contains graphite nodules. Ductile cast iron (also known as nodular graphite cast iron, ductile cast iron, spheroidal graphite cast iron or SG cast iron) is essentially a family of materials with a wide variety of properties for different engineering requirements. Even though the exact reasons for the formation of the graphite nodules are not fully understood, cast iron has a wide range of properties that are achieved by the controlled process of production. The base material of a ductile iron, namely the iron matrix, contains spheroidal graphite inclusions randomly distributed. Due to its low melting point and its good flowing properties while in the liquid state fabrication of parts out of cast iron is achieved through molding the melted material into the desired form. This stands in contrast to most steels, where the final shape is obtained through cutting and forming processes [Martin, 2006].

After a continuous development SG cast iron has reached a level of reliability that justifies its increasing use for highly stressed structures and components (*e.g.*, powerful wind power plants). Engineering components of the wind turbine during their lifetime are subjected to extreme (over)loading conditions imposing complex stresses that induce nonlinear material behaviour [Hübner et al., 2007, Costa et al., 2010], crack initiation [Iacoviello et al., 2008, Čanžar et al., 2012], damage [Iacoviello et al., 2008]. When the latter phenomena occur it is necessary to predict [Mottitschka et al., 2010] how the material response will be in the future. In order to obtain more reliable data on SG cast iron it is desirable to perform multiaxial experiment (*e.g.*, in-plane biaxial test) under different loading regimes to access more trustworthy nonlinear material parameters corresponding to exploitation conditions.

Conventional methods for measuring experimental data were not capturing all the phenomena occurring due to the material. This trend stimulated in the last few decades scientists to describe the material behaviour with more reliable and complex constitutive

laws and to develop advanced methods for identification and validation of material parameters. Furthermore, new identification procedures have been developed to explicitly deal with full-fields [Grédiac, 1989a, Calloch et al., 2002b, Claire et al., 2002, Grédiac et al., 2006, Avril et al., 2008a, Leclerc et al., 2009, Robert et al., 2012, Mathieu et al., 2014]. In terms of kinematic fields measured via Digital Image Correlation, new procedures are considered. For instance, *Digital Image Correlation* (DIC) [Lucas and Kanade, 1981, Peters and Ranson, 1982, Sutton et al., 1983, Chu et al., 1985, Sutton et al., 1986, Besnard et al., 2006] as a full-field measurement technique coupled with Finite Element algorithms is perfectly suited for identification purposes [Cooreman et al., 2007, Gras et al., 2013, Mathieu et al., 2014]. The sought elasto-plastic [Grédiac and Pierron, 2006, Avril et al., 2008a, Robert et al., 2012, Gras et al., 2013, Mathieu et al., 2014] and damage parameters [Claire et al., 2002, Claire et al., 2004, Chalal et al., 2004, Rossi et al., 2006, Bouterf et al., 2015, Hild et al., 2014] were identified via various identification procedures (CHAP. 1) using full-field measurements.

Damage mechanisms that occur upon loading the structure made from SG cast iron are not completely clear since on heterogeneous microstructures several paths were observed. Microscopic investigations [Iacoviello et al., 2008] made on different grades of ductile cast iron showed that damage can be initiated inside of the graphite nodule, from microcavities, casting imperfections, debonding of the matrix and the nodules. These results were observed on the surface of samples. With the development of X-ray computed tomography a new path is opened when performing and analysing the material behaviour since it is revealed in the specimen bulk. Hence, due to its heterogeneity SG cast iron is interesting to observe at the microscale [Limodin et al., 2009, Rannou et al., 2010, Limodin et al., 2010]. X-ray tomography coupled with Digital Volume Correlation (DVC) allows damage mechanisms to be captured and models to be improved.

## Hypothesis and objectives

The research presented in this thesis concerns the identification of elastoplastic and damage parameters of SG cast iron for different loading regimes. Simple (*i.e.*, uniaxial) and complex (*i.e.*, in-plane biaxial) experiments will be carried out. The material parameters obtained with simple tests are not necessarily suitable for the description of more complex loading histories. The aim of the proposed methodology is to determine trustworthy non-linear material parameters for each loading definition coupling full-field measurements and numerical simulations. Global DIC is strategically suitable to couple with numerical simulations since the formulation is based on the Finite Element (FE) method and the resolution is lower than in the local DIC [Hild and Roux, 2012]. Finite Element Model Updating (FEMU) [Avril et al., 2008a, Robert et al., 2012, Mathieu et al., 2013, Gras et al., 2013] will be applied for identification purposes of constitutive laws of cast iron. The next aim is to get the growth law of damage in cast iron from cyclic tests. The main challenge will be to couple the elastoplastic and damage parts in the identification process.

In order to better capture the damage behaviour (*i.e.*, crack initiation) complex tests

will be monitored at two scales, namely, macro- and mesoscales. The obtained results will be compared. For the mesoscale, the natural texture of cast iron is used in DIC analyses. If a poor natural texture arises at the mesoscale conventional or even standard global DIC approaches may fail to capture accurately the displacement fields. Due to the increase of the measurement uncertainty, it is likely that regularization techniques will be needed [Leclerc et al., 2009]. Furthermore, to have access to the damage mechanisms occurring in the investigated SG cast iron an in-situ uniaxial experiment will be carried out in a lab tomograph. Global DVC (C8-DVC [Roux et al., 2008] and/or regularized RC8-DVC [Leclerc et al., 2011]) will be used.

## Expected scientific contribution of proposed research

The research results will contribute to a better understanding of the nonlinear behaviour of nodular cast iron under different loading regimes. Since nodules act as crack arresters, analysing the parameters that influence crack propagation based upon the identification results obtained in this project will enable for a more accurate assessment of the integrity of various engineering components with respect to exploitation conditions.

The aim is to get more reliable data on different complex loading histories. After identifying material parameters, the quantification of the uncertainty/residuals will be assessed for different loading regimes and various material models. Residuals (*i.e.*, difference of measured and calculated force and displacement) will be used to estimate the quality of the estimated parameters. The novelty of the identification procedure will be using 2D DIC measurements for application as boundary conditions (BC) on 3D FE models.

To compare the results on macro- and mesoscales it will be necessary to overcome the problem of low grey level dynamic range of the observed area. It is expected that the standard displacement resolution can be decreased with the help of regularization in such a way that it includes the mechanical admissibility of the expected measured displacement field.

## Outline of the thesis

This work describes the identification of elastoplastic and damage parameters of the investigated SG cast iron for different loading regimes. The proposed identification procedure is based on the coupling of full-field measurements and Finite Element simulations. First, a bibliographic research is presented and focused on the properties of nodular cast iron. The various tools used in this work are then presented.

Simple (*i.e.*, uniaxial) experiments are performed in order to obtain the first estimates of material parameters describing isotropic and kinematic hardening. Johnson-Cook and Armstrong Frederick constitutive models are considered. Second, in-plane biaxial experiments are carried out and analysed with advanced identification methods. The material parameters to describe nonlinear behaviour will be identified and compared.

Besides the present **Introduction**, the manuscript is organized as follows:



- **Part 1** presents the current research on the investigated material, nonlinear constitutive laws, advanced identification procedures and full-field measurement techniques (namely, DIC and DVC):
  - **Chapter 1** first introduces a brief bibliographical overview on SG cast iron where the heterogeneous microstructure is presented with the corresponding mechanical properties which has led to the direction of research. Second, the nonlinear material models are described with an emphasis on Johnson-Cook's isotropic hardening, Armstrong-Frederick's kinematic hardening and Lemaitre's damage model. In the final part advanced identification strategies using DIC measurements are summarised.
  - **Chapter 2** introduces the DIC approaches. Local (*i.e.*, subset-based) and global (*i.e.*, FE-based) approaches are discussed and presented. Two variants of global DIC are introduced. A regularized correlation procedure is presented with a validation on artificially deformed images considering measurement uncertainty as a criterion to satisfy. The second route is Integrated DIC that can be interpreted as a measurement and identification method. The last part introduces the recently developed DVC technique.
- **Part 2** presents the identification of elastoplastic and damage parameters on uniaxial experiments.
  - **Chapter 3** is devoted to the identification of elastoplastic and damage material parameters. Two different uniaxial loading histories are considered (*i.e.*, monotonic and cyclic). First the monotonic loading history is presented with its experimental setup and uncertainty analysis. The identified parameters are reported for elastoplasticity via direct curve fitting. The material parameters identified via FEMU are assessed and compared with those previously determined. A cyclic uniaxial test is analysed in the same way as the previous one. Additional elastoplastic and damage identifications are reported. The damage parameters are first introduced for a simple case when a representative volume element is modelled and later on results are determined on the whole 3D FE model. Last, a uniaxial experiment conducted in a lab tomograph is presented. Displacement fields and residual maps are shown and a damage mechanism is proposed.
- **Part 3** introduces the identifications carried out on biaxial experiments.
  - **Chapter 4** first presents a short bibliographical overview on in-plane biaxial experiments and introduces the triaxial servo-hydraulic testing machine AS-TREE, which was used in the present work. In the sequel a two-scale optical setup is used to capture kinematic changes occurring on the both sides of the sample. Macro- and mesoscale results are discussed and compared. For the

proportional (*i.e.*, equibiaxial) and non-proportional (*i.e.*, “snail”) loading histories FEMU will couple 2D-DIC and 3D-FE analyses to identify material parameters (*i.e.*, elasticity, isotropic and kinematic hardening).

- **Chapter 5** is devoted to biaxial fatigue experiments. Two series of fatigue experiments are presented. First, a series of five equibiaxial experiments is performed, and second, “snail” loading regimes on five other samples. The goal is to assess the fatigue lifetime for these two loading paths in order to evaluate the more damaging one. Two-scale DIC analyses are performed to measure displacement fluctuations on both sample sides. From mesoscale observation crack networks are detected and observed with respect to the number of cycles. A further validation of the nonlinear kinematic hardening model will also be assessed.

Last, **Conclusions and prospects** close the manuscript with an overall summary of the work and a list of potential future developments.

# **Part I**

## **State of the art**



# Chapter 1

## Material, models and methodology

*This chapter introduces a brief overview on mechanical features of SG cast iron correlated with its heterogeneous microstructure. Elastoplastic and damage constitutive models are described. Advanced identification methods will be presented with a focus on the nonlinear behaviour.*

### Contents

---

<b>1</b>	<b>Preface</b> . . . . .	<b>11</b>
<b>2</b>	<b>Studied material: SG cast iron</b> . . . . .	<b>11</b>
2.1	Introduction . . . . .	11
2.2	Microstructure . . . . .	12
2.3	Mechanical properties . . . . .	16
2.4	Application of cast iron . . . . .	19
2.5	SG cast iron produced with sandwich technique . . . . .	21
<b>3</b>	<b>Constitutive equations describing elastoplasticity and damage</b> . . . . .	<b>22</b>
3.1	Introduction . . . . .	22
3.2	Elastoplastic models . . . . .	23
3.3	Damage law . . . . .	27
<b>4</b>	<b>Advanced identification procedures for elastoplastic and damage models</b>	<b>31</b>

4.1	Intoduction . . . . .	31
4.2	Identification of elastoplastic and damage behaviour . . . . .	31
4.3	Finite Element Model Updating . . . . .	32
<b>5</b>	<b>Conclusion . . . . .</b>	<b>34</b>

---

# 1 Preface

In this chapter a bibliographical review on ductile cast iron is given. Due to its heterogeneous microstructure and wide variety of mechanical properties it is found in many construction components that are mainly used in cyclic working conditions. The aim of this research is to identify elastoplastic and damage models of SG cast iron. The emphasis will be given on isotropic and kinematic hardening material models. Johnson-Cook and Armstrong-Frederick models will be used to describe hardening behaviour (see CHAP. 3, CHAP. 4, CHAP. 5). Lemaitre damage model coupled with Johnson-Cook's isotropic hardening law will be used for the investigated SG cast iron subjected to uniaxial cyclic loading.

The challenge of this work will be to identify parameters of nonlinear models using full-field measurements and 3D finite element computations. The last section will be introducing the inverse identification procedures with a special focus on Finite Element Model Updating (FEMU). The procedure is well-adapted to full-field measurements so it was a natural choice since it is allowing the identification of material parameters of complex constitutive law and geometry.

## 2 Studied material: SG cast iron

### 2.1 Introduction

Ductile cast iron (also known as nodular graphite cast iron, spheroidal graphite cast iron or SG cast iron) is essentially a family of materials with a wide variety of properties for different engineering requirements. The major constituent is iron, with important amounts of carbon and silicon. Cast irons are natural composite materials whose properties are determined by their microstructures, namely, the stable and metastable phases formed during solidification and subsequent heat treatment(s). The major microstructural constituents of cast irons are the chemical and morphological forms taken by carbon, and the continuous metal matrix in which the carbon and/or carbide are dispersed.

SG cast iron was patented in 1948 [Millis et al., 1948]. After just a decade of intensive development work in the 1950s, ductile iron had a phenomenal nine-times increase in use as an engineering material during the 1960s, and an increase in commercial applications still continues today. Cast iron has become a popular cast metallic material, which is widely utilised in modern industrial production because of its low cost and desirable properties such as good castability, convenient machining property, and wear resistance.

Within the technological project *The development of methods to increase the reliability of wind turbines* (FIG. 1.1) between the Croatian Institute of Technology KONCAR-Electrical Engineering Institute and Faculty of Mechanical Engineering and Naval Architecture, Zagreb (Laboratory of Experimental Mechanics (LEM) and Laboratory of Numerical Mechanics (LNM)) the behaviour of ductile nodular cast iron EN-GJS-400-18LT was investigated. Under consideration were taken four different grades of EN-GJS-400-18LT produced with different casting techniques (non-standard technique - type 100,

flotret - type 200, tundish - type 300, and inmould - type 400). The aim of the project was the modelling of the hub FIG. 1.1 with material parameters obtained from cyclic experiments. In this chapter some of the results and data concerning SG cast iron will be presented from the latter project. First, general examples of microstructure, chemical composition and mechanical properties will be shown for the four different grades. Second, the investigated SG cast iron will be presented and compared with those dealt with in the project.

## 2.2 Microstructure

At the macroscopic level SG cast iron is considered to be homogeneous with isotropic mechanical properties, although it is heterogeneous at a microscopic level. The heterogeneous microstructures of ductile cast iron consist of iron matrix containing spheroidal graphite inclusions randomly distributed (FIG. 1.2) [Čanžar et al., 2012]. Even though the exact reasons for the formation of graphite nodules is not fully understood, cast iron has a wide range of properties that are achieved by the controlled process of production. Spheroidal graphite irons are very unique engineering materials, possessing good castability and mechanical properties. The feature that all the members of SG cast irons share is the roughly spherical shape of the graphite nodules. However, with a high percentage of graphite nodules present in the structure, the control of the SG cast iron matrix structure is of potential importance.

An unusual combination of properties is obtained in ductile iron because the graphite forms as spheroids rather than as individual flakes as in gray iron. This mode of solidification is obtained by adding a very small, but specific, amount of magnesium to molten iron of a proper composition (see TAB. 1.1 [Čanžar et al., 2012]). The base iron is severely restricted in the allowable contents of certain minor elements that can interfere with the graphite spheroid formation. The added magnesium reacts with sulphur and oxygen in the molten iron and changes the way the graphite is formed. Control procedures [Karaman and Cetinarslan, 2010] have been developed to make the processing of ductile iron dependable. The high carbon and silicon contents of ductile iron provide the casting process advantages, but the graphite spheroids have only a nominal influence on the mechanical properties of the metal.

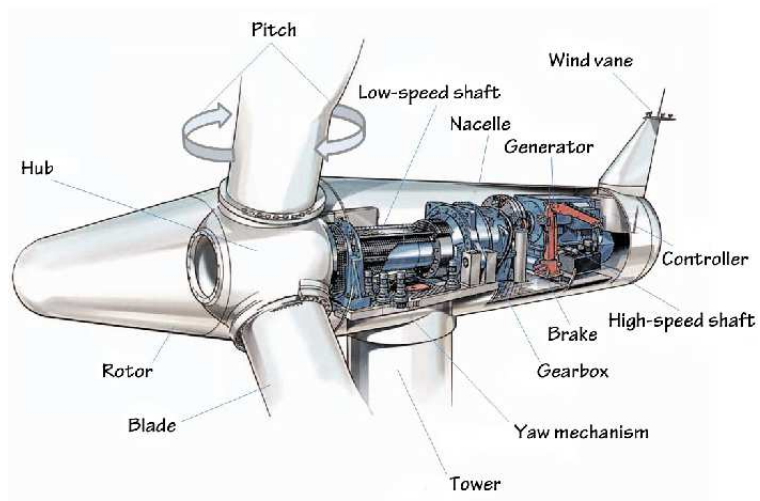
TAB. 1.1 shows the chemical composition of the four tested materials in the wind turbine project in comparison with the recommended chemical composition [Filetin et al., 2007]. The chemical compositions of the investigated materials are similar except that manganese, nickel and magnesium contents are higher in the grade 100 material.

A number of variables including chemical composition, cooling rate, type, amount and method of post-inoculation, amount of residual magnesium and pouring temperature can control the matrix structure of ductile cast iron [Martin, 2006]. Heat treating SG cast iron is also another route to produce a family of materials offering a wide range of properties obtained through the matrix microstructure control [Bayati and Elliott, 1995]. The importance of matrix in controlling mechanical properties is emphasised by the use of matrix names to designate the types of SG cast iron [Adewara and Loper, 1976, Fuller,





(a) Koncar windmill K80 (2500 kW)



(b) Main parts of wind turbine (Source: Center of Globalization, Governance and Competitiveness, Duke University)

**Figure 1.1:** (a) Končar wind turbine. (b) Main parts of the wind turbine

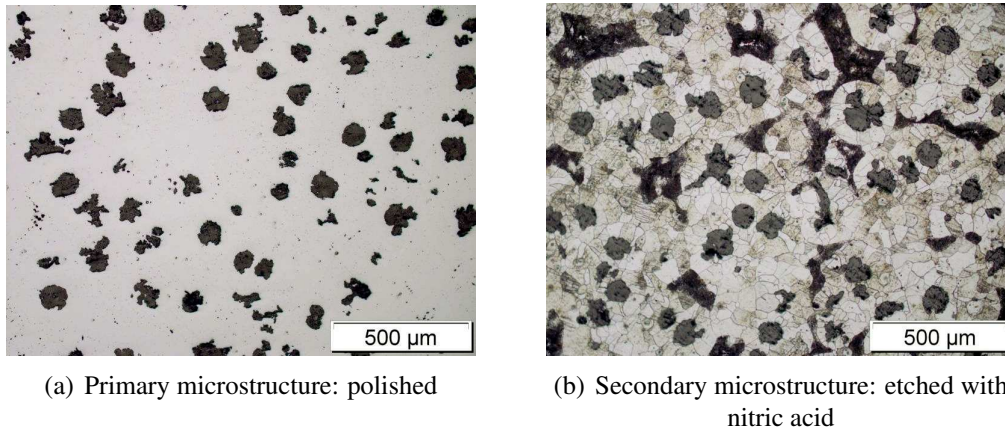


**Figure 1.2:** Metallography of flotret - type 200 SG cast iron [Čanžar et al., 2012]

**Table 1.1:** Chemical compositions in mass% of different SG cast irons.

Element	C	Si	Mn	P	S	Ni	Mg	Fe
Recommended chemical composition	3.2-3.8	2.4-2.8	<0.5	<0.045	<0.01			Bal.
100	3.6	2.122	0.204	0.023	0.004	0.978	0.046	Bal.
200	3.6	2.044	0.112	0.023	0.003	0.619	0.037	Bal.
300	3.6	1.968	0.114	0.024	0.003	0.572	0.039	Bal.
400	3.6	1.976	0.102	0.021	0.002	0.674	0.033	Bal.

1977].

The different grades are produced by controlling the matrix structure around the graphite either as-cast or by subsequent heat treatment. Only minor compositional differences exist among the regular grades, and these adjustments are made to promote the desired matrix microstructures. Alloy additions may be made to ductile iron to assist in controlling the matrix structure as-cast or to provide response to heat-treatment. Special grades of SG cast iron manufactured by alloying (*i.e.*, high-alloy ductile irons) provide unusual properties for special applications.

Depending on the matrix microstructure and the heat-treatment performed during the production the following groups can be distinguished:

- “As-casted” matrices

- Ferritic matrix

Graphite spheroids in a ferritic matrix provide a cast iron with good ductility [Hafiz, 2001] and impact resistance. The tensile and yield stresses are equivalent to low carbon steel. With an annealing heat-treatment of ferritic

ductile iron it is possible to get maximum ductility and low temperature toughness [Unkić et al., 2008].

– **Ferritic Pearlitic matrix**

Ferrite and pearlite are the most common components in SG matrices. The advantage of this iron matrix in comparison with others is its good machinability because of intermediate properties between ferritic and pearlitic grades and low production costs.

– **Pearlitic matrix**

SG cast iron having pearlitic matrices has a high strength, good wear resistance, and moderate ductility and impact resistance. This type of matrix gives also superior machinability compared with steels of similar physical properties.

• **Alloyed and/or heat-treated matrices**

– **Martensitic matrix**

Martensitic ductile cast iron matrix is produced following two conditions. The first one is using sufficient alloy additions that will prevent pearlite formation and the second is quenching and tempering that produce a martensitic SG iron. The tempered martensite matrix develops very high strength and wear resistance but with lower levels of ductility and toughness.

– **Bainitic matrix**

Bainitic SG iron can be either obtained through alloying and/or by heat-treatment. This kind of matrix provides a hard, wear-resistant material.

– **Austenitic matrix**

Alloying the cast iron with nickel produces austenitic matrices. It offers good corrosion and oxidation resistance, good magnetic properties, and good properties at elevated temperatures.

– **Austempered matrix**

The most recent developed subgroup of SG cast iron is austempered ductile iron. The matrix is subjected to a special austempering heat-treatment after which the iron still retains high elongation and toughness. This heat treatment also results in a material with superior wear resistance and fatigue strength.

To summarize, SG cast iron is a prime example of materials where the properties achieved depend upon the characteristics of the microstructure. The latter is determined in part during solidification (graphite shape, size and distribution) and in part during solid-state transformation (matrix).

As shown in FIG. 1.2 type - 200 SG cast iron has ferritic and pearlitic phases with 5 wt% of pearlite. The other types have also the same matrix microstructure but with different volume fractions of pearlite. Type - 100 has the highest portion (9 %), while type - 200 and type -300 have approximately the same amount (7 %). The graphite morphology

of the cast irons was performed from metallography on many samples. It is observed that type - 200 has the biggest size of the nodules with lower density while other types have about the same size and density. For conducting any experimental investigation on SG cast iron it is necessary to know the microstructural features of the material so the proper conclusions on mechanical properties can be made.

### 2.3 Mechanical properties

A wide range of mechanical properties can be achieved by controlling the microstructure with chemical composition or heat-treatment. Taking into account these features general properties of SG cast iron in comparison with other steels are [Filetin et al., 2007]:

- Better mechanical properties in comparison with gray cast iron, but poorer than steels. Yield stress of ductile cast iron ranges from 250 MPa for ferritic grades to 620 MPa for martensitic grades and tensile strength generally range from 400 MPa for ferritic grades to 1400 MPa for martensitic or austempered ductile iron grades. Young's modulus varies within the range 150-180 GPa.
- Higher fatigue limits due to the sphere-shaped graphite nodules especially after quenching and tempering. Ductile cast iron has better fatigue features in comparison with gray cast iron in which graphite flakes act as stress concentrators (FIG. 1.3).

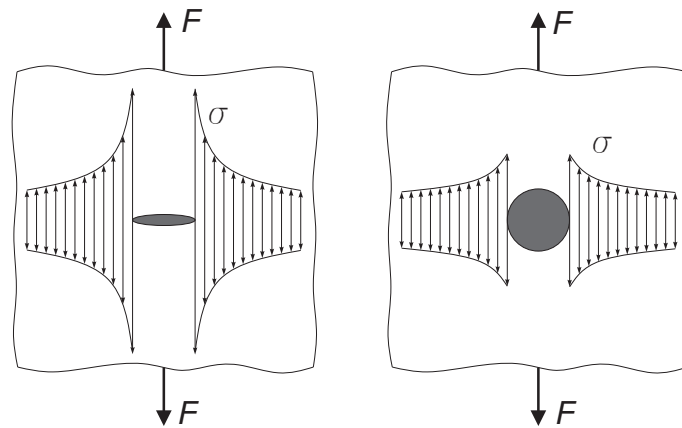


**Figure 1.3:** Influence of graphite shape on stress concentration

- Graphite nodules act as crack arresters. If the crack arrives at a nodule it can follow two paths depending on the nodule size. The crack will circumvent the big nodule and debonding with the iron matrix occurs. Conversely, the crack will propagate across the small nodules [Ferro et al., 2012]. In both cases cracks will be slowed down.

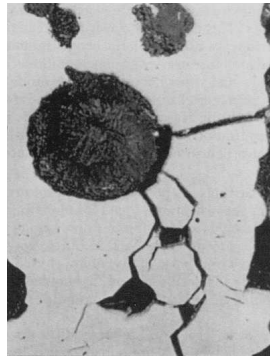


**Figure 1.4:** Crack propagating around nodules

- Increased ductility [Hafiz, 2001] and toughness [Unkić et al., 2008] in comparison with other cast irons with ferrite matrices but similar to other cast irons and malleable steels. The toughness of ductile cast iron is closely related to its microstructure, *i.e.*, shape, size distribution of graphite and matrix structure (proportion of ferrite or pearlite). The number of nodules per  $\text{mm}^3$  is an important microstructural feature whose values influence the toughness of SG cast iron. Higher number of nodules in the cast will increase the toughness.
- Wear and corrosion resistance [Grilec et al., 2010] is better than with gray cast iron
- Good welding capability [Pascual et al., 2009].
- Capacity of vibration damping is two times lower than that of grey cast iron but higher than steels.
- Good ability for machining [Chiang et al., 2007].
- Better casting properties than gray cast iron.
- Lower casting production costs.

FIG. 1.5 shows the true stress strain curve of the investigated grades of SG cast iron within the project *The development of methods to increase the reliability of wind turbines*. It can be observed that the non-standard casting technique has the highest yield stress and tensile strength due to the highest portion of pearlite in the iron matrix. Elongation to failure is varying from 16 % for type - 400 to 25 % for type - 100. It follows that the heat-treatment of each casting technique affects the ductility.

As a result of continuous development over many years ductile cast iron has achieved a level of reliability to justify its increasingly large number of applications for highly stressed structures and components [Clément et al., 1984, Nadot et al., 1997, Yaacoub-Agha et al., 1998, Chantier et al., 2000, Hübner et al., 2007, Limodin et al., 2009, Limodin et al., 2010, Mottitschka et al., 2010, Čanžar et al., 2010, Čanžar et al., 2011, Čanžar

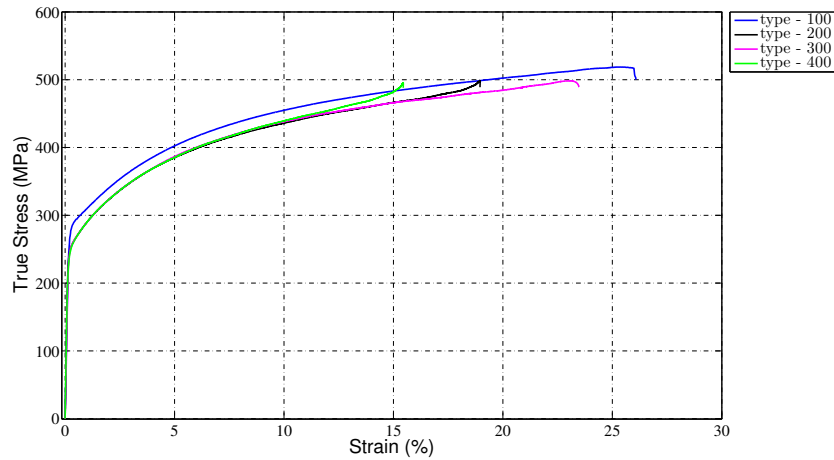


**Figure 1.5:** True stress-strain curves for four different types of EN-GJS-400-18LT cast irons

et al., 2012]. Since most commonly used in randomly loaded engineering components, it is necessary to investigate its fatigue properties (*i.e.*, low cycle and high cycle fatigue).

In previous studies, fatigue and fracture mechanics parameters of ductile cast iron have been examined at the macroscale [Hübner et al., 2007] and microscale [Iacoviello et al., 2008]. It has been shown that the fatigue strength is influenced by the size and the shape of graphite nodules [Hübner et al., 2007, Iacoviello et al., 2008, Costa et al., 2010, Čanžar et al., 2010]. The crack growth behaviour depends on graphite particle size and distribution in addition to casting defects (*e.g.*, microshrinkage cavities [Yaacoub-Agha et al., 1998, Chantier et al., 2000]). Increasing the size of graphite nodules leads to higher stress intensity and lower fatigue crack growth rates [Hübner et al., 2007].

In comparison with steels interesting phenomena are occurring when the cyclic strains are observed. For a cumulated plastic strain lower than 1 % SG cast iron exhibits a specific Bauschinger effect [Bauschinger, 1881] characterized by a high internal stress and an unusual hysteresis loop shape [Guillemer-Neel et al., 1999]. This effect is mainly due to inhomogeneities in strains between the inclusions and the matrix, and the development of increased dislocation density in the matrix from the interfaces. The Bauschinger effect is reduced when plastic flow develops in the matrix with further cycling.

Studies have been conducted on different types of SG cast iron (*i.e.*, size, shape, density and distribution of graphite nodules in the iron matrix) [Hübner et al., 2007, Iacoviello et al., 2008, Costa et al., 2010, Čanžar et al., 2012]. The formation and properties of graphite nodules have no significant influence on cyclic hardening of the material. On the contrary different microstructural properties play a significant role in crack initiation and propagation processes [Čanžar et al., 2012]. The ductile cast iron with larger irregularly shaped nodules has reduced fracture toughness and fatigue strength. The results considering the two-phase (*i.e.*, ferritic-pearlitic) matrix demonstrate that the pearlitic phase does not strongly affect the fatigue life if its volume fraction does not exceed 10 %.

Applications in cyclic loaded structures, mechanical properties, heterogeneous microstructure and side effects of casting production is a challenging area of the research. When describing the fatigue limits as functions of intrinsic material properties, shrinkage defects at the origin of the failure [Yaacoub-Agha et al., 1998, Chantier et al., 2000], and graphite nodule size and distribution [Costa et al., 2008] show that the main crack does not always initiate on casting defects (microshrinkage cavities or pores) and may also have its origin in graphite nodules.

During the casting process if the heat-treatment is not performed correctly appearance of irregular graphite nodules is possible. The latter ones reduce significantly both the ultimate tensile strength and the elongation to fracture, but it does not influence the yield stress of the cast iron (if compared to specimens containing only fully nodular graphite). From the investigation of [Ferro et al., 2012] it was found that a mean content of 40 % of irregular graphite in the microstructure (with respect to the total graphite content) does not influence significantly the fatigue strength of the analysed cast iron.

During operating time engineering components are subjected to variable amplitude loading, which influences the lifetime considerably. Therefore, fracture mechanics assessment of the fatigue crack growth behaviour under variable amplitude loading and the study of load history effects plays an important role in many areas of application of ductile cast iron. The experimental investigations under variable amplitude loading [Mottitschka et al., 2010] show acceleration effects in fatigue crack growth. Such acceleration effects affect the accuracy of lifetime predictions significantly.

Damage micromechanisms that appear in SG cast iron are fully coupled with the microstructure (graphite nodules and metal matrix are involved) and the production processes. [Iacoviello et al., 2008] detected different damage micromechanisms with different matrices. Damage initiation in SG cast irons with a ferritic matrix appears at matrix/spheroid interfaces and propagates in the matrix, while in fully pearlitic matrices the cracks initiate in the matrix already in the elastic stage. From the experiments carried out on a microscopic level and using a Scanning Electron Microscope (SEM) [Iacoviello et al., 2008] reached the conclusion that void growth due to spheroid/matrix debonding is less important than crack initiation and propagation inside spheroids.

Some of the most advanced research carried out on SG cast iron was conducted with Digital Volume Correlation (DVC) analyses of 3D microtomographic images obtained with laboratory and synchrotron setups. For example, fatigue crack closure has been studied in nodular graphite cast iron. The graphite nodules are well adapted to correlation techniques (FIG. 1.6) since they act as natural markers [Limodin et al., 2009, Limodin et al., 2010].

## 2.4 Application of cast iron

Because of the previously mentioned properties, its exploitation is increasing, and has found applications in many industrial application. Big parts of the annual production of ductile cast iron is in the form of pipes, which are used for water and sewer lines. Ductile cast iron pipes are stronger and easier to tap, require less maintenance and provide greater

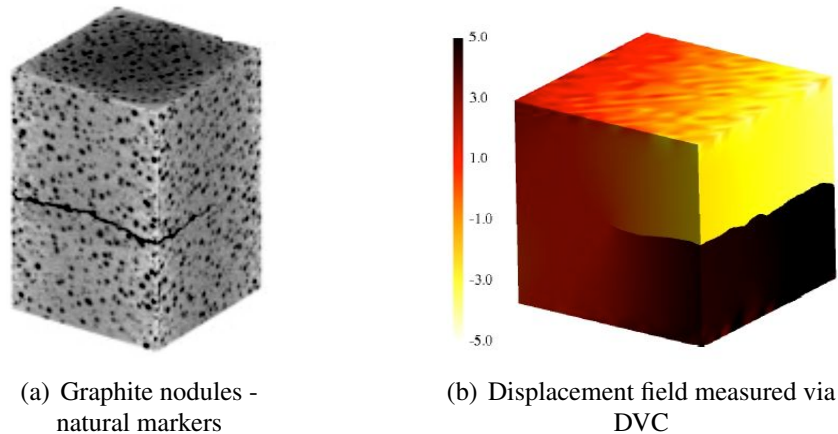


**Figure 1.6:** DVC results on SG cast iron [Rannou et al., 2010]

flow areas compared with pipes made from other materials. In difficult terrain it can be a better choice than PVC, concrete, polyethylene, or steel pipes.

Ductile cast iron is specifically useful in many automotive components, where strength needs to surpass that of aluminium but not necessarily that of steel. Other major industrial applications include highway diesel trucks, agricultural tractors, and oil well pumps. Since ductile cast irons have properties similar to steels their application has been extended to:

- Caskets in the nuclear industry
- Suspension arms [Chantier et al., 2000]
- Check beam for lifting track
- Mine cage guide brackets
- Gear wheel and pinion blanks and brake drum
- Flywheel
- Thrust bearing
- Frame for high speed diesel engine
- Four throw crankshaft
- Fully machined piston for large marine diesel engine
- Bevel wheel
- Hydraulic clutch on diesel engine for heavy vehicle
- Fittings overhead electric transmission lines
- Wind turbine parts
- Undercarriage and trains.



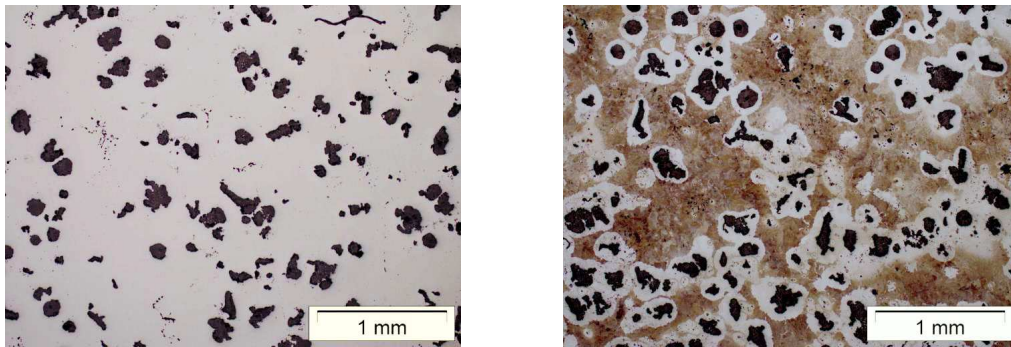
## 2.5 SG cast iron produced with sandwich technique

The SG cast iron investigated in this thesis is produced with the newly developed casting technique referred to as *sandwich*. The chemical composition and microstructure are presented in TAB. 1.2 and FIG. 1.7. If we compare the chemical composition of sandwich SG cast iron with those investigated in the project on *The development of methods to increase the reliability of wind turbines* (TAB. 1.1, FIG. 1.2) the following differences are observed. All chemical constituents of sandwich cast iron are within the recommended limits except the volume fraction of carbon and magnesium. The mass fraction of carbon is lower than the recommended value, while the mass fraction of magnesium is higher than in the four grades of EN-GJS-400-18LT.

Material type	C	Si	Mn	P	S	Cr	Ni	Mo	Cu	Mg	Fe
Sandwich	2.26	2.09	0.15	0.041	<0.01	0.04	0.63	<0.01	0.025	0.06	Bal.

**Table 1.2:** Chemical compositions in mass% of SG cast iron produced by the sandwich technique

Observing the microstructure of SG cast iron produced by the sandwich casting process (FIG. 1.7) we can note that the size of graphite nodules is larger in comparison with the previously presented microstructures (FIG. 1.2). In the ferritic-pearlitic matrix a distribution of irregular shaped nodules (*i.e.*, nodules do not have sufficient roundness) is very dense. These microstructural features play an important role in terms of mechanical properties (see FIG. 1.8).



(a) Primary microstructure: polished

(b) Secondary microstructure: etched with nitric acid

**Figure 1.7:** Metallography of sandwich SG cast iron

Figure 1.8 shows a stress-strain curve of the investigated cast iron. The mechanical characteristics are different in comparison with EN-GJS-400-18LT grades. The ultimate strength is of the same order but the maximum elongation is about 4.5 %.

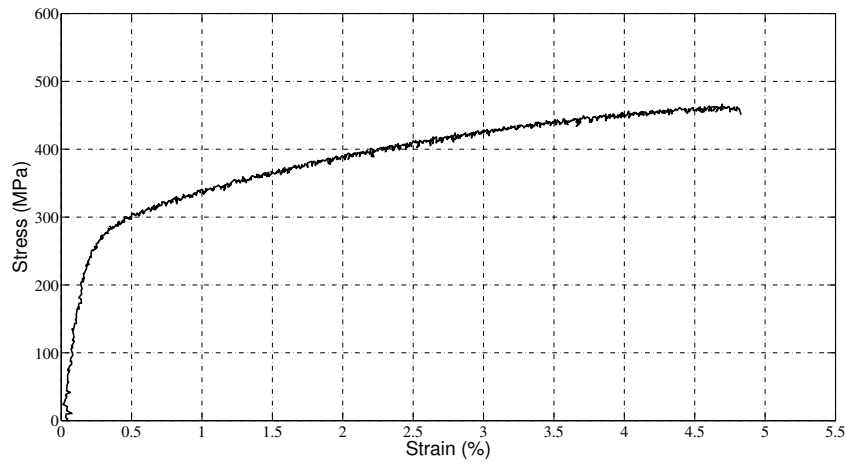


**Figure 1.8:** True stress-strain curve of sandwich cast iron

It is important to emphasize that the casting block had a different shape than the standard one (FIG. 1.9). For validation purposes of the material properties a Y-block ingot is usually cast with dimensions  $40 \times 140 \times 160 \text{ mm}^3$ . It was necessary to cast a bigger block of dimensions  $280 \times 280 \times 500 \text{ mm}^2$  due to the size of the biaxial samples (see CHAP. 4). The heat-treatment and especially the cooling rate of the cast part needed to be performed in a different way. It is believed that the heat-treatment was not performed in an appropriate way for the square block, which introduced lower ductility of the investigated SG cast iron.

## 3 Constitutive equations describing elastoplasticity and damage

### 3.1 Introduction

The theory of linear elasticity is used for describing the material behaviour, which undergoes small strains and after removal of stress returns to its original configuration. Almost all real materials will undergo some permanent strain, which remains after the removal of stress. Significant permanent strains for metals will usually occur beyond the yield point (*i.e.*, yield stress  $\sigma_y$ ). Elastic strains are reversible; the energy expended in the deformation process is stored and is completely recovered upon stress removal. Permanent strains (*e.g.*, plastic behaviour) involve the dissipation of energy; such processes are irreversible in the sense that the original state can be found only by the expenditure of more energy.

Another irreversible process occurring in the mechanical behaviour is damage. Failure of most structural members on the macroscale follows irreversible and heterogeneous microprocesses of time and environment dependent deterioration of materials. The existence of distributed microscopic voids, cavities, or cracks of the size of crystal grains is

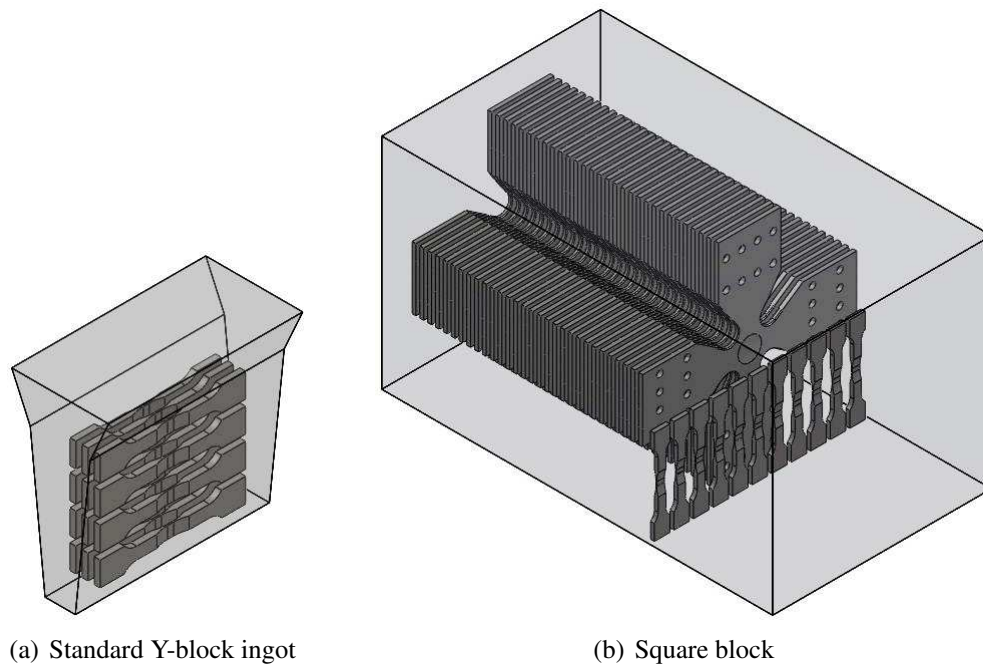


**Figure 1.9:** Cast shapes

referred to as material damage, whereas the process of void nucleation, growth, or crack initiation, propagation and coalescence, which both initiate macrocracks and cause progressive material degradation through strength and stiffness reduction, are called ductile damage [Murakami, 1988, Chaboche, 1988].

Constitutive models are used to describe the material behaviour caused by various phenomena. Within this research plastic (*i.e.*, isotropic and kinematic hardening) parameters and damage parameters will be identified.

### 3.2 Elastoplastic models

All solid materials possess a domain in the stress space within which a load variation results only in a variation of elastic strains. These elastic strains consist of reversible movements of atoms, molecules, or cells, corresponding to strains not exceeding  $(0.2 - 0.5) \times 10^{-2}$  for metals, composites, concrete and wood. This fact, therefore, justifies the hypothesis of small strain elastic behaviour where the energy dissipation is null. The limit between the elastic and plastic domains is at the yield stress. This is the stress above which irreversible strains appear. The detection of this limit is an experimental challenge since it depends on the resolution of the used strain measuring device. In the interest of an objective measure, we adopt a conventional definition of this limit. The conventional elastic limit is the stress that corresponds to the occurrence of a specified amount of permanent strain. For quality control of materials, a conventional value of permanent strain equal to 0.2 % is commonly used. If the above value of permanent strain

is too high (*i.e.*, of the same order of magnitude as the accompanying elastic strain) a more refined value of 0.05 or 0.02 % permanent strain is sometimes adopted.

The linear elastic domain is defined by the generalized Hooke's law

$$\boldsymbol{\sigma} = \mathbf{C} : \boldsymbol{\epsilon} \quad (1.1)$$

where  $\mathbf{C}$  is a fourth order tensor whose components are the elastic moduli. The elastic properties for isotropic materials are defined with Poisson's ratio ( $\nu$ ) and Young's modulus ( $E$ )

$$E = \frac{\sigma_1}{\epsilon_1} \quad (1.2)$$

and

$$\nu = -\frac{\epsilon_2}{\epsilon_1} \quad (1.3)$$

for a uniaxial tensile experiment, where  $\sigma_1$  is the axial stress,  $\epsilon_1$  is the longitudinal strain (in the loading direction) and  $\epsilon_2$  is the transverse strain.

After exceeding the yield stress some permanent strains are accumulated. If the strain levels remain moderate the total strain tensor ( $\boldsymbol{\epsilon}$ ) is decomposed into elastic ( $\boldsymbol{\epsilon}_{el}$ ) and plastic ( $\boldsymbol{\epsilon}_{pl}$ ) parts

$$\boldsymbol{\epsilon} = \boldsymbol{\epsilon}_{el} + \boldsymbol{\epsilon}_{pl} \quad (1.4)$$

The uniaxial stress space is defined by the yield stress. To define such a stress space for a multiaxial case it is necessary to propose an equivalent stress  $\sigma_{eq}$ . It defines in the stress space of six dimensions a domain within which any stress variation generates only elastic strains. Depending on how the limiting threshold is set different criteria are proposed

- *Von Mises criterion* is linked to the elastic shear energy,
- *Tresca criterion* is defined by the maximum shear stress
- *Hill criterion* corresponds to a particular type of anisotropy in which three planes of symmetry are conserved during hardening of the material.

In the elastic range the stress-strain behaviour for most engineering materials (*e.g.*, metals, rocks, plastics, but not soils) is linear. After passing the elastic limit, further increases in stress are usually required to maintain an increase in strain. This phenomenon is known as *work-hardening* or *strain-hardening*. During hardening, the elastic domain undergoes a certain evolution. The elastic domain of a virgin material is bounded by the initial yield surface, also called the elastic limit envelope. Due to microstructural changes in the material induced by plastic flow, the elastic domain changes its size (*isotropic hardening*) or position (*kinematic hardening*), or both (*combined hardenings*).

From an isotropic yield criterion arises an isotropic hardening where the yield surface has the same shape but expands with increasing stress. In particular, the yield function takes the form [Lemaitre and Chaboche, 1990]

$$f(\boldsymbol{\sigma}, R) = f_y(\boldsymbol{\sigma}) - \Gamma(R) = 0 \quad (1.5)$$

where the function  $f_y$  indicates the form of the yield criterion, and the function  $\Gamma$  introduces hardening through the relationship between the thermodynamic force  $R$  and the hardening variable ( $p$  or  $w_p$ ). For an isotropic material (with an initially isotropic yield surface)  $f_y$  is a function of the stress tensor invariants.

The shape of the yield function is specified by the initial yield function and its size changes as the hardening function  $\Gamma$  changes. Even though most materials exhibit a strong hardening induced anisotropy, the isotropic hardening representation is very often used. This is because of its simplicity and because it is a good representation in the case of proportional loading, *i.e.*, when the eigen frame does not change. To describe isotropic hardening different constitutive models can be used such as:

- Linear hardening law

$$\sigma_{eq} = \sigma_y + K\bar{\epsilon}_{pl} \quad (1.6)$$

- Hollomon's power law [Hollomon, 1945]

$$\sigma_{eq} = K\bar{\epsilon}_{pl}^n \quad (1.7)$$

- Ludwik's hardening law [Ludwik, 1909]

$$\sigma_{eq} = \sigma_y + K\bar{\epsilon}_{pl}^n \quad (1.8)$$

- Swift's hardening law [Swift, 1952]

$$\sigma_{eq} = K(\epsilon_y + \bar{\epsilon}_{pl})^n \quad (1.9)$$

- Voce's hardening law [Voce, 1948]

$$\sigma_{eq} = \sigma_Y + R_{sat} \left(1 - e^{-b\bar{\epsilon}_{pl}}\right). \quad (1.10)$$

For the first four laws the isotropic hardening modulus is denoted by  $K$ , while in Voce's law  $R_{sat}$  defines the saturation level. Hardening laws except the linear one include also a hardening exponent  $n$ .

Isotropic hardening is not useful in situations where components are subjected to cyclic loading. As an alternative hardening rule, the current loading surface is assumed not to expand but to move as a rigid body within the stress space. This is known as kinematic hardening. The use of kinematic hardening is necessary to model the Bauschinger effect [Bauschinger, 1881]. Even if the magnitudes of the yield stress in tension and in compression are initially the same, this is no longer the case when the material is preloaded into the plastic range and then unloaded. This is why the yield surface has the same shape and size but moves in the stress space.

The yield function now takes the general form [Lemaitre and Chaboche, 1990]

$$f(\boldsymbol{\sigma}, \mathbf{X}) = f_y(\boldsymbol{\sigma} - \mathbf{X}) - \sigma_y = 0 \quad (1.11)$$

The hardening parameter is the stress  $\mathbf{X}$  (second order tensor), known as the back-stress. The yield surface is shifted relative to the stress-space axes by  $\mathbf{X}$  while  $\sigma_y$  is the value of the yield stress. To describe kinematic hardening different models can be used [Prager, 1956, Armstrong and Frederick, 1966, Chaboche, 1991, Wang and Ohno, 1991, Voyiadjis and Kattan, 1991, Voyiadjis and Sivakumar, 1994, Voyiadjis and Basuroychowdhury, 1998]. In the present research the Armstrong-Frederick model (see Section 3.2.2) will be used for describing kinematic hardening.

More complex hardening rules can be used. For example [Lemaitre and Chaboche, 1990], the mixed hardening rule combines features of both isotropic and kinematic hardening models, and the loading function takes the general form

$$f(\boldsymbol{\sigma}, \mathbf{X}) = f_y(\boldsymbol{\sigma} - \mathbf{X}) - R - \sigma_y = 0 \quad (1.12)$$

where the hardening parameters are now the scalar  $R$  and the tensor  $\mathbf{X}$ .

### 3.2.1 Johnson-Cook and Ludwik isotropic hardening law

To identify isotropic hardening of SG cast iron Johnson-Cook's constitutive law [Johnson and Cook, 1983] will be used since it is implemented in the FE code Abaqus. The model is a particular type of von Mises plasticity with analytical forms of the hardening law and rate dependence. It is suitable for high-strain-rate models of many materials, including most metals typically used in adiabatic transient dynamic simulations. A von Mises yield surface with associated flow rule is used. The general equation of the model is

$$\sigma_{eq} = [A + B (\bar{\epsilon}_{pl})^n] [1 + C \ln(\epsilon^*)] [1 - (\hat{T})^m] \quad (1.13)$$

where  $A, B, C, n$  and  $m$  are material constants,  $\bar{\epsilon}_{pl}$  is cumulated plastic strain and  $\epsilon^* = \dot{\epsilon}_{pl}/\dot{\epsilon}_0$  the dimensionless strain rate.  $\dot{\epsilon}_{pl}$  and  $\dot{\epsilon}_0$  are plastic strain rate and reference strain rate, respectively.

As presented in Equation (1.13) the second member includes the strain rate. Since this was not an objective of this research this term is excluded. The isotropic hardening model is expressed as

$$\sigma_{eq} = [A + B (\bar{\epsilon}_{pl})^n] [1 - (\hat{T})^m] \quad (1.14)$$

The material parameters that should be determined are measured at or below the transition temperature  $T_{transition}$ .  $\hat{T}$  is the non dimensional temperature defined as

$$\hat{T} \equiv \begin{cases} 0 & \text{for } T < T_{transition} \\ (T - T_{transition}) / (T_{melt} - T_{transition}) & \text{for } T_{transition} \leq T \leq T_{melt} \\ 1 & \text{for } T > T_{melt} \end{cases} \quad (1.15)$$

The part of Johnson-Cook equation that takes into account the temperature changes will also be neglected. Only the plastic parameters ( $A, K, n$ ) will be identified. Removing the temperature part of Johnson-Cook's law will lead to *Ludwik's law* (see Equation (1.8))

$$\sigma_{eq} = [A + B (\bar{\epsilon}_{pl})^n] \quad (1.16)$$

where  $A \equiv \sigma_y$  is the yield stress,  $B \equiv K$  the hardening modulus and  $n$  the hardening exponent.

### 3.2.2 Armstrong-Frederick kinematic hardening

The material models to be identified are implemented in the commercial software Abaqus. In Abaqus nonlinear kinematic hardening is described with Armstrong and Frederick's model [Armstrong and Frederick, 1966]. Kinematic hardening was introduced by [Prager, 1956]. According to this first model, the simulation of the plastic response of materials is linearly related with the plastic strain. The equation proposed by Prager to describe the change of the backstress tensor reads

$$\dot{\mathbf{X}} = C_0 \dot{\boldsymbol{\epsilon}}_{pl} \quad (1.17)$$

where  $C_0$  is the hardening modulus derived from a cyclic uniaxial test and  $\dot{\boldsymbol{\epsilon}}_{pl}$  denotes the rate of the plastic strain tensor.

In the Armstrong and Frederick model a memory term is added to the linear kinematic law (1.17) and becomes

$$\dot{\mathbf{X}} = C \dot{\boldsymbol{\epsilon}}_{pl} + \gamma \mathbf{X} \dot{p} \quad (1.18)$$

where  $C$  and  $\gamma$  are material parameters to be identified and  $\dot{p}$  the rate of cumulated plastic strain

$$\dot{p} = \sqrt{\frac{2}{3} \dot{\boldsymbol{\epsilon}}_{pl} : \dot{\boldsymbol{\epsilon}}_{pl}}. \quad (1.19)$$

The proposed model simulates the multiaxial Bauschinger effect (motion of the yield surface in the stress space). When compared with experimental results, Armstrong-Frederick's predictions are generally more accurate than Prager and von Mises's models for cyclic uniaxial loadings and torsion-tension of thin tube tests on annealed copper [Armstrong and Frederick, 1966].

## 3.3 Damage law

### 3.3.1 Introduction

As mentioned in Section 3.1 the damage phenomenon is a progressive physical process of the material subjected to loading where in the end it experiences failure. Damage by the creation of free surfaces of discontinuities reduces the value of many properties [Lemaitre and Desmorat, 2005]. There is a decrease of elastic modulus, yield stress before or after hardening, hardness, electric conductivity, density. Depending on the material, type of loading and temperature the following manifestations of damage may occur [Lemaitre, 1996]:

- Brittle damage
- Ductile damage
- Creep damage
- Low cycle fatigue damage (*i.e.*, *LCF* damage)

- High cycle fatigue damage (*i.e.*, *HCF* damage).

Depending on the observation scale, models can study damage on the atomic scale (molecular dynamics), the microscale (micromechanics) and the meso/macro scale (quasi-continuum mechanics). The material structure on the atomic scale represented by a configuration of atoms ordered in a crystal lattice or molecular chains bonded by inter-atomic forces is not continuous. Damage laws at this level determine configurations of atomic bonds (*i.e.*, breaking and reestablishing bonds) [Skrzypek and Ganczarski, 1999]. Microscale material structures are in general discontinuous and heterogeneous. At this level damage is due to the accumulation of microstresses close to defects, interfaces and the breakage of bonds. When observing material damage at the scale of the Representative Volume Element (RVE), it corresponds to the growth and the coalescence of microcracks or microvoids, which initiate a macrocrack. At the macroscale damage corresponds to the growth of that crack, which is usually studied using fracture mechanics [Griffith, 1920].

The undamaged material behaviour is described with classical state variables *e.g.*, strain and stress tensors ( $\epsilon, \sigma$ ), isotropic hardening variables ( $r, R$ ), tensor variables for kinematic hardening ( $\alpha, \mathbf{X}$ ). However, within continuum mechanics damage is approximated by effective state variables  $\tilde{\epsilon}$ ,  $\tilde{\sigma}$ ,  $\tilde{r}$ ,  $\tilde{R}$ ,  $\tilde{\alpha}$ ,  $\tilde{\mathbf{X}}$ . The effective state variables are defined with different equivalence principles [Skrzypek and Ganczarski, 1999]:

- **Principle of strain equivalence - the effective stress concept** [Rabotnov, 1968, Lemaitre, 1971, Lemaitre and Chaboche, 1978]

The strain associated with a damaged state under the applied stress  $\sigma$  is equivalent to the strain associated with the undamaged state under the effective stress  $\tilde{\sigma}$

$$\tilde{\epsilon}(\tilde{\sigma}) = \epsilon(\sigma, D), \quad \tilde{\sigma} = \frac{\sigma}{1 - D}. \quad (1.20)$$

- **Principle of stress equivalence - the effective strain concept** [Simo and Ju, 1987]

The stress associated with a damaged state under the applied strain  $\epsilon$  is equivalent to the stress associated with the undamaged state under the effective strain  $\tilde{\epsilon}$

$$\tilde{\sigma}(\tilde{\epsilon}) = \sigma(\sigma, D), \quad \tilde{\epsilon} = (1 - D)\epsilon \quad (1.21)$$

In the strain or the stress damage equivalent configurations the stiffness reduction due to microcracks or microvoids affects the effective stress or the effective strain, respectively, whereas the strain or the stress remain unchanged.

- **Elastic energy equivalence** [Cordebois and Sidoroff, 1979]

The complementary elastic energy equivalence defines the fictitious pseudo-undamaged equivalent configuration and the corresponding effective variables  $\tilde{\sigma}$  and  $\tilde{\epsilon}$ . The complementary elastic energy of the pseudo-undamaged solid  $\tilde{\Phi}_{el}$  is obtained directly from the virgin undamaged one  $\Phi_{el}$ , except that the stress and strain variables  $\sigma$  and  $\epsilon$  are replaced by the effective variables  $\tilde{\sigma}$  and  $\tilde{\epsilon}$

$$\Phi_{el}(\sigma, D) = \tilde{\Phi}_{el}(\tilde{\sigma}, 0), \quad \epsilon_{el} = \frac{\partial \Phi_{el}}{\partial \sigma} \quad (1.22)$$



where  $\Phi_{el} = (1/2)\boldsymbol{\sigma} : \boldsymbol{\epsilon}_{el}$  and  $(1/2)\tilde{\boldsymbol{\sigma}} : \tilde{\boldsymbol{\epsilon}}_{el}$  whereas  $D$  denotes a set of damage variables. In the energy based damage equivalence model the microcrack and/or microvoid growth influences both the stress and the strain tensors, which is more realistic than in the strain or stress damage equivalence postulate where the local stiffness drop results in a local stress decrease or local strain increase, exclusively. However, it is limited as it does not allow for the physically adequate description of phenomena other than damage coupled with elasticity.

- **Total energy equivalence** [Chow and Lu, 1992]

The total energy equivalence postulates that there exists a pseudo-undamaged (homogeneous) solid made of the virgin material in the sense that the total work done by the external tractions on infinitesimal strains during the same loading history as that for the real, damaged (heterogeneous) solid is not changed

$$d\Phi_t = d\Phi_{el} + d\Phi_{pl} + d\Phi_d \quad (1.23)$$

where  $d\Phi = \boldsymbol{\sigma} : d\boldsymbol{\epsilon}$  is the infinitesimal work of the applied stresses, and  $d\Phi_{el}$ ,  $d\Phi_{pl}$ , and  $d\Phi_d$  denote the elastic (reversible) energy, the work done by (visco)plastic (irreversible) strains and the work associated with damage nucleation and growth.

To characterize the damage state, damage variables are defined as scalars  $D$  [Kachanov, 1958], vector  $D_\alpha$  [Davison and Stevens, 1973], second rank tensor  $\boldsymbol{D}$  [Rabotnov, 1969, Murakami and Ohno, 1981] or fourth rank tensor  $\tilde{\boldsymbol{D}}$  [Chaboche, 1982, Krajcinovic, 1989]. To summarize the effective state variables, associated with the pseudo-undamaged state, are defined in such a way that the strains, the stresses, the elastic energy, or the total energy in the true (damaged) and the (undamaged) states are the same.

### 3.3.2 Lemaitre damage model

The derivation of [Lemaitre, 1984] unifies a damage model coupled with Ludwik's elastoplastic hardening law (1.8). It will be considered to describe the nonlinear behaviour of SG cast iron. The damage model is written as

$$\dot{D} = \left(\frac{Y}{S}\right)^s \dot{p} \quad (1.24)$$

where  $s$  and  $S$  are material-dependent parameters. The identification of the damage behaviour will consist of determining those two parameters.

The energy release rate density ( $Y$ ) is the associated force with the damage variable. It is derived from the state potential  $\psi^*$  and based on the effective stress (1.20) using the strain equivalence

$$Y = \rho \frac{\partial \psi^*}{\partial D} = \frac{\tilde{\boldsymbol{\sigma}}_{eq}^2 R_v}{2E} \quad (1.25)$$

where  $R_v$  is the triaxiality function

$$R_v = \frac{2}{3}(1 + \nu) + 3(1 - 2\nu) \left( \frac{\sigma_H}{\sigma_{eq}} \right)^2 \quad (1.26)$$

where  $\sigma_H = \sigma_{kk}/3$  is the hydrostatic stress,  $\sigma_{eq} = \sqrt{\frac{2}{3}\sigma_{ij}^D\sigma_{ij}^D}$  von Mises' equivalent stress, and  $\sigma_{ij}^D$  the deviatoric stress tensor.

Lemaitre's damage model (1.24) unifies many particular models such as [Lemaitre and Desmorat, 2005]: ductile damage if it is governed by plasticity, creep damage coupled with Norton's (power) law, fatigue damage if calculated from cyclic plasticity, quasi-brittle damage if written at a microscopic level.

The proposed damage model has been implemented in an Abaqus User Material Subroutine (UMAT). It is coupled with Ludwik's elastoplastic power law (1.8). The stress-strain relationship is given as an input of tabulated values for 30 points prescribing the plastic strain (FIG. 1.10). It was observed that the stress-strain curve was not described properly in the first part (until 1 % strain) when the equally spaced points of plastic strain. To bypass this discrepancy the points were spaced more densely from 0 to 1 % with an increment 0.1 %.

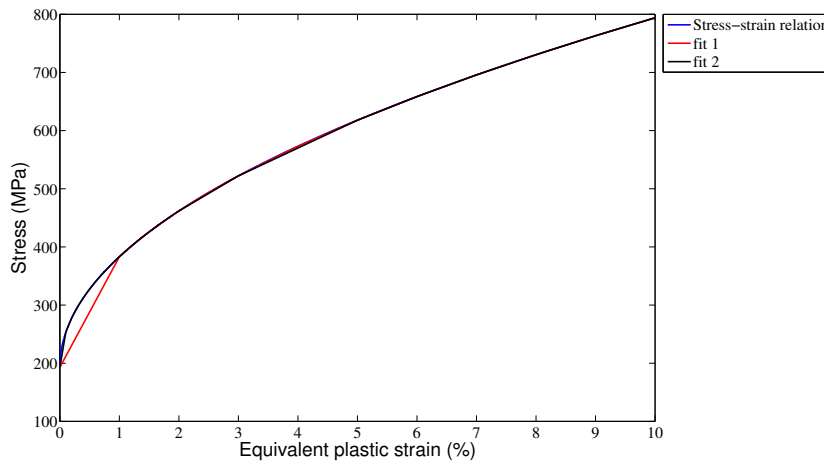


**Figure 1.10:** Change of stress with respect to plastic equivalent strain. The curve 1 is a fit of the reference stress-strain curve when the points are equally spaced with 1 % plastic strain increments. For curve 2 the points are spaced more densely from 0 to 1 % with 0.1 % increments

## 4 Advanced identification procedures for elastoplastic and damage models

### 4.1 Introduction

The way of identifying material parameters to describe constitutive postulates has experienced major changes with the development of full-field measurement techniques (*e.g.*, Digital Image Correlation (DIC-see CHAP. 2), moiré and speckle interferometry, and grid methods [Grédiac and Hild, 2012]). Different approaches [Avril et al., 2008a] are developed to obtain the sought parameters with different measured data (*i.e.*, displacement or strain fields, load levels). These identification methods are applied to model different phenomena (elasticity [Avril et al., 2008a, Gras et al., 2013], plasticity [Grédiac and Pierron, 2006, Cooreman et al., 2007, Robert et al., 2012, Mathieu et al., 2014], damage [Claire et al., 2002, Chalal et al., 2004, Bouterf et al., 2015]) from a wide range of experiments.

### 4.2 Identification of elastoplastic and damage behaviour

In a review on the identification of elastic properties [Avril et al., 2008a] five different identification methods were introduced. In general the material parameters can be obtained by updating or straightforward identification procedures. The following iterative methods *Finite Element Model Update* (FEMU), *Constitutive Equation Gap Method* (CEGM), *Reciprocity Gap Method* (RGM) use computed displacement and/or stress fields by FEM analyses. An FE computation with an initial guess of the constitutive parameters is needed, while material parameters are identified by minimising a cost function where the available measurements are compared to their computed counterparts. The cost functions for FEMU-U (*displacement method*), FEMU-F (*force method*) and FEMU-UF (*displacement & force method*) are usually defined as the quadratic error of measured and computed values.

Contrary to the updating procedures, non iterative methods such as the *Virtual Fields Method* (VFM) [Grédiac, 1989b] and *Equilibrium Gap Method* (EGM) [Claire et al., 2002] use measured strain/displacement fields to determine material parameters [Avril et al., 2008a]. In comparison with updating techniques a big advantage of the latter methods is the smaller duration of computation since they do not require a series of finite element calculations.

Very few identifications have been done on elastoplastic and damage behaviour. However, both phenomena were investigated separately with non-iterative (EGM - [Claire et al., 2004, Claire et al., 2007], and iterative identification methods, namely, FEMU [Cooreman et al., 2007, Robert et al., 2012, Mathieu et al., 2014], VFM [Avril et al., 2008b, Pierron et al., 2010], CEGM [Latourte et al., 2008]). Damage identification from full-field measurements was first proposed by [Claire et al., 2004] with the equilibrium gap method. It consists of a finite element formulation in which the nodal displacements are known and the elastic properties (*i.e.*, the damage field) are unknown.

Elastic properties are assumed to remain uniform over each element, but vary from element to element. The damage field is nothing but a simple way to account for a heterogeneous stiffness throughout the sample. The additional step that is proposed here, and tested against experimental data, is to require for an additional consistency, namely, that the damage inhomogeneity results from a homogeneous damage law, combined with a heterogeneous loading [Roux and Hild, 2008]. EGM has the advantage of being directly applicable as a post-processor to the current displacement field measurement techniques such as digital image correlation.

[Rossi et al., 2006] identified damage parameters of Lemaitre's model from a uniaxial experiment. The main aim was to show how digital image processing may be used in material testing and characterisation. DIC was used to obtain the plastic strain from which five parameters were obtained. [Pierron et al., 2010] made an extension of the virtual fields method to combined isotropic and kinematic hardening. Displacements were obtained by using the grid method. Since stress-related parameters were identified load measurements were included in the identification procedure. Based on the effect of noisy data to the cost function the choice of optimal virtual fields was investigated.

CEG-based methods [Latourte et al., 2008] have also been proposed and applied in the context of nonlinear constitutive models. The identification of heterogeneous elastoplastic properties (*i.e.*, linear kinematic hardening) and strain energy densities from kinematic field measurements have been addressed. The identification was based on an incremental version of CEG where tangent or secant stiffness associated with elastoplastic models are sought.

In the following section FEMU will be explained in detail. The method was already applied for identification of elastoplastic material parameters [Cooreman et al., 2007, Robert et al., 2012, Mathieu et al., 2014]. Special emphasis will be put on measurement uncertainty.

### 4.3 Finite Element Model Updating

The challenge of this work is to identify elastoplastic coupled with damage phenomena. In previous works FEMU was mostly used to determine (visco)plastic parameters [Cooreman et al., 2007, Robert et al., 2012, Mathieu et al., 2014]. The minimisation of the cost function can be based on the difference between measured and calculated strains [Cooreman et al., 2007] or displacements [Robert et al., 2012, Gras et al., 2013, Mathieu et al., 2014]. When applying the minimisation to strain fields [Cooreman et al., 2007] it is not clear how the boundary conditions are prescribed. When using displacement fields, all identification methods compare a measured displacement field with a calculated field. Simulations and measurements (with *local* DIC - CHAP. 2) are usually carried out with different softwares. As a consequence the reference points from measured and calculated data are not at the same position. With additional interpolation the two fields are compared. This is adding extra interpolation errors and uncertainties. On contrary, *global* DIC (CHAP. 2) is based on FE formulations. Hence, coupling FE simulations with global DIC in FEMU is a consistent tool to determine material parameters because the same mesh

can be used [Gras et al., 2013, Mathieu et al., 2014]. The results will be compared on the nodes of the very same mesh, which excludes any interpolation operation.

To determine elastic parameters FEMU-U is appropriate [Gras et al., 2013]. However, if the sought mechanical parameters are affected by stresses the minimisation of the cost function based on displacement/strain fields is not sufficient. This case requires the introduction of the force balance method in the identification procedure [Robert et al., 2012, Mathieu et al., 2014]. The identification is then the result of minimising [Mathieu et al., 2014]

$$\chi_{tot}^2 = (1 - \omega)\chi_u^2 + \omega\chi_F^2 \quad (1.27)$$

where  $\chi_{tot}$  is total residual summed over all states where an image is captured,  $\chi_u$  the displacement residual,  $\chi_F$  the force residual.  $\omega$  is a (dimensionless) weight with limits  $0 \leq \omega \leq 1$ . Since different types of data are gathered in  $\chi_{tot}$  [Mathieu et al., 2014] proposed to use  $\omega = 1/2$  so the credit given to any source of information is gauged by the uncertainty it provides. Depending on the value of  $\omega$ , different techniques are obtained

- *FEMU-U* ( $\omega = 0$ )

As mentioned earlier FEMU consists of minimising the cost function as the squared error between measured  $\{\mathbf{u}_m\}$  (*i.e.*, a vector gathering all measured nodal displacements) and computed  $\{\mathbf{u}_c\}$  (*i.e.*, vector gathering all calculated nodal displacements) data written as [Gras et al., 2013, Mathieu et al., 2014]

$$\chi_u^2(\{\mathbf{p}\}) = \frac{1}{\gamma_u^2 N_u} \|\{\mathbf{u}_m\} - \{\mathbf{u}_c\}\|^2 \quad (1.28)$$

where  $\{\mathbf{p}\}$  is the column vector gathering all unknown material parameters of a chosen constitutive model, and  $\gamma_u$  is measurement resolution (if the measurements are uncorrelated). Since different data are considered in  $\chi_{tot}$  (displacement and force residuals) it is necessary to introduce the normalisation factor  $1/N_u$  [Mathieu et al., 2014], where  $N_u$  denotes the total number of kinematic degrees of freedom. The minimisation is performed by resorting to the  $\chi$ -squared estimate

$$\chi_u^2(\{\mathbf{p}\}) = \frac{1}{N_u} (\{\mathbf{u}_m\} - \{\mathbf{u}_c\})^t [\mathbf{C}_u]^{-1} (\{\mathbf{u}_m\} - \{\mathbf{u}_c\}) \quad (1.29)$$

where  $[\mathbf{C}_u]$  is the covariance matrix equal to  $2\gamma_f^2 [\mathbf{M}]^{-1}$  [Besnard et al., 2006]. The connection between  $[\mathbf{C}_u]$  and DIC matrix  $\mathbf{M}$  for a global DIC approach will be presented in CHAP. 2.

Minimisation of  $\chi_u^2$  is performed by successive linearisations and corrections [Gras et al., 2013, Mathieu et al., 2014]. In the present case, the new estimate (*i.e.*, at iteration  $i$ ) of the computed displacement field reads

$$\mathbf{u}_c(\mathbf{x}, t, \{\mathbf{p}^{(i)}\}) = \mathbf{u}_c(\mathbf{x}, t, \{\mathbf{p}^{(i-1)}\}) + \frac{\partial \mathbf{u}_c}{\partial \{\mathbf{p}\}}(\mathbf{x}, t, \{\mathbf{p}^{(i-1)}\}) \{\delta \mathbf{p}\} \quad (1.30)$$

where  $\{\mathbf{p}^{(i-1)}\}$  is the set of parameters at iteration  $i - 1$ , and  $\{\delta\mathbf{p}\}$  the sought parameter increment. The computation of the sensitivity fields

$$[\mathbf{S}] = \frac{\partial \mathbf{u}_c}{\partial \{\mathbf{p}\}} \quad (1.31)$$

can be performed analytically or numerically by computing the fields for small variations of each parameter of the considered set. For iteration  $i$  it is necessary to calculate the sensitivity fields and once they are obtained the correction of the sought parameters read [Gras et al., 2013, Mathieu et al., 2014]

$$\{\delta\mathbf{p}\} = \left( [\mathbf{S}^{(i-1)}]^t [\mathbf{M}] [\mathbf{S}^{(i-1)}] \right)^{-1} [\mathbf{S}^{(i-1)}]^t [\mathbf{M}] \left( \{\mathbf{u}_m\} - \{\mathbf{u}_c^{(i-1)}\} \right) \quad (1.32)$$

Convergence is usually written in terms of relative variations of the sought parameters.

- *FEMU-F* ( $\omega = 1$ )

Similar to FEMU-U, the  $\chi$ -squared load estimate  $\chi_F$  is minimized [Mathieu et al., 2014]

$$\chi_F^2(\{\mathbf{p}\}) = \frac{1}{\gamma_F^2 N_F} (\mathbf{F}_c - \mathbf{F}_m)^t (\mathbf{F}_c - \mathbf{F}_m) \quad (1.33)$$

where  $\gamma_F$  is the standard resolution of the load measurement, and  $N_F$  the total number of load data. Thus the expected value of  $\chi_F$  is unity when only noise is at play. The identification is then the result of the minimisation of  $\chi_F^2$ .

- *FEMU-UF* ( $0 < \omega < 1$ )

The last procedure is a combination of the two previous approaches [Mathieu et al., 2014].

## 5 Conclusion

This chapter has presented a review on the three main issues of the investigation presented hereafter. First, nodular graphite cast iron was chosen as the material of interest. The combination of heterogeneous microstructure, additional alloying elements and heat-treatment results in a (very large) family of SG cast iron grades with a wide variety of mechanical properties. The main characteristic of the most commonly used SG cast iron is its ductility. However, the investigated cast iron manufactured by a sandwich production technology possesses quasi-brittle features (*e.g.*, an elongation to failure of only 5 %).

The objective of this thesis is to determine the material parameters of nonlinear constitutive laws. A brief overview on nonlinear models is presented with a focus on the elastoplastic (*i.e.*, isotropic and kinematic hardening) laws and damage models. Johnson-Cook and Armstrong-Frederick hardening models were considered since they are implemented in the commercial FE code Abaqus. Damage was also identified via Abaqus with

an existing user material subroutine (UMAT). In the latter Lemaitre's damage model is implemented and is coupled with Ludwik's law.

The third review corresponds to the applied methodology. Advanced identification procedures will consider elastoplastic and damage models. Among the proposed methods Finite Element Model Updating was a natural choice since the previous models were available in Abaqus. Moreover, global (*i.e.*, FE-based) DIC will be used (see CHAP. 2) to measure displacements fields, which has the additional advantage that measured and calculated data (*i.e.*, displacement fields) are expressed within the same framework.





# Chapter 2

## Digital Image Correlation

*Digital Image Correlation (DIC) and Digital Volume Correlation (DVC) are full-field measurement techniques that will be introduced in this chapter. Existing approaches will be explained and compared. Special emphasis will be given to global DIC, its regularized and integrated variants (R-DIC and I-DIC).*

### Contents

---

<b>1</b>	<b>Preface</b> . . . . .	<b>39</b>
<b>2</b>	<b>Introduction</b> . . . . .	<b>39</b>
<b>3</b>	<b>Digital Image Correlation</b> . . . . .	<b>40</b>
	3.1 Local DIC approach . . . . .	41
	3.2 Global DIC approach . . . . .	43
	3.3 Comparison between local and global DIC . . . . .	44
<b>4</b>	<b>Regularized DIC</b> . . . . .	<b>47</b>
	4.1 Introduction . . . . .	47
	4.2 Regularized correlation principle . . . . .	48
	4.3 Validation of R-DIC . . . . .	49
<b>5</b>	<b>Integrated DIC</b> . . . . .	<b>57</b>

5.1	Introduction . . . . .	57
5.2	I-DIC principle . . . . .	57
<b>6</b>	<b>Digital Volume Correlation - DVC . . . . .</b>	<b>58</b>
<b>7</b>	<b>Conclusion . . . . .</b>	<b>59</b>

---

## 1 Preface

As mentioned in the previous chapter advanced inverse identification uses full-field measurements (*i.e.*, displacement or strain fields) to obtain material parameters of a constitutive postulate. DIC is one of the most used full-field measurement techniques. In this chapter DIC is going to be introduced with the two existing approaches (*i.e.*, local and global). From global DIC whose framework is generally based on FE formulations many additional approaches are derived. Regularized DIC is based on mechanics-aided DIC. Displacement/strain fields are regularized to be mechanically admissible. *Integrated* DIC derives from global DIC. Yet instead of measured kinematic degrees of freedom the measured field gives directly access to material parameters.

DIC measures planar or 3D surface displacements. With the development of tomographs a new way of measuring displacements is available by developing *Digital Volume Correlation* (DVC). Analysing the reconstructed volume from CT scans with DVC algorithms reveals the displacement fields in the specimen bulk.

## 2 Introduction

The conventional way of measuring displacement/strain via strain gauges, mechanical extensometers (*e.g.*, clip gauges) or LVDTs determines only the global material behaviour in one or few points of the investigated area. Effects such as strain localization, microcracking, necking cannot be captured. With the development of digital cameras (*Charge-Coupled Device* - CCD, *Complementary Metal-Oxide Semiconductor* - CMOS) image analyses became more popular in fluid (*Particle Image Velocimetry* - PIV) and solid mechanics (*Digital image Correlation* - DIC). Apart from DIC other full field measurement techniques are developed such as moiré interferometry, speckle interferometry, grid method or infrared thermography.

Ductile cast iron is particularly interesting to observe at the microscale because of its heterogeneity [Limodin et al., 2009]. Using appropriate optical magnifications it is possible to observe the behaviour of graphite nodules within the ferrite matrix. Imaging techniques including photography, cinematography and analog / digital video techniques are always favourite tools for research scientists to investigate the motion of solid objects and fluids. Based on digital image processing and numerical techniques, Digital Image Correlation (DIC) can accurately evaluate full-field displacements and strains of specimens by registering grey level images (in the reference and deformed configurations). DIC was first proposed in the early 1980s [Lucas and Kanade, 1981, Sutton et al., 1983, Chu et al., 1985, Sutton et al., 1986]. After more than 20 years of development, this method has matured and has become a useful tool to determine numerous mechanical parameters.

The DIC method has found application in fracture mechanics because of its remarkable sensitivity [McNeill et al., 1987, Abanto-Bueno and Lambros, 2002, Forquin et al., 2004, Roux and Hild, 2006, Yoneyama et al., 2007]. It is possible not only to detect cracks with sub-pixel openings, which would not be visible, but also to provide accurate

estimates of stress intensity factors. Working with digital images allows the experimentalist to deal with a wide range of scales. Recent research was conducted with Digital Volume Correlation (DVC) analyses of 3D microtomographic images obtained with a laboratory X-ray setup. Fatigue crack closure was studied in a nodular graphite cast iron. This material is well adapted to correlation techniques, with graphite nodules that act as natural markers [Limodin et al., 2009, Limodin et al., 2010].

### 3 Digital Image Correlation

The general concept of DIC is pattern matching to determine the displacement field by correlating the image taken in the reference configuration and another one in the deformed configuration. The most important ingredient of DIC is the black and white stochastic speckle pattern. The reference configuration  $f(\mathbf{x})$  is usually an image taken in the undeformed state (*i.e.*, the observed structure is unloaded) and the deformed configuration  $g(\mathbf{x})$  is an image taken while the investigated object is loaded. However, sometimes when large strains are observed two consecutive loaded images are used for correlation purposes.

Images  $f$  and  $g$  are matrices of grey level values where  $\mathbf{x}$  denotes the position of pixels. For the two latter images grey level conservation (*i.e.*, rule of optical flow) is usually assumed

$$f(\mathbf{x}) = g(\mathbf{x} + \mathbf{u}(\mathbf{x})) \quad (2.1)$$

where  $\mathbf{u}$  is the unknown displacement field to be measured, and  $\mathbf{x}$  the pixel location. The matching criterion over a *Zone of Interest* (ZOI) can be the minimization of the Sum of Squared Differences (SSD) between intensity values of the image pair

$$\min_{\mathbf{u}} \|f(\mathbf{x}) - g(\mathbf{x} + \mathbf{u})\| = \int_{ZOI} [f(\mathbf{x}) - g(\mathbf{x} + \mathbf{u})]^2 d\mathbf{x} \quad (2.2)$$

or equivalently, the maximization of their Cross-Correlation Coefficient (CCC)

$$(f * g) = \int_{ZOI} f(\mathbf{x}) g(\mathbf{x} + \mathbf{u}) d\mathbf{x} \quad (2.3)$$

when a uniform translation is to be determined.

When discussing DIC it is also necessary to mention the terms *displacement resolution* and *spatial resolution*. The displacement resolution is defined as the smallest change to be measured that produces a perceptible change [ISO/IEC Guide 99–12, 2007]. Many features concerning DIC influence the displacement resolution such as bias (*e.g.*, image distortions), noise (*e.g.*, in image acquisition), grey level scale, texture quality. The spatial resolution is the smallest distance between two points for which two independent measurements can be obtained. In the following two concepts of DIC will be presented and compared.

### 3.1 Local DIC approach

Originally the applied principle of DIC was a local approach and it is still the most widely used in commercial codes. A local approach consists of a discretization of the sought displacement field on a selected grid (*i.e.*, setting center points of multiple virtual displacement gauges over a Region Of Interest - ROI). The correlation is performed on zones of interest (ZOIs - small windows of the considered image, which are also called subsets, facets in commercial codes). Generally, a ZOI is of square shape where the size is defined as  $\ell$ . Each ZOI is considered independently, which explains the name *local*. The local approach consists of the following steps. First the ROI is defined in reference configuration on which are subsequently placed equally spaced grid points (*i.e.*, centres of ZOIs). Since the distance between points is optional, *i.e.*, user defined, the following cases are distinguished (FIG. 2.1):

- Overlapping ZOIs (the distance between two centres of neighbouring ZOIs is less than  $\ell$ )
- Contiguous edges of ZOIs (the distance between two centres of neighbouring ZOIs is equal to  $\ell$ )
- Separate ZOIs (the distance between two centres of neighbouring ZOIs is greater than  $\ell$ ).

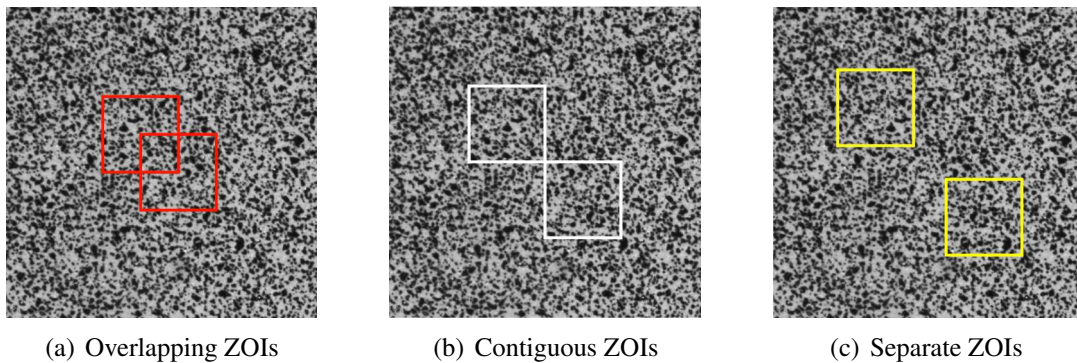


**Figure 2.1:** Three possible situations between neighbouring ZOIs

The high density of ZOIs directly increases the number of measuring points, which increases the richness of the measured field. However, it also increases the computation time since more points are taken into account but also the subpixel interpolation is performed multiple times.

The aim is to identify the new location of the pixels in the deformed image so that the displacements can be calculated in a way that pattern matching is applied on ZOIs between reference and deformed images (see FIG. 2.2). Initially the quantity measured was a rigid body translation in the physical space [Sutton et al., 1983] or in Fourier space [Chen et al., 1993]. Later on were taken into account ZOI warping by implementing linear [Chu

et al., 1985], cubic and spline [Schreier and Sutton, 2002] interpolations. Measuring the degrees of freedom of the whole ZOI gives a better information of the local motions. However, it is introducing more uncertainties since more unknowns are sought. In the end although different interpolations are used to describe the ZOI motions only the mean value of the ZOI displacement is kept [Hild and Roux, 2012].

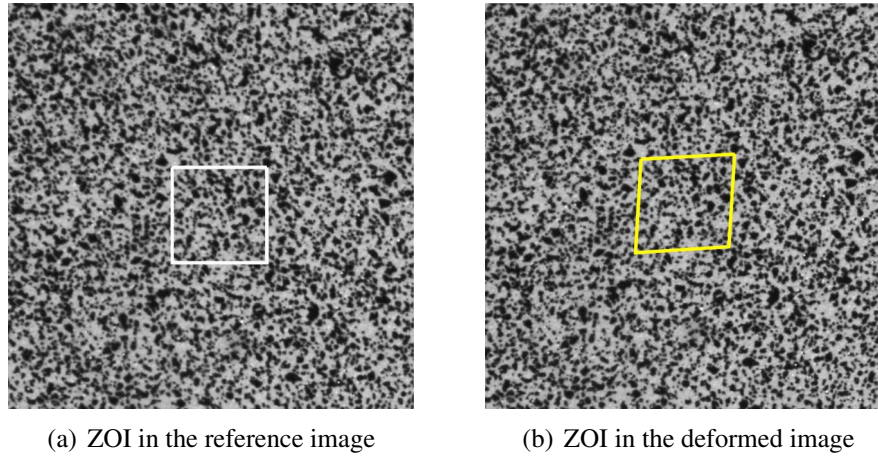


**Figure 2.2:** Principle of local approach that registers the ZOI in the reference configuration with that in the deformed configuration

To find the new position of ZOI in the deformed image several matching criteria are based on the comparison of the grey level scale. The standard and mostly used criterion is based on the cross-correlation product [Sutton et al., 1983]

$$C_{fg}(u, v) = \frac{\sum_{i=1}^m \sum_{j=1}^n [f(x_i, y_i) - \bar{f}] [g(x_i^*, y_j^*) - \bar{g}]}{\sqrt{\sum_{i=1}^m \sum_{j=1}^n [f(x_i, y_i) - \bar{f}]^2 \sum_{i=1}^m \sum_{j=1}^n [g(x_i^*, y_j^*) - \bar{g}]^2}} \quad (2.4)$$

where the ZOI grey level values are defined as  $f(x_i, y_j)$  while  $\bar{f}$  denotes the mean grey level of the ZOI in the reference configuration. The same applies to  $g(x_i^* + y_j^*)$  and  $\bar{g}$  for the deformed configuration. The global coordinates  $(x, y)$  and  $(x^*, y^*)$  are related to the shape functions. When the parameters of the shape functions describe the actual deformation, the correlation coefficient  $C$  is equal to 1, provided noise is neglected. Hence the maximization of coefficient  $C_{fg}$  provides the best estimate of the displacement. To achieve sub-pixel resolutions, the interpolation or fitting of correlation coefficient schemes are implemented. Different shape functions can be used (*e.g.*, zero- [Sutton et al., 1983], first- [Bruck et al., 1989] or second-order [Lu and Cary, 2000] interpolations). Schreier et al. [2000] showed that for a local approach second-order shape functions yield fewer systematic errors than linear shape functions at approximately the same levels of random error.

### 3.2 Global DIC approach

In middle of the last decade global DIC was introduced [Broggiato, 2004, Sun et al., 2005, Besnard et al., 2006]. Also called *Finite-Element* DIC (FE-DIC), it usually considers the whole ROI of an image for correlation purposes (instead of performing multiple minimizations/correlations on ZOIs) to find the sought displacement field (FIG. 2.3). The objective of global DIC is to reduce measurement uncertainties with the reduction of the number of unknowns by introducing known information (continuity of the displacement between the elements). Different forms of shape functions can be chosen to discretise the displacement field (*e.g.*, 4 noded quadrangles (Q4) [Besnard et al., 2006], three-noded triangles (T3) [Leclerc et al., 2009]).

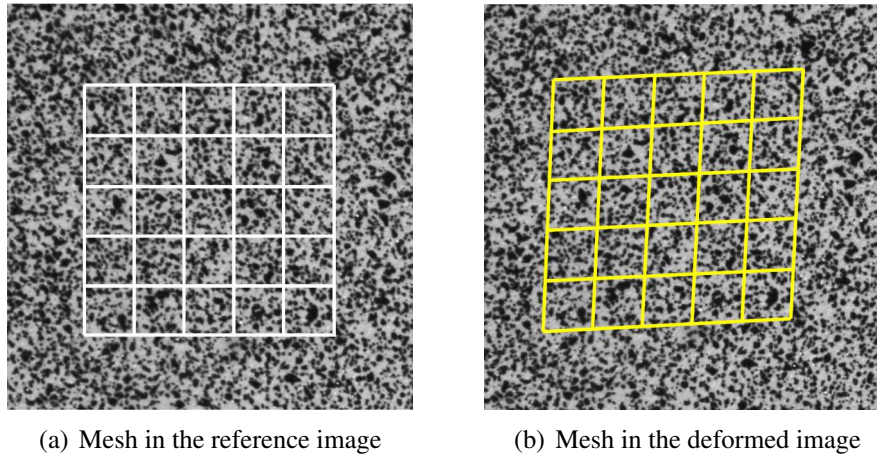


**Figure 2.3:** Principle of global approach where the whole ROI is taken into account and discretized with Q4 elements in the reference and deformed configurations

The registration of two gray level pictures in the reference,  $f$ , and deformed,  $g$ , configurations is based upon the conservation of the gray levels (equation (2.1)). The sought displacement field minimizes the sum of squared differences  $\Phi_c^2$  over the Region Of Interest (ROI)

$$\Phi_c^2 = \int_{\text{ROI}} \varphi_c^2(\mathbf{x}) d\mathbf{x} \quad (2.5)$$

where  $\varphi_c(\mathbf{x})$  defines the field of correlation residuals

$$\varphi_c(\mathbf{x}) = |f(\mathbf{x}) - g(\mathbf{x} + \mathbf{u}(\mathbf{x}))| \quad (2.6)$$

The minimization of  $\Phi_c^2$  is a nonlinear and ill-posed problem. If no additional information is available, it is *impossible* to determine the displacement for each pixel independently since there are two unknowns for a given (scalar) gray level difference. This explains the reason for choosing a weak formulation in which the displacement field is expressed in a (chosen) basis as

$$\mathbf{u}(\mathbf{x}) = \sum_n u_n \psi_n(\mathbf{x}) \quad (2.7)$$

where  $\psi_n$  are (chosen) vector fields, and  $u_n$  the associated degrees of freedom. The measurement problem then consists of minimizing  $\Phi_c^2$  with respect to the unknowns  $u_n$ . By assuming small increments  $\mathbf{du} = \mathbf{u}^{i+1} - \mathbf{u}^i$  of the solution, a Taylor expansion is used to linearize  $g(\mathbf{x} + \mathbf{u}(\mathbf{x}) + \delta\mathbf{u}(\mathbf{x})) \approx g(\mathbf{x} + \mathbf{u}(\mathbf{x})) + \delta\mathbf{u}(\mathbf{x}) \cdot \nabla g(\mathbf{x} + \mathbf{u}(\mathbf{x})) \approx g(\mathbf{x}) + \delta\mathbf{u}(\mathbf{x}) \cdot \nabla f(\mathbf{x})$ . A Newton iterative procedure is followed to circumvent the nonlinear aspect of the minimization problem [Besnard et al., 2006]. The following linear systems are solved iteratively

$$[\mathbf{M}]^i \{\delta\mathbf{u}\} = \{\mathbf{b}\}^i \quad (2.8)$$

with

$$M_{mn}^i = \int_{\Omega} \nabla f(\mathbf{x}) \cdot \psi_m(\mathbf{x}) \nabla f(\mathbf{x}) \cdot \psi_n(\mathbf{x}) \quad (2.9)$$

and

$$b_m^i = \int_{\Omega} [f(\mathbf{x}) - \tilde{g}(\mathbf{x})] \nabla f(\mathbf{x}) \cdot \psi_m(\mathbf{x}) d\mathbf{x} \quad (2.10)$$

where Matrix  $[\mathbf{M}]$  is formed from the dyadic product of fields  $\nabla f \cdot \psi_n$  [Hild and Roux, 2012],  $\{\mathbf{b}\}$  a vector that vanishes when a perfect registration is obtained for each pixel (*i.e.*, Equation (2.1) is satisfied), and  $\{\delta\mathbf{u}\}$  collects the corrections to the measured degrees of freedom  $u_n$ . The search direction is given by  $\nabla f(\mathbf{x})$  because matrix  $[\mathbf{M}]$  is calculated once for all and only vector  $\{\mathbf{b}\}$  is updated for each new iteration [Besnard et al., 2006].  $\tilde{g}(\mathbf{x})$  is equal to  $g(\mathbf{x} + \mathbf{u}(\mathbf{x}))$  and it is called *corrected deformed image*. The use of a Taylor expansion requires that the displacement be small when compared with the correlation length of the texture. For a fine texture and a large initial displacement, this requirement appears as inappropriate to converge to a meaningful solution.

The latter issue can be circumvented by arbitrarily expanding the correlation length of the texture with low pass filtering in Fourier or Wavelet spaces. Another path is a multiscale scheme [Besnard et al., 2006]. The multiscale strategy consists of down-sampling the images to sufficiently low sampling resolutions, so that the sought displacement field becomes of the order of a few coarse grains (the finest grain is a pixel in this sense). Thus, the iterations start using zero values for the unknown degrees of freedom (or an initially determined rigid body motion). This determination is iterated using a corrected image  $\tilde{g}$  where the previously determined displacement is used. This process is stopped once the displacement is stabilized at the finer scale resolution, *i.e.*, dealing with the original images.

### 3.3 Comparison between local and global DIC

Both presented approaches, local and global, are widely used in different applications even though local ones have been more established due to their longer history and simplicity [Sutton et al., 2009]. Since each subset/ZOI is considered as an independent part of an image, this opens a way of performing in parallel DIC/DVC computations on different computers [Gates et al., 2011]. However, this advantage of faster analysis may become a drawback when compared with global approaches. The lack of information in between the ZOIs increases the sensitivity of the displacement resolution. [Besnard et al., 2006] in



one of the first applications of global DIC showed that by using a continuous description of the displacement field, it enables for a decrease of the displacement uncertainty when the same ZOI and element size is used. Conversely, for a given displacement uncertainty, the Q4-DIC algorithm allows one to reduce significantly the element size, thereby increasing the number of measurement points when compared to a classical FFT-DIC technique (FIG. 2.4).

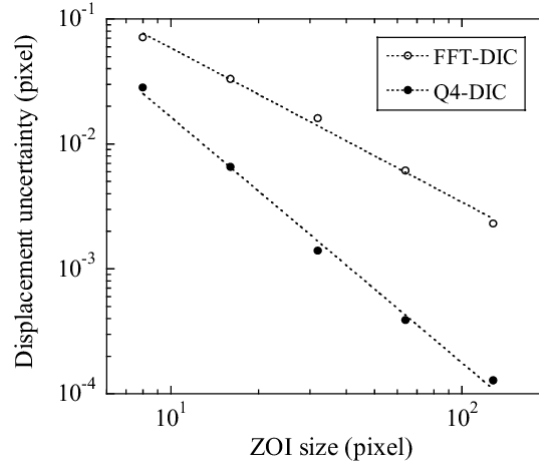


**Figure 2.4:** Standard displacement uncertainty as functions of the ZOI or element size  $\ell$ . The results are obtained by Q4-DIC and compared with FFT-DIC. The dashed lines correspond to power-law fits [Besnard et al., 2006]

When comparing local and global approach with the same minimization procedure (sum of squared differences) Hild and Roux [2012] derived standard displacement resolutions ( $\sigma_u$ ) for both cases. For a local approach each DOF has a displacement uncertainty given by

$$\sigma_u = \frac{4\sqrt{2}\gamma_f p}{G_f \ell} \quad (2.11)$$

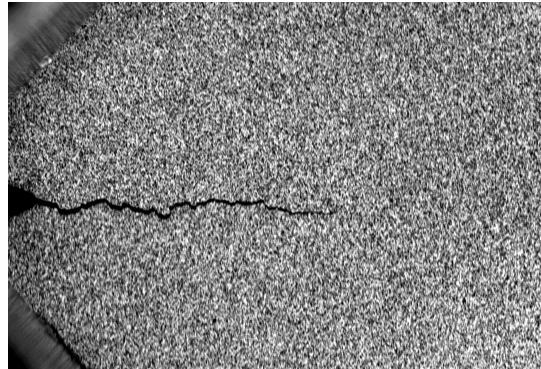
whereas for inner nodes of a global approach it becomes

$$\sigma_u = \frac{\sqrt{6}\gamma_f p}{G_f \ell}. \quad (2.12)$$

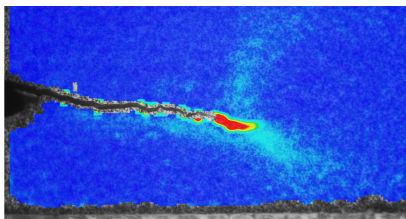
where  $G_f$  denotes the root mean square of the image gradient,  $\gamma_f^2$  the variance of Gaussian white noise,  $\ell$  the ZOI/element size and  $p$  the physical size of one pixel.

A special case that can be challenging for DIC is when dealing with displacement fields containing discontinuities (*e.g.*, cracks, shear bands). Both approaches were tested to see how the macrocrack will influence the displacement field. The analysed image shown in FIG. 2.5(a) was taken from [Čanžar et al., 2012]. The aim of the fatigue experiment conducted on a CT sample was to identify Paris's law parameters. To obtain the displacement field the commercial DIC code Aramis (FIG. 2.5(b)) based on a local

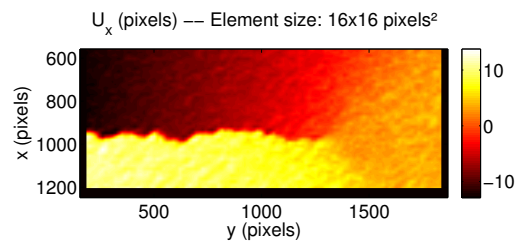
approach was used and Q4-DIC (FIG. 2.5(c)) based on global approach. The presented results of the global algorithm successfully measured the displacement field inside of the chosen ROI. There is an obvious discontinuity along the crack path while Aramis could not converge in the same area. The global approach outperforms the local one when discontinuities appear during a mechanical test [Réthoré et al., 2007].



(a) Picture of cracked CT specimen [Čanžar et al., 2012]



(b) Strain field measured with local DIC code



(c) Displacement field obtained with Q4-DIC

**Figure 2.5:** Comparison of local and global approach when discontinuities appear in the image. Cracked CT sample (a) analysed with local (b) and global (c) DIC approaches

It is worth mentioning that global DIC is more generic since it is based on FE formulation, which opens a way of more convenient couplings with numerical simulations. The measured displacement fields are very often used for comparison purposes with numerical simulations. The latter ones are, for instance, used for identification and/or validation purposes of constitutive laws and numerical models [Claire et al., 2004, Réthoré, 2010, Gras et al., 2013, Mathieu et al., 2014]. If these issues are addressed, it is desirable to have the same kinematic basis whenever possible. If it is not the case, the measured field can be interpolated by using the shape functions of the underlying discretization, and not some exogenous interpolation that was not checked during the measurement stage.

## 4 Regularized DIC

### 4.1 Introduction

One of the limitations of DIC comes from its ill-posedness. The limited available information, generally two gray-level images to be registered, impedes the measurement of very rapid fluctuations of the displacement field, and hence constitutes a potential barrier to very small scale displacement resolutions. Consequently, a compromise has to be found between the standard measurement uncertainty and the spatial resolution [Bergonnier et al., 2005, Triconnet et al., 2009, Bornert et al., 2009].

Different strategies have been designed to overcome this limitation. As noted earlier, classical method (*i.e.*, local approach [Lucas and Kanade, 1981, Sutton et al., 1983]) work with a coarse description of the displacement field based on a discretization scale that is much larger than the pixel scale where the size of the ZOI can be seen as a natural regularization. Apart from this coarse description, no additional assumption is made on the displacement field, which finally has to be interpolated between ZOI centers. In practice, this choice limits the ZOI size to typically 10 pixels or more [Sutton et al., 2000, Sutton et al., 2009].

To achieve smaller resolutions or spatial resolutions, some additional information has to be provided. One possibility is to assume that the displacement field is continuous (see Section 2.3.2). The latter can be decomposed over a convenient basis of functions that fulfill this constraint. The problem to solve no longer consists of a collection of independent correlation computation for each ZOI as was the case for local DIC [Sutton et al., 2009]. The problem is formulated as a whole and all degrees of freedom are determined simultaneously. This coupling involves an over-cost in terms of computation time. This extra cost is however rewarding in terms of result quality [Hild and Roux, 2012]. Further, the post-processing step of data interpolation and smoothing becomes essentially useless, and hence a good control of the displacement determination is preserved. In favourable cases, element sizes as small as  $4 \times 4$  pixels can be used [Rupil et al., 2011].

The spatial resolution can be further decreased (*i.e.*, down to pixel [Passieux and Périé, 2012] or voxel scales [Leclerc et al., 2011, Leclerc et al., 2012]) by adding other terms in the minimization of the gray level conservation [Réthoré et al., 2009]. A natural choice stems from the general propositions associated with the regularization of ill-posed problems [Tikhonov and Arsenin, 1977]. It consists of minimizing the fluctuations associated with the Laplacian of the displacement field [Passieux and Périé, 2012]. This type of filter does work, but it may discard fluctuations that are mechanically admissible. Within this section a mechanics-based regularization strategy [Tomičević et al., 2013] will be presented. It consists of considering a mechanical filter, namely, the regularization term allows the mechanical admissibility to be enforced in a weak sense. The advantage of such a regularization will be shown when assessing the resolution, and with very difficult textures that are not tractable with classical DIC codes [Tomičević et al., 2013, Taillandier-Thomas et al., 2014] (CHAP. 4).

## 4.2 Regularized correlation principle

The mechanics-based regularization is presented herein acts as a filter for bulk degrees of freedom. In the following studies, 3-noded elements will be considered. They are the simplest in terms of displacement interpolations, even though they are seldom used, if ever, in the framework of global DIC. The other novelty of the developed procedure is that the resolution/spatial resolution (or regularization length) limit can be broken through an *appropriate driving* of the DIC algorithm.

Regularized DIC starts with a global approach formulation (equation (2.8)). To enforce mechanical admissibility in an FE sense, the equilibrium gap is first introduced [Claire et al., 2004]. If linear elasticity applies, the equilibrium equations read

$$[\mathbf{K}]\{\mathbf{u}\} = \{\mathbf{f}\} \quad (2.13)$$

where  $[\mathbf{K}]$  is the stiffness matrix, and  $\{\mathbf{f}\}$  the vector of nodal forces. When the displacement vector  $\{\mathbf{u}\}$  is prescribed and if the (unknown) stiffness matrix is not the true one, force residuals  $\{\mathbf{f}_r\}$  will arise

$$\{\mathbf{f}_r\} = [\mathbf{K}]\{\mathbf{u}\} - \{\mathbf{f}\} \quad (2.14)$$

Similarly, if the displacement field does not satisfy equilibrium it will induce an equilibrium gap. In the absence of body forces, interior nodes are free from any external load. Consequently, the equilibrium gap method consists of minimizing

$$\Phi_m^2 = \{\mathbf{u}\}^t [\mathbf{K}]^t [\mathbf{K}] \{\mathbf{u}\} \quad (2.15)$$

where  $^t$  is the transposition operator, and  $\Phi_m^2$  corresponds to the sum of the squared norm of all equilibrium gaps at *interior nodes only*. Any displacement field prescribed on the boundary gives rise to a displacement field for which  $\Phi_m = 0$ . This observation requires an additional regularization for boundary nodes. It is proposed to introduce a penalization of short wavelength displacement fluctuations along the edges of the region of interest. The third objective function to be considered has to vanish for *any* rigid body motion

$$\Phi_b^2 = \{\mathbf{u}\}^t [\mathbf{L}]^t [\mathbf{L}] \{\mathbf{u}\} \quad (2.16)$$

where  $[\mathbf{L}]$  is an operator acting on the ROI boundary [Leclerc et al., 2011].

The minimization of correlation residuals ( $\Phi_c^2$ ), equilibrium gap ( $\Phi_m^2$ ), and boundary fluctuations ( $\Phi_b^2$ ), requires the introduction of a total functional  $\Phi_t$

$$(1 + w_m + w_b)\Phi_t^2 = \tilde{\Phi}_c^2 + w_m \tilde{\Phi}_m^2 + w_b \tilde{\Phi}_b^2 \quad (2.17)$$

where  $w_m$  and  $w_b$  are weights that define length scales associated with  $\tilde{\Phi}_m^2$  and  $\tilde{\Phi}_b^2$ , and  $\tilde{\Phi}$  denote *normalized* residuals. To normalise the residuals displacement field in the form of a plane wave was considered  $\mathbf{v}(\mathbf{x}) = \mathbf{v}_0 \exp(i\mathbf{k} \cdot \mathbf{x})$ , where  $\mathbf{v}_0$  is the amplitude and  $\mathbf{k}$  the wave vector. The normalized residuals then become

$$\tilde{\Phi}_c^2 = \frac{\Phi_c^2}{\{\mathbf{v}\}^t [\mathbf{M}] \{\mathbf{v}\}} \quad , \quad \tilde{\Phi}_m^2 = \frac{\Phi_m^2}{\{\mathbf{v}\}^t [\mathbf{K}]^t [\mathbf{K}] \{\mathbf{v}\}} \quad , \quad \tilde{\Phi}_b^2 = \frac{\Phi_b^2}{\{\mathbf{v}\}^t [\mathbf{L}]^t [\mathbf{L}] \{\mathbf{v}\}} \quad (2.18)$$

where  $\{\mathbf{v}\}$  collects all the nodal displacements associated with displacement field  $\mathbf{v}$ . The wavelength dependence of  $\{\mathbf{v}\}^t [\mathbf{K}]^t [\mathbf{K}] \{\mathbf{v}\}$  and  $\{\mathbf{v}\}^t [\mathbf{L}]^t [\mathbf{L}] \{\mathbf{v}\}$  is of fourth order whereas  $\{\mathbf{v}\}^t [\mathbf{M}] \{\mathbf{v}\}$  is wavelength-independent [Leclerc et al., 2011]. The equilibrium gap and boundary regularization kernels thus act as fourth-order low-pass filters, damping deviations from mechanical admissibility and edge displacement fluctuations below a given wavelength. Weights  $w_m$  and  $w_b$  are chosen as

$$w_m = (2\pi|\mathbf{k}|\ell_m)^4 \quad , \quad w_b = (2\pi|\mathbf{k}|\ell_b)^4 \quad (2.19)$$

where  $\ell_m$  and  $\ell_b$  denote the regularization lengths for  $\Phi_m^2$  and  $\Phi_b^2$ , respectively. With this choice,  $\tilde{\Phi}_c(\mathbf{v}) = \tilde{\Phi}_m(\mathbf{v}) = \tilde{\Phi}_b(\mathbf{v}) = 1$  and  $\tilde{\Phi}_t(\mathbf{v}) = 1$  if  $\ell_m = \ell_b = 1/2\pi|\mathbf{k}|$ .

It is to be emphasised that other forms of regularization kernels could have been chosen. The specific form of the equilibrium gap comes from the strong penalization of high frequency oscillations (fourth power of the wavenumber), and thus also very weak influence on long wavelength modes. The higher  $\ell_m$ , the more weight is put on the equilibrium gap functional  $\tilde{\Phi}_m^2$ , therefore the equilibrium residuals have to reach lower levels. Similarly, the edge regularization term is designed to have the same scaling properties as the bulk term. The higher  $\ell_b$ , the more weight is put on the boundary functional  $\tilde{\Phi}_b^2$ , therefore the corresponding displacement fluctuations will decrease.

When the material parameters are known, the minimization of  $\Phi_t^2$  with respect to the unknown degrees of freedom can be performed [Leclerc et al., 2011]. The above mechanical regularization procedure can be used for an arbitrary supporting mesh, even down to the pixel [Passieux and Périé, 2012] or voxel [Leclerc et al., 2011, Leclerc et al., 2012] scales.

### 4.3 Validation of R-DIC

The validation of mechanical-based DIC will be conducted on artificially deformed images. Two different displacement fields will be considered. In both examples a true texture is considered (FIG. 2.6(a)). The picture definition is  $531 \times 531$  pixels with an 8-bit digitization. It corresponds to the central part of the cross-shaped sample analyzed in [Claire et al., 2004]. To create the deformed configuration, two different displacement fields are considered, namely, a first one that is a sine wave, and a second one that is mechanically admissible. In both cases, a linear interpolation of the gray levels is used to generate picture  $g$  in the deformed configuration. No noise is included. In the following, the elements will be considered to be 3-noded triangles (T3) with a linear displacement interpolation. The same mesh with an element size of 10 pixels (FIG. 2.6(b)) is used in both cases and is made of 2,313 inner nodes and 197 edge nodes.

In the following, series of calculations are generally run with different regularization lengths  $\ell_m$  and  $\ell_b$ . Different initial values of  $\ell_m$  are considered and each time a first calculation is run with an initial value of  $\mathbf{u}^0 = \mathbf{0}$ . The next calculation is carried out with the regularization length *divided by two*. It takes as initial guess  $\mathbf{u}^0$  the displacement field at convergence of the previous calculation, and so on. This procedure will be referred to as relaxation. To judge the quality of the image registration itself, the norm of  $\phi_c$ -field

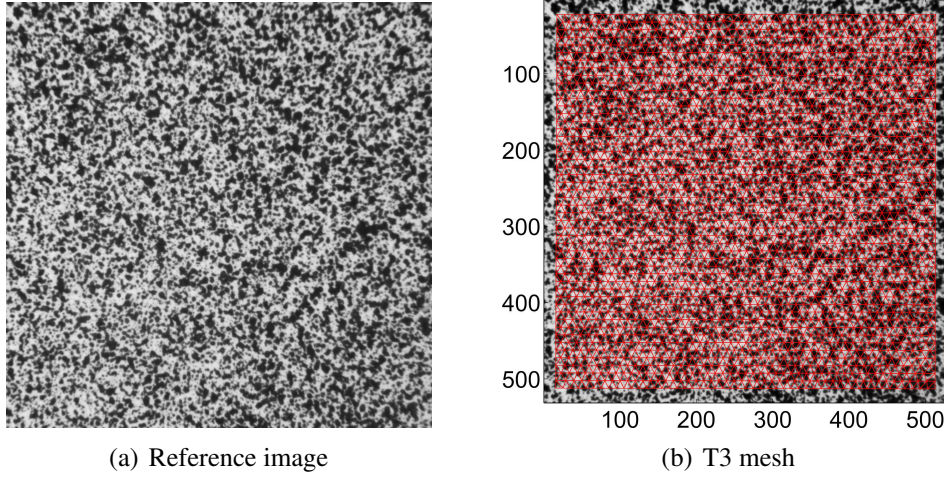


**Figure 2.6:** Reference image of the two artificial cases (a) and the T3 unstructured mesh with the element size of 10 pixels (b)

will be evaluated. The latter can be affected by a mean change of gray levels between the pictures in the deformed and reference configurations. To cancel out this effect (simply contributing as an offset in gray levels), it is convenient to resort to the standard deviation of  $\varphi$ . A dimensionless estimator consists of comparing this standard deviation to the dynamic range

$$\Delta f = \max(f) - \min(f) \quad (2.20)$$

of the reference picture. Thus

$$\hat{\Phi}_c^2 = [\langle \varphi^2 \rangle - \langle \varphi \rangle^2] / (\Delta f)^2 \quad (2.21)$$

where  $\langle \bullet \rangle$  denotes an average of the ROI.  $\hat{\Phi}_c$  will be used in the sequel for estimating the quality of image registration.

### 4.3.1 Sine wave displacement

The sine wave is an interesting case since it corresponds to one of the standard baseline analyses for optical systems (in particular in the context of DIC [Bornert et al., 2009]). The choice of the spatial resolution has to be compared with the wavelength of the prescribed displacement. The two components of the latter read

$$u_x(x, y) = 2 \sin(2\pi x/n_x) \quad , \quad u_y(x, y) = 2 \sin(2\pi y/n_y) \quad (2.22)$$

where  $n_x \times n_y$  is the number of pixels in the ROI. To artificially deform the picture in reference configuration (FIG. 2.6(a)) displacement components (FIG. 2.7) are prescribed.

First, the ratio between  $\ell_b$  and  $\ell_m$  will be identified. A series of calculation was performed where different  $\ell_m$  (i.e.,  $\ell_m = 32$ ,  $\ell_m = 256$ ,  $\ell_m = 1024$  pixels) were taken into

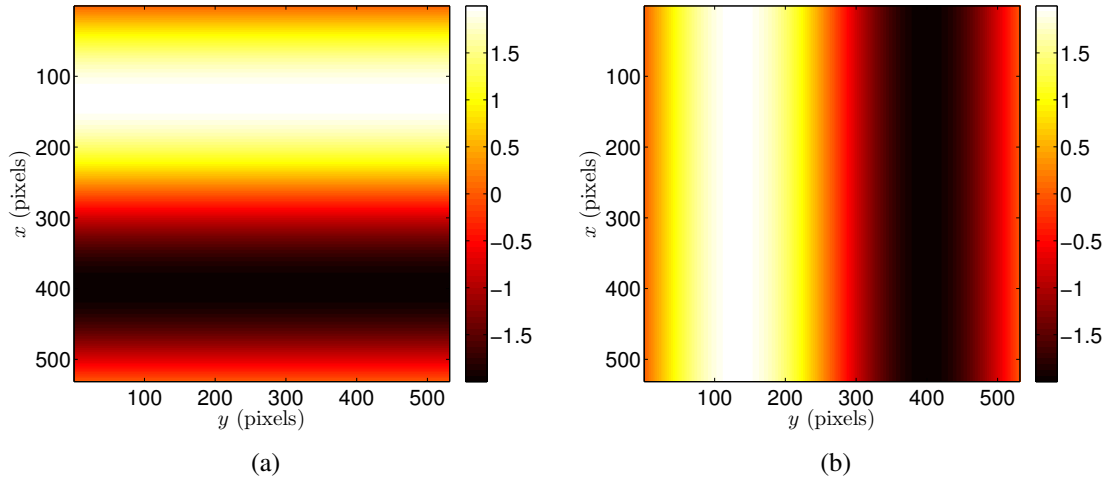


**Figure 2.7:** Prescribed displacement field in the sine wave test case in (a) vertical and (b) horizontal directions. The displacements are expressed in pixels

account. Figure 2.8 shows the change of the standard error between the measured and prescribed displacement field when  $\ell_b/\ell_m$  is set to different values. The same trends are observed for the two components of the displacement field. When the edge regularization is too large (*i.e.*,  $\ell_b/\ell_m > 1$ ), the error is high. This corresponds to an interpolation error since the displacement fluctuations are filtered out. As the edge regularization length decreases, the error decreases too. In the present case,  $\ell_b/\ell_m$  ratios less than 1 lead to very good results even if  $\ell_m$  is relaxed to very small values. This observation justifies the choice of selecting a fixed ratio  $\ell_b/\ell_m = 1/2$  and decreasing both lengths at the same time. For each curve, the relaxation process is to read from right to left.

The second step of the validation will consider the relaxation process when different initial regularization lengths  $\ell_m$  on the inner nodes are applied. FIG. 2.9 shows the change of the standard deviation between the measured and prescribed displacement fields for the different cases when  $\ell_b/\ell_m = 1/2$ . The standard displacement error is virtually identical for the two displacement components (except for very large initial regularization lengths), even though an unstructured mesh is used. No bias is noted due to the fact that the mesh is not regular. Different trends are observed. First for very large initial regularization lengths (*i.e.*,  $\ell_m > n_x, n_y$ ), the standard error is very high. This is caused by interpolation errors as very large regularization lengths prevent from assessing small displacement fluctuations. FIG. 2.10 shows the residual fields when different initialization lengths are used (*i.e.*, FIG. 2.10(a) for  $\ell_m = 128$  and FIG. 2.10(b)  $\ell_m = 1024$  pixels). Both results are taken at the end of the relaxation process. At that point a smaller but still significant error is observed in FIG. 2.9. When larger regularization is applied residuals are higher on the corners since smaller displacements are prescribed in that area. Conversely, for small regularization lengths, the standard error remains small but the relaxation increases slightly the error. When an initial value  $\ell_m = 128$  pixels is chosen, the smallest errors are

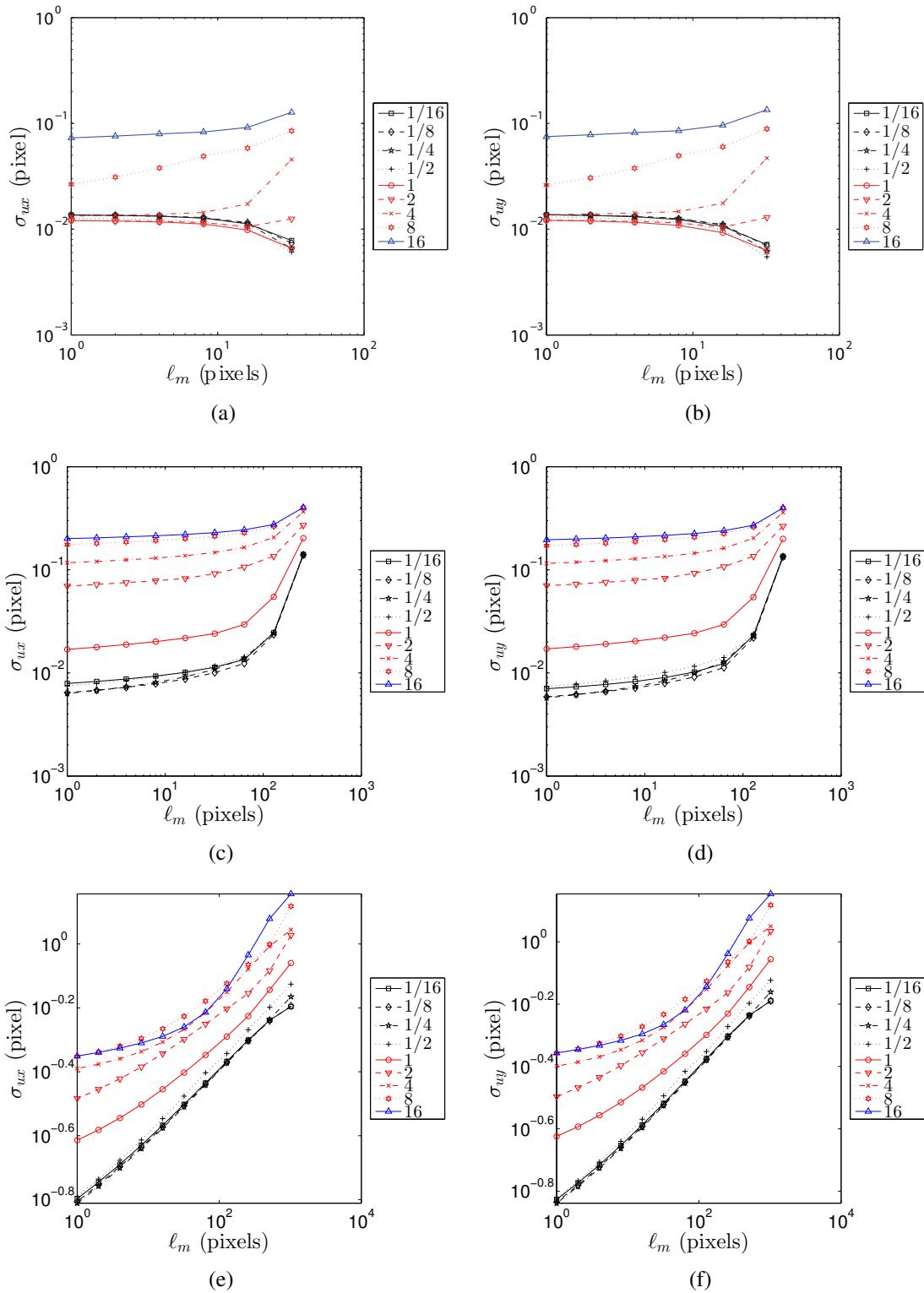


**Figure 2.8:** Change of standard displacement error for different regularization lengths and different  $\ell_b/\ell_m$  ratios in the vertical (left) and horizontal (right) directions. Three initial regularization lengths  $\ell_m$  are considered: (a) & (b) 32, (c) & (d) 256, and (e) & (f) 1024 pixels



observed. For initial lengths less than  $\ell_m = 128$  pixels, error levels of the order of or less than  $10^{-2}$  pixel are achieved.

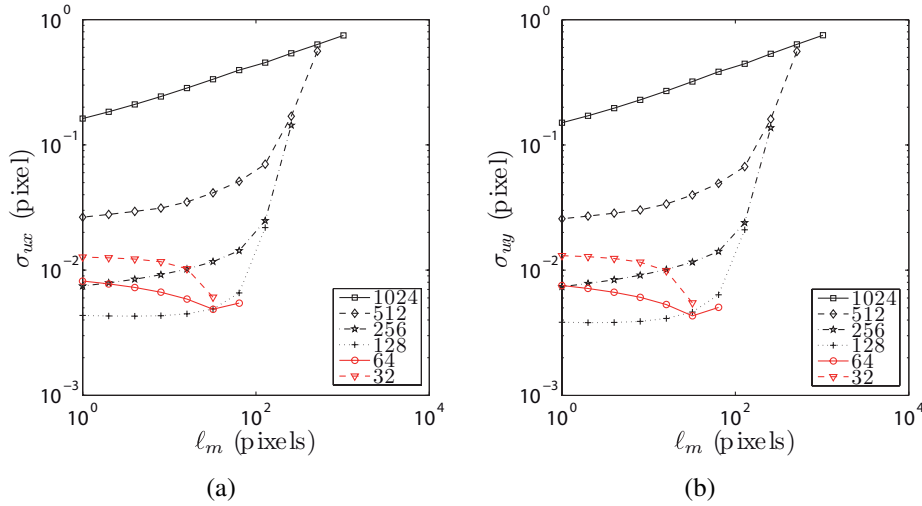


**Figure 2.9:** Sine wave test case. Change of the standard displacement error for different regularization lengths and different  $\ell_m$  initialization lengths (in pixels) indicated in the legend: (a) error in vertical and (b) in horizontal directions

For the same series of computations, FIG. 2.11(a) shows the change of the dimensionless correlation residuals  $\hat{\Phi}_c$ . When the initial regularization lengths are such that  $\ell_m < n_x, n_y$ , the correlation residuals reach similar values, thereby indicating that the results are trustworthy. For the quality of image registration, it indicates that for initial regularization lengths  $\ell_m$  less than 256 pixels, the overall registration quality is very close for any initial or subsequent regularization length. This conclusion is in very good agreement with what is observed in FIG. 2.9. For large initial regularization lengths, the mean correlation residuals reach high levels (*i.e.*, almost an order of magnitude higher). The next choice is then to seek more or less mechanical content in the measured displacement field. This is characterized by the equilibrium gap whose mean normalized value is shown in FIG. 2.11(b). For larger regularization lengths, the measured field displays less equilibrium gap as its weight in the total functional (Equation (2.17)) is increased. There is a whole range of initial values ( $128 < \ell_m < 512$  pixels) for which the equilibrium gap is independent of the initial value of  $\ell_m$ . This zone is the most favorable in the present case.

### 4.3.2 Mechanics-based displacement field

The displacement field prescribed in this test case was obtained from an elastic calculation (with Poisson's ratio  $\nu = 0.3$ ) performed on a plate whose size is exactly the same as the reference picture shown in FIG. 2.6(a). The boundary of the top part only moves in the horizontal direction, and the boundary of the bottom part has a prescribed displacement that is again a sine wave of unitary amplitude and wave length equal to the length of the

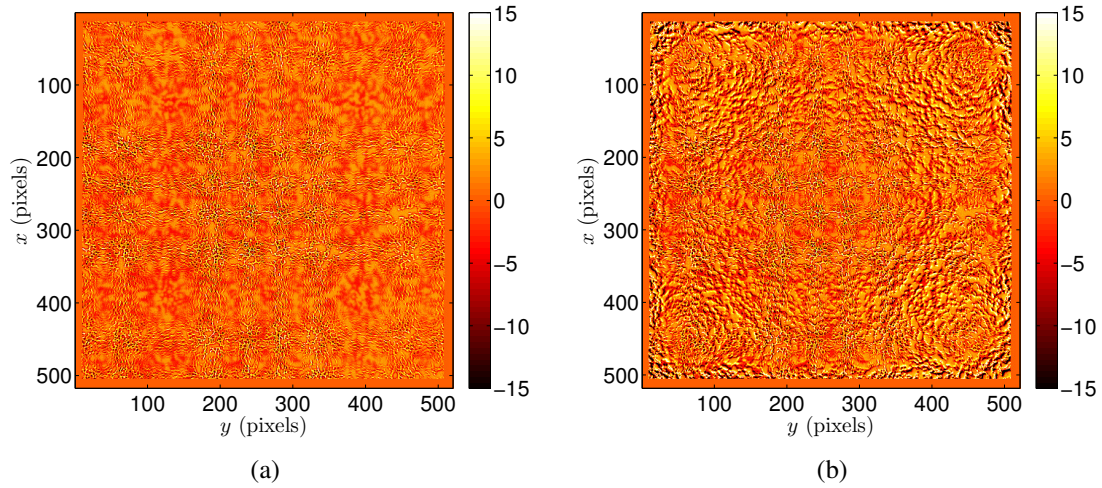


**Figure 2.10:** Residual fields when  $\ell_m = 1$  pixel with an initial length of 128 (a) and 1024 pixels (b). The fields are expressed in grey levels

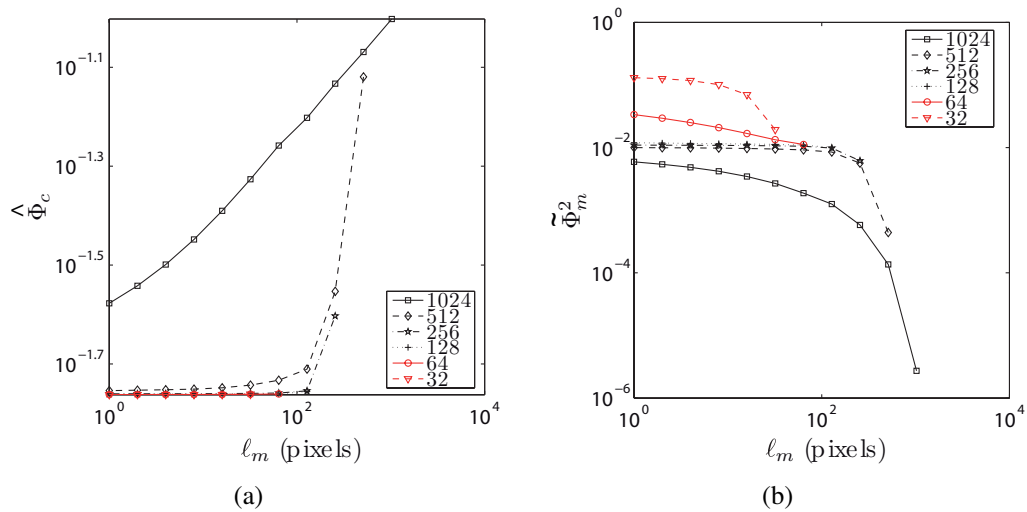


**Figure 2.11:** Sine wave test case. Change of (a) the dimensionless correlation residuals and (b) equilibrium residuals for different regularization lengths and different initialization lengths  $\ell_m$  (in pixels) indicated in the legend

lower edge. A mesh consisting of  $50 \times 50$  Q4 elements is considered. The corresponding displacement is subsequently interpolated at the pixel level by using bilinear shape functions of Q4 elements. FIG. 2.12 shows the displacement components that are used to deform the reference picture of Figure 2.6(a). The range of vertical displacement is equal to 2 pixels, and that of the horizontal displacements is of the order of 1.7 pixel.

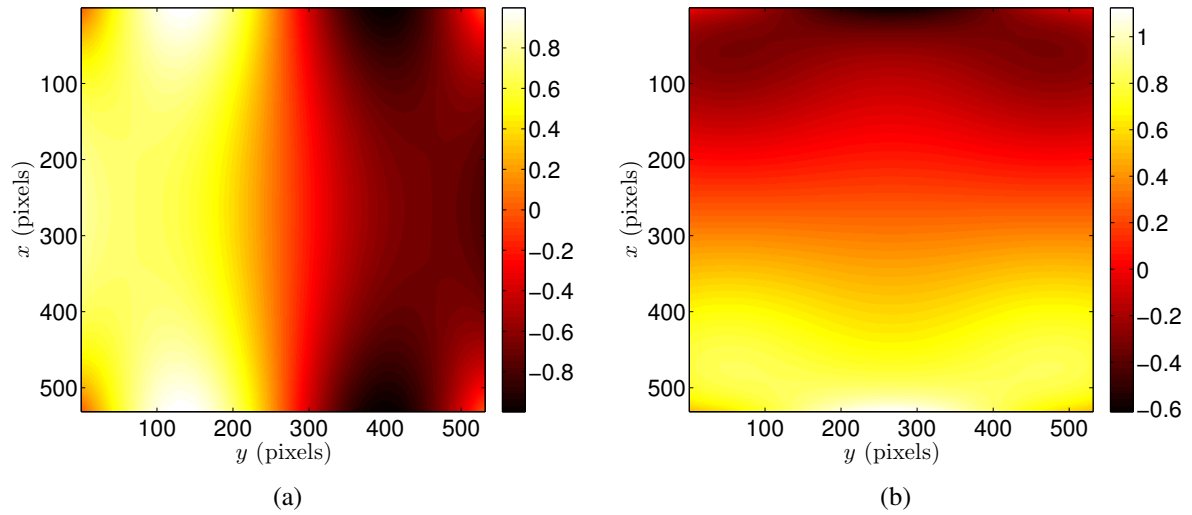


**Figure 2.12:** Prescribed displacement field in the mechanical test case in (a) vertical and (b) horizontal directions. The displacements are expressed in pixels

The same type of computation as before is performed in the present case when  $\ell_b/\ell_m = 1/2$ . FIG. 2.13 shows the change of the standard displacement error. The same trends are observed when compared to FIG. 2.9 for the same reasons. For initial regularization lengths  $\ell_m$  ranging from 64 to 512 pixels the error level is less than  $10^{-2}$  pixel at the end of the relaxation process. It is worth remembering that this error includes the approximations of the reference solution (on a regular Q4 mesh), those of the T3 mesh used in the DIC analysis, and the inevitable gray level interpolation.

The same conclusions are drawn when the trends observed in terms of correlation residuals (FIG. 2.14(a)) and equilibrium residuals (FIG. 2.14(b)) are compared with those of the previous test case FIG. 2.11.

There are however differences to be noted. First, the correlation residuals do not vary over a large dynamic range when compared to the previous case. It is concluded that even though large regularization lengths are used, they still allow for more fluctuations of the displacement field. Second, the minimum levels of the equilibrium residuals are less than those observed in the previous case. This is to be expected since the present test case is associated with a mechanically admissible displacement field (in an FE sense). It is necessary to note how the regularization principle is very powerful but if inappropriate regularization lengths are used it can neglect (*i.e.*, filter) small displacement fluctuations. Hence, it is recommended to perform the presented parametric analysis to find the suitable

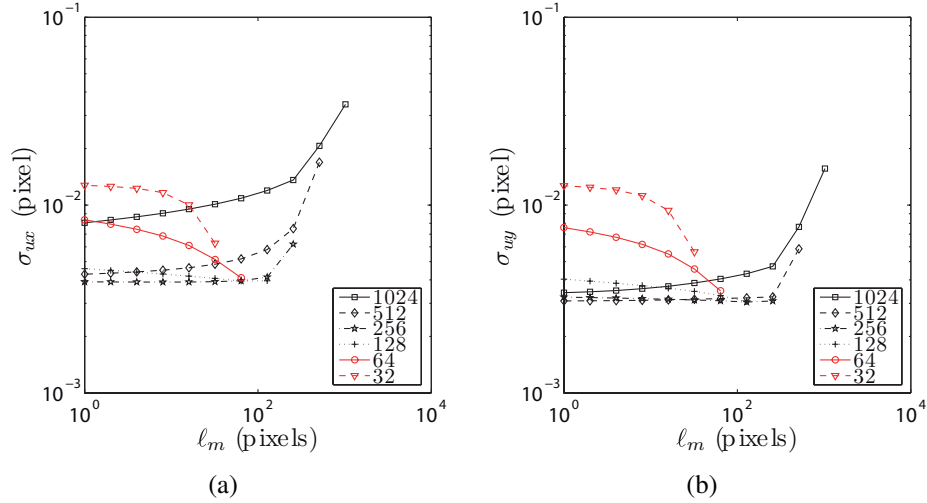


**Figure 2.13:** Mechanical test case. Change of the standard displacement error for different regularization lengths and different  $\ell_m$  initialization lengths (in pixels) indicated in the legend. (a) Standard error in vertical and (b) in horizontal direction

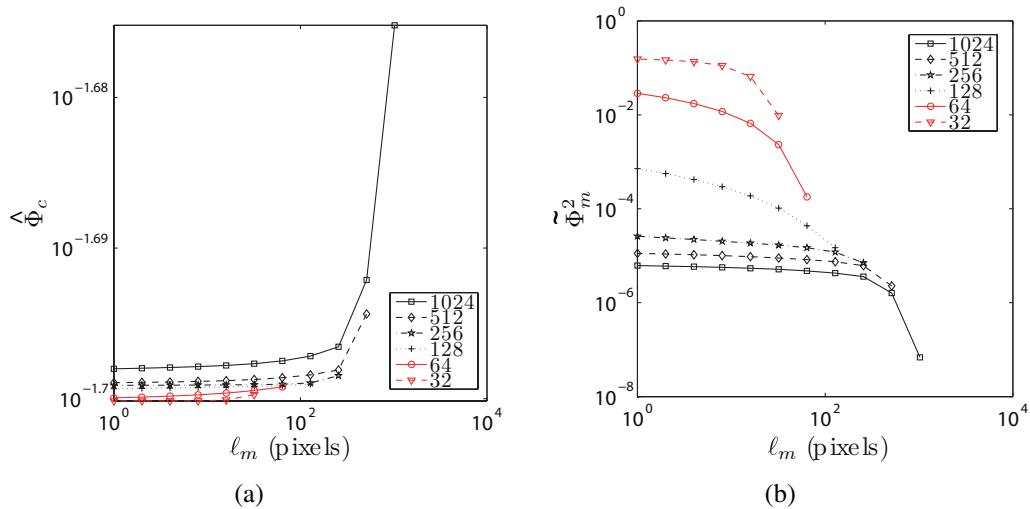


**Figure 2.14:** Mechanical test case. Change of (a) the dimensionless correlation residuals and (b) equilibrium residuals for different regularization lengths and different initialization lengths  $\ell_m$  (in pixels) indicated in the legend

parameters for R-DIC (*i.e.*,  $\ell_m$  and  $\ell_b$ ) especially in case of poor textures (see CHAP. 4).

## 5 Integrated DIC

### 5.1 Introduction

The previously mentioned identification procedures in (Section 1).4 use measured data as inputs. Hence, prior to the identification the measurement step is performed. A different route is taken in *Integrated* DIC (I-DIC) where identification and measurement are carried out in a single analysis. In standard DIC (local or global) the measured degrees of freedom correspond to displacements while in I-DIC they are material parameters (*e.g.*, elastic parameters [Hild and Roux, 2006, Leclerc et al., 2009], Paris's law [Mathieu et al., 2013], damage parameters [Réthoré, 2010]) or mechanical parameters (*e.g.*, stress intensity factors [Roux and Hild, 2006, Hamam et al., 2007, Mathieu et al., 2012, Mathieu et al., 2014]). The latest development on integrated approach [Leclerc et al., 2009, Réthoré, 2010, Mathieu et al., 2014] are more generic when dealing with nonlinear constitutive models since numerical solutions were considered while [Hild and Roux, 2006, Roux and Hild, 2006, Hamam et al., 2007, Mathieu et al., 2012] obtained results with closed-form (elastic) solutions.

### 5.2 I-DIC principle

Integrated DIC is based on a global DIC approach that relies on a specific choice for the measured displacement field. Global DIC offers the possibility of choosing a better displacement space than the general FE form. The latter option can be powerful with a valid assessment of the sample behaviour. In this case a minimization problem of correlation is written in terms of a set of material/mechanical parameters  $\{\mathbf{p}\}$ .

Before presenting how the I-DIC procedure identifies the sought parameters it is necessary to explain the sensitivity of the global approach to image noise [Besnard et al., 2006]. While the reference image  $f$  is considered to be noise free the deformed image  $g$  is affected by noise  $\zeta$  in the difference  $(g - f)$  of variance  $2\gamma_f^2$ . From Equation (2.7) just vector  $\mathbf{b}$  is influenced by noise while matrix  $[\mathbf{M}]$  is unaffected. On average,  $\langle \delta \mathbf{b} \rangle = 0$  and its covariance reads [Besnard et al., 2006]

$$C(\delta \mathbf{b}) = 2\gamma_f^2[\mathbf{M}] \quad (2.23)$$

By linearity (Equation (2.7)) the mean value of  $\langle \delta \mathbf{u} \rangle$  vanishes and its covariance becomes

$$C(\delta \mathbf{u}) = \mathbf{C}_{\mathbf{u}} = 2\gamma_f^2[\mathbf{M}]^{-1} \quad (2.24)$$

[Mathieu et al., 2014] used the sensitivity field  $[\mathbf{S}_{\mathbf{u}}]$  with the same boundary conditions in FE calculation and in I-DIC. The sensitivity fields can only be applied if the same

discretization is provided in both analysis. The problem consists of solving series of linear systems

$$[\mathbf{N}^{(i)}] \{\delta \mathbf{p}\} = \{\mathbf{B}^{(i)}\} \quad (2.25)$$

where  $[\mathbf{N}^{(i)}] = [\mathbf{S}_{\mathbf{u}}^{(i)}]^t [\mathbf{M}] [\mathbf{S}_{\mathbf{u}}^{(i)}]$ , which is the projection of the DIC matrix onto the sensitivity fields and  $\{\mathbf{B}^{(i)}\} = [\mathbf{S}_{\mathbf{u}}^{(i)}]^t \{\underline{\mathbf{b}}^{(i)}\}$  the corresponding projection of the DIC vector  $\{\underline{\mathbf{b}}^{(i)}\}$ . Matrix  $[\mathbf{M}]$  denotes the block diagonal matrix with the same matrix  $[\mathbf{M}]$  while  $\{\underline{\mathbf{b}}^{(i)}\}$  gathers all vectors  $\{\mathbf{b}^{(i)}\}$  for a spatio temporal analysis. With this setting it is necessary to perform only one spatio-temporal analysis. If Equation (1.32) is studied the presented I-DIC procedure is linked with FEMU [Mathieu et al., 2014] since the same matrix  $[\mathbf{N}]$  is obtained. Hence, when measurements are performed via I-DIC, the covariance matrix  $\mathbf{C}_{\mathbf{p}}$  is evaluated as in the global DIC setting (see Equation (2.24)), as

$$[\mathbf{C}_{\mathbf{p}}] = 2\gamma_f^2 [\mathbf{N}]^{-1} \quad (2.26)$$

## 6 Digital Volume Correlation - DVC

X-ray computed tomography (X-ray CT), which developed in the late 1970's, is an imaging technique that uses computer-processed X-ray radiographs to produce 3D images of specific areas of the scanned object, allowing the user to see inside without cutting the sample (non-destructive technique). From a large series of 2D radiographic images taken around one axis of rotation a 3D volume is reconstructed. Most common applications of X-ray CT are in the medical field where low X-ray radiations are used to make their dose as small as possible for the patient.

Except in medicine X-ray tomography found also applications in materials science [Baruchel et al., 2000] using industrial tomographs or synchrotron radiation facilities. Accessing the features in the bulk of the component allows one to observe microstructural changes during solidification of alloys [Ludwig et al., 2005], microstructural details during sintering of steel powders [Vagnon et al., 2006, Bernard et al., 2005], damage mechanisms [Buffière et al., 1999, Babout et al., 2001]. X-ray reconstructed volumes are not only used for inspection purposes. In situ mechanical experiments are also carried out on tomographs [Limodin et al., 2009, Limodin et al., 2010]. Acquired scans during the loading process of the experiment are subsequently used for the measurement via Digital Image Correlation (DVC) of displacement fields [Bay et al., 1999, Smith et al., 2002] or strain fields [Taillandier-Thomas et al., 2014]. These fields can also be used for identification purposes [Limodin et al., 2009, Limodin et al., 2010, Bouterf et al., 2015].

To measure displacements of a 3D reconstructed volume it is possible to resort to local or global DVC. Local DVC consists of correlating small volumes of interest [Bay et al., 1999, Smith et al., 2002, Verhulp et al., 2004] as in 2D local DIC (Section 2.3.1). [Roux et al., 2008] proposed a global scheme for DVC as an extension of global DIC

based on a continuous and global field as commonly practiced in finite element simulations. Both global and local DVC approaches use the same algorithms as 2D-DIC. The only difference is that the former ones are extended to the third dimension. When comparing both approaches, global DVC, due to the assumption of continuous displacement field, outperforms local DVC in terms of displacement resolution and measurement uncertainty [Leclerc et al., 2012].

One of the frequent solutions is to enforce a restricted kinematics requiring a compromise between the richness of the solution (*i.e.*, the spatial resolution) and the measurement uncertainty. With the implementation of mechanically regularized DVC using the equilibrium gap method, and an additional boundary regularization [Leclerc et al., 2011] allows for the measurement of displacements at a voxel level, exploiting the assumption of an elastic behaviour at a small scale. When the voxel scale (*i.e.*, one element is one voxel) is used it leads to a system with a large number of DOFs. [Leclerc et al., 2012] overcame this problem with GPU implementations of R-DVC that allowed for the analysis of representative volumes with more than 6 million DOFs in less than 10 minutes that out-performed local and global DVC analyses with C8 elements.

Since DVC uses a natural texture of the investigated material it can be a barrier if the material does not have some features that can act as markers. Poor natural textures lead to a convergence problem. It is necessary to increase the spatial resolution in local and global DVC approaches to successfully run the computations. Introducing regularization [Taillandier-Thomas et al., 2014] allows the problem to be solved.

## 7 Conclusion

The chosen FEMU procedure uses measured displacement fields. First, the measured displacements are used to define an FE model (*i.e.*, displacements are prescribed as boundary conditions to the FE model). The aim is then to minimize the difference between the measured and calculated displacement fields. In order to obtain trustworthy parameters the measured displacements need to be captured with lowest error. This chapter introduced existing DIC approaches with a special focus on the measurement uncertainty and resolution. Local and global approaches were presented and compared. It was reported that a global approach outperforms local ones [Hild and Roux, 2012] in terms of measurement resolution. Another advantage is related to the identification protocol. Global DIC can easily be coupled with FE simulations since the same meshes can be used. The displacement fields can be compared node to node without introducing any additional interpolation errors.

A new variant of global DIC was developed for this work, namely, regularized (*i.e.*, mechanically based) DIC was introduced. It is known [Besnard et al., 2006, Hild and Roux, 2012] how a decrease of spatial resolution induces an increase of standard displacement resolution. This limitation was bypassed thanks to regularized DIC. This new approach was validated on artificially deformed images. However, one should be careful when using such techniques since relevant features can be smeared out if too big

regularization lengths are chosen. To avoid such effect it is proposed to perform a parametric analysis in order to estimate the most eligible regularization lengths. Furthermore, it is necessary to emphasise that in CHAP. 3 this regularization protocol was applied on poor natural textures of SG cast iron. This is related with mesoscale observations where conventional or even standard global DIC approaches fail to capture accurately the displacement fields. The regularization procedure successfully overcomes this problem even with small spatial resolutions (*e.g.*, triangular element of 10 pixel size). More information can be found in Appendix D.



## **Part II**

# **Identification of nonlinear material behaviour via uniaxial experiments**



# Chapter 3

## Identification of elastoplastic and damage parameters under uniaxial loading regimes

*The identification of elastoplastic and damage parameters will be presented in this chapter. The sought parameters will be identified via FEMU and compared with those determined by direct curve fitting of the measured data. The results will be derived from 2 different loading histories. Uniaxial experiments will also be carried out on a lab X-ray tomograph. A DVC algorithm will reveal displacements in the bulk of the sample from acquired scans and a microdamage mechanism.*

### Contents

---

<b>1</b>	<b>Preface</b> . . . . .	<b>65</b>
<b>2</b>	<b>Monotonic loading history</b> . . . . .	<b>65</b>
2.1	Experimental setup of monotonic tensile test . . . . .	65
2.2	Parametric analysis of measurement resolution . . . . .	66
2.3	Conventional determination of material parameters . . . . .	71
2.4	Identification of material parameters via FEMU . . . . .	76

<b>3</b>	<b>Cyclic loading history</b>	<b>84</b>
3.1	Experimental setup	84
3.2	Standard displacement resolution	87
3.3	Identification of elastic properties	91
3.4	Identification of Johnson-Cook parameters	93
3.5	Identification of Armstrong-Frederick parameters	94
3.6	Identification of isotropic hardening coupled with damage	96
<b>4</b>	<b>Uniaxial cyclic experiment monitored via X-ray tomography</b>	<b>99</b>
4.1	Experimental procedure	100
4.2	A priori analysis	100
4.3	Analysis of the results	103
<b>5</b>	<b>Conclusion</b>	<b>107</b>

---

# 1 Preface

The most applied mechanical tests in the domain of material science are carried out in a uniaxial loading regime. To start with experimental research on the material behaviour uniaxial experiments are a natural choice. Throughout the past, with requirements of industry in order to evaluate the requested material properties (*i.e.*, monotonic, fatigue, fracture properties) uniaxial tests are described in different standards. When compared with other testing devices (*e.g.*, triaxial machine, hexapod) uniaxial experiments are considered as simple but yet challenging.

Two different types of uniaxial experiments will be carried out. First, uniaxial experiments will be conducted on standard testing machines with two different loading histories, namely, monotonic and cyclic loadings will be applied. From the latter experiments the sought parameters will be identified in a conventional way (*i.e.*, mean strain and applied load level). The same parameters will be validated/identified with the FEMU procedure (*i.e.*, displacement fields measured via DIC will be coupled with an FE simulation in an identification algorithm). The sought material parameters refer to elasticity (*i.e.*, Young's modulus and Poisson's ratio), and two nonlinear models, namely, Johnson-Cook (*i.e.*, yield stress, hardening modulus, and hardening exponent) and Armstrong-Frederick (*i.e.*, yield stress, hardening modulus, characteristic strain).

The last part of this chapter will consider a uniaxial in situ experiment performed in a lab tomograph. DVC will be applied to measure displacement fields in the bulk of the sample using the natural texture of cast iron. From correlation residual maps microdamage is detected. Standard C8- and regularised RC8-DVC methods will be compared in terms of measurement quality since the texture is not perfect.

## 2 Monotonic loading history

### 2.1 Experimental setup of monotonic tensile test

A monotonic uniaxial (*i.e.*, tensile) experiment was performed on an *MTS* servo-hydraulic testing machine (FIG. 3.1) with a maximum nominal force of 100 kN. A dog-bone sample made of SG cast iron is considered. The region of interest is approximately 50 mm long, its ligament is 10 mm wide, and the sample is 5 mm thick. The experiment was conducted in a displacement controlled mode with a loading rate of 3  $\mu\text{m/s}$ .

The measurement protocol used herein consisted of an optical setup (for DIC measurements) on one side of the sample while for validation purposes a strain gauge was mounted on the other side. Before the experiment, the specimen was prepared for DIC purposes. An artificial texture (*i.e.*, speckle pattern) was applied with white and black paints (FIG. 3.2(a)) sprayed over the ligament. The latter was observed with a single camera (*i.e.*, 2D-DIC measurement). A *Manta* CCD camera (sensor definition: 1022  $\times$  1024 pixels, digitisation: 12 bits, physical pixel size: 6.45  $\mu\text{m}$ ) and a telecentric lens (magnification:  $\times 8$ ) were used to acquire images during the test. The chosen lens allows us to minimise (if not completely cancel out) artifacts related to out-of-plane motions.

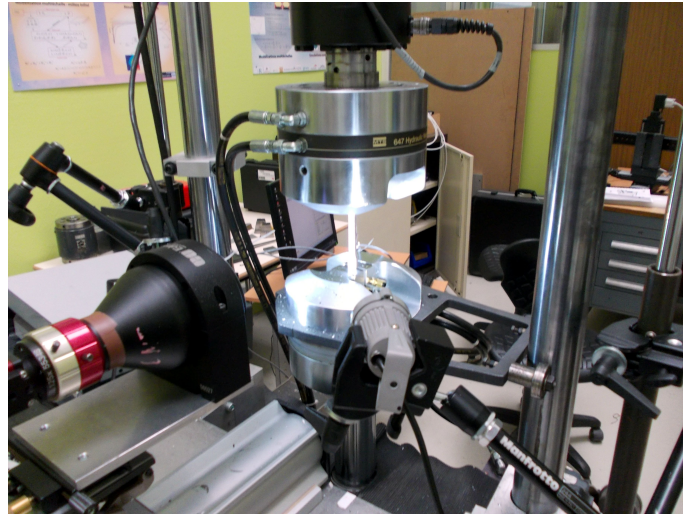


**Figure 3.1:** Uniaxial setup on an *MTS* servo-hydraulic machine with the optical equipment

The physical size of one pixel is equal to  $51.6 \mu\text{m}$ . The camera was triggered with a testing machine output analogue signal so that the load level is known for each acquired picture. 1,140 images were captured during the test with an acquisition rate of 1 frame per second. The displacement fields were calculated with the RT3-DIC code. The correlation was performed with the reference image (FIG. 3.3(a)) shot in the unloaded state and the deformed ones in the loaded state. In the following, a parametric analysis regarding the regularisation parameters and element size of the correlation procedure will be discussed.

In order to validate the displacements measured via DIC the specimen was equipped with an HBM XY51 ring core rosette (FIG. 3.2(b)). The latter measures strains in  $0^\circ/90^\circ$  directions. The rosette was aligned with the loading axis of the sample.

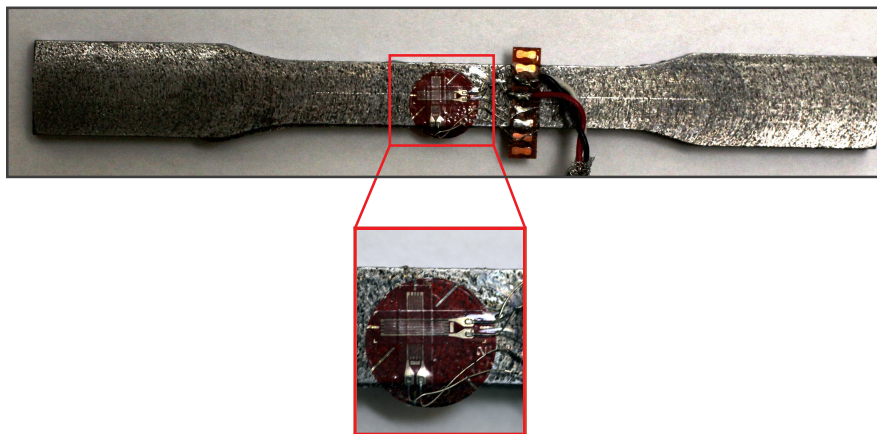
## 2.2 Parametric analysis of measurement resolution

Before performing a DIC measurement a parametric analysis is carried out with different regularisation lengths  $\ell_m$  and  $\ell_b$  to estimate the measurement resolution (see CHAP. 2). The analysis was run on a pair of two consecutive pictures shot when the sample was already mounted in the testing machine with  $F = 0$  (see FIG. 3.3(a) - reference image). Two meshes were selected over the same area. The first mesh consists of 756 nodes with 14-pixel elements (FIG. 3.3(a)), and the second one with 25-pixel elements has 224 nodes (FIG. 3.3(b)).

The parametric analysis consists of using different initial regularisation lengths in correlation analyses. As in CHAP. 2, the relaxation process is performed with a decreasing length  $\ell_m/2$  for every new calculation. The ratio  $\ell_b/\ell_b = 1/2$  was kept identical during the whole analysis. FIG. 3.4 shows the standard displacement resolution for the two displacement components with the two mesh sizes. The application of the larger regu-



(a) Speckle pattern on the dog-bone sample



(b) HBM XY51 ring core rosette

**Figure 3.2:** Dog-bone sample for uniaxial tensile tests. (a) One side has a black and white texture used for DIC measurements, and (b) the other one has a rosette measuring strains in the longitudinal and transverse directions

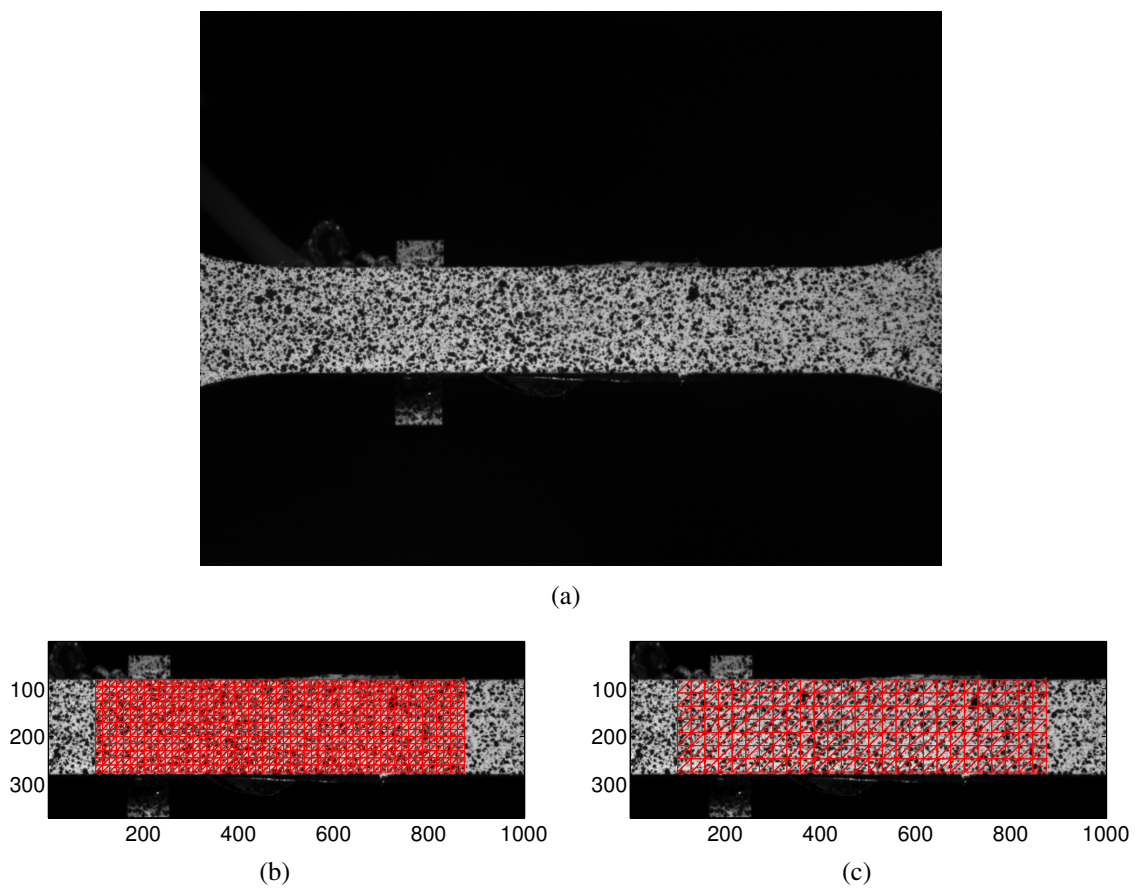


**Figure 3.3:** Reference image with no applied load (a) and T3 mesh with an element size of 14 (b) and 25 (c) pixels



larisation lengths leads to smaller displacement resolutions (FIG. 3.4 (a) and (c)). It can be noted that the standard displacement resolution between the different element sizes is approximately equal (just a slight difference was noted). The measurement resolution is higher in the horizontal direction (FIG. 3.4 (b) and (d)), which corresponds to the loading direction. It is believed that it stems from the control system of the servo-hydraulic testing machine causing displacement fluctuations in the longitudinal direction.

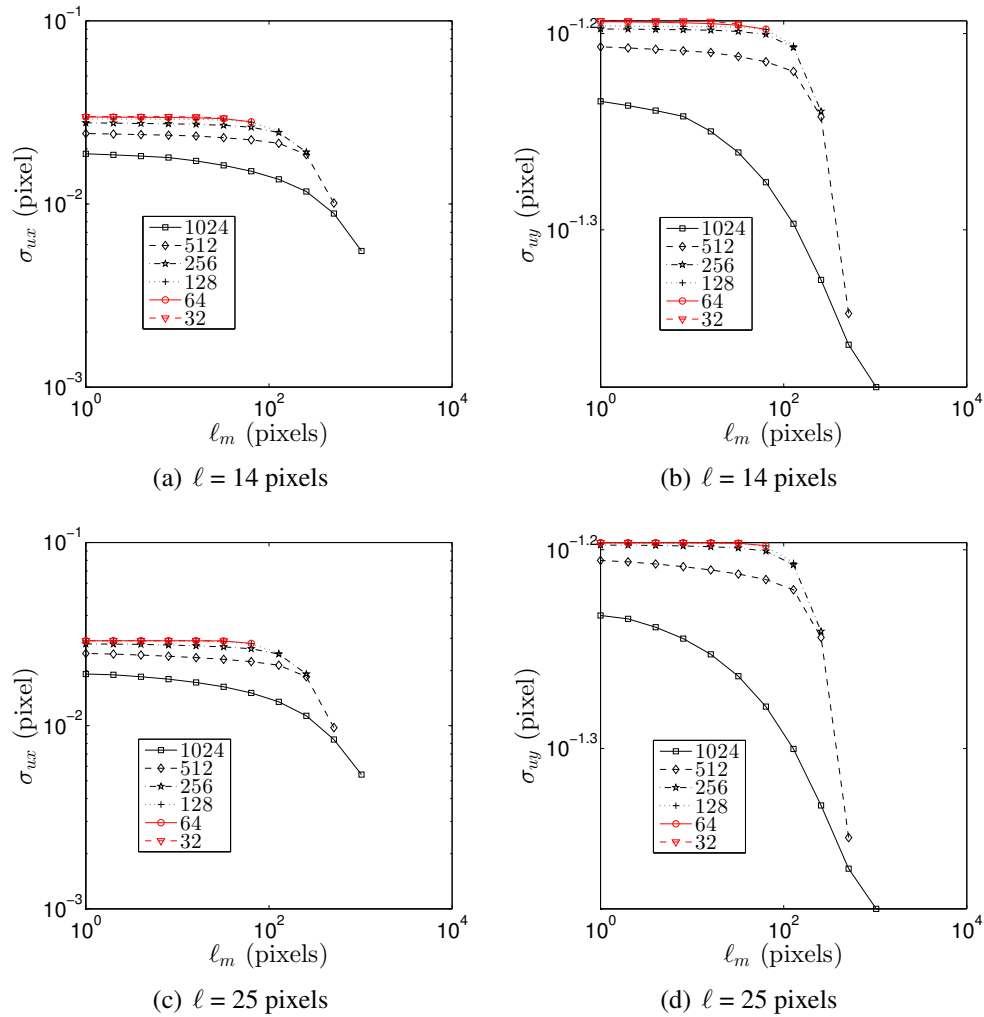


**Figure 3.4:** Change of the standard displacement resolution in (left) transverse and (right) longitudinal directions for different regularisation lengths  $\ell_m$  and the two meshes. The legend indicates the initial length  $\ell_m$  (in pixels)

FIG. 3.5(a) and (c) shows the dimensionless correlation residuals for different initial regularisation lengths when 14 and 25-pixel element sizes are chosen. Both mesh sizes reach the same level, which remains almost constant and very small for any value of the regularisation length. This result indicates that in the present case, it is impossible to discriminate any displacement from the analysis of the correlation residuals alone. However,

the equilibrium residuals (FIG. 3.5(b) and (d)) vary very strongly with the regularisation lengths. When comparing the mechanical residuals with respect to the mesh size it is observed that they are higher for smaller elements (*i.e.*, 14 pixels, see FIG. 3.5 (b)) then for the larger ones (FIG. 3.5 (d)). For  $\ell_m$  lower than 128 pixels both cases have the same order of magnitude for the mechanical residuals. 25-pixel elements are chosen since the sample geometry is simple. With this choice, faster computation time is expected for running the FEMU procedure. The measurement uncertainty being sufficiently low even for smaller regularisation lengths enables for the selection of  $\ell_m = 32$  pixels.

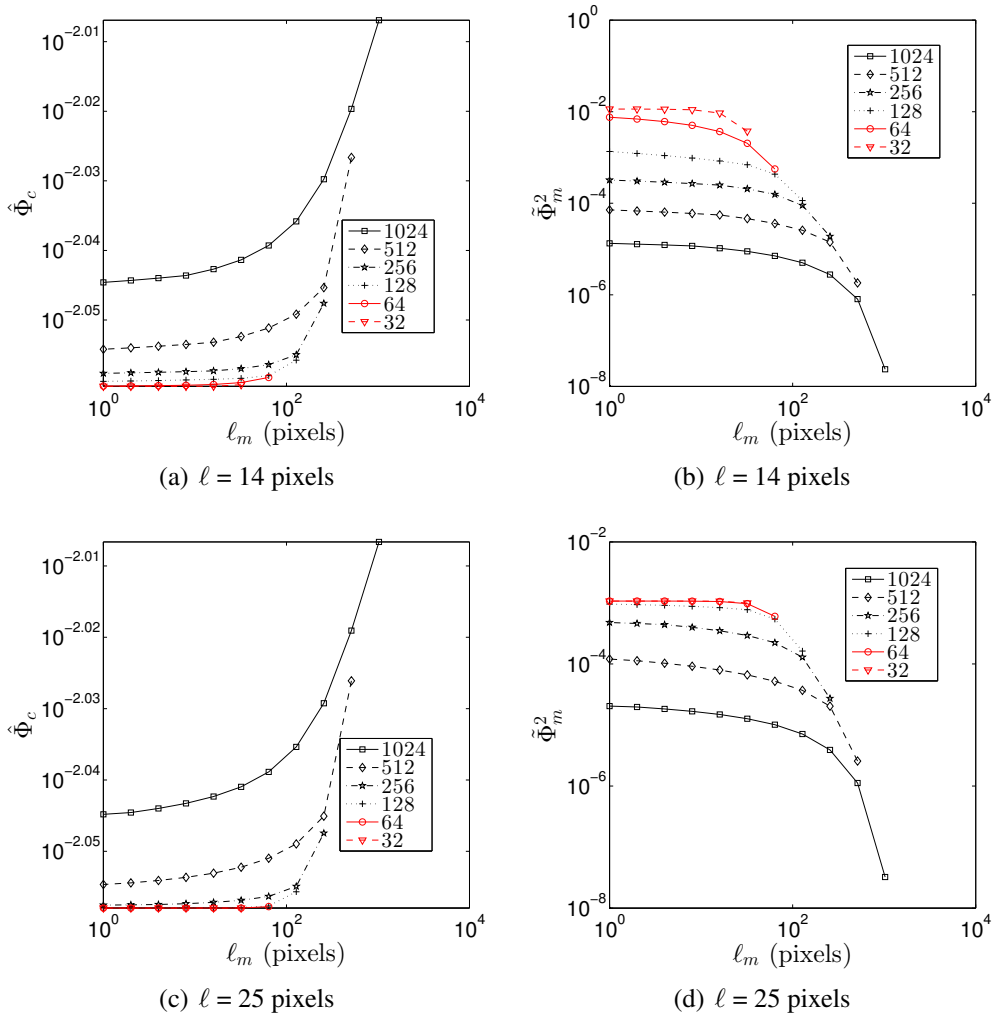


**Figure 3.5:** Change of (left) the dimensionless correlation residuals and (right) equilibrium residuals for different regularisation lengths and different initialisations for (a) & (b) 14-pixel, and (c) & (d) 25-pixel element size. Note the narrow range of variation of  $\hat{\Phi}_c$

## 2.3 Conventional determination of material parameters

In the following the identification of Poisson's ratio and Young's modulus will be presented. The elastic parameters will be identified in a classical way using the strains measured with the rosette. Via FEMU the Young's modulus will be validated. The identification of Poisson's ratio and the limitations associated with full-field measurements will be indicated.

### 2.3.1 Elastic parameters

#### Poisson's ratio

The measurement of the *instantaneous* Poisson's ratio is performed in two ways. The first one considers strain gauge measurements and the second one uses average strains obtained from full-field measurements (*i.e.*, DIC gauge). Both paths will be followed to calculate Poisson's ratio directly from

$$\nu = -\frac{\varepsilon_2}{\varepsilon_1} \quad (3.1)$$

where  $\varepsilon_1$  is the maximum eigen strain and  $\varepsilon_2$  in the minimum eigen strain.

The estimation of the Poisson's was performed on two test cases in the elastic region (FIG. 3.6). The first test was loaded up to 0.015 %, and the second up to 0.07 % of longitudinal strain. A good agreement is observed for the measured strains in both directions, thereby proving the repeatability of the experiment. FIG. 3.6(c) shows the measured Poisson's ratio with respect to the longitudinal strain  $\varepsilon_L$ . For the first case, which is in the elastic regime, the Poisson's ratio is equal to 0.265, while for the second one it becomes equal to 0.282. FIG. 3.6(c) shows the change of the Poisson's ratio with time. The two cases do not completely follow the same path, which indicates the sensitivity of Poisson's ratio in the elastic regime since small displacements are not perfectly captured due to the resolution of the strain gauge. Hence, fluctuations in the measured displacements lead to different curves of the analysed tests.

From the second test up to 0.02 % of longitudinal strain, (FIG. 3.6(a)) and -0.004 % of transverse strain (FIG. 3.6(b)) a slope increase is observed. This effect causes an increase of Poisson's ratio (FIG. 3.6(c)) after the longitudinal strain level exceeds 0.02 %. The assumption is that the material exceeds the elastic limit, which causes a change in material behaviour.

In the following example, the estimate of the elastic parameters will be performed during the whole tensile test. Strain gauge and DIC measurements will be compared. During the experiment 1,140 images were shot (FIG. 3.7). All the images were analysed with the RT3-DIC code. The regularisation of the boundary considered only the loaded nodes. Traction-free nodes were treated as inner nodes (FIG. 3.7). To assess the standard displacement and load resolutions nine images are captured when the specimen is mounted and the load level is constant (approximately equal to 0 N). From the measured

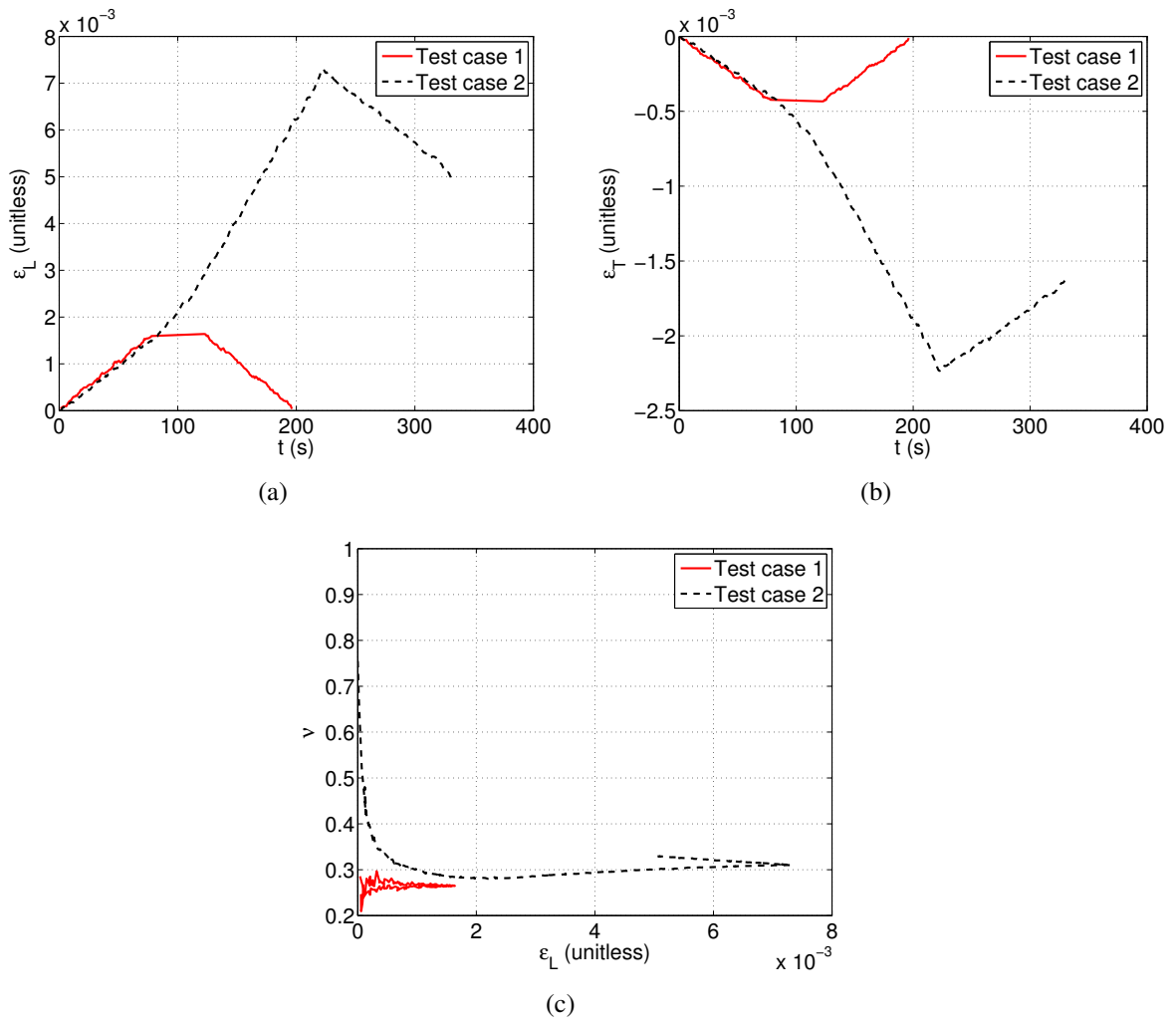


**Figure 3.6:** Two analyses performed in the elastic regime where longitudinal (a) and transverse (b) strains were measured with the rosette. (c) Poisson's ratio evaluated via Equation (3.1)

displacement field  $u_i^{meas}$  for image  $i$  and corresponding load level  $F_i^{meas}$  the displacement and load resolutions are given by

$$\gamma_u = \sqrt{\frac{1}{\tilde{n} n_{DOF}} \sum_{i=1}^{\tilde{n}} (u_i^{meas})^2} \quad (3.2)$$

and

$$\gamma_F = \sqrt{\frac{1}{\tilde{n}} \sum_{i=1}^{\tilde{n}} (F_i^{meas})^2} \quad (3.3)$$

where  $\tilde{n}$  is the number of images,  $n_{DOF}$  the number of kinematic unknowns. The level of  $\gamma_u$  for this experiment is equal to 0.04 pixel with a corresponding load resolution  $\gamma_F$  of 200 N. These high values are believed to be due to the controller of the testing machine.

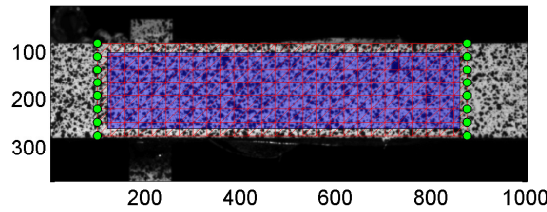


**Figure 3.7:** Reference picture of monotonic uniaxial experiment used for a DIC analysis with 25-pixel elements. The blue rectangle depicts the zone where the DIC gauge was measuring the mean strain. Edge regularisation was applied on the green nodes while all the others were treated as inner nodes. In the FEMU procedure, boundary conditions measured with DIC were prescribed on the edge nodes labelled with green circles

FIG. 3.11(a) and (b) show the comparison of mean eigen strain components estimated with the rosette and DIC gauge. The latter is chosen (see FIG. 3.7) to calculate the average strain over the selected zone. A good agreement is observed between results given by both measurement techniques. After 2 % longitudinal strain the rosette reached its limit, while the transverse signal was still measured until the end of the experiment. This is an advantage of DIC measurements since data are obtained during the whole experiment without any limitations.

In both directions the levels measured with the rosette are in very good agreement with the DIC measurements. At 0.75 % of transverse strain the strain gauge and DIC measurements start to diverge (see FIG. 3.7(b)). During loading microcracks start to appear, which is causing the difference between the two measurement techniques. DIC captures better this phenomenon since it is measuring strain fluctuations over the whole observed domain as opposed to the strain gauge (over a smaller gauge length). As in the previous measurement of the longitudinal and transverse strains (FIG. 3.6(a) and (b)) a change of strain path is observed for approximately the same level (*i.e.*,  $\epsilon_L = 0.02$  % and  $\epsilon_T = -0.004$  %).

Introducing the measured eigen strains in Equation (3.1) the change of instantaneous Poisson's ratio is estimated (FIG. 3.11(c)). The Poisson's ratio assessed with the strain gauge equals 0.283 in elasticity, while it increases to 0.33 in plasticity. Both curves follow the same trend even though DIC data are more affected by fluctuations introduced by the experimental setup (*i.e.*, servo-hydraulic testing machine). Elastic strains are very low in comparison with the standard resolution, which makes it more difficult to evaluate them. The fluctuations are mainly introduced via the controller of the servo-hydraulic testing machine. When strains exceed the yielding level (*i.e.*,  $\epsilon_L > 1\%$ ) the transverse displacements become higher than the measurement uncertainties, which leads to lower fluctuations in the instantaneous Poisson's ratio ( $\nu=0.33$ ). To assess the fluctuations introduced by the testing machine another uniaxial experiment was performed on an electro-mechanical machine (see Section 3).

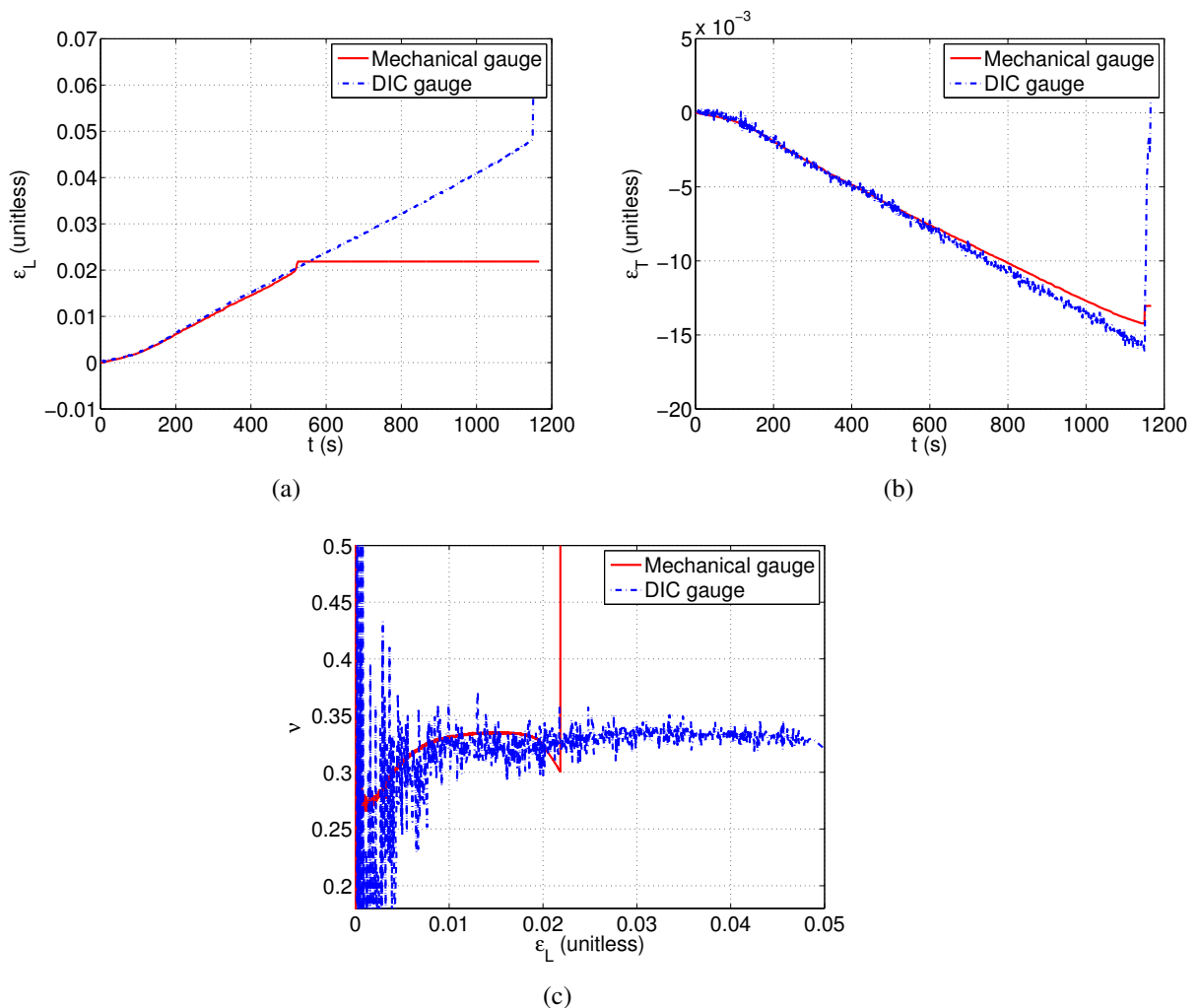


**Figure 3.8:** Comparison of measured (a) longitudinal ( $\epsilon_L$ ) and (b) transverse ( $\epsilon_T$ ) strains with rosette and DIC gauge. (c) Poisson's ratio is calculated with Equation (3.1)

## Young's modulus

The identification of Young's modulus consists of fitting the stress-strain curve (FIG. 3.9) in the elastic domain (*i.e.*, Hooke's law). Since the material has a small elongation to failure and no necking was observed, the engineering stress (*i.e.*, nominal stress) was used

$$\sigma = \frac{F}{A} \quad (3.4)$$

where  $F$  is the prescribed load, and  $A$  the initial cross-sectional area of the specimen. TAB. 3.1 shows the identified Young's modulus.

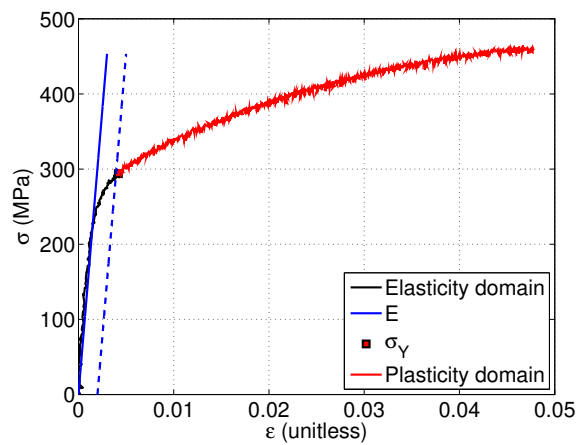


**Figure 3.9:** Stress-strain curve for the tensile test. The curve is divided in two parts (back line) elastic, and (red line) plastic part. The marker denotes the yield point while the blue line fits the slope of Young's modulus.

**Table 3.1:** Identified elastoplastic parameters

Parameter	E (GPa)	$\nu$	$\sigma_0$ (MPa)	K (MPa)	n
Identified value	155	0.28	289	1200	0.6

### 2.3.2 Plastic parameters

Before identifying the isotropic hardening parameters the elastic limit (*i.e.*, yield stress) is evaluated. First the line that describes Hooke's law is shifted horizontally by an offset of 0.2 % strain. The intersection of the shifted line and the stress-strain curve gives the conventional yield stress (see TAB. 3.1).

The plastic behaviour will be described with Johnson-Cook's constitutive law (Equation (1.16)). Parameters  $K$  and  $n$  are modelling the evolution of the equivalent stress with

the corresponding equivalent plastic strain. The identified Johnson-Cook parameters presented in TAB. 3.1 will be used as inputs for the FEMU procedure. The initial parameters describing kinematic hardening (Equation (1.18)) will be taken from the literature.

## 2.4 Identification of material parameters via FEMU

### 2.4.1 Implementation of FEMU

As presented in CHAP. 1, the FEMU method relies on the comparison of the measured displacement fields (FIG. 3.10) with those calculated by FE simulations. It is mandatory for the calculated and the measured displacements to be ‘superimposed’. FE calculations and experimental measurements are usually performed with different softwares so additional adjustments are necessary. They may introduce some extra errors. However, when using an FE-DIC algorithm this challenge is overcome since the DIC mesh can be imported in the FE code, or vice versa. Hence, the measurement of the displacement field is carried out with the same mesh as that used in simulations. The dialogue between simulation and experimental data can also be limited by the common assumption that the loading conditions of the simulation are associated with ideal boundary conditions that are not reflecting the inherent imperfection of the test. On the FE model actual boundary conditions extracted from the experiment can be applied (*e.g.*, measured displacements, static loading information).

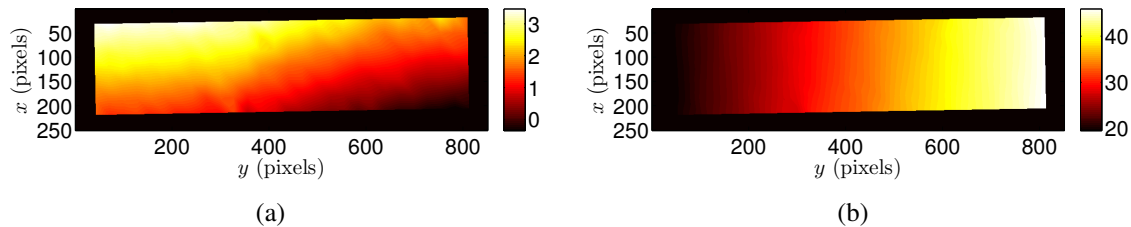


**Figure 3.10:** Measured displacement fields via RT3-DIC in (a) transverse and (b) longitudinal directions for a load level corresponding to 18 kN

The FEMU procedure applied herein utilises the same framework. In this chapter the identification is carried out on a simple specimen geometry. Hence, a 2D model in the commercial FE code Abaqus will be created from the RT3-DIC mesh. Boundary conditions prescribed in the simulations will be extracted from DIC measurements (FIG. 3.7). It is important to emphasise that many issues can influence the performance of an experiment. Usually, even simple tests (*e.g.*, uniaxial tension) are not perfect and their response includes some anomalies. Observing the displacement field in the transverse direction (FIG. 3.10(a)) an additional rotation is observed even though the test was carried out in tension. Applying the measured displacements to the boundary of the FE model accounts for all these imperfections. The material parameters obtained previously will be used as initial inputs to describe the constitutive law. Displacement fields and reaction forces are



calculated in Abaqus and extracted via Python scripts. The minimisation procedure is carried out in Matlab.

### 2.4.2 Identification of elastic parameters

The identification of elastic parameters is performed with the first 75 images where Hooke's law is satisfied. The Poisson's ratio and Young's modulus were validated via three variants of FEMU (*i.e.*, U, F, UF). The first parameter to be identified is Young's modulus. This is possible only if the load information is considered (*i.e.*, minimizing the difference between the measured force and the sum of reaction forces). Consequently, FEMU-F (identification of  $E$  while  $\nu$  is fixed) and -UF (identification of  $E$  and  $\nu$ ) procedures are used. With both variants the same value is obtained approximately. A slight difference is observed (see TAB. 3.2) due to the change of Poisson's ratio from 0.28 to 0.11. The identified Young's modulus is validated and the slight difference of the identified value is followed by a decrease of the force residuals  $\chi_F$  of 33 N. The level of  $\chi_F$  is very close to the in situ load resolution (*i.e.*, this high level is due to displacement fluctuations of the actuator). Similarly, the displacement residual  $\chi_u$  is very close the displacement resolution (*i.e.*, 0.04 pixel).

**Table 3.2:** Elastic parameters identified with FEMU. The reference values denote conventionally determined data. The FEMU-U procedure is carried out with fixed  $E$ , and FEMU-F with fixed  $\nu$ . In FEMU-UF both parameters are identified at the same time

Parameter	E (GPa)	$\nu$	$\chi_u$ (pixel)	$\chi_F$ (kN)
Reference	155	0.28	0.0433	0.393
FEMU-U	155	0.11	0.0425	0.395
FEMU-F	159	0.28	0.0433	0.360
FEMU-UF	159	0.11	0.0425	0.360

For the Poisson's ratio, FEMU-U and FEMU-UF procedures are used. In both cases a stable value of  $\nu = 0.11$  is reached. This result is in conflict with the classically measured value  $\nu = 0.28$ . It should be remembered that the longitudinal displacement is higher than the transverse one, and the elongated geometry makes the evaluation of Poisson's contraction more difficult to assess.

All acquired (*i.e.*, 1,140) images of the yielding material are now used to determine Johnson-Cook coefficients (Equation (1.16)) for isotropic hardening, and Armstrong-Frederick (Equation (1.18)) for kinematic hardening. To estimate the most reliably procedure, the three (U, F and UF) variants are run with the proposed identification method (FEMU).

### 2.4.3 Johnson-Cook's parameters

The three sought parameters ( $\sigma_y$ ,  $K$  and  $n$ ) are identified in one procedure (Equation (1.28)). The elastic properties are chosen as  $E = 159$  GPa and  $\nu = 0.28$ . FIG. 3.11 shows the iterative changes of Johnson-Cook's parameters for different variants of FEMU. Of the three variants, only FEMU-U leads to significant differences in the identified parameters. Stable values of  $\sigma_y$ ,  $K$  and  $n$  are not reached, and the identified parameters drastically differ from the initial values. The expected value of hardening exponent should be  $0 < n < 1$ , while in this case it is 3 times higher. The other two parameters  $\sigma_y$  and  $K$  are identified with unreasonably high values. By observing the change of the displacement cost function (FIG. 3.12(a)) high fluctuations occur even though at the last iteration its level is lower than for FEMU-F and FEMU-UF variants. The force residual (FIG. 3.12(b)) is off since no force information is included in the minimisation. As mentioned in the literature [Avril et al., 2008a, Mathieu et al., 2014] the consideration of the load information is necessary to match the measured load with the computed reaction forces.

The results of the other two FEMU variants (*i.e.*, -F, -UF) are similar for the sought Johnson-Cook parameters FIG. 3.11. After a few iterations a stable value of all three parameters is found.  $\chi_u$  is lower when the minimisation is carried out via FEMU-UF. Conversely, FEMU-F yields slightly lower force residuals (*i.e.*,  $\chi_F$ ).

When analyzing the measured and computed load levels (FIG. 3.13(a)), it is concluded that the displacement residuals alone (FEMU-U) are not sufficient to ensure the quality of the identified results. The identification carried out via FEMU-F and FEMU-UF variants lead to parameters different from the initial ones (*i.e.*, determined conventionally), see TAB. 3.3. The standard way of determining the yield stress is not the most appropriate for Johnson-Cook's constitutive law. A discrepancy of 60 MPa between the initial and identified yield stress shows that for this type of material it is more reliable to take lower yield stresses (*i.e.*, when the stress-strain response becomes nonlinear). The identified isotropic hardening modulus  $K$  and hardening exponent  $n$  change as well (TAB. 3.3).

The parameters identified with FEMU-UF yield a decrease of the force residuals by 260 N. The final level is still higher than the measurement resolution, but getting close to the levels observed in elasticity. A better agreement than the initial parameters is clearly observed (FIG. 3.13(b)).

**Table 3.3:** Identified Johnson-Cook parameters with the three different variants of FEMU

Parameter	$E$ (GPa)	$\nu$	$\sigma_y$ (MPa)	$K$ (MPa)	$n$	$\chi_u$ (pixel)	$\chi_F$ (kN)
Reference	159	0.28	289	1260	0.614	0.2040	0.58
FEMU-U	159	0.28	24	5.2e+7	3.2	0.1985	11.6
FEMU-F	159	0.28	228	850	0.379	0.2041	0.313
FEMU-UF	159	0.28	229	860	0.384	0.2038	0.314

In the implemented FEMU techniques the sensitivity of the displacement field is characterised with respect to each sought parameter. For the four material parameters ( $E$ ,  $\sigma_y$ ,

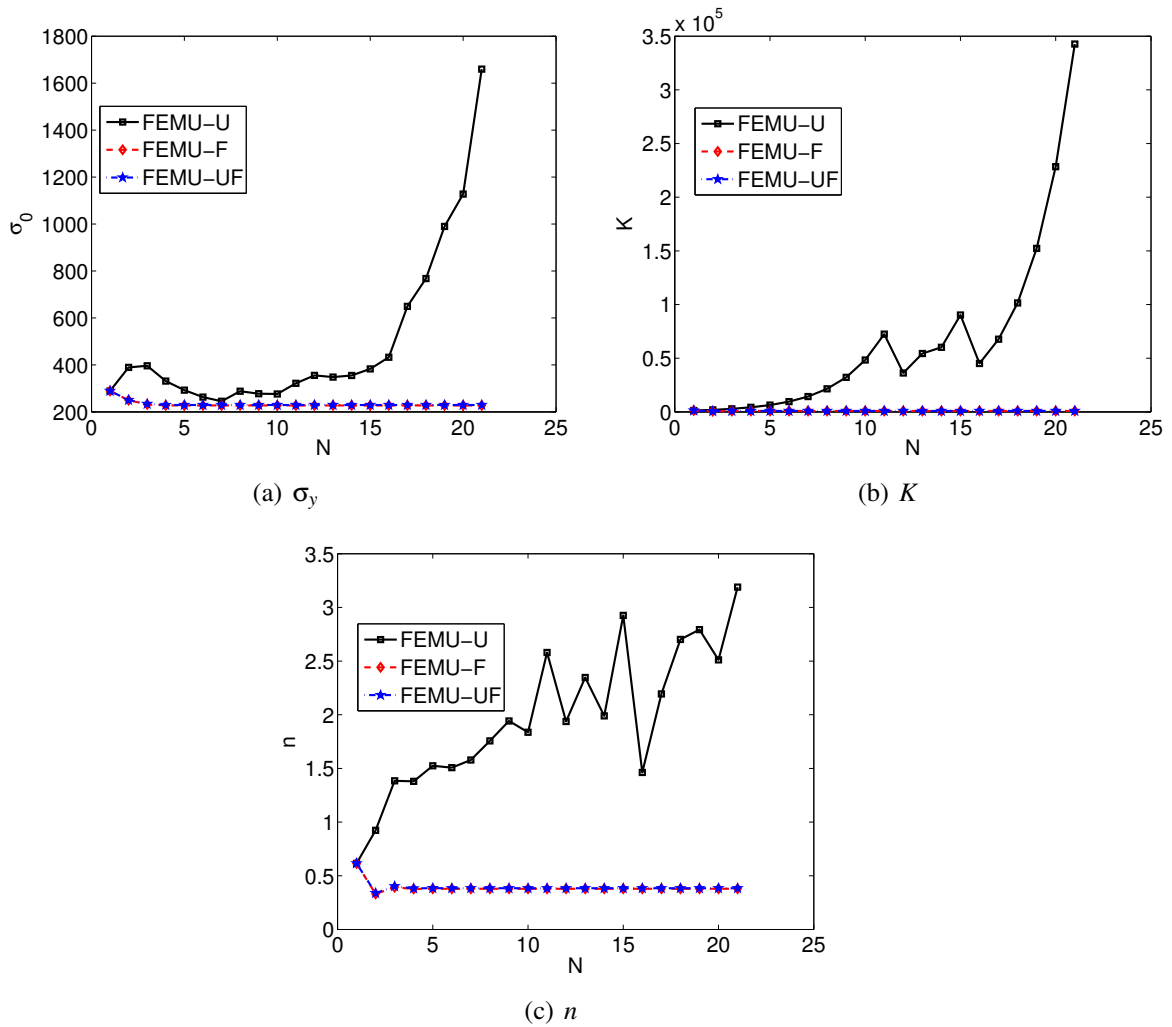


**Figure 3.11:** Change of the three identified Johnson-Cook parameters with the number of iterations. Three variants (-U, -F, -UF) of FEMU are compared

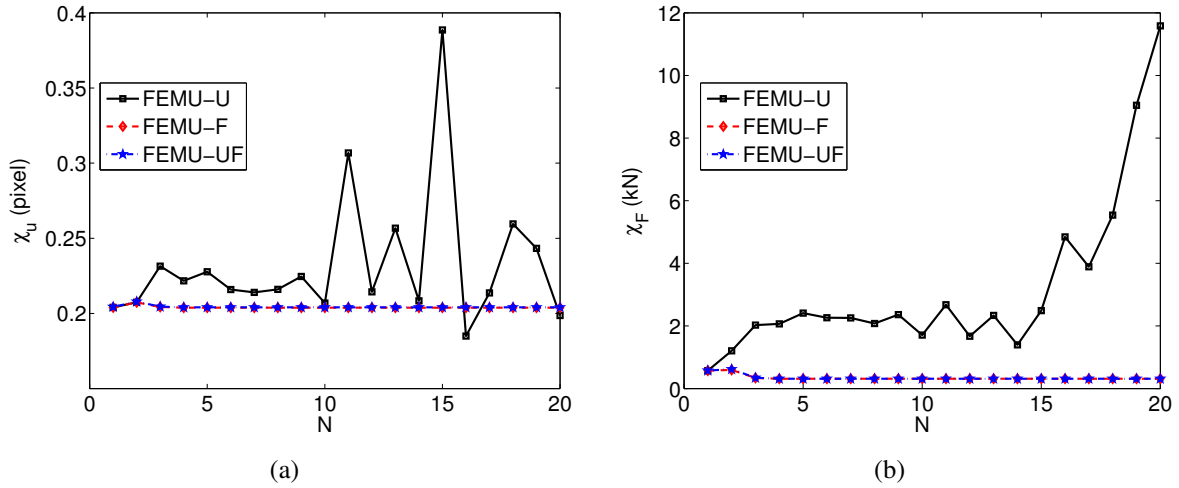


**Figure 3.12:** Change of displacement ( $\chi_u$ ) and force ( $\chi_F$ ) residuals with the number of iterations when identifying Johnson-Cook’s parameters. Three variants (-U, -F, -UF) of FEMU are compared

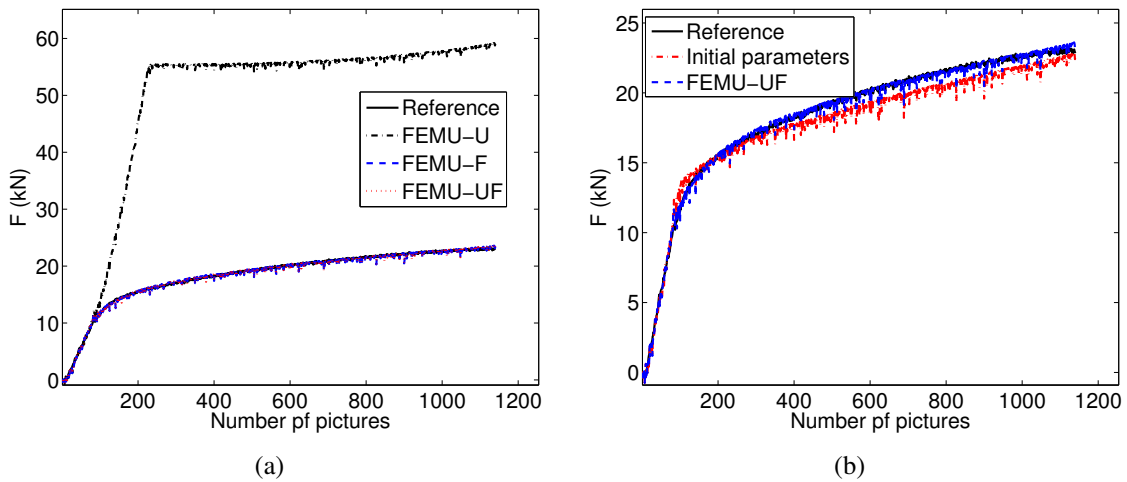


**Figure 3.13:** (a) Comparison of measured force and sum of the reaction forces for the three FEMU variants. (b) Comparison of measured force and sum of reaction forces computed with initial and identified Johnson-Cook’s parameters via FEMU-UF

$K$  and  $n$ ), the sensitivity maps are presented in FIG. 3.14. These maps are obtained numerically by computing the difference between the displacement fields for 1 % variations of each parameter of the considered set. The sensitivity map for the longitudinal direction is extracted from a cut made in the middle of the transverse direction of the sample for all instants of time.

The sensitive parts are mainly located on the side parts of the longitudinal direction of the dog-bone sample (*i.e.*, close to the gripped parts of the specimen). For all the parameters the displacement fields start to capture fluctuations when the elastic limit is exceeded. The highest influence is observed after the four hundredth image, which corresponds to a stress level of 340 MPa. For the four parameters the highest sensitivity is observed approximately at the same location.

FIG. 3.15 shows the sensitivity of the load vector for the parameters describing Johnson-Cook's constitutive law. The reaction force sensitivity is observed in the same way as displacement sensitivity maps. The change of load levels is obtained numerically as the sum of the reaction forces when each parameter varies by 1 %. The sensitivity to  $E$  linearly increases in the elastic region. However, it can be noted that  $E$  does not influence strongly the sum of reaction forces in the plastic region. For the other parameters this effect is not noted. The parameters describing isotropic hardening  $\sigma_y$ ,  $K$  and  $n$  influence in a different way the load sensitivity. A 1 % variation of yield stress leads to a 110-N load increment, which remains constant over the whole nonlinear domain. The sensitivity to  $K$  and  $n$  gradually increases with the equivalent plastic strain. FIG. 3.15 shows that the hardening exponent has the highest influence (*i.e.*, 150 N).

From the changes of displacement sensitivity fields and force sensitivity vectors with time it is possible to assess which parts of the experiment are the most suitable for the identification of the sought parameters. In elasticity the displacement sensitivity map to  $E$  does not capture any displacement fluctuations, which is expected. However, a significant load sensitivity is detected. It is not possible to identify Young's modulus just by minimising the displacement residual. It is necessary to include the load level information to obtain reliable values for  $E$ . Isotropic hardening parameters are the most sensitive in terms of displacement and force at the end of the experiment. The constant level of load sensitivity for the yield stress denotes a unique influence in the nonlinear part of the uniaxial tensile test.

#### 2.4.4 Armstrong-Frederick parameters

As for the identification of the parameters describing isotropic hardening three FEMU variants are used to identify Armstrong-Frederick (Equation (1.18)) nonlinear kinematic hardening. The initial parameters for the proposed law  $C$  and  $\gamma$  are arbitrarily selected from the literature [Lemaitre and Desmorat, 2005], while the elastic properties and yield stress  $\sigma_y$  were taken from the results of Section 2.3.

The identification of the three sought parameters ( $\sigma_y$ ,  $C$  and  $\gamma$ ) is performed in one identification procedure (*i.e.*, at the same time). The results obtained from the three variants of FEMU are presented in TAB. 3.4. With FEMU-U the identified values of the three

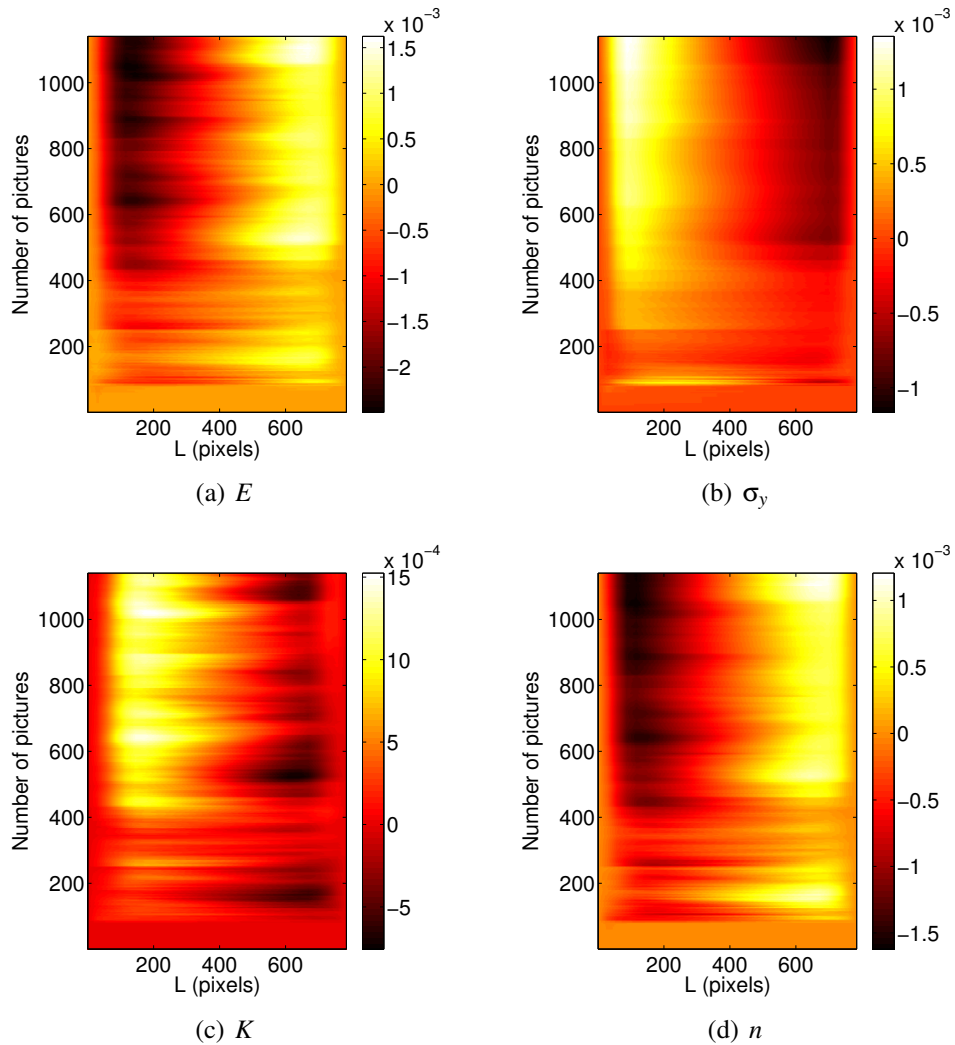


**Figure 3.14:** Sensitivity of the displacement field with respect to each sought parameter. The maps correspond to differences of displacements (expressed in pixel) when the sought parameter is changed by 1 %

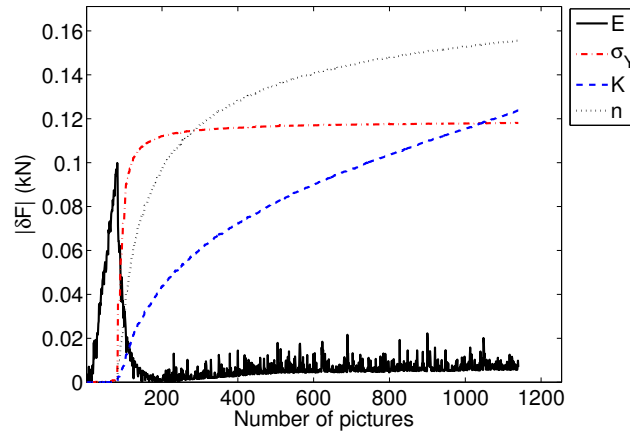


**Figure 3.15:** Sensitivity of the load level (*i.e.*, sum of reaction forces) with respect to each sought parameter of Johnson-Cook's law for a 1 % variation

**Table 3.4:** Identified Armstrong-Frederick's parameters with three different variants of FEMU

Parameter	$E$ (GPa)	$\nu$	$\sigma_y$ (MPa)	$C$ (GPa)	$\gamma$	$\chi_u$ (pixel)	$\chi_F$ (kN)
Reference	159	0.28	289	13	20	0.1906	2.88
FEMU-U	159	0.28	0.02	343	0.002	0.0962	70
FEMU-F	159	0.28	290	10.2	46.1	0.2051	0.3533
FEMU-UF	159	0.28	290	10.2	45.7	0.2050	0.3534

parameters are completely off. Even though a 50 % drop of  $\chi_u$  is achieved the load residuals increase dramatically. Without the load information in the minimisation procedure the results are not captured in a reliable way. The sought parameters found by FEMU-F and FEMU-UF are very close. The hardening modulus  $C$  decreases by 3 GPa while  $\gamma$  increases by more than 50 % in comparison with the initial values. These changes lead to significant drops of  $\chi_F$  (2.5 kN) and a small increase of  $\chi_u$  (TAB. 3.4). Since the initial values of  $C$  and  $\gamma$  were arbitrarily chosen a large gap between the identified and initial stress-strain curve is noted in FIG. 3.16. The latter shows a comparison of measured force with the calculated one for the two sets of parameters (*i.e.*, initial and identified). Even though the initial parameters were not close to the optimal solution the validity of the identified set is confirmed since  $\chi_F$  has significantly decreased.

FIG. 3.17 shows the displacement sensitivity maps for the sought parameters, while the change of force sensitivity vector is shown in FIG. 3.17. The sensitivity maps of the longitudinal cut made in the center of the observed ROI for parameters  $E$  and  $\sigma_y$  are the same as in the previous example (FIG. 3.14(a) and (b)). The hardening modulus  $C$  induces changes in displacements at the beginning of yielding (FIG. 3.17(c)) and more strongly at the end of the experiment. During the loading in the plastic regime, the sensitivity of

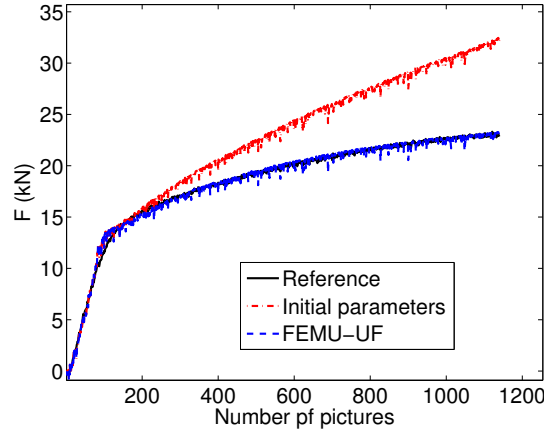


**Figure 3.16:** Comparison of measured force and sum of reaction forces computed with the initial and identified parameters for Armstrong-Frederick's law

the load vector to  $C$  follows a nonlinear trend, which is lower than the sensitivity of the yield stress and  $E$ . The parameter  $\gamma$  influences the displacement just in the end of the test (FIG. 3.17(d)).

### 3 Cyclic loading history

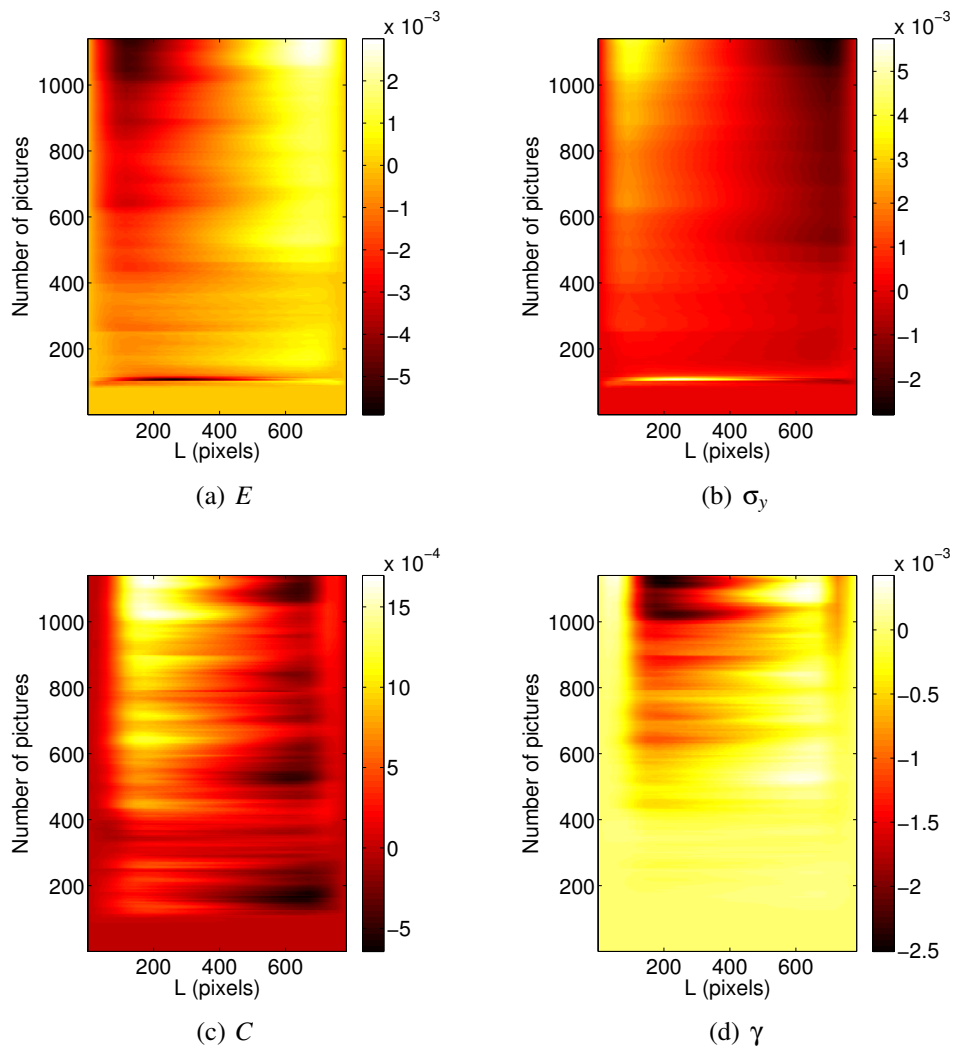
The previously presented uniaxial experiment showed that the servo-hydraulic machine by its nature introduces significant displacement/force fluctuations. Consequently it yields higher measurement uncertainties. The latter ones are limiting factors when identifying Poisson's ratio (Section 2). Due to these limitations, the following cyclic experiment is performed on an electro-mechanical machine to lower the standard displacement resolution. Elastoplastic parameters will be identified and compared with the previous results. In addition, over the cycles damage is detected. One identification will be carried out coupling elastoplastic and damage laws.

#### 3.1 Experimental setup

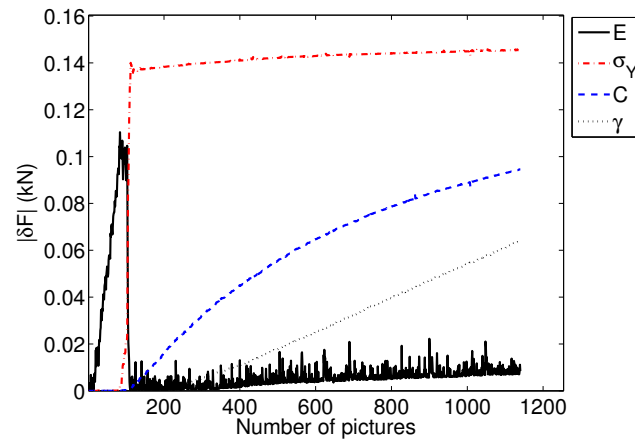
A cyclic tensile test was carried out on an *Instron* electro-mechanical testing machine (FIG. 3.1) with a maximum force of 100 kN. The experimental setup used hereafter did not differ a lot from the previous test. The sample (FIG. 3.2) was prepared as explained in Section 2. Strain measurements were carried out with a strain gauge (FIG. 3.1(b)) and DIC gauge (Section 2). A telecentric lens with a magnification  $\times 4$  was mounted on a *PCOedge* camera (16-bit digitisation, definition:  $2560 \times 2160$  pixels). The physical size of one pixel on an acquired image (FIG. 3.21(a)) corresponds to  $52 \mu\text{m}$ .

FIG. 3.20 shows the cyclic loading path. The experiment was conducted in a displacement controlled mode with a loading rate of  $3 \mu\text{m/s}$  except for the first cycle ( $0.5 \mu\text{m/s}$ ).





**Figure 3.17:** Sensitivity of the displacement field with respect to each sought parameter. The maps correspond to differences of displacements (expressed in pixel) when the sought parameter is changed by 1 %



**Figure 3.18:** Sensitivity of the load level (*i.e.*, sum of reaction forces) with respect to each sought parameter of Armstrong-Frederick's law for a 1 % variation

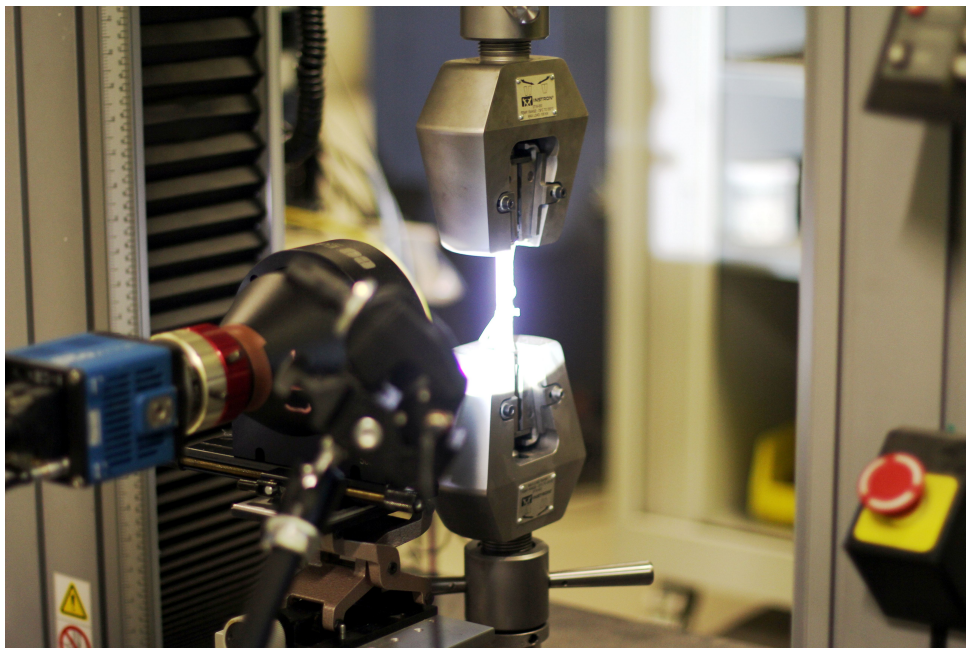


**Figure 3.19:** Experimental setup on an *Instron* electro-mechanical machine

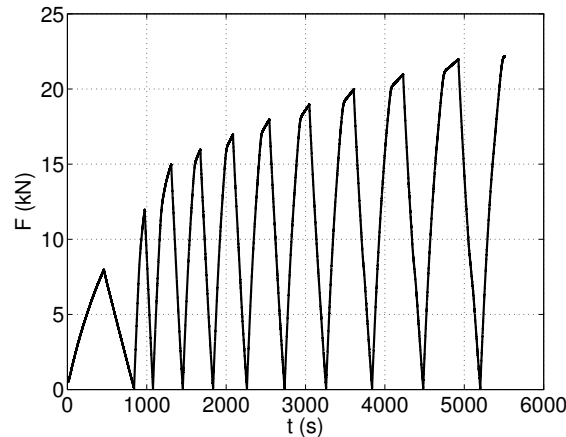


**Figure 3.20:** Loading history for the uniaxial cyclic experiment. The image acquisition rate was 1 frame/s

The first two cycles with maximum loads 8 and 12 kN were performed in the elastic regime. After the third one (*i.e.*, 15 kN peak load) plastic strains were observed. Cycling was continued with 1 kN load increase in each following cycle with respect to the previous one. After eleven unloading/reloading sequences the sample broke and 5,520 images were taken with an acquisition rate of 1 frame per second.

### 3.2 Standard displacement resolution

An a priori analysis of the DIC resolution is performed. As in the previous section the standard displacement resolution is estimated with two images of the mounted specimen (FIG. 3.21(a) - reference configuration) at the initial load level ( $F = 0$ ). Two meshes with 14-pixel elements (FIG. 3.21(a) - reference configuration) and 25-pixel elements (see FIG. 3.21(a) - reference configuration) are analysed. The relaxation procedure is performed as described in CHAP. 2 and Section 2 to evaluate the displacement resolution.

FIG. 3.22 shows the standard displacement resolution for the two meshes. The same resolutions are reached when the initial length  $\ell_m$  is used. The relaxation process carried out with 14-pixel elements with an initial length  $\ell_m = 32$  and 64 pixels ends with higher values (FIG. 3.22(a) and (b)) in comparison with bigger elements. For  $\ell_m > 128$  pixels the displacement resolution is the same throughout the whole relaxation process. When 25-pixel elements are used and  $\ell_m = 32$  or 64 pixels is selected the displacement resolution does not differ (FIG. 3.22(c) and (d)). This fact confirms that higher spatial resolution acts as a natural regularisation (*i.e.*, a lower displacement resolution is obtained). The standard displacement resolution reaches the same levels in both longitudinal and transverse directions as opposed to the previous case (see FIG. 3.4). When compared with the resolution of the monotonic experiment a large difference is observed.

The dimensionless correlation residuals (FIG. 3.23 (a-b)) for different initial regular-

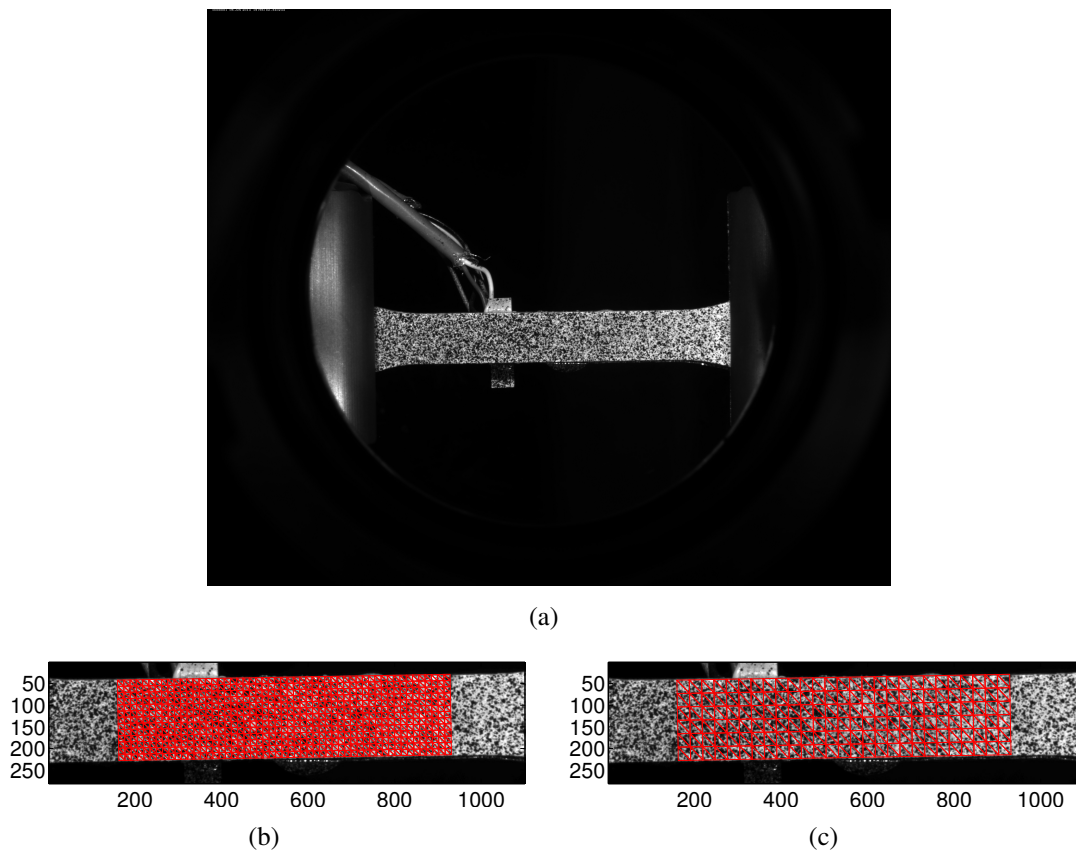


**Figure 3.21:** Reference image without applied load (a) and T3 mesh with an element sizes of 14 (b) and 25 (c) pixels

isation lengths  $\ell_m$  remain small and constant as in the previous analysis (FIG. 3.5). On the contrary mechanical residuals strongly vary. At the end of the relaxation process for  $\ell_m = 32$  and 64 pixels with smaller element sizes, higher levels of mechanical residuals are observed. This is to be expected since spurious fluctuations are present. With the increase of regularisation the latter ones are filtered out. As in the previous case, 25-pixel elements are chosen for DIC analyses since the spatial resolution is acceptable with respect to the experimental kinematics. A low regularisation length (32 pixels) will be applied.

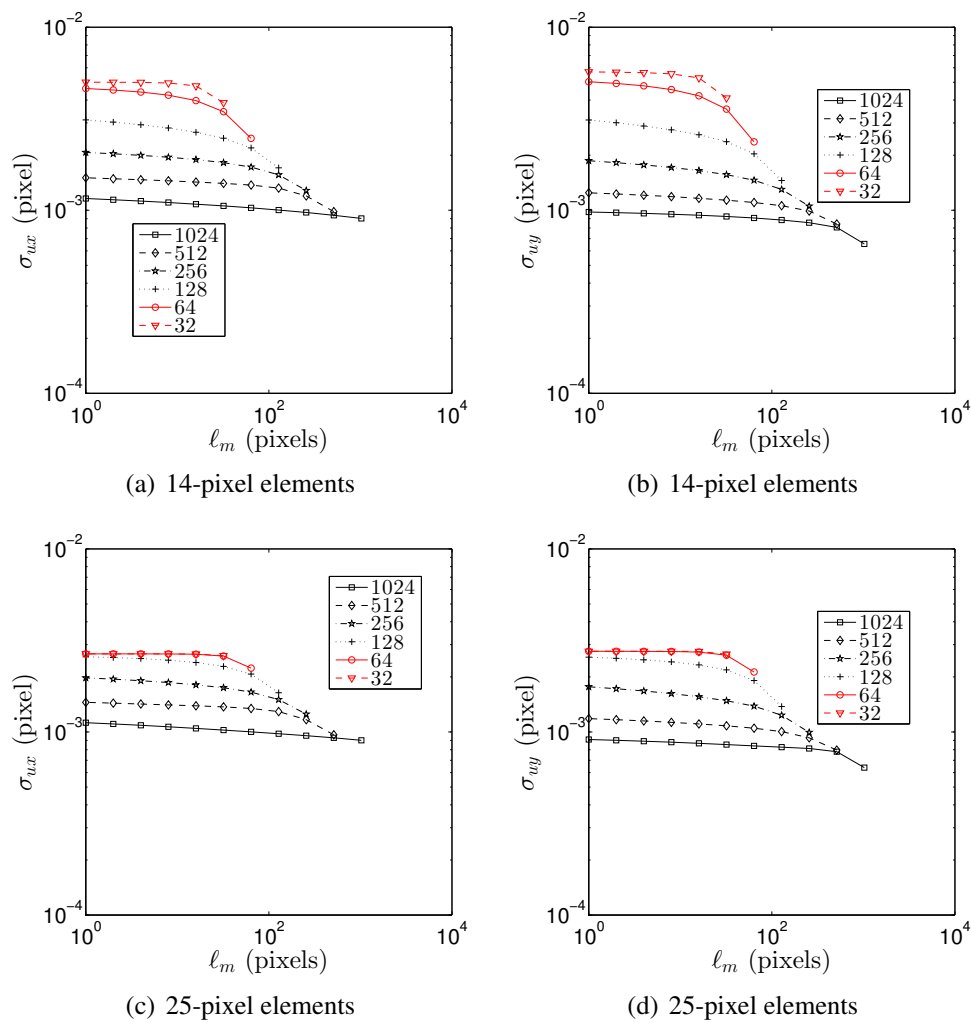


**Figure 3.22:** Change of standard displacement resolution in (left) transverse and (right) longitudinal directions for different regularisation lengths  $\ell_m$  with two meshes. The legend indicates the initial length  $\ell_m$  (in pixels)

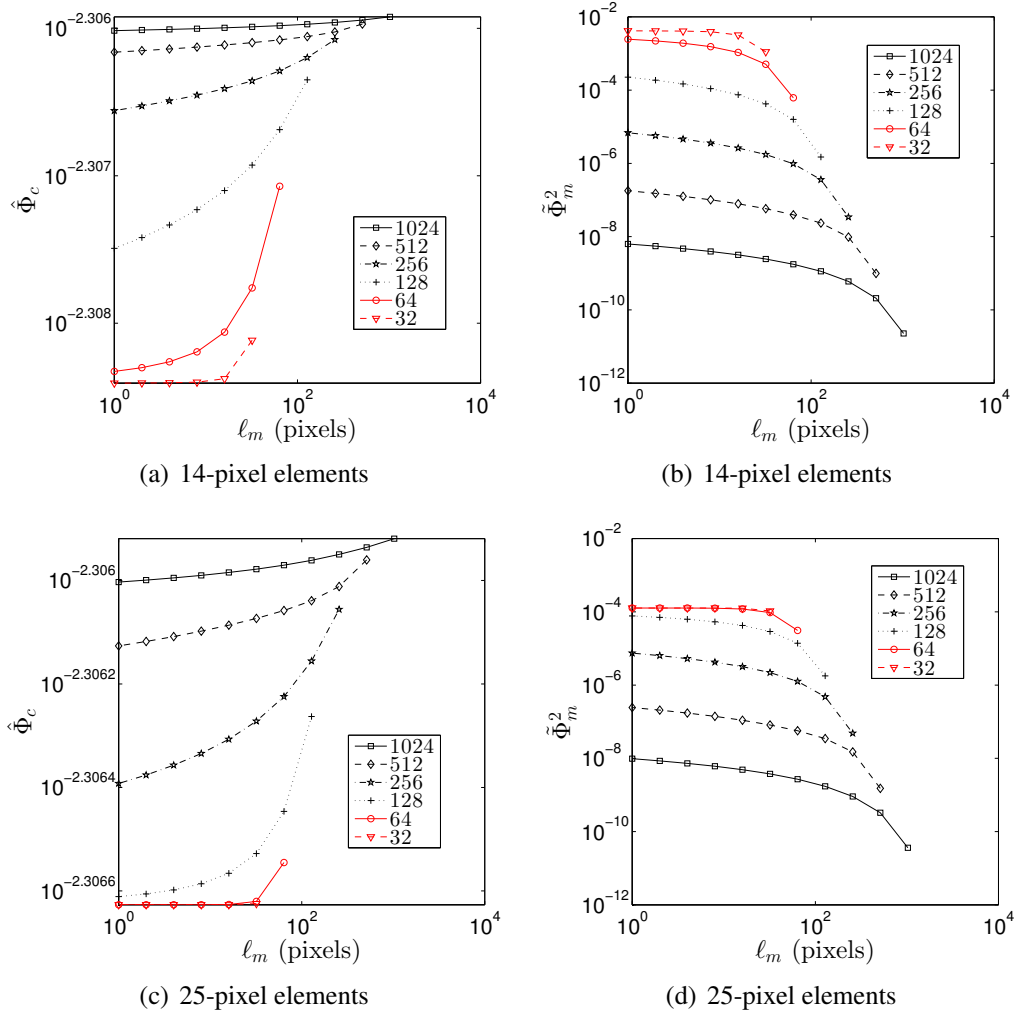


**Figure 3.23:** Change of (left) the dimensionless correlation residuals and (right) equilibrium residuals for different regularisation lengths and different initialisations for two element sizes. Note the narrow range of variation of  $\hat{\Phi}_c$

### 3.3 Identification of elastic properties

#### 3.3.1 Conventional determination of parameters

Strain measurements were carried out with a strain gauge (FIG. 3.2(a)) and DIC gauge (FIG. 3.7). The results obtained with the latter are presented in FIG. 3.24(a) and (b). The gauge measurements were stopped at 1 % of longitudinal strain. For the working range of the strain gauge a good agreement is noted with the DIC gauge. The measured strain in the transverse direction shows less fluctuations when compared to the monotonic experiment (FIG. 3.11(b)). After the first two cycles nonlinearity occurs since the strain in the unloaded state does not vanish.

Introducing the measured strain in Equation (3.1) the instantaneous Poisson's ratio is obtained. FIG. 3.24(c) shows the change of instantaneous Poisson's ratio with the longitudinal strain. In the elastic regime, less fluctuations are noted with both gauges. After 0.1 % of strain the Poisson's ratio calculated with DIC gauge stabilises around 0.278. When the strain level exceeds the elastic limit different paths are observed for the two measurement techniques. The reason of this phenomena can be explained by multiple microcrack initiations (see Section 4). In plasticity the value of Poisson's ratio is equal to 0.33.

FIG. 3.25 shows the stress-strain curve for cyclic and monotonic loading histories. A very good agreement is found between the two responses. The monotonic curve describes well the upper peaks of the cyclic loading history. A lower elongation to rupture of 1 % is noted when compared with the monotonic tensile test. Fitting the linear parts of the stress-strain curve for the first two cycles gives a Young's modulus of 156 GPa. The identified value, as in the monotonic test, is in very good agreement with known values of SG cast iron (see CHAP. 1).

#### 3.3.2 Determination of parameters via FEMU

The aim of the present section is to identify Young's modulus and Poisson's ratio in a single identification procedure. The FEMU-UF variant is chosen. Before performing the identification the measurement uncertainty was estimated on 10 images acquired when the specimen was mounted and without loading. The standard displacement resolution is equal to 0.004 pixel and the corresponding load resolution  $\gamma_F$  is equal to 5 N. The electro-mechanical testing machine introduces significantly less fluctuations.

**Table 3.5:** Initial and identified elastic parameters for cyclic uniaxial tension

Parameter	E (GPa)	$\nu$	$\chi_u$ (pixel)	$\chi_F$ (kN)
Reference	156	0.33	0.0089	0.29
FEMU-UF	158	0.282	0.0088	0.26

The identification was performed on the first 929 images that correspond to the first 2 loading cycles. The initial parameters for the FEMU-UF analysis are given in TAB. 3.5.

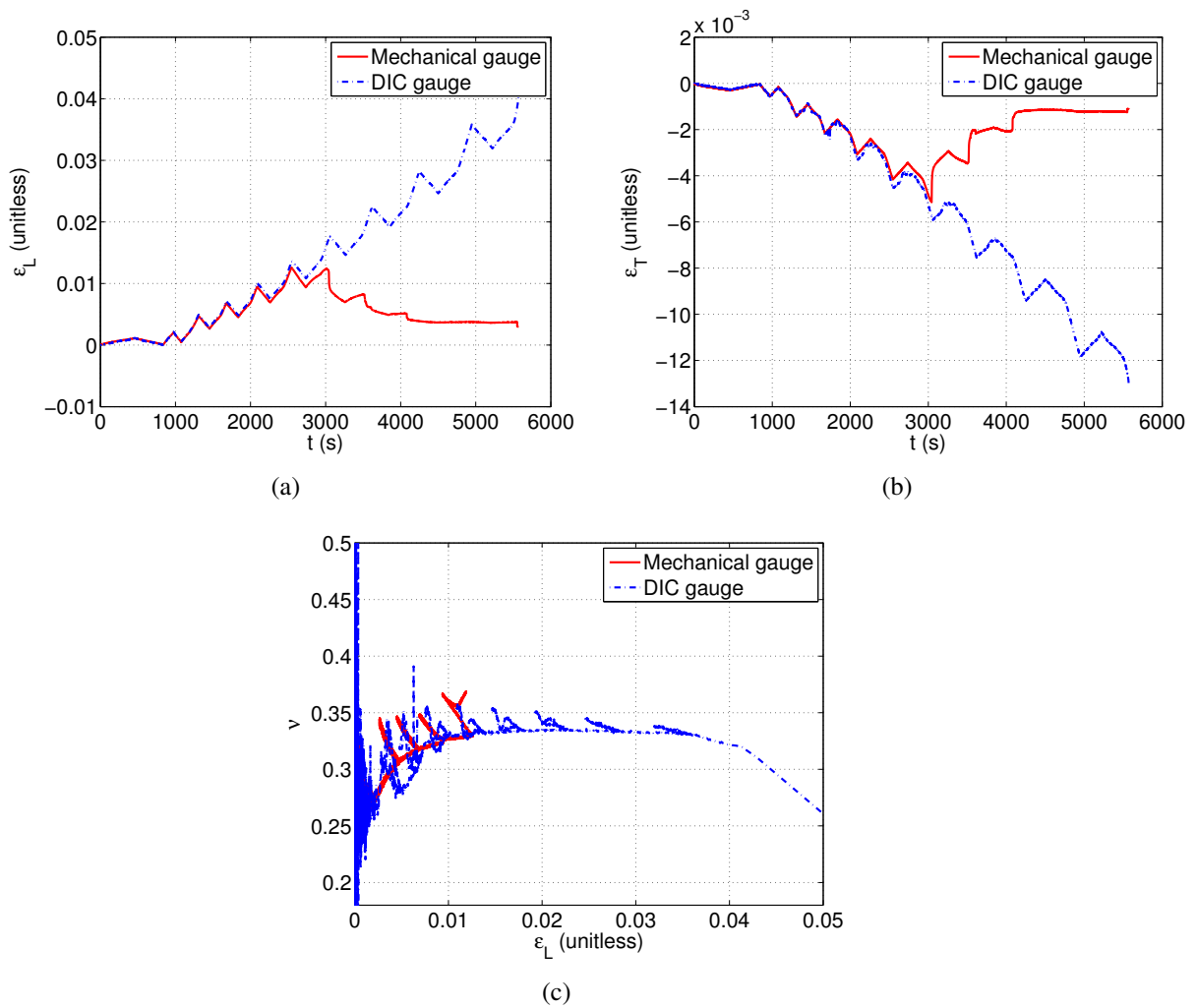


**Figure 3.24:** Comparison of measured  $\epsilon_L$  (a) and  $\epsilon_T$  (b) with strain gauge and DIC gauge. (c) Instantaneous Poisson's ratio calculated with Equation (3.1)



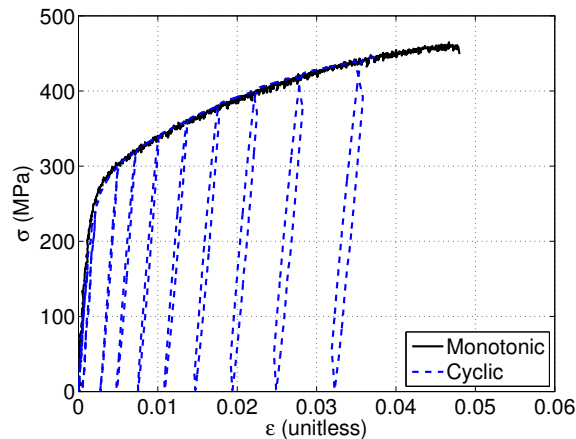


**Figure 3.25:** Stress-strain curve for monotonic and cyclic tensile tests

The reference value for the Young's modulus was taken from the previous analysis. However, the initial value of Poisson's ratio was chosen to be equal to 0.33. The initial parameters lead to lower  $\chi_F$  levels than in the previous experiment, while  $\chi_u$  is significantly lower.

The identified Young's modulus via FEMU-UF (see TAB. 3.5) changes slightly in comparison with the reference value. This is mainly causing the drop of  $\chi_F$  by 30 N. A decrease of  $\chi_u$  is induced by the identified Poisson's ratio, which corresponds to the value measured with the strain gauge. From the sensitivity of the displacement field (see FIG. 3.26) a bigger change of displacements is observed in the transverse direction of the specimen. The most appropriate regions for identifying Poisson's ratio is around the maximum load levels of the two cycles since highest sensitivities are observed.

### 3.4 Identification of Johnson-Cook parameters

The identification of Johnson-Cook parameters was performed on all acquired images (*i.e.*, 5,527 pictures). The initial (*i.e.*, reference) Johnson-Cook parameters were taken from the monotonic curve (see TAB. 3.6). The first calculation of the FEMU-UF analysis yielded high levels of force residuals (*i.e.*,  $\chi_F = 1.73$  kN). The reference (*i.e.*, monotonic) Johnson-Cook parameters do not describe in a reliable way the cyclic loading history (FIG. 3.27).

The identified values of the sought parameters ( $\sigma_y$ ,  $K$  and  $n$ ) given in TAB. 3.6 decrease  $\chi_u$  and  $\chi_F$ . FIG. 3.27 shows the comparison of the measured force and calculated sum of reaction forces for both sets of parameters. It is observed that the yield stress decreases by almost 30 %, which requires parameters  $K$  and  $n$  to change. A 1 kN difference is observed for  $\chi_F$  when compared with the monotonic experiment (see TAB. 3.3). The displacement residual  $\chi_u$  is significantly lower in the cyclic experiment.

For comparison purposes the elastic (see TAB. 3.5) and elastoplastic analyses can be studied. When the whole experiment (*i.e.*, 5,527 images) is analysed  $\chi_u=0.15$  pixel while

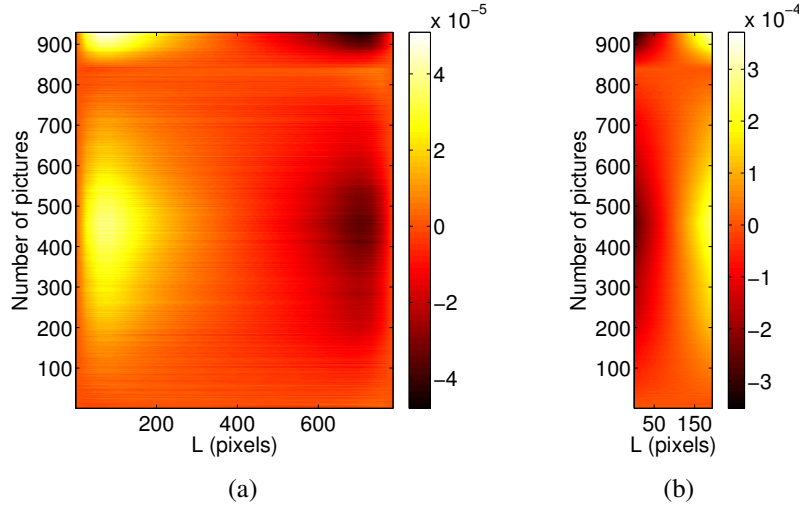


**Figure 3.26:** Sensitivity of the displacement field with respect to a change of 1% of Poisson’s ratio  $\nu$  (in pixel). (a) Cut in the middle of the longitudinal direction and (b) in the middle of the transverse direction of the ROI

for the elastic identification (950 images)  $\chi_u=0.09$  pixel. The fact that lower levels of  $\chi_u$  are obtained when compared with the elastoplastic analysis indicates a model error.

**Table 3.6:** Identified Johnson-Cook parameters via FEMU-UF

Parameter	$E$ (GPa)	$\nu$	$\sigma_y$ (MPa)	$K$ (MPa)	$n$	$\chi_u$ (pixel)	$\chi_F$ (kN)
Reference	151	0.282	289	1260	0.62	0.16	1.73
FEMU-UF	151	0.282	207	1300	0.44	0.15	1.22

FIG. 3.27 shows that higher levels of  $\chi_F$  are due to a model error. The stiffness of the specimen is too high after the second cycle since the sum of the reaction forces does not stop at 0 N when unloading. This leads to the hypothesis that damage may occur early on. Before discussing this phenomenon, let us first analyse the experiment with a kinematic hardening model.

### 3.5 Identification of Armstrong-Frederick parameters

The identification of Armstrong-Frederick’s nonlinear kinematic hardening was performed over the whole cyclic experiment. The reference parameters were taken from the monotonic test (TAB. 3.5). The sought Armstrong-Frederick parameters for the cyclic loading history take different values than those obtained in monotonic loading. FIG. 3.28 illustrates the different load levels reached. The initial parameters better describe the unloading parts of the history, while the identified parameters better capture the various fluctuations of the loading path.

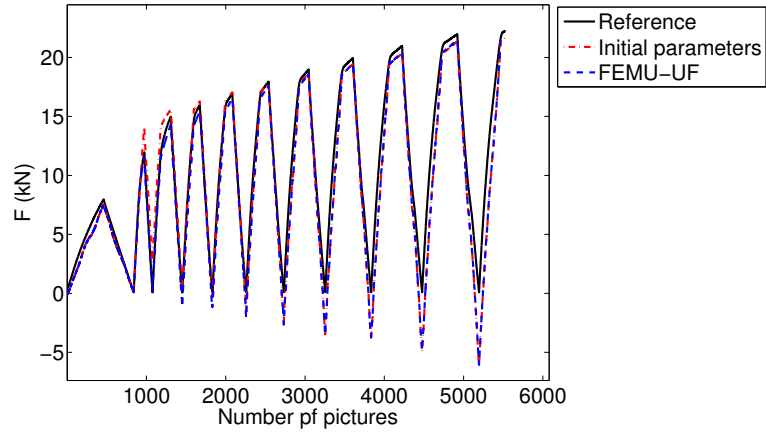


**Figure 3.27:** Comparison of measured force and sum of reaction forces computed with initial and identified material parameters for Johnson-Cook's law

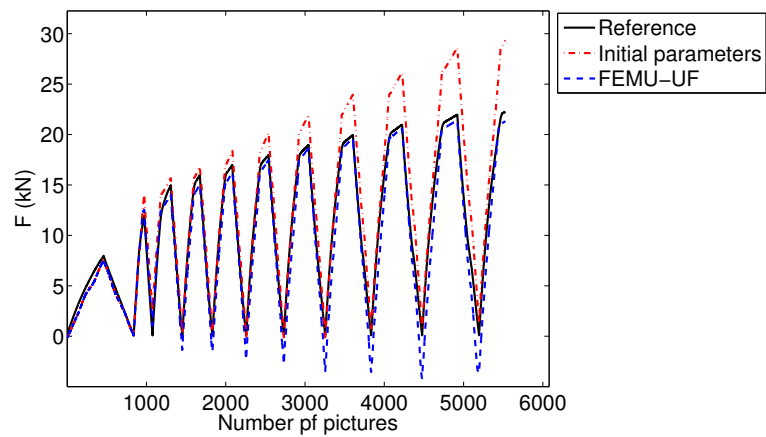


**Figure 3.28:** Comparison of measured force and sum of reaction forces computed with the initial and identified parameters for Armstrong-Frederick's constitutive law

Armstrong-Frederick parameters identified for a cyclic loading history yield higher values of  $\chi_u$  and  $\chi_F$  with respect to the monotonic test. However, when the same test is identified they lead to lower residuals than Johnson-Cook's law (TAB. 3.5). The fact that the loading cycles are not fully captured may be due to damage. This hypothesis will be checked in the next section.

**Table 3.7:** Identified Armstrong-Frederick's parameters with the FEMU-UF variant

Parameter	$E$ (GPa)	$\nu$	$\sigma_y$ (MPa)	$C$ (GPa)	$\gamma$	$\chi_u$ (pixel)	$\chi_F$ (kN)
Reference	158	0.28	289	13	20	0.14	2.00
FEMU-UF	158	0.28	222	27	106	0.16	0.93

### 3.6 Identification of isotropic hardening coupled with damage

Without including damage phenomena in the identification procedure of Johnson-Cook's model it is not possible to describe the cyclic behaviour in a reliable way. Since damage represents the progressive material deterioration, it can be defined in terms of relative reduction of the net section of a representative volume element (RVE). With the additional assumption of isotropic damage, the damage tensor is reduced to a scalar  $D$  for which a practical definition can be given

$$D = 1 - \frac{\tilde{E}}{E_0} \quad (3.5)$$

where  $E_0$  and  $\tilde{E}$  are Young's moduli of the undamaged and damaged material state.

To identify the nonlinear behaviour from a cyclic experiment isotropic hardening (Johnson-Cook's model) is coupled with Lemaitre's damage model in a single UMAT routine. Since, FE calculations considering damage are time consuming the identification will first be carried out on an RVE. The identified parameters will give closer initial guesses to the total residual in the FE model.

#### 3.6.1 Results on RVE

One cube element (FIG. 3.29) with unitary size is used as an RVE to obtain a first evaluation of the damage parameters. Two boundary conditions are prescribed on the simple RVE model. First, the bottom surface is motionless in the loading direction, while on the upper surface the displacement is prescribed in the vertical direction. The prescribed displacement corresponds to measured axial strain with the DIC gauge (FIG. 3.24(a)). The identification procedure consists of minimising the stress difference from the cyclic stress-strain data (FIG. 3.25).

The sought parameters describing isotropic hardening are extended with the two damage parameters ( $S$  and  $s$ ) of Lemaitre's law (Equation (1.24)). Except the two parameters it is necessary to define an equivalent plastic strain threshold (*i.e.*,  $\bar{\epsilon}_{pl}^{th}$ ) at which damage

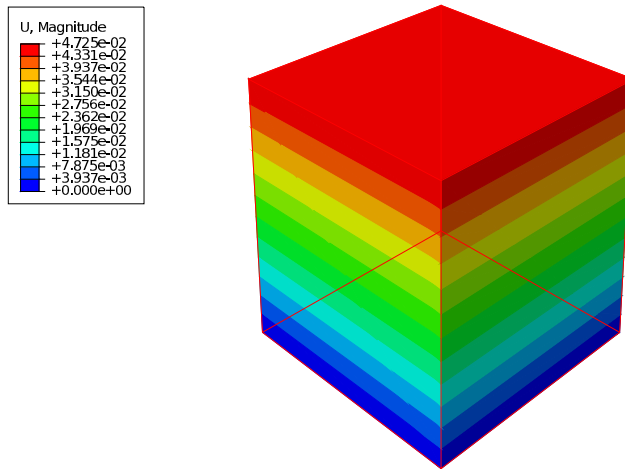


**Figure 3.29:** RVE used to get a first estimate of the damage parameters. Displacement distribution of the last loading level of the cyclic experiment corresponding to 22 kN

starts to grow). To have access to the latter, the change of Young’s modulus for each loading/unloading cycle was identified (FIG. 3.30). An early loss of stiffness is detected. After the second cycle damage involves a nonlinear behaviour. Hence,  $\bar{\epsilon}_{pl}^{ih}$  is set to 0. apart from setting the plastic strain threshold, it is mandatory to provide a limit defining microcrack initiation (*i.e.*,  $D > D_{cr}$ ). Since  $D_{cr}$  was difficult to identify, an arbitrary value of 0.3 was chosen from the literature [Lemaitre and Desmorat, 2005].

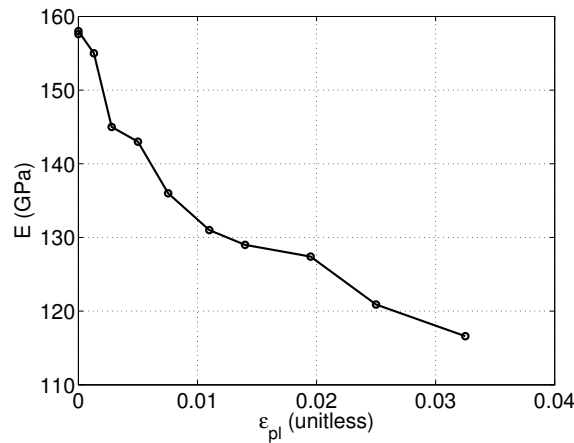


**Figure 3.30:** Change of Young’s modulus with cumulative plastic strain

The FEMU-UF procedure aims to identify/validate six parameters ( $E$ ,  $\sigma_y$ ,  $K$ ,  $n$ ,  $S$  and  $s$ ). Initial values of the sought parameters are shown in TAB. 3.8. The reference elastoplastic parameters are chosen from the monotonic test while the damage parameters were arbitrarily chosen from the literature [Lemaitre and Desmorat, 2005]. During the

first few identification calculations it was noted that it is not possible to identify both damage parameters at the same time since it started to diverge. Hence, the first iterations consisted of the identification of all the parameters except the damage exponent  $s$ , and the second one just  $s$ . This approach successfully identified the sought parameters (see TAB. 3.8).

**Table 3.8:** Identified elastoplastic and damage parameters on an RVE via FEMU-UF

Parameter	$E$ (GPa)	$\nu$	$\sigma_y$ (MPa)	$K$ (MPa)	$n$	$S$ (MPa)	$s$ (MPa)	$\chi_F$ (N)
Reference	157.6	0.28	289	1257	0.62	0.5	1.5	36
FEMU-UF	158.3	0.28	242	2876	0.61	0.25	1.2	12

The biggest change of identified elastoplastic parameters was the hardening modulus (57 %) and yield stress (20 %) while Young's modulus and hardening exponent hardly changed. The damage parameters also decreased ( $S$  by 50 % and  $s$  by 25 %). FIG. 3.31 shows the comparison of the measured load levels and sum of reaction forces for the initial and identified parameters. The decrease of  $\chi_F$  is observed in TAB. 3.8, which results in a better agreement of measured force and load levels obtained with the identified parameters. It is worth noting that the load residuals reach levels closer to the resolution (*i.e.*, 5 N).

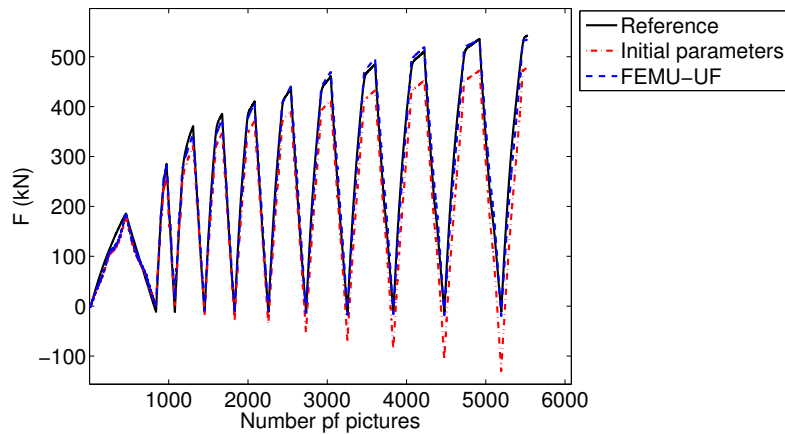


**Figure 3.31:** Comparison of the measured force and sum of reaction forces computed with the initial and identified material parameters of an elastoplastic law coupled with damage for the RVE

### 3.6.2 Results on FE model

The same identification procedure as in the RVE evaluation of elastoplastic and damage parameter was applied to determine the sought parameters on the FE model. The initial

parameters are those obtained from the previous identification procedure (TAB. 3.9) and the identified results slightly differ from those obtained on the RVE.

**Table 3.9:** Identified elastoplastic and damage parameters with an FE model

Parameter	$E$ (GPa)	$\nu$	$\sigma_y$ (MPa)	$K$ (MPa)	$n$	$S$ (MPa)	$s$	$\chi_u$ (pixel)	$\chi_F$ (kN)
Reference	157.6	0.28	242	2876	0.62	0.25	1.2	0.138	0.74
FEMU-UF	157.9	0.28	234	2529	0.59	0.26	1.2	0.137	0.46

FIG. 3.32 shows an excellent agreement between the sum of reaction forces extracted on the prescribed boundary with the measured load (in comparison with the previous case shown in FIG. 3.27). Both components of the total residual decrease in comparison with the elastoplastic case (TAB. 3.6). Hence, the coupled elastoplastic and damage models described in a better way the cyclic experiment. Similarly, the present identification outperforms that with kinematic hardening since the latter leads to load residuals twice as high as the former.

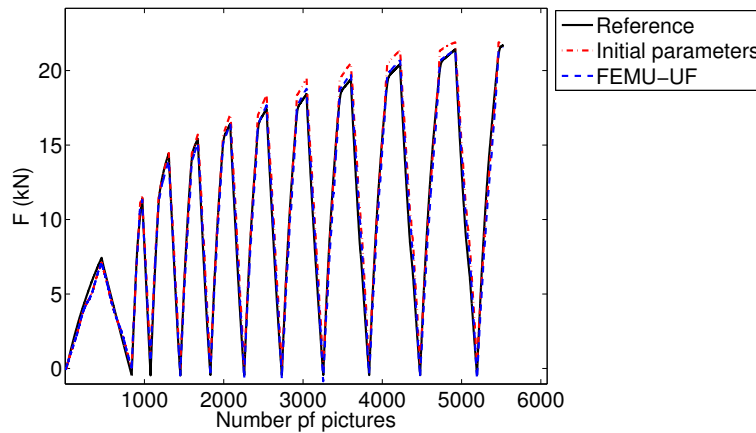


**Figure 3.32:** Comparison of measured force and sum of reaction forces computed with the initial and identified parameters of the elastoplastic and damage law

## 4 Uniaxial cyclic experiment monitored via X-ray tomography

X-ray computed tomography is increasingly used to visualise the complete microstructure of various materials. One of its main advantages lies in the non destructive way of obtaining 3D views of various materials. By analysing 3D reconstructed volumes, one has access, for instance, to the true microstructure of the material and sometimes to the

way it deforms by using in situ experiments analyzed by volumetric correlation algorithms [Roux et al., 2008, Taillandier-Thomas et al., 2014]. From the measured 3D displacements in the bulk of a scanned material more reliable information about its behaviour is determined [Limodin et al., 2009, Limodin et al., 2010]. In the previous sections cast iron was observed on the macroscopic level without any access to phenomena appearing within its heterogeneous microstructure. In this section a cyclic uniaxial experiment carried out in an X-ray tomograph is presented. The aim is to analyse from the displacement and residual fields the interaction of the ferrite matrix and the graphite nodules under tensile loading. In particular, the development of damage will be discussed.

## 4.1 Experimental procedure

The X-ray microtomographic experiments were performed using the X50+ system (North Star Imaging, see FIG. 3.33(a)) of LMT-Cachan. A uniaxial specimen of the investigated nodular graphite cast iron is loaded in situ in a testing machine (FIG. 3.33(b)). The custom made uniaxial device is placed on the turn table (while scanning the sample it is rotated  $360^\circ$  along its vertical axis). The gripped specimen is placed inside of the composite carbon tube whose purpose is to transmit the load and hold the load cell above the sample. The specimen is loaded from 200 up to 750 N in twelve incremental loading and unloading steps (FIG. 3.34). To estimate the standard displacement resolution the first two scans were taken at equal load level ( $F = 200$  N).

The dog-bone specimen made by electrodischarge machining of a 1.6-mm thick plate. To ensure that the specimen will brake in the ligament area and not in the grips the central part is rounded with a radius of 20 mm (FIG. 3.35(a)). The ligament is 9 mm high, while the smallest cross-section of the sample is  $1.6 \times 1$  mm<sup>2</sup>.

Each tomographic scan was initially acquired with a definition of  $1280 \times 1280 \times 1860$  voxels, whose physical size is  $6.4 \mu\text{m}$ , encoded as 8-bit deep gray levels. In those images, a region of interest is defined in which the displacement field will be analysed. The size of the ROI was adjusted to the sample geometry (FIG. 3.35) focusing on the thinned part of the sample corresponding to an image size of  $160 \times 196 \times 608$  voxels.

## 4.2 A priori analysis

Before studying the displacement field between two scans, it is important to evaluate the level of uncertainty attached to the natural texture of the image. FIG. 3.35(b) shows the ROI of the reference scan used for DVC analyses. Two volumes acquired with the same load level ( $F = 200$  N) are correlated to evaluate the standard displacement resolution.

Even though a fine contrast was found between the ferritic matrix and the graphite nodules, a large size of nodules is noted in comparison with previous works [Limodin et al., 2009, Limodin et al., 2010]. Since the investigated cast iron has a coarse texture it is necessary to make a compromise between the spatial and displacement resolutions. The only difficulty is to be able to capture the displacement without being trapped in secondary minima of the objective function. Two DVC algorithms (*i.e.*, C8-DVC [Roux



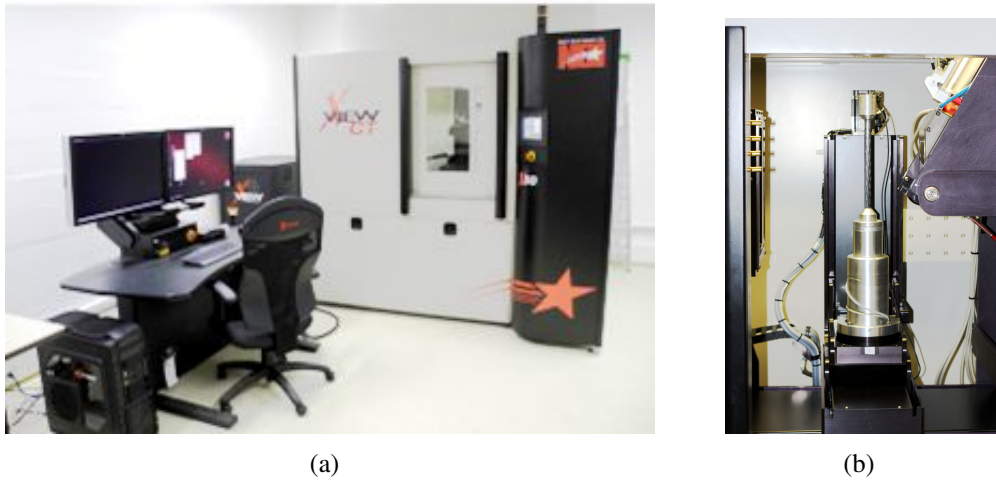


**Figure 3.33:** X50+ Computed Tomography System (a) and corresponding custom made uniaxial tensile machine for in situ tomography experiments (b)

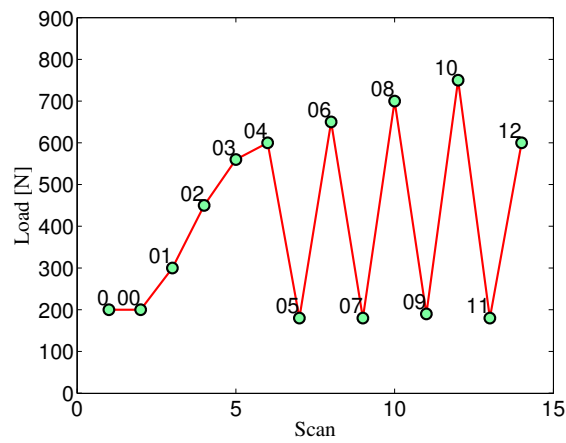


**Figure 3.34:** Loading history of the in situ experiment on X50+ CT system

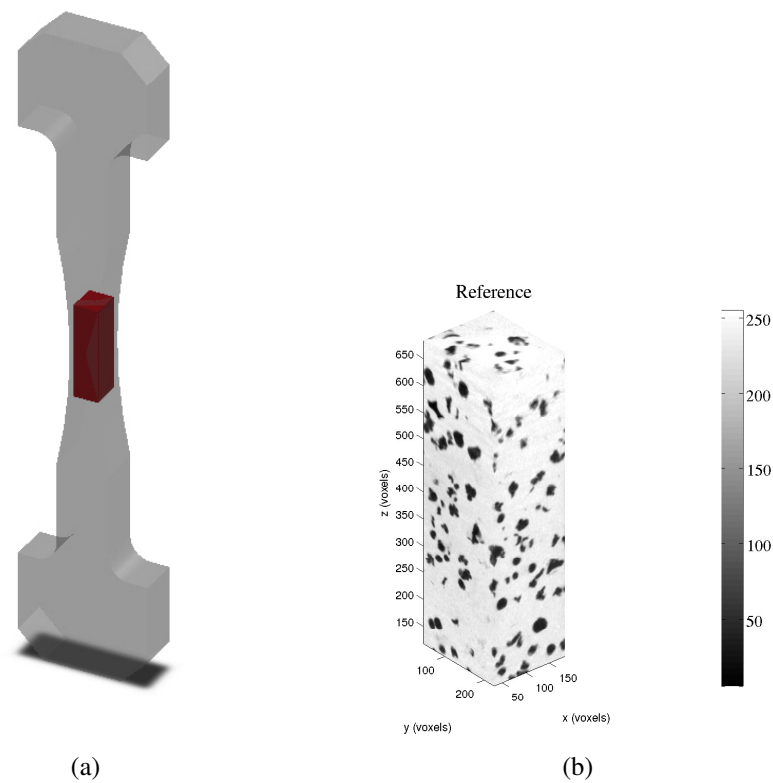


**Figure 3.35:** (a) Dog-bone sample used for tomography. The red zone inside the sample denotes the investigated ROI ( $160 \times 196 \times 608$  voxels). (b) Reference volume ( $F = 200$  N)

et al., 2008] and RC8-DVC [Taillandier-Thomas et al., 2014]) are used to evaluate the measurement uncertainty.

First, C8-DVC was used. The smallest possible element size was 32 voxels. With smaller elements convergence was not reached. Bigger elements (*i.e.*, 64 voxels) were also useless since the ROI thickness of the sample in the  $x$  direction is 160 voxels. Regularised C8-DVC was also used with 16-voxel elements. The initial regularisation length was 64 voxels in the three directions. During the relaxation process  $\ell_m$  is decreased by 16 pixels in the every subsequent computation. When the regularisation length was smaller than 16 voxels the algorithm could not converge since the regularisation does not have a significant impact if  $\ell_m$  is less than the element size  $\ell$ .

FIG. 3.36 shows the standard displacement resolution when C8 and RC8-DVC are used to measure displacement fluctuations. When  $\ell_m = 64$  voxels is used a significant gap is noted when compared to classical C8-DVC. However, the relaxation of the regularisation increases the displacement resolution (*i.e.*, the larger the regularisation length, the smaller the displacement resolution). It is important to stress that the computation with 16-voxel elements converged even when  $\ell_m = 16$  voxels was used.

### 4.3 Analysis of the results

Several results are presented from RC8 analyses when  $\ell_m = 32$  voxels. The correlation was performed between the undeformed volume (scan 0) and deformed ones (scans 00-11). First, the displacement fields of the volumes corresponding to scan 05 (*i.e.*, 560 N) and the last loading scan 11 (*i.e.*, 750 N) are studied, which show different distributions over the volume. Observing the displacement in the  $x$ -direction of the scan 05 we can clearly see the contraction due to the Poisson's ratio (FIG. 3.37(a)). The displacement fields revealed in  $y$  and  $z$ -directions (FIG. 3.37(c) and (e)) show how the sample was not loaded in pure tension. Additional rotations occur due to the gripping system of the testing machine. It is necessary to emphasise that no localisation was observed on the displacement fields. However, the measured displacement fields for scan 11 detect localised phenomena. Displacements in  $x$  and  $y$  directions (FIG. 3.37(b) and (d)) show the presence of a macrocrack between  $z = 500$  and 600 voxels in the longitudinal direction.

Von Mises' equivalent strain fields are presented in FIG. 3.38(a) and (b). When the sample was loaded at 560 N (FIG. 3.38(a)) two critical locations were detected, one in the lower (*i.e.*,  $z = 200$  voxels) part and another one in the upper (*i.e.*,  $z = 440$  voxels) part of the ROI. For the load level corresponding to 760 N (FIG. 3.38(a)) localisation becomes dominant. Plotting the gray level residual volumes a damage mechanism was revealed (FIG. 3.38(c) and (d)). Observing the reference volume (FIG. 3.35(b)) higher residual values are observed around the nodules. This phenomenon is caused by debonding between the matrix and the nodules. In the last step of loading the residuals show the macrocrack path that was caused by the localisation of the displacement and strain fields.

In the sequel, the 12 volumes will be considered. The gray level residual maps (FIG. 3.39) corresponding to the plane normal to the  $y$ -axis  $\varphi_c(x, y = 30 \text{ voxels}, z)$  are chosen. The dynamic range of the residuals is fixed so that an increase of fluctuations can

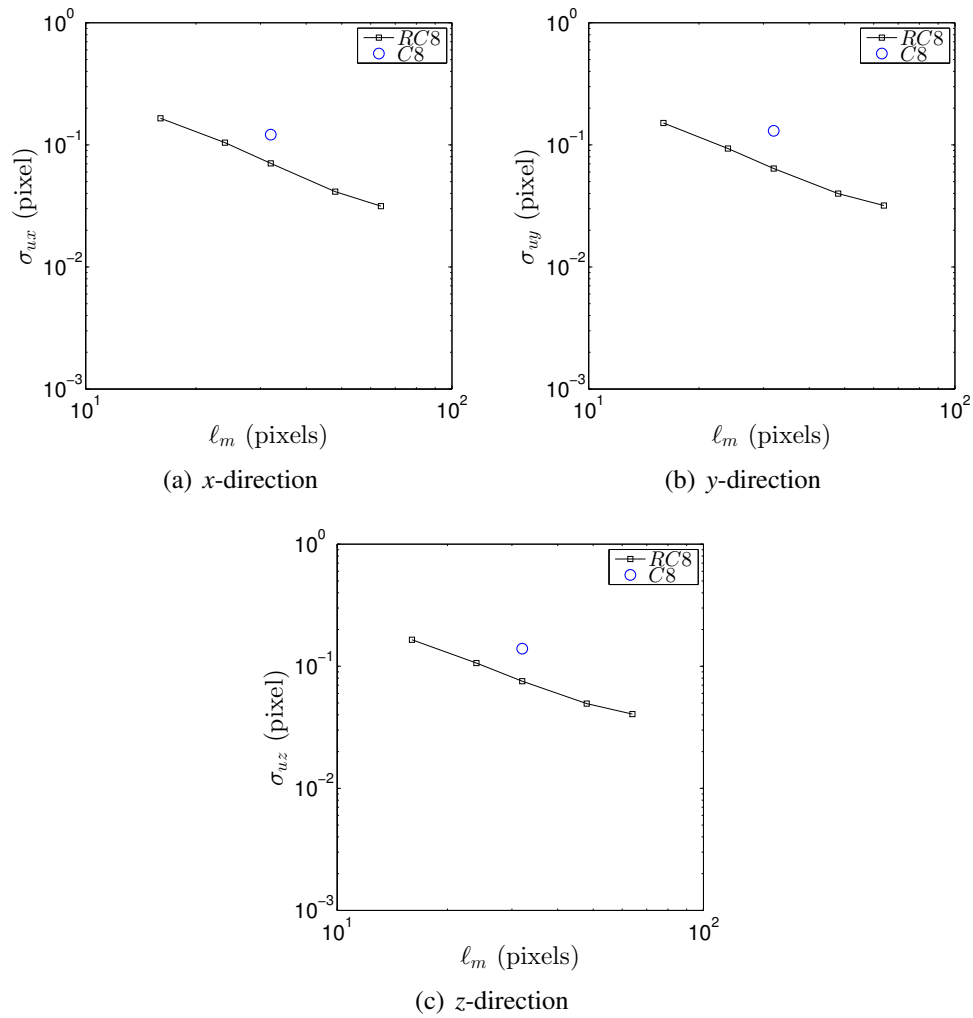


**Figure 3.36:** Standard displacement resolution with C8 and RC8-DVC for different regularisation lengths  $\ell_m$  (RC8-DVC) or element size  $\ell$  (C8-DVC, circle). 16-voxel elements are used in RC8-DVC

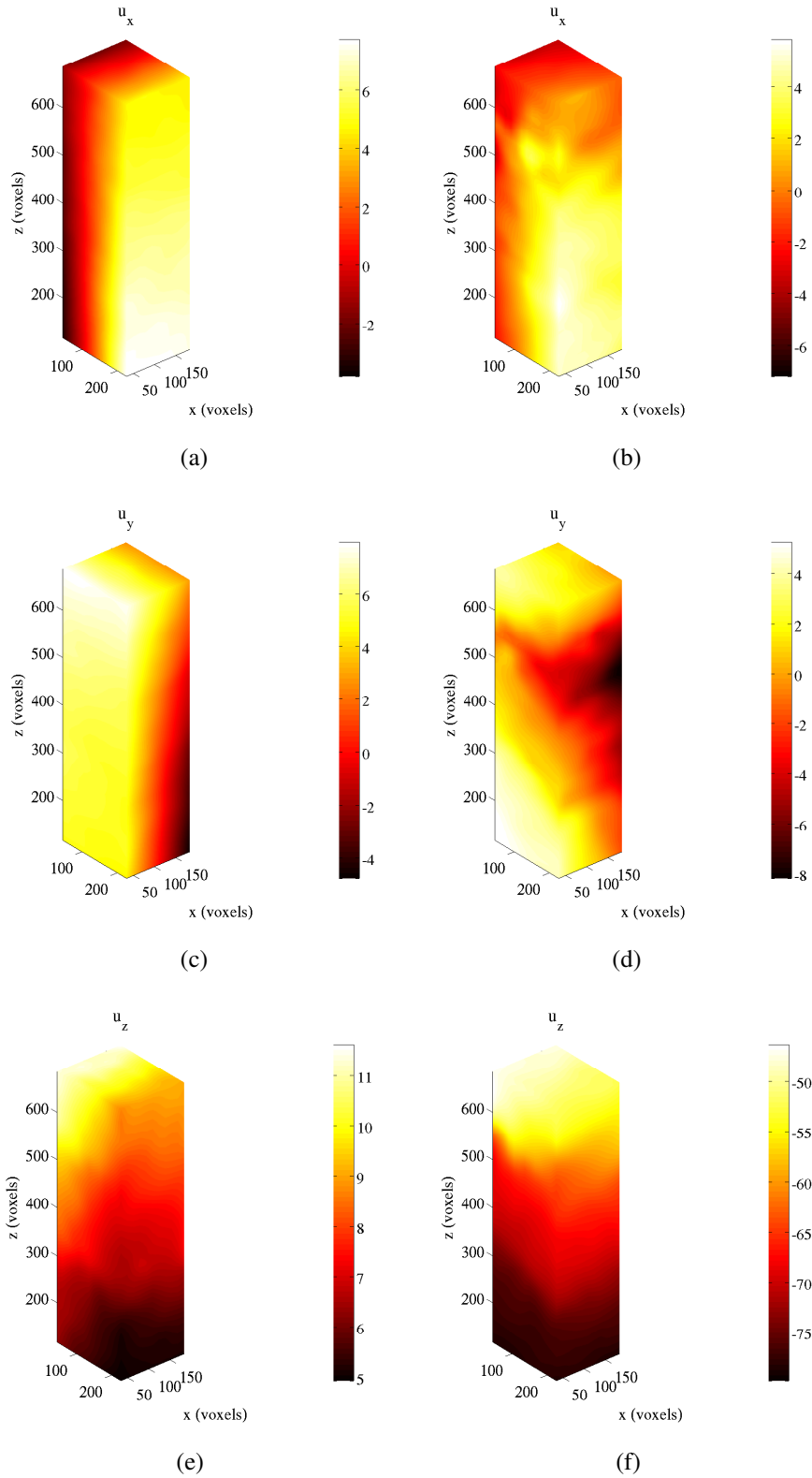


**Figure 3.37:** Measured displacement fields in (a) & (b)  $x$ , (b) & (c)  $y$  and (c) & (d)  $z$ -directions corresponding to load levels 560 N (left) and 750 N (right).

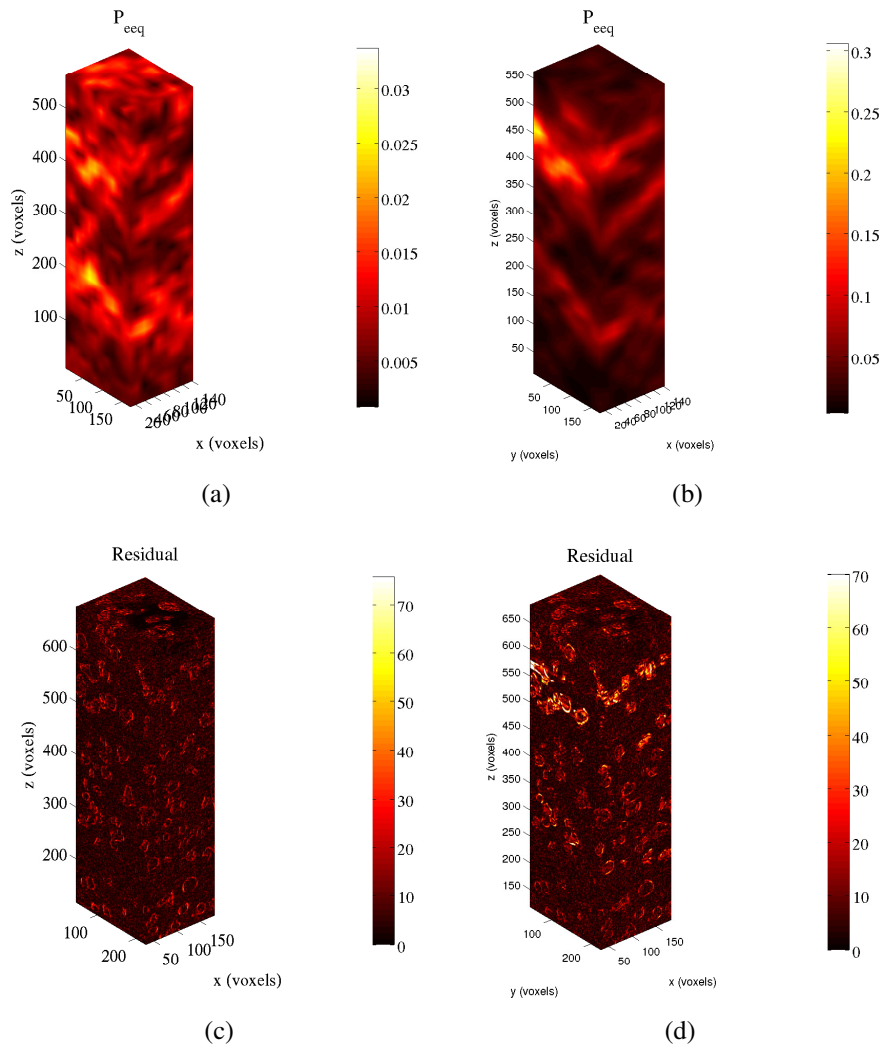


**Figure 3.38:** Von Mises' equivalent strain fields (a) & (b), and gray level residual fields (c) & (d) for load levels 560 N (left) and 750 N (right)

be captured. Debonding between the matrix and the nodules is detected in the very early stages (*i.e.*, even for scan 01). There is an increase of residuals as the loading levels become higher. Segmentation of the SG cast iron constituents even at the first loading level defines the damage micromechanism. This fact explains the loss of stiffness observed in the cyclic tensile experiment (see FIG.3.30).

From the SEM analysis of the broken sample (FIG. 3.40) brittle damage is recognised. Two brittle fracture mechanisms were found. First, transgranular damage is observed in the green window of the latter figure since transcrySTALLINE surface profiles are characterised by separated grains. Second, cleavage fracture is detected (in the red window of FIG. 3.40). It is distinguished by an even crack surface and corresponds to restricted plastic flow.

## 5 Conclusion

The goal of this chapter was to identify elastic and nonlinear properties (*i.e.*, isotropic and kinematic hardening) for two uniaxial loading histories. The identification was performed via FEMU procedures comparing the measured and calculated displacement fields. Two identification procedures (*i.e.*, FEMU-U and FEMU-UF) determined Poisson's ratio when the experiment was not corrupted with fluctuations introduced by the testing machine. The Poisson's ratio showed a high sensitivity to displacement field changes. It could be identified with FEMU-U and FEMU-UF variants. However, the change of Young's modulus does not impact the displacement field in elasticity so only FEMU-UF and FEMU-F could identify it. A very good agreement was found with elastic parameters identified in a conventional way and via FEMU procedure.

The identification of isotropic (Johnson-Cook's law) and kinematic (Armstrong-Frederick's model) hardening laws was performed via FEMU-UF and FEMU-F variants. Slight differences were noted between the latter ones. It is worth emphasising how FEMU-U alone without the introduction of a stress (or load) component in the minimisation algorithm could not yield reliable parameters. It is shown that minimizing the total residual for the monotonic tensile test in order to find optimal set of isotropic and kinematic material parameters has led to a higher reliability (*i.e.*, a decrease of displacement and force residuals is noted).

The identification of the same constitutive behaviour for different uniaxial loading histories (monotonic and cyclic) yields different parameters. The force residuals for the monotonic loading history are lower than those for cyclic loading. The reason why the cyclic loading regime cannot be described with lower force residuals lies in modelling errors since Johnson-Cook/Armstrong-Frederick's laws do not account for damage phenomena. When a coupled elastoplastic and damage law (*i.e.*, Johnson-Cook's isotropic hardening and Lemaitre's damage model) is considered the force residuals are the lowest. It is the best of the three models in the present case.

By measuring the displacement fields at a macroscale it was detected that the investigated SG cast iron has a low elongation to failure. When identifying the elastoplastic

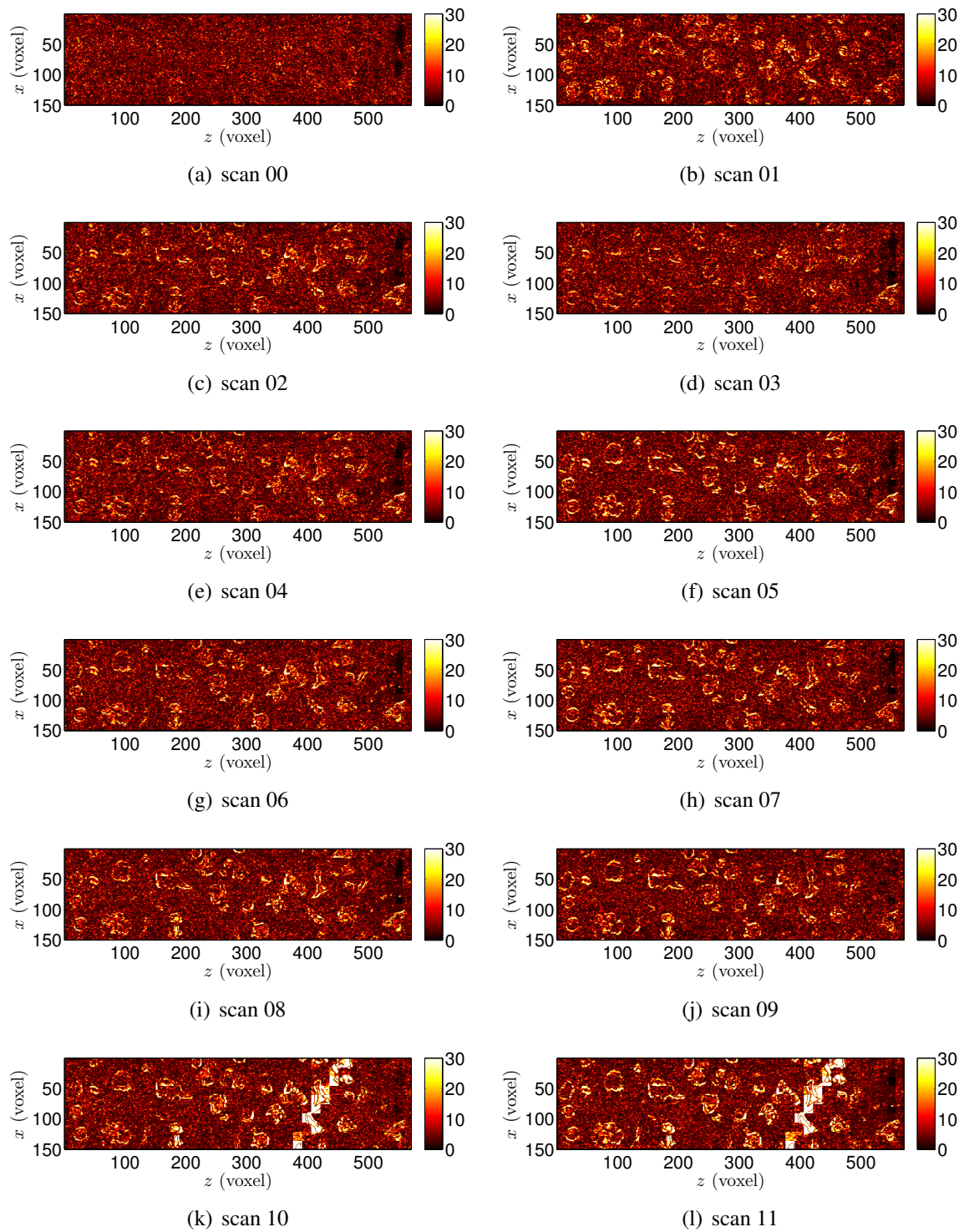


**Figure 3.39:** Residual maps corresponding to the plane normal to the  $y$ -axis for the 12 scans



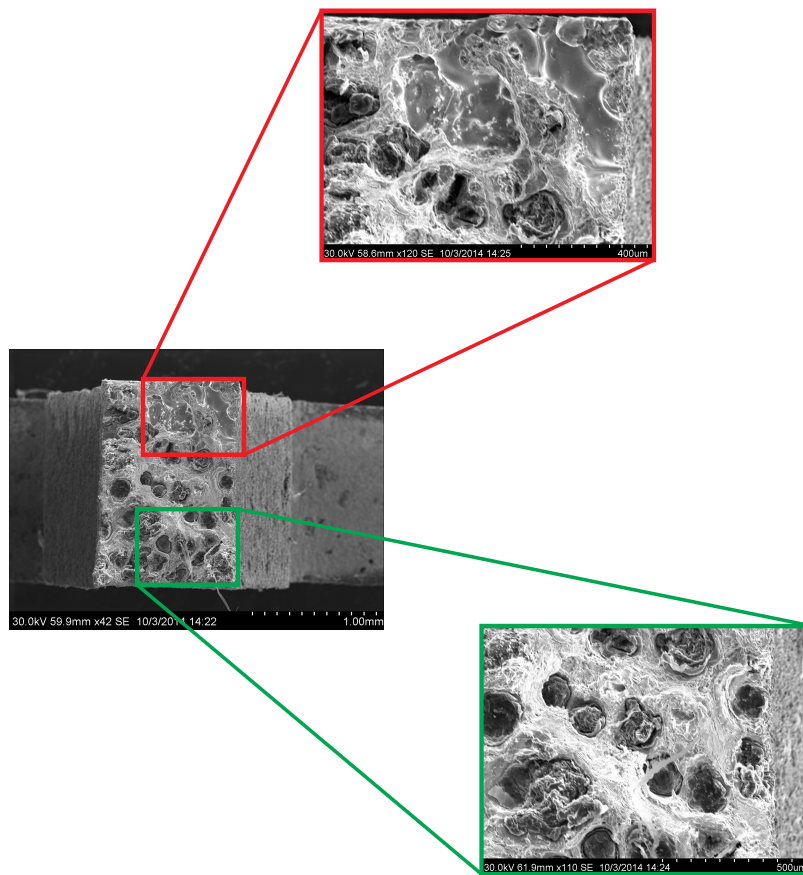


**Figure 3.40:** SEM analysis of the broken tomographic sample

material response early damage initiation was observed. From the latter the micromechanisms could not be distinguished. Hence, a cyclic experiment was carried out in an X-ray tomograph. Debonding between the matrix and the nodules was detected in the first loading step (*i.e.*, in elasticity).

## **Part III**

# **Identification of nonlinear material behaviour via biaxial experiments**



## Chapter 4

# Analysis of the elastoplastic behaviour under biaxial loading regimes

*In this chapter the material behaviour of the investigated SG cast iron is investigated under biaxial loading regimes. Two different loading histories are applied, namely equibiaxial and “snail” loading paths. The central part of the cross-shaped sample will be observed on two scales (i.e., macro and meso). From the displacement measurements the strain histories are obtained and compared in terms of different scales and different loading regimes. The other part considered in this chapter is the identification of elastoplastic parameters from the macroscale measurements.*

### Contents

---

<b>1</b>	<b>Preface</b> . . . . .	<b>115</b>
<b>2</b>	<b>Experimental setup</b> . . . . .	<b>116</b>
2.1	ASTREE: Triaxial testing machine . . . . .	116
2.2	In-plane cruciform specimen . . . . .	117
2.3	Two scale optical setup . . . . .	117
2.4	Applied loading histories . . . . .	120

<b>3</b>	<b>Displacement resolution on macro- and mesoscales . . . . .</b>	<b>124</b>
3.1	Macroscale analysis . . . . .	124
3.2	Mesoscale analysis . . . . .	125
<b>4</b>	<b>Equibiaxial loading history . . . . .</b>	<b>130</b>
4.1	Two scale strain analysis . . . . .	130
4.2	Implementation of 3D FEMU procedure using 2D-DIC measurements	133
4.3	Identification of elastic parameters . . . . .	135
4.4	Identification of parameters describing isotropic and kinematic hardening . . . . .	137
<b>5</b>	<b>“Snail” loading history . . . . .</b>	<b>140</b>
5.1	Two-scale measurements . . . . .	140
5.2	Validation of elastic parameters . . . . .	141
5.3	Identification of plastic parameters . . . . .	148
<b>6</b>	<b>Conclusion . . . . .</b>	<b>151</b>

---

# 1 Preface

Most of the time, engineering structures experience different and complex (*i.e.*, multi-axial) loading regimes. This is the reason why it is necessary to run multi-axial tests during which different types of load histories are prescribed. For 20 years, biaxial tests have been performed at LMT. The history of conducting biaxial tests can show how experiments were used and analyzed.

Since it is very important to prescribe realistic loading conditions in engineering structures, a large variety of loading histories have been considered. This was true since the very first biaxial tests for which the aim was to validate a fatigue criterion for a steel [Batisse et al., 1996]. Various types of materials have been subsequently tested (*e.g.*, elastomer [Chevalier et al., 2001, Promma et al., 2009], shape memory alloy [Calloch et al., 2002a], composite [Périé et al., 2002], concrete [Plé et al., 2002]). First, strain gauges have been used so that the sample geometry was designed in such a way that the strains are uniform in a small part of the sample [Batisse et al., 1996, Calloch et al., 2002a]. Full-field measurements have opened new ways to perform and analyse the experiment [Chevalier et al., 2001, Calloch et al., 2002a, Périé et al., 2002, Plé et al., 2002, Doudard et al., 2007]. In particular, various sample geometries have been considered when associated with full-field measurements.

Furthermore, identification procedures have been developed to explicitly deal with full-fields [Calloch et al., 2002b, Claire et al., 2002, Leclerc et al., 2009]. In terms of kinematic fields measured via DIC, new procedures are also considered. First, regularization techniques can be introduced. This type of procedure enables us to deal with poor textures and/or rapidly varying displacement fields. Second, when dealing with multi-axial tests, 2D-DIC may yield spurious measurements due to out-of-plane motions. One way of circumventing this limitation is to resort to stereoDIC on a more regular basis. This technique was very useful when measuring stress intensity factors in modes I, II and III when nonproportional loadings have been prescribed [Mathieu and Fremy, 2012, Fremy et al., 2014]. Another trend that will require new developments is related to the simultaneous measurement of various full-fields (*e.g.*, displacements measured by DIC, temperature via IR thermography, elastic strains and phases via X-Ray diffraction).

The work of this chapter consists of two parts. First, from a new experimental setup (*i.e.*, two-scale DIC) the behaviour of the investigated SG cast iron will be revealed. Since in-plane biaxial experiments give an opportunity to apply a wide variety of loading histories two different biaxial loading paths (*i.e.*, equibiaxial and “snail”) will be used. Images acquired on macro- and mesoscales will be used to perform DIC analyses. The challenging part is the performance of DIC with the poor natural texture of the studied material since classical DIC techniques require fine artificial speckles. The regularization technique will be used to overcome this limitation. From the measured displacement fields, the strain histories will be extracted and compared on both scales. The second part of this chapter will consider the identification of elastic and plastic (*i.e.*, isotropic and kinematic hardening) parameters via the FEMU-UF procedure for the two applied loading histories. The novelty of the identification procedure consists of using 2D DIC measurements

coupled with 3D FE models.

## 2 Experimental setup

### 2.1 ASTREE: Triaxial testing machine

Biaxial tests were conducted on the triaxial servo-hydraulic machine ASTREE (FIG. 4.1). The loading frame of the machine is composed of a fixed base, four vertical columns and a mobile crosshead. Among the six available servohydraulic actuators, the four horizontal ones are used for the tests. They have a load capacity of 100 kN and a 250-mm stroke range. They can be freely and independently relocated along the vertical columns. For this test, they are placed in the same horizontal plane. Such a setup has already been used for monotonic as well as cyclic biaxial tests [Sermage et al., 2000, Doudard et al., 2007, Poncelet et al., 2010, Fremy et al., 2014]. For protection against potential side and twist forces applied by the other actuators, additional hydraulic bearings are installed in front of each actuator. The hydraulic power is supplied by stations that can generate a 600 l/min maximum flow rate.

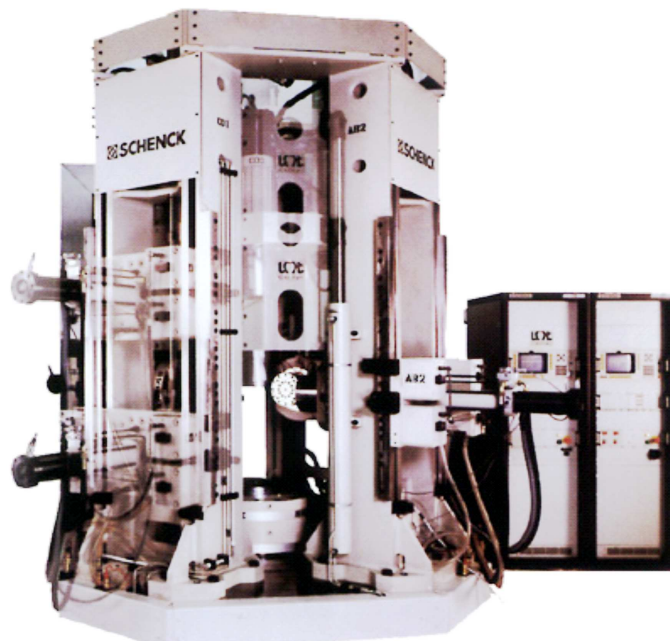


**Figure 4.1:** Triaxial testing machine ASTREE (LMT-Cachan)

The testing machine is equipped with a highly versatile digital controller (Instron 8800) and by its related interface software (Consol 8.2 build 133). This allows each actuator to be controlled independently, but also to perform virtually any closed-loop control using linear combinations of the different input signals. For the biaxial tests presented hereafter, a “modal control” type is used. It is based on a relationship between the two



forces  $F_1$  and  $F_2$  of two opposite actuators along the same load axis ( $X$ ,  $Y$  or  $Z$ ) to control both the mean force  $(F_1 + F_2)/2$  and the force difference  $(F_1 - F_2)/2$ . Consequently the loading is “balanced” between the two actuators if the prescribed force difference is zero.

## 2.2 In-plane cruciform specimen

The tested specimens for biaxial experiments were maltese crosses thinned in the central part with non homogeneous strain/stress fields. The sample was designed in order to allow for crack initiation in biaxial conditions (*i.e.*, in the central part). The prime design of a maltese cross shaped specimen was tested in this machine [Sermage et al., 2000]. By the following two stage procedure [Poncelet et al., 2010] improvements were implemented on the sample shape used herein:

- First, elastic calculations were performed using the damage equivalent stress [Poncelet et al., 2010] to ensure that higher stress levels appear in the center of specimen rather than in the fillets between the arms. The advantage of using the damage equivalent stress criterion takes into account the stress triaxiality in the design.
- Second, the theoretical location of the first initiated crack is checked from the damage post-processing (DAMAGE\_2005) using a two-scale damage model [Lemaitre et al., 1999].

One ends up with the optimized geometry presented in FIG. 4.2. The global size of the sample equals  $274 \times 274 \text{ mm}^2$ . The thickness at the centre is equal to 1 mm and it is gradually increasing to 5 mm out of the gauge zone, which creates a calotte with of circular base 30 mm in diameter. The dimension of the fillets of the gripping arms is 12 mm. Note that the thinned maltese cross-specimen was originally designed for positive load ratios [Poncelet et al., 2010].

## 2.3 Two scale optical setup

Since the geometry of the specimen is complex, the natural choice is to use full-field measurements to have access to the displacement/strain distribution during the experiment. The goal of experiments presented herein is to observe the material response to biaxial loading regimes on two scales. In order to capture displacement fluctuations a two scale optical setup is used (FIG. 4.3).

As previously mentioned, the experiments are carried out in the horizontal plane. The thinned central part of the cross-shaped specimen was observed on both sides (FIG. 4.3(a-b)). The bottom side of the sample is observed on a macroscale (FIG. 4.3(b)) for which the camera monitors the whole gauge zone. Images were taken with a CCD camera (*Dalsa*, 12-bit digitization) and a telecentric lens with a magnification  $\times 4$  (FIG. 4.3(c)). The picture definition is  $1024 \times 1024$  pixels with a physical pixel size of  $48 \mu\text{m}$  (FIG. 4.3(d)). This optical setup is classical for DIC analyses.

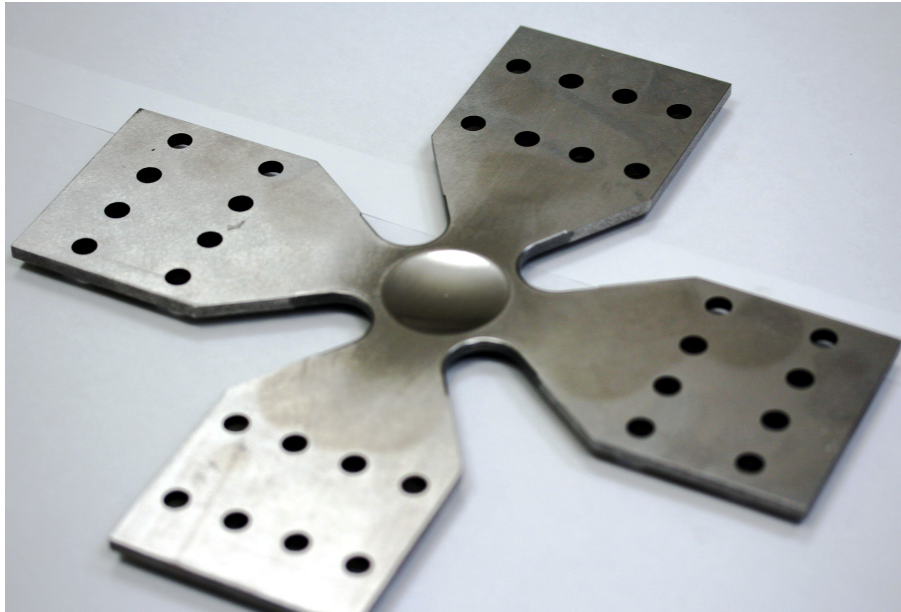


**Figure 4.2:** Maltese cross-shaped specimen designed for in-plane biaxial experiments

For the mesoscale, a second optical setup with a higher magnification is mounted on the upper side of the sample (FIG. 4.3(a)). To reveal the natural texture of cast iron it was necessary to create a custom made optical microscope since the specimen needs to be lighted perpendicularly to the sample surface. This is obtained by using a beam-splitter (FIG. 4.3(e)) and a DedoCool lighting device (FIG. 4.3(g)). The principle of this setup is shown in FIG. 4.3(a). The light is directed perpendicular to the beam-splitter (FIG. 4.3(g)). Half of the light passes through the beam-splitter while the other half is deflected and illuminates the gauge zone of the specimen. Since there is light loss it was necessary to use a more powerful source (*i.e.*, DedoCool lamp). The main advantage is low heating during the application, which results in longer lifetime of the bulbs. This feature is important for long-term experiments (*i.e.*, fatigue tests reported in CHAP. 5).

To have access to the natural texture of SG cast iron the sample surface needs to be illuminated with a perpendicular light and the camera sensor needs to be parallel with the observed zone. To achieve diffuse illumination oil paper is placed on the beam-splitter surface illuminated by the DedoCool lamp. Another CCD camera (*PixelFly*, 12-bit digitization, see FIG. 4.3(f)) is used to monitor the gauge zone. A telecentric lens with a magnification  $\times 1$  is mounted. Mesoscale pictures (FIG. 4.3(g)) have a definition of  $1280 \times 1024$  pixels of physical size  $6.7 \mu\text{m}$ . The gauge zone has a size of  $8.6 \times 6.9 \text{ mm}$ .

Before conducting the two-scale analyses it was necessary to prepare the appropriate texture of the investigated ROIs. To enable for DIC analysis of macroscale pictures an artificial texture was applied. A fine speckle pattern was printed by an airbrush (*i.e.*, ink jet printer, see FIG. 4.4(a)). On the other side of the sample the gauge zone is polished (FIG. 4.4(b)) in order to reveal the natural texture of SG cast iron. At the mesoscale the

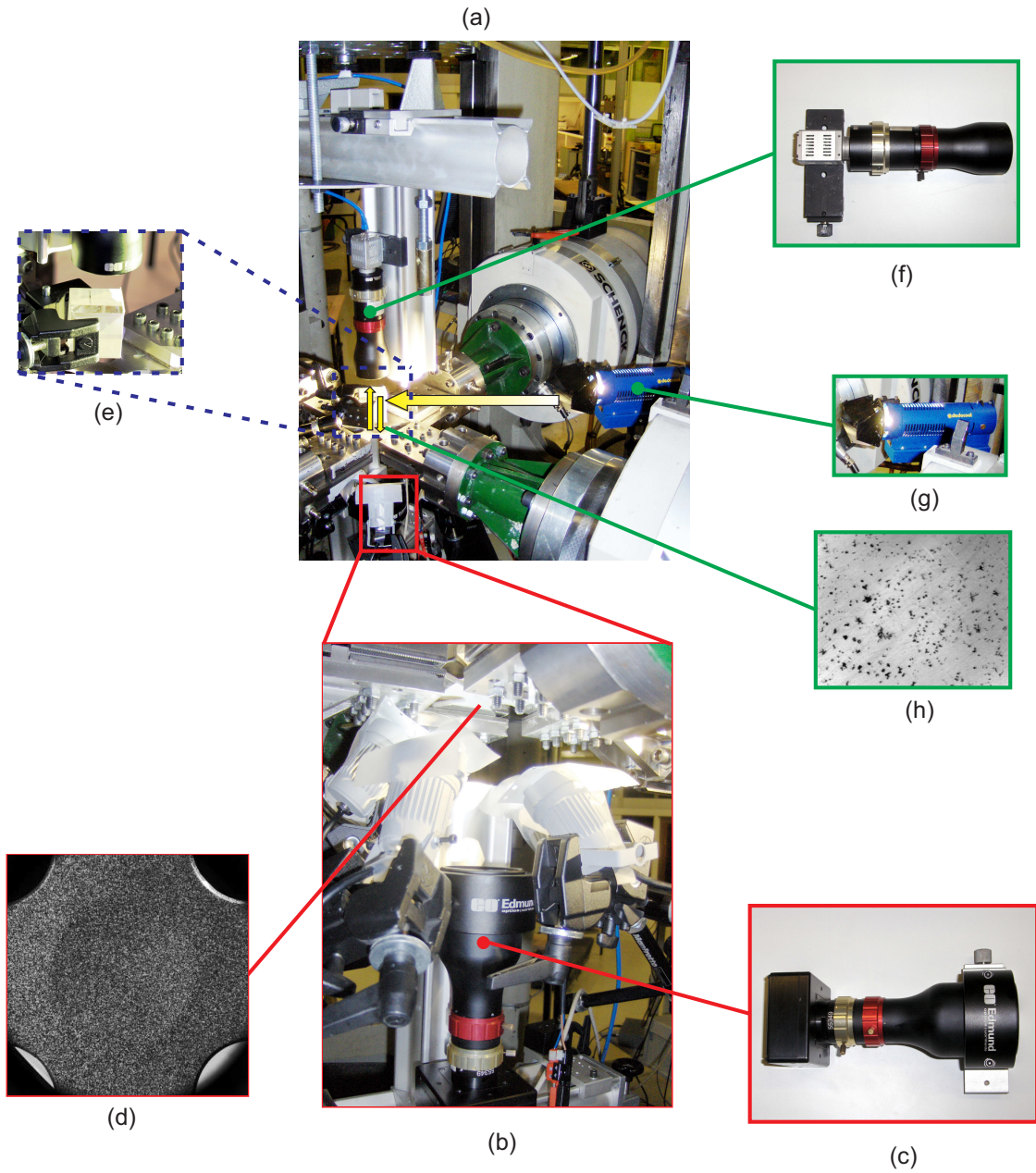


**Figure 4.3:** Two-scale experimental setup. (a) Mesoscale optical setup, (b) macroscale optical setup, (c) CCD camera *Dalsa* with telecentric lens (magnification  $\times 4$ ), (d) macroscale image, (e) beam-splitter, (f) CCD camera *Pixelfly* with telecentric lens (magnification  $\times 1$ ), (g) DedoCool light source, (h) mesoscale image

graphite nodules are used as a natural texture, which is very difficult to analyze with conventional DIC procedures (see FIG. 4.3(h) and FIG. 4.12(a)). In the following section 3 the evaluation of the standard displacement resolution for classical and regularized DIC techniques will be presented.

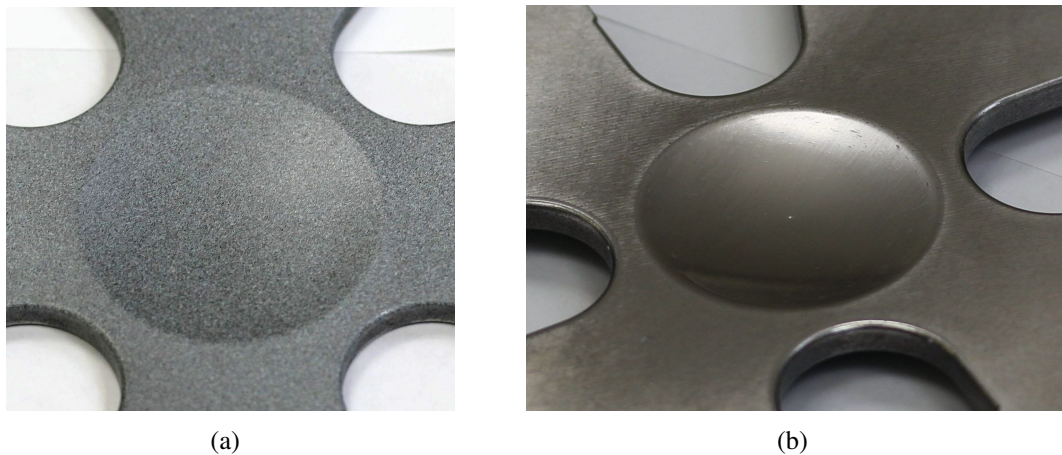


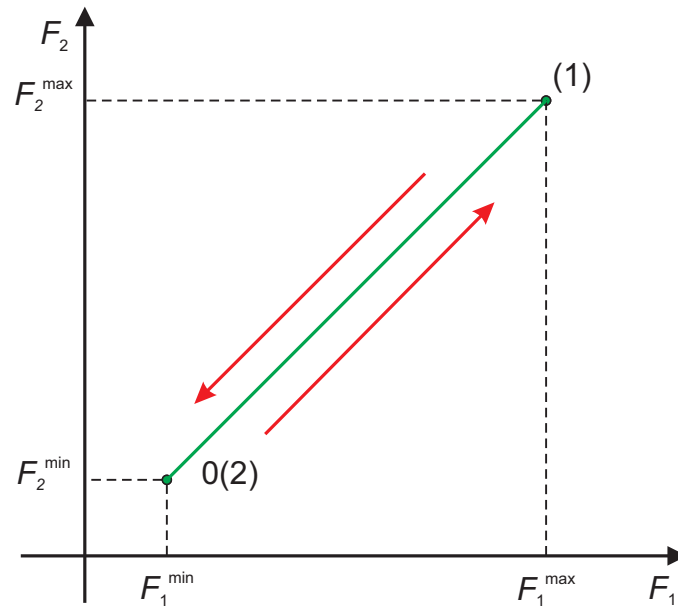
**Figure 4.4:** The two prepared sides of the cross-shaped specimen for two-scale observations. (a) Artificial texture for macro- and (b) polished surface for mesoscale observations

## 2.4 Applied loading histories

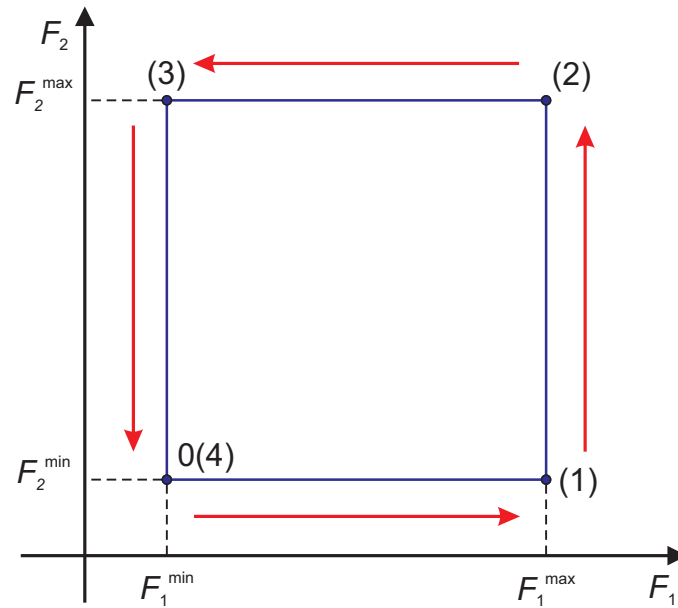
Multiaxial experiments (*e.g.*, in-plane biaxial tests) allow for a wide range of loading paths, without any protocol change (especially no specimen geometry modification), which is an important parameter in the case of a fatigue test campaign (see CHAP. 5). In this investigation two different histories are considered, namely, equibiaxial and “snail” loading paths.

The equibiaxial loading history (FIG. 4.5(a)) corresponds to a proportional in-plane biaxial loading where both perpendicular axes are loaded and unloaded at the same level. The “snail” regime (FIG. 4.5(b)) first (un)loads the specimen in the 1-direction while the (un)loading in the 2-direction is constant. In the next (un)loading step the specimen is (un)loaded in direction 2 while the load is constant in direction 1. Both loading paths were cycled with increasing maximum force (*i.e.*,  $F^{\max}$ ) in loading part while the minimum (*i.e.*,  $F^{\min}$ ) was constant.

Before conducting in-plane biaxial experiments an FE analysis is performed to determine the increase of peak forces for each cycle. Considering the two planes of symmetry, a quarter of the cross-shaped sample is used for the FE model (FIG. 4.6). A Johnson-Cook isotropic hardening model is chosen with the elastoplastic parameters obtained from the monotonic uniaxial experiment (TAB. 3.2 and TAB. 3.3). The results obtained with the FE analysis showed that plastic strains occurs when the applied load is greater than 30 kN.



(a) Equibiaxial loading path



(b) "Snail" loading path

**Figure 4.5:** One cycle for (a) equibiaxial and (b) "snail" loading histories. Equibiaxial loading consists of two (*i.e.*, (1)-(2)) characteristic points while "snail" history has four (*i.e.*, (1)-(2)-(3)-(4))

For both loading histories, the first 3 steps of loading and unloading were chosen with an increment of 10 kN, and then the increment was set to 7.5 kN.

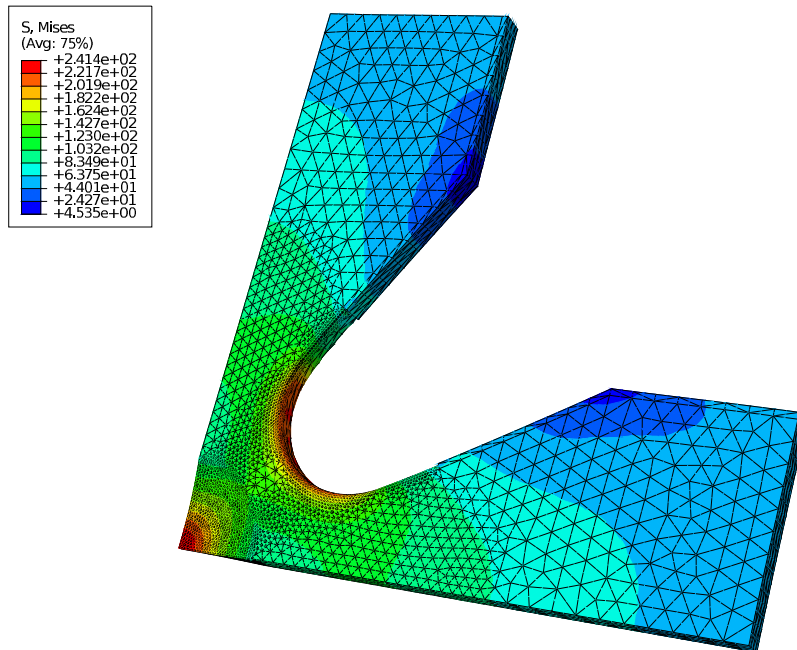


**Figure 4.6:** FE model used to estimate the (un)loading path of equibiaxial and “snail” regimes

The cyclic biaxial experiments were performed in a load control mode with a loading rate of 0.5 kN/s. To successfully associate each image to a point in the loading sequence both CCD cameras are triggered by the load controller. FIG. 4.7 shows the applied equibiaxial loading path with the corresponding image number. Images were captured for each (un)loading increment of 1 kN (*i.e.*, the acquisition rate equals 0.5 frames/s). During the seven loading/unloading sequences 594 images were shot. The specimen broke for a load level of 59 kN (FIG. 4.7).

Two experiments with the “snail” path are carried out with different boundary conditions. First, the “snail” experiment (FIG. 4.8(a)) was fully load-controlled. The experiment was performed with the same parameters as previously mentioned for the equibiaxial loading regime. During the seven loading cycles 897 images were acquired, and the sample broke for a load level of 56 kN. The second “snail” experiment (FIG. 4.8(b)) used a hybrid loading history (*i.e.*, when specimen is (un)loaded in direction 1 with a force control, the displacement of direction 2 is constant). FIG. 4.8(b) shows a load relaxation for a constant displacement. From the measured load in both directions it is observed that the force in direction 2 (*i.e.*,  $F_2$ ) leads to a higher decrease of load. The applied load rate was the same as in the previous experiment, while the acquisition rate was 40 frames/cycle. The specimen broke at the eighth loading cycle at a level of 52 kN.

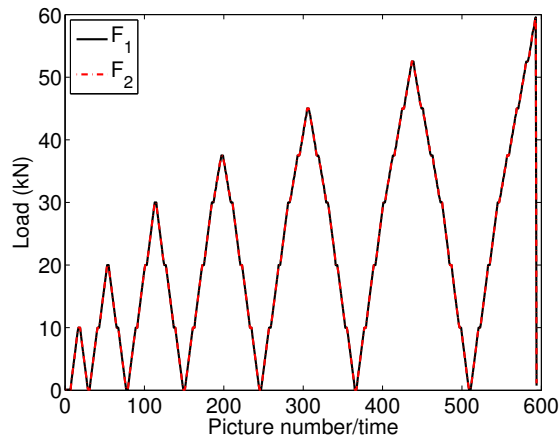


**Figure 4.7:** Equibiaxial loading regime. Applied load level with respect to number of pictures

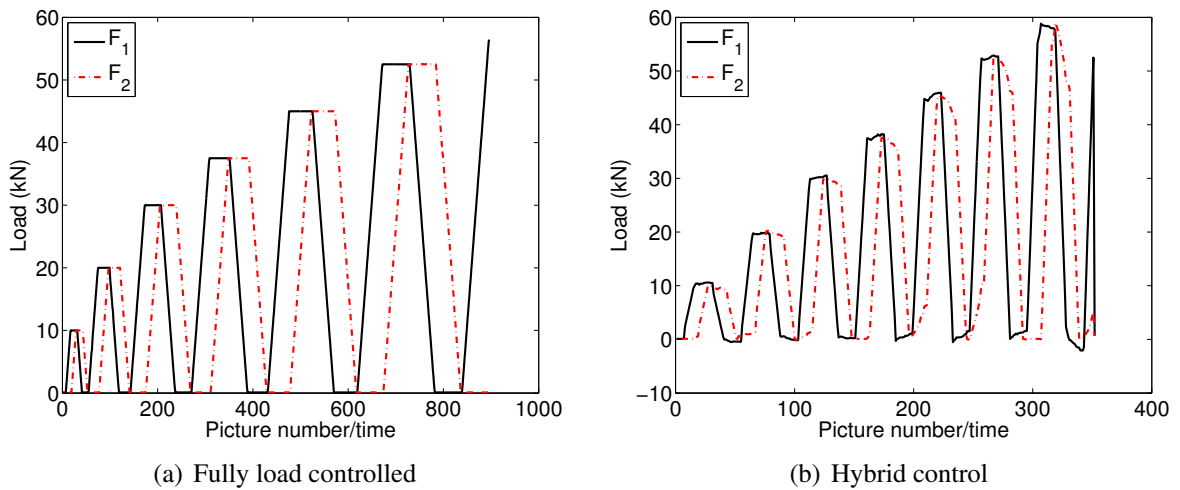


**Figure 4.8:** “Snail” loading paths. Applied load level with respect to number of images

### 3 Displacement resolution on macro- and mesoscales

In order to estimate the resolution of the measurement technique for the biaxial experiments, the parametric analysis of CHAP. 2 and CHAP. 3 is performed again. Images acquired at the macro- and mesoscales are considered. More emphasis is given on the standard displacement resolution of pictures using the natural texture of SG cast iron.

#### 3.1 Macroscale analysis

FIG. 4.9(a) shows the reference image captured at the macroscale. In order to correctly match the geometry and mesh used for identification purposes it was necessary to include free edges (Section 4.2). The image pair corresponds to two consecutive pictures shot when the sample was already mounted in the testing machine with  $F_1 = F_2 = 0$  (of the nine images taken without any load).

In the present case, the boundary of the ROI is adapted to the geometry of the sample (FIG. 4.9(b)). No special care was exercised to match the connecting radii to the straight parts. Consequently, the edge regularization discussed previously is still used. Had the geometry been fully matched with the external boundary, a traction-free condition could have been used instead. A T3 unstructured mesh is adopted, which consisted of 7,314 nodes with an element size of 10 pixels.

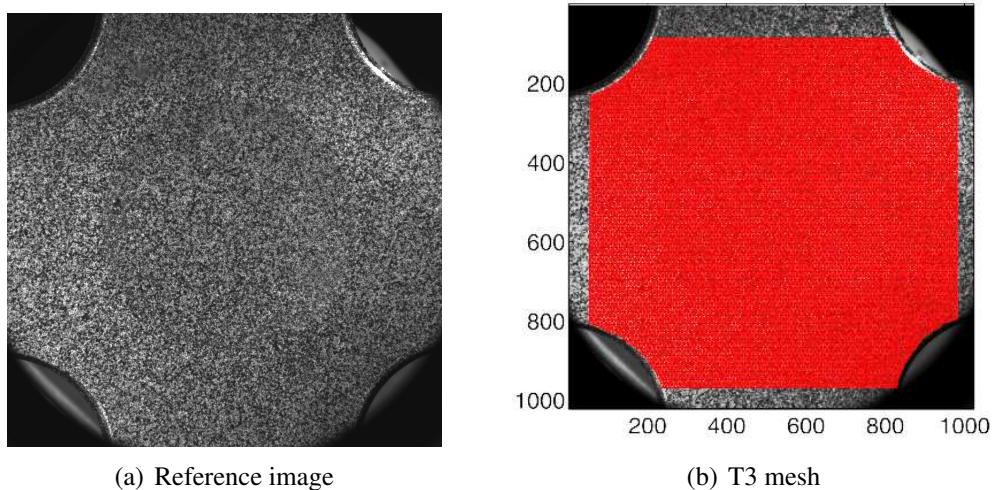


**Figure 4.9:** Reference image at the macroscale (a) and corresponding T3 unstructured mesh with an element size of 10 pixels (b)

The standard displacement resolution for the vertical (FIG. 4.10(a)) and horizontal (FIG. 4.10(b)) directions is obtained. Slightly lower errors are noted in the horizontal direction. Higher initial regularization lengths yield lower displacement resolutions but the difference is negligible for all analyses in the end of the relaxation process.



FIG. 4.11(a) shows the dimensionless correlation residuals for different initial regularization lengths with the same type of computations as before ( $\ell_b/\ell_m = 1/2$ ). Their level remains almost constant for any value of the correlation length and very low. This result indicates that all the evaluations are close. However, as expected, the equilibrium residuals (FIG. 4.11(b)) are the smallest for large initial regularization lengths. For small initial regularization lengths, the equilibrium residuals are less than those observed in the previous case. This result allows us to fully relax the regularization length (*i.e.*,  $\ell_m = 1$  pixel) and even start with a modest one (*e.g.*,  $\ell_m = 64$  or 32 pixels). This is made possible thanks to the texture quality that is better than that at the mesoscale.

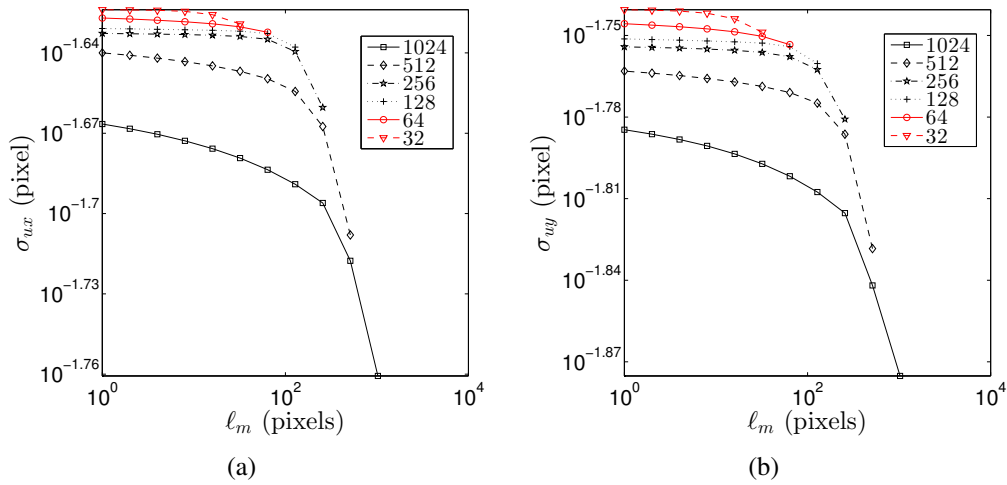


**Figure 4.10:** Change of the standard displacement resolutions for different regularization lengths  $\ell_m$  and different initialization lengths (in pixels) indicated in the legend. (a) Displacement resolution in vertical and (b) in horizontal directions

## 3.2 Mesoscale analysis

The second part of this section is dealing with the correlation using the (poor) natural texture of SG cast iron (FIG. 4.12(a)). Local DIC was applied to measure displacement fields [Sjögren et al., 2011] but without estimating the resolution of the measurement technique. Without knowing the latter the accuracy of the displacement/strain fields cannot be quantified. Two different cases are considered when analysing the natural texture. First, artificially prescribed displacement fields will be correlated and compared with the results obtained in CHAP. 2 (Section 4). The second case is dealing with the parametric analysis as for the macroscale analysis with two images acquired in the unloaded state.

### 3.2.1 Artificially prescribed displacement field

The first analysis on the natural texture aims to evaluate the quality of measured fields when the solution is known. Hence, the picture of FIG. 4.12(a) is artificially deformed. A

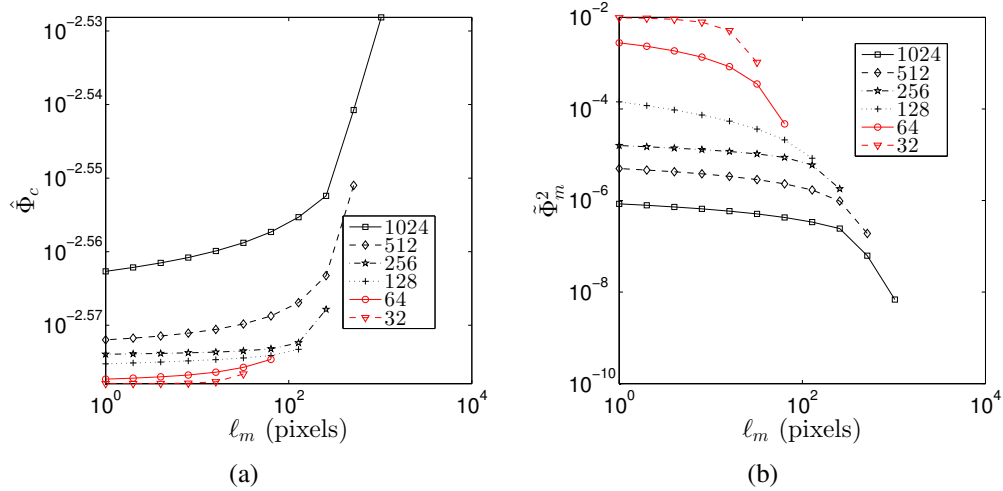
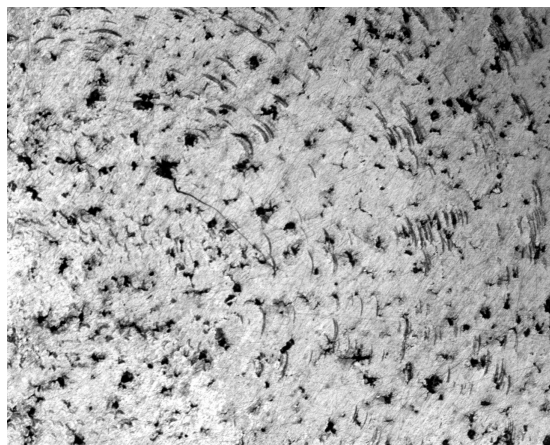
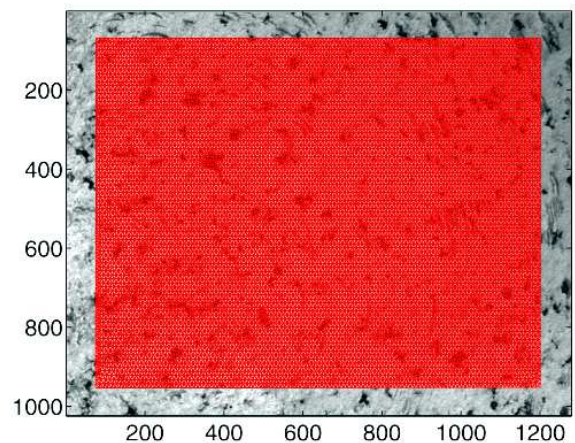


**Figure 4.11:** Change of (a) the dimensionless correlation residuals and (b) equilibrium residuals for different regularization lengths and different initializations. Note the narrow range of variation of  $\hat{\Phi}_c$



(a) Reference image



(b) T3 mesh

**Figure 4.12:** Reference image of the mesoscale resolution analysis (a) and corresponding T3 unstructured mesh with an element size of 10 pixels

sine wave is considered (see CHAP. 2). A linear interpolation of the grey levels is used to generate the picture in the deformed configuration. The parametric analysis is performed via RT3-DIC for different initial regularization lengths  $\ell_m$  and the relaxation process for which in every new initialized computation  $\ell_m$  was divided by 2. Even though the texture is poor 10-pixel elements are chosen since regularization is considered.

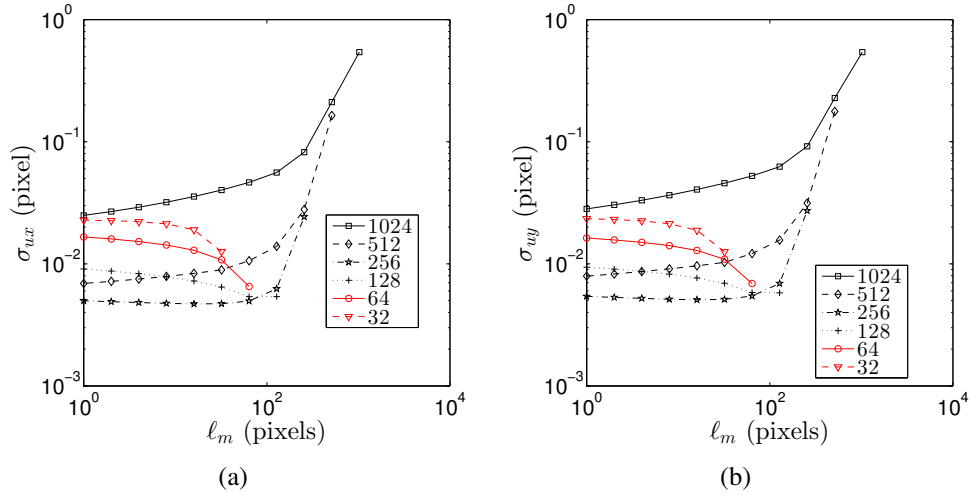
FIG. 4.13 shows the standard displacement error comparing the prescribed (*i.e.*, known) and measured displacement fields. It can be noted that higher regularization lengths ( $1024 < \ell_m < 256$  pixels) yield higher displacement errors since small displacement fluctuations are smeared out. The lowest standard displacement error is recorded when a regularization length of 128 pixels is considered while for smaller  $\ell_m$  lengths (*i.e.*, 32 and 64 pixels) the error is higher (but still not as high as for  $1024 < \ell_m < 256$  pixels). In the end of the relaxation process the computations with initial regularization lengths of 1024, 64 and 32 pixels yield approximately the same standard displacement error. When comparing these results with the analysis performed on an artificial texture (FIG. 2.9) and a prescribed displacement field the same trend is observed for the error changes during the relaxation process although different values at the end.

The change of dimensionless correlation residuals  $\hat{\Phi}_c$  (FIG. 4.14(a)) leads to higher values for  $\ell_m = 1024$  and 512 pixels. For the other regularization lengths the correlation residuals reach similar levels (*i.e.*, the results are trustworthy). This property is even noted during the relaxation process. When compared to the artificial texture (FIG. 2.11(a)) higher lengths  $\ell_m$  do not affect the residuals as strongly, which leads to the conclusion that it is necessary to put more effort to successfully perform RT3-DIC on poor textures. For larger regularization lengths, the measured field displays less equilibrium gap. This is explained by the increase of its weight in the total functional. The most favorable zone in the present case lies in the range of initial values ( $256 < \ell_m < 512$  pixels) for which the equilibrium gap is independent of the initial value of  $\ell_m$ .

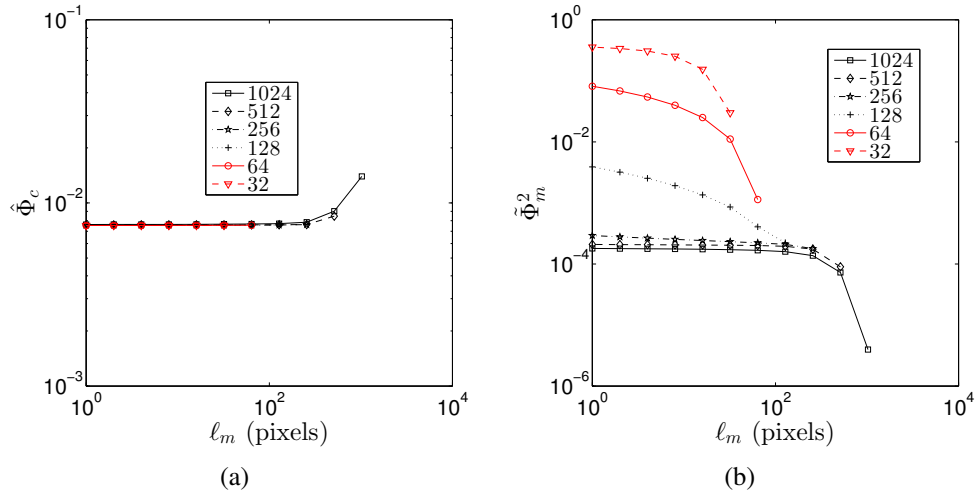
### 3.2.2 Parametric analysis on natural texture

FIG. 4.15 shows the standard displacement resolution for the two displacement components of displacement. The larger the regularization length, the smaller the displacement resolution. It is worth noting that any value less than one centipixel is very seldom encountered. This is even more noteworthy that the texture of the pictures is very difficult to analyze. To get all the results reported in FIG. 4.15 (requiring 51 simulations), less than one hour of CPU time was needed on an Intel Xeon X5660 processor. The mesh consisted of 8,749 nodes, and therefore involved 17,498 kinematic unknowns.

To compare the present results with more standard approaches, a local and global Q4-DIC analysis is run. It is based on 4-noded ZOIs for the local approach, and 4-noded elements in a global approach. In both cases a bilinear displacement interpolation is considered. The implementation details of both approaches follow very closely those used herein [Hild and Roux, 2012] *except* that no regularization length is used. The right envelope of the regularized results virtually coincides with those of the global Q4-DIC analysis (FIG. 4.15). The global analysis, as expected when the same ZOI and element size is con-



**Figure 4.13:** Standard displacement errors in (a) the vertical and (b) horizontal directions for different regularization lengths  $l_m$  when  $l_b/l_m = 1/2$ . The legend indicates the initial regularization length  $l_m$  (in pixels)



**Figure 4.14:** Change of (a) the dimensionless correlation residuals and (b) equilibrium residuals for different regularization lengths and different initializations. Note the narrow range of variation of  $\hat{\Phi}_c$

sidered, out-performs the local analysis [Hild and Roux, 2012]. With this difficult texture, there is a clear gain to consider global vs. local approaches. The regularization proposed herein induces a very significant additional gain as all the non-mechanical fluctuations are filtered out. Last, the relaxation process of the regularization length leads to very significant reductions of the displacement fluctuations.

FIG. 4.16(a) shows the dimensionless correlation residuals for different initial regularization lengths. Their level remains almost constant and very small for any value of the regularisation length. This result indicates that in the present case, it is impossible to discriminate any displacement from the analysis of the correlation residuals alone. However, the equilibrium residuals (FIG. 4.16(b)) vary very strongly with the regularization lengths. In this particular case, the gain provided by the mechanical regularization is big, namely, all the spurious fluctuations are filtered out.

If an estimate of the displacement field is sought with a very light mechanical regularisation, the procedure to follow is to run a first correlation with a very large regularisation length, say  $\ell_m = 1024$  pixels. At convergence, a second calculation is run with  $\ell_m = 512$  pixels by using an initial guess that is the displacement field at convergence with  $\ell_m = 1024$  pixels. If this path is followed, it can be stopped when  $\ell_m = 1$  pixel. The result given in FIG. 4.15 shows that the displacement resolution is very small and the equilibrium residual remains very small (FIG. 4.16(b)). Applications of the regularization strategy to real experimental cases showed that even poor image textures could be dealt with successfully.

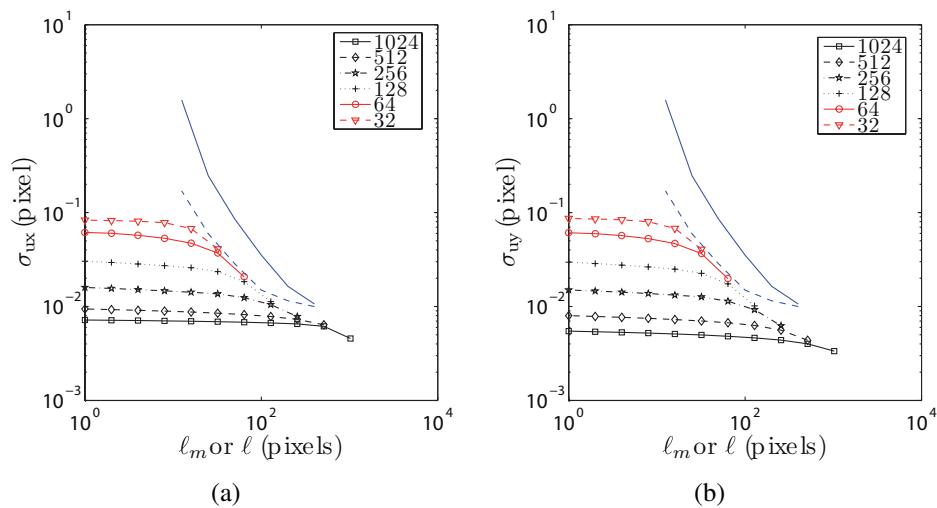


**Figure 4.15:** Standard displacement resolution in (a) the vertical and (b) horizontal directions for different regularization lengths  $\ell_m$ , ZOI (dashed blue line) or element (solid blue line) sizes  $\ell$  when  $\ell_b/\ell_m = 1/2$ . The legend indicates the initial length  $\ell_m$  (in pixels)

The following sections deal with strain components on the two scales and the identification of elastoplastic parameters. A regularization length of 32 pixels is chosen for

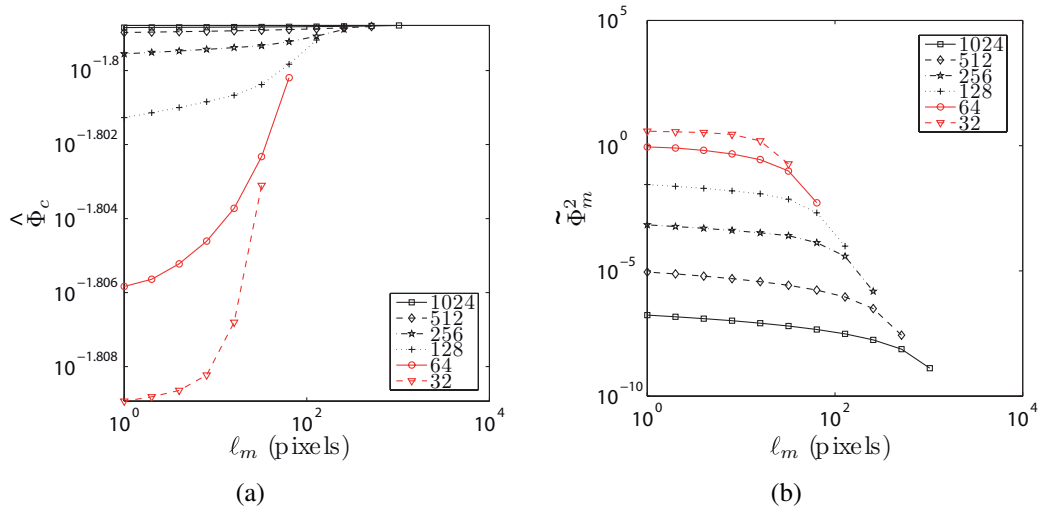


**Figure 4.16:** Change of (a) the dimensionless correlation residuals and (b) equilibrium residuals for different regularization lengths and different initializations. Note the narrow range of variation of  $\hat{\Phi}_c$

macroscopic measurements and  $\ell_m = 128$  pixels at the mesoscale due to the poor texture of the material. In both cases, the  $\ell_b/\ell_m$  ratio is chosen to be 1/2.

## 4 Equibiaxial loading history

The experiments carried out on the multiaxial servo-hydraulic machine in the equibiaxial loading regime (FIG. 4.7) are considered in this section. The latter consists of two parts. The aim is first to extract the strain components from the displacement fields measured on the two sides of the cross-shaped specimen. Second, the identification of elastoplastic parameters will be carried out on the images acquired at the macroscale. Using FEMU the elasto-plastic parameters will be determined for Johnson-Cook and Armstrong-Frederick's laws.

### 4.1 Two scale strain analysis

RT3-DIC is applied to measure the displacement and strain fields on two scales (*i.e.*, macro, see FIG. 4.17 and meso, see FIG. 4.18). The commented image pairs correspond to the reference configuration when  $F_1 = F_2 = 0$ , and a deformed configuration for which  $F_1 = F_2 = 30$  kN. When this load level is reached yielding of the material starts to occur.

From the measured displacement fields at the macroscale in the horizontal (FIG. 4.17(a)) and vertical (FIG. 4.17(b)) directions it can be noted that in center of the specimen the lowest displacements occur [Poncelet et al., 2010, Decreuse et al., 2012]

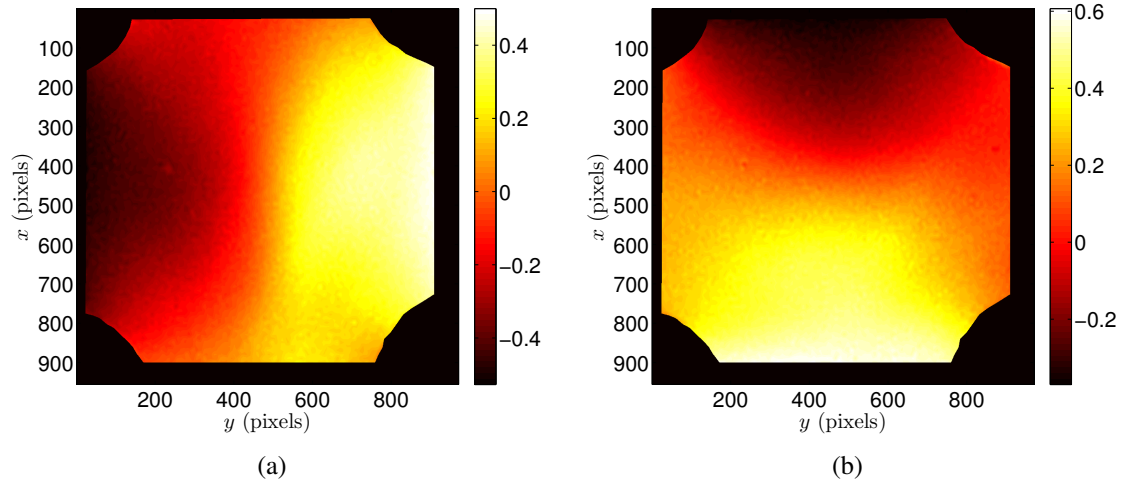


**Figure 4.17:** Measured displacement fields at the macroscale in the horizontal (a) and vertical (b) directions for a load level equal to 30 kN. The displacements are expressed in pixels. The physical size of one pixels is equal to  $48 \mu\text{m}$

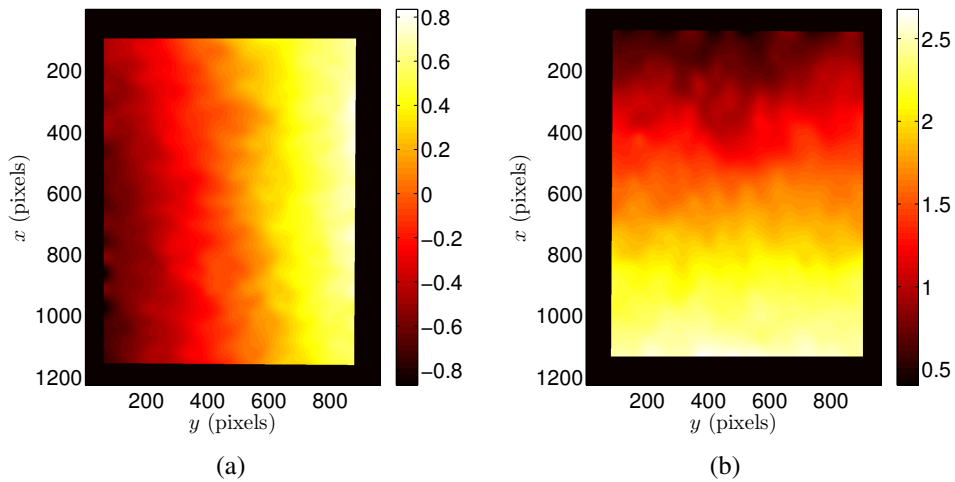


**Figure 4.18:** Measured displacement fields at the mesoscale in the horizontal (a) and vertical (b) directions for a load level corresponding to 30 kN. The displacements are expressed in pixels. The physical size of one pixels is equal to  $6.7 \mu\text{m}$

while getting closer to the boundary they increase (the highest displacements are observed on the boundary of the ROI). The same trends occur on the opposite side of the sample (*i.e.*, at the mesoscale). The motionless point is close to the centre of the sample.

Even though the geometry of the specimen is complex, the mean strain is evaluated in the central zone. Moreover one of the goal of the present study is to detect crack initiation. Hence, DIC gauges (of same physical size) are applied on macro- (FIG. 4.19(a)) and meso- (FIG. 4.19(b)) scales. From the 594 acquired images the change of the mean strain is obtained for the chosen areas.

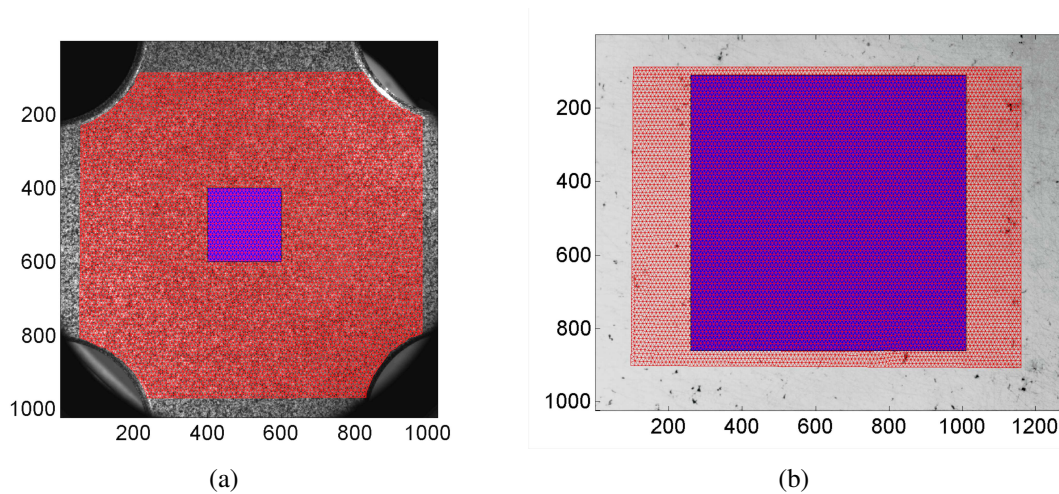


**Figure 4.19:** DIC gauges at the two scales. (a) Macroscale and (b) mesoscale DIC gauges depicted as square (blue) zones over the T3 unstructured mesh with 10 pixel elements (red)

The measured strain components  $\epsilon_{11}$  and  $\epsilon_{22}$  correspond to the normal levels in the loading directions (FIG. 4.20). Even though the strains are measured on two different sides a very good agreement between the two scales is observed. However, for the last two cycles a bigger gap is detected between the two sides. The difference between macro- and mesoscale data is due to the formation of a crack network that is more visible at the mesoscale (FIG. 4.22). Low levels of  $\epsilon_{12}$  strains are shown in FIG. 4.20(c). At the macroscale it is virtually constant while on the mesoscale bigger fluctuations are detected after picture no. 300 due to microcrack formation and detection.

From FIG. 4.20(a) and FIG. 4.20(b) it is concluded that the strain components  $\epsilon_{11}$  and  $\epsilon_{22}$  follow the same trend, which corresponds to an equibiaxial loading. Similarly, the eigen strains for the macroscale shown in FIG. 4.21 coincide until the very end of the test. This results explains why small fluctuations of  $\epsilon_{12}$  occur. In terms of eigen strain component  $\epsilon_1$  and  $\epsilon_2$ , the experiment was fully proportional until cracks developed as opposed to the non-proportional loading regime of the snail test (see Section 5).

FIG. 4.21(b) shows the relationship between the mean eigen strains. From the latter plot it is concluded that an isotropic material response applies until the microcracks start to



grow. In comparison with uniaxial experiments where the maximum elongation was 4.5% it is lower for an equibiaxial loading regime (*i.e.*, 2.3%). However it is worth remembering that the strain field is not uniform over an area where thickness changes (*i.e.*, thinned center part of the cross-shaped sample).

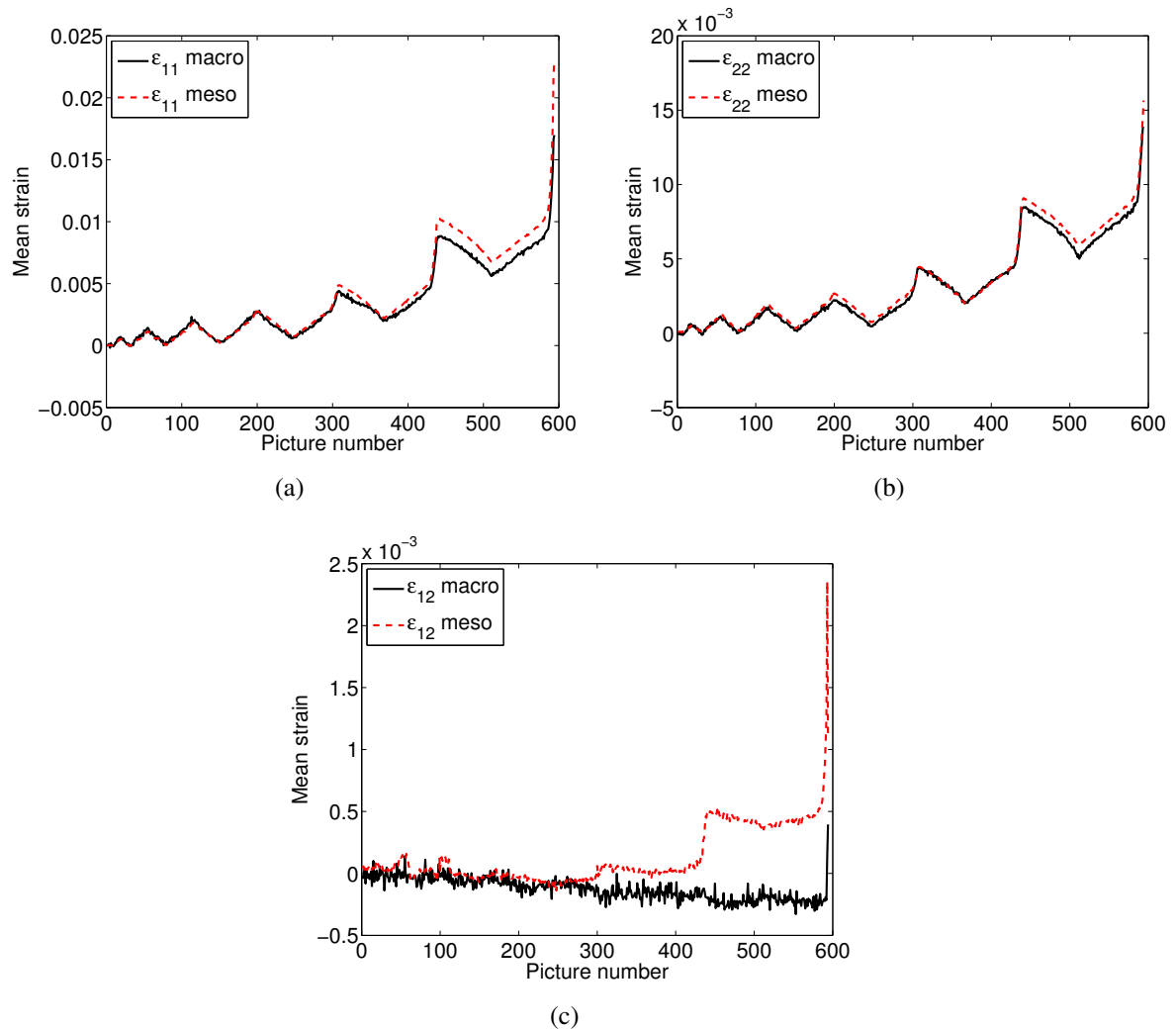


**Figure 4.20:** Change of (a)  $\varepsilon_{11}$ , (b)  $\varepsilon_{22}$ , (c)  $\varepsilon_{12}$  during the equibiaxial test on macro- and mesoscales

## 4.2 Implementation of 3D FEMU procedure using 2D-DIC measurements

The central part of the cross-shaped sample is observed during biaxial loading. The highest stress levels occur in its thinned gauge zone (calotte). Since the sample has a complex geometry it is necessary to resort to a 3D FE model even though 2D-DIC measure-

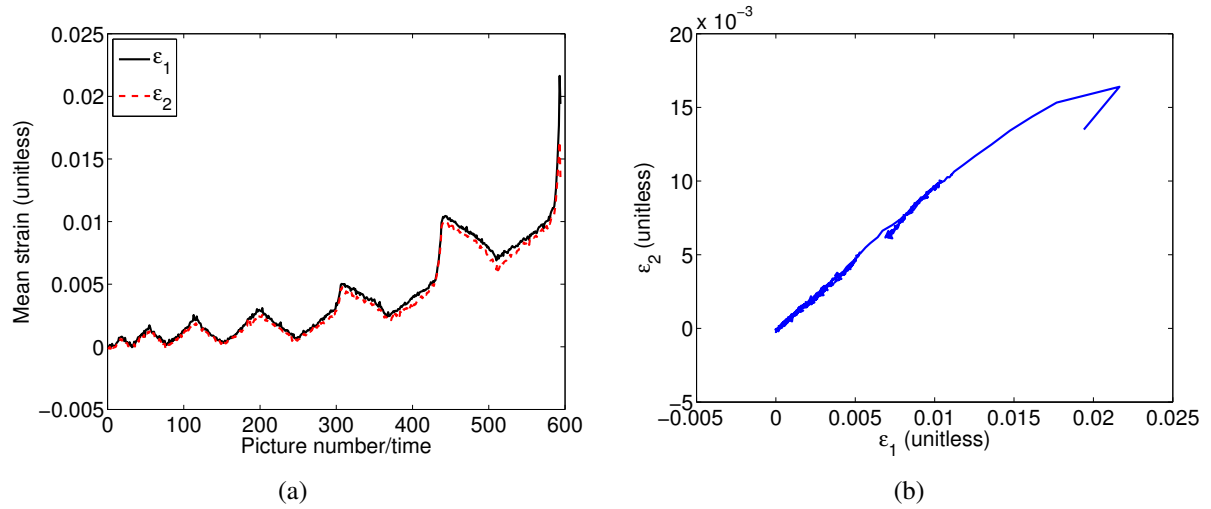


**Figure 4.21:** (a) Change of mean eigen strain components on the macroscale with time. (b) Dependence of mean eigen strains (*i.e.*,  $\varepsilon_1$  vs.  $\varepsilon_2$ )

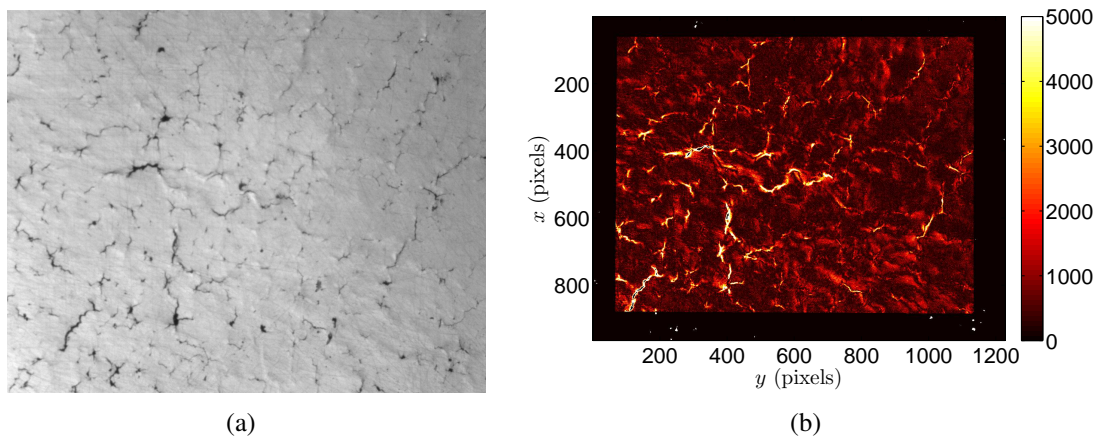


**Figure 4.22:** (a) Image at mesoscale corresponding to a load level of 55 kN, (b) correlation residuals (expressed in gray levels) revealing the crack network

ments are available. First, the 3D mesh is designed in the commercial FE code Abaqus (FIG. 4.23(a)). From the model surface (FIG. 4.23(b)) the nodes were extracted into a set that defines the 2D mesh that is imported in the RT3-DIC code. The 2D mesh is adjusted and scaled (FIG. 4.23(d)) to the macroscopic scale on the reference image of the tested sample.

The RT3-DIC code provides the measured displacement fields. The in-plane nodal displacements on the boundary of the T3 mesh (FIG. 4.23(d)) are extracted and prescribed to the 3D FE model (FIG. 4.23(e)). The same displacements are prescribed through the thickness along the edges (FIG. 4.23(f-c)). Since the radii of the cross-shaped specimen are traction-free during the test they were treated as such and displacements were not prescribed in that region. To save for computation time only one symmetry was applied with respect to the surface normal (FIG. 4.23(f)).

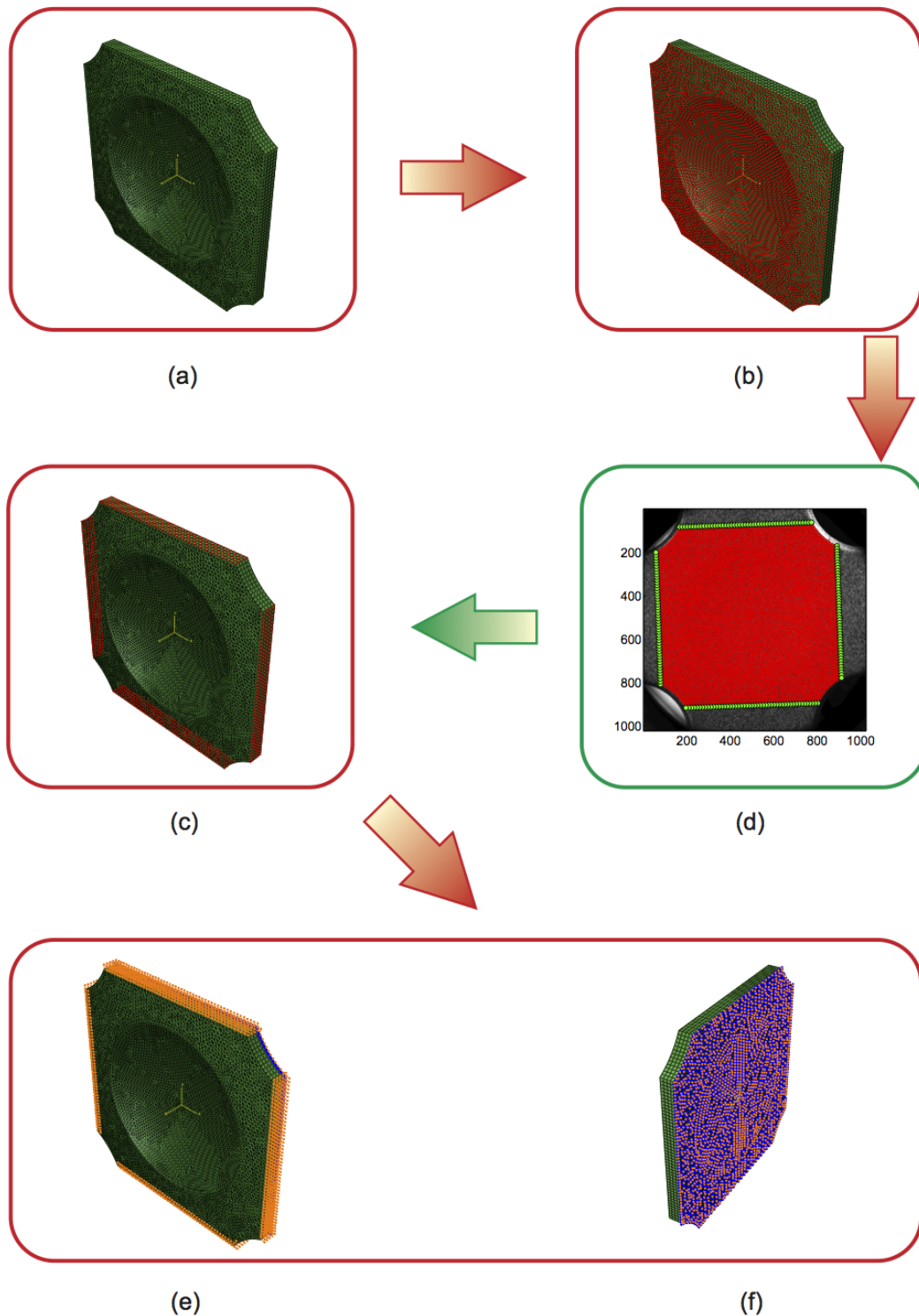
For each iteration of the FEMU procedure the displacements of the surface nodes are extracted and compared with measured ones in the  $\chi_u$  residual. The sum of reaction forces is obtained from the boundary nodes in the simulations. Reaction forces along both directions are gathered in one column vector. Differences of the measured and calculated force vector is assessed in  $\chi_F$ . The initial parameters are taken from the identification results of uniaxial experiments. Hence, the identified elastoplastic parameters of the two loading histories will be compared.

### 4.3 Identification of elastic parameters

The identification of elastic parameters is carried out on the first two and a half cycles, which corresponds to 104 pictures. The parameters used for the FE simulation in order to determine loading levels of the biaxial experiments differ from the parameters identified via uniaxial tests (TAB. 3.3). Hence, the chosen maximum load level considered in the analysis of elastic parameters is equal to 20 kN. Before performing the identification over the whole series of images in the elastic region the measurement uncertainty is evaluated (see Equations (3.2) and (3.3)). Nine pictures were shot at the beginning of experiment when the specimen was mounted and the load was constant (*i.e.*,  $F_1 = F_2 = 0$ ). The standard displacement resolution is 0.02 pixel and the load resolution equals 3.9 N.

Poisson's ratio and Young's modulus are identified via the FEMU-UF procedure. The initial values are chosen from the uniaxial experiment analysed previously (TAB. 4.1). The identified values lead to a decrease of  $\chi_u$  and  $\chi_F$ . Low displacement residuals between the measured and calculated displacement fields are reported even though a 3D model is run with displacements measured with 2D-DIC. Conversely, the load residual remains significantly higher than the resolution of the load cell. Since a small part of the boundary of the FE model has traction-free edges, initial and identified values of the functional  $\chi_u$  are close to the standard resolution. This does not allow for successfully identifying Poisson's ratio (TAB. 4.1). Another reason is related to the results of FIG. 4.21(b), which shows that the experiment is purely equibiaxial in the considered part of the test.

The second parameter identified with this procedure (*i.e.*, Young's modulus) yields a small decrease of  $\chi_F$  of 300 N (TAB. 4.1)) for the identified value (156 GPa). FIG. 4.24

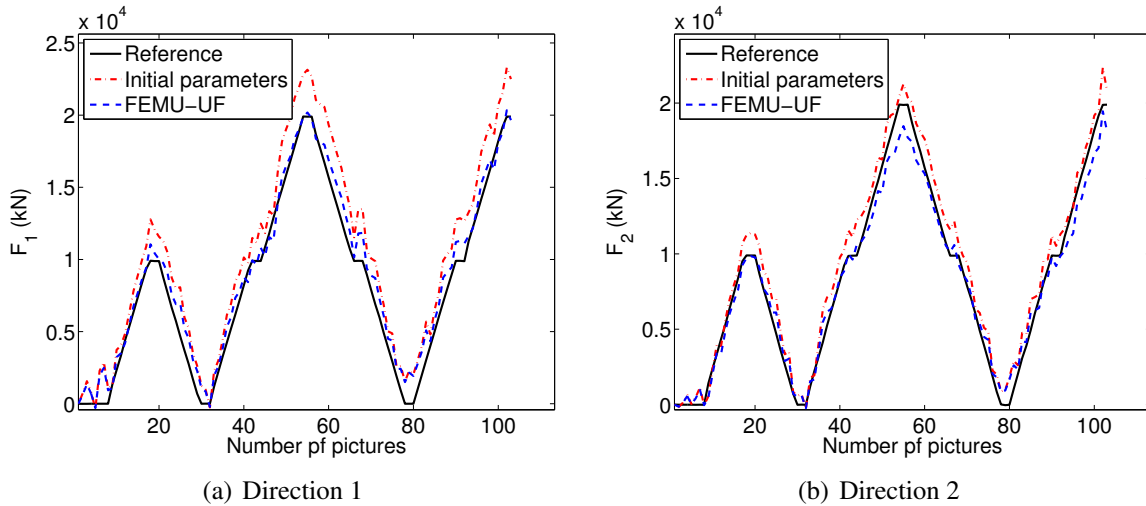


**Figure 4.23:** Implementation of boundary conditions obtained from 2D-DIC measurement onto the 3D FE model. (a) 3D FE model created in Abaqus, (b) nodes (red circles) extracted from the 3D model to create a 2D mesh for RT3-DIC, (c) model nodes (red circles) used to prescribe the measured displacements from DIC analyses, (d) T3 mesh fitted and scaled onto the reference image, (e) DIC displacements prescribed as boundary conditions of the FE model, (f) symmetry boundary condition

**Table 4.1:** Initial and identified elastic material parameter for equibiaxial experiment

Parameter	E (GPa)	$\nu$	$\chi_u$ (pixel)	$\chi_F$ (kN)
Reference	159	0.28	0.025	1.24
FEMU-UF	156	0.09	0.023	0.96

shows the comparison of initial and identified load levels in the two loading directions with respect to the measured ones. Significant load fluctuations are noted at the beginning of the experiment (nine images where shot when the specimen was mounted and the applied load was  $F_1 = F_2 = 0$  N). They are due to measurement uncertainties and modeling errors. Further, at the end of unloading of the second cycle the load level does not reach 0 kN. These phenomena contribute to higher levels of the force residual  $\chi_F$ .

**Figure 4.24:** Comparison of measured force and sum of reaction forces computed with initial and identified elastic parameters

#### 4.4 Identification of parameters describing isotropic and kinematic hardening

The first part of the identification of nonlinear material parameters will deal with isotropic hardening. In a second step kinematic hardening will be considered. The identification will be carried out with all images acquired during the equibiaxial experiment (*i.e.*, 594 pictures). The goal is to compare the identified parameters from the biaxial experiments with those determined from uniaxial tests (CHAP. 3). Hence, the identified parameters on uniaxial tests are introduced as initial estimates.

#### 4.4.1 Johnson-Cook's law

Three material parameters (*i.e.*,  $\sigma_y$ ,  $K$  and  $n$ ) describing Johnson-Cook's model are identified in one FEMU-UF identification procedure. The initial parameters are listed in TAB. 4.2. They correspond to the identified parameters from a uniaxial tensile test. When the latter ones are introduced in the first iteration of the identification procedure the displacement residuals are equal to 0.06 pixel, while the force residual is equal to 4.7 kN. The equilibrium gap  $\chi_F$  indicates how uniaxial material parameters are not suitable to describe the equibiaxial loading path (see FIG. 4.25).

The three identified values yield a decrease of the displacement residuals by 30% and by 40% for the force residuals (TAB. 4.2). Observing the load levels in both directions (FIG. 4.25) the identified equibiaxial loading history corresponds better to the measured one. The unloading level of the last cycle does not describe properly the applied loading level. From this result, it can be concluded that kinematic hardening or damage phenomena in combination with already reported modelling errors cause higher force residuals (*i.e.*,  $\chi_F = 2.8$  kN).

**Table 4.2:** Initial and identified Johnson-Cook parameters by FEMU-UF for an equibiaxial loading path

Parameter	$E$ (GPa)	$\nu$	$\sigma_Y$ (MPa)	$K$ (MPa)	$n$	$\chi_u$ (pixel)	$\chi_F$ (kN)
Reference	156	0.28	228	850	0.38	0.06	4.7
FEMU-UF	156	0.28	218	1591	0.44	0.04	2.8

It is also necessary to emphasize that the identified load levels are better captured in the loading parts of the equibiaxial path. Similar trends were reported for the cyclic uniaxial test (CHAP. 3). The identified values of the latter experiment (see TAB. 3.6) correspond closely to the parameters identified from the equibiaxial loading regime. It is concluded that Johnson-Cook's parameters identified on the uniaxial cyclic experiment are validated for a proportional biaxial loading regime.

#### 4.4.2 Armstrong-Frederick's law

In the analysis of the elastoplastic behaviour of cast iron under cyclic uniaxial loading history (CHAP. 3) it was noted that kinematic hardening better described the cyclic response than isotropic hardening. For the same experimental data the identified parameters of Armstrong-Frederick's law yielded lower force residuals when compared with Johnson-Cook's model. The same trend is reported for the equibiaxial loading regime (see TAB. 4.3). When observing the load residual  $\chi_F$  for the two models (TAB. 4.2 and TAB. 4.3) Armstrong-Frederick's results lead to a 1 kN decrease, so that the final level is only two times that obtained in elasticity.

As in the previous case (*i.e.*, identification of isotropic hardening parameters) the initial values of the sought parameters were taken from uniaxial data (TAB. 3.4). The iden-

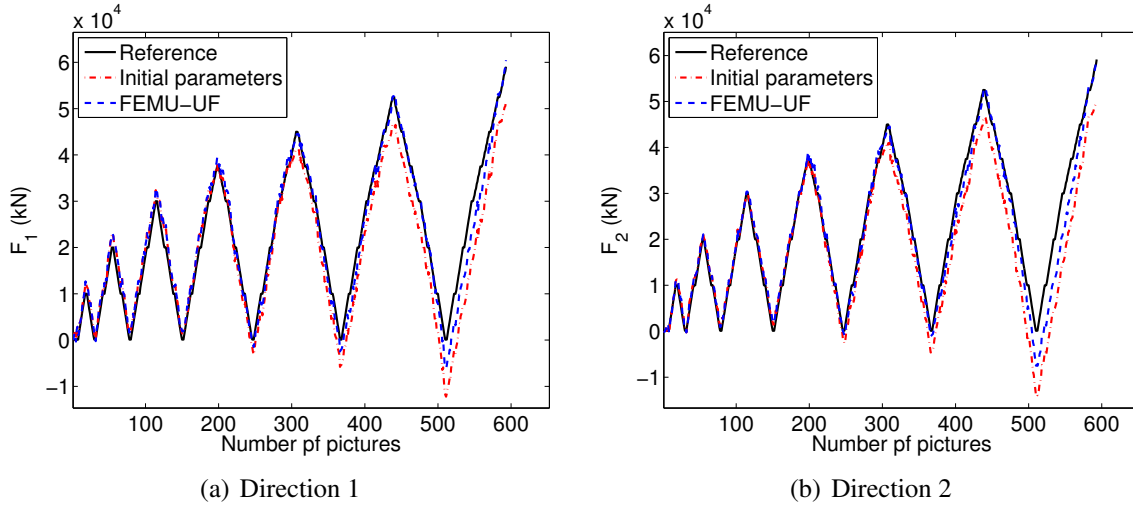


**Figure 4.25:** Comparison of measured force and sum of reaction forces computed with initial and identified material parameters for Johnson-Cook's constitutive law

**Table 4.3:** Initial and identified Armstrong-Frederick's parameters via FEMU-UF for an equibiaxial loading path

Parameter	$E$ (GPa)	$\nu$	$\sigma_Y$ (MPa)	$C$ (GPa)	$\gamma$	$\chi_u$ (pixel)	$\chi_F$ (kN)
Reference	158	0.28	289	10	46	0.06	4.50
FEMU-UF	158	0.28	259	23	18	0.04	1.95

tified parameters are shown in TAB. 4.3. A slight decrease by 30 MPa of yield stress is noted. The identified hardening modulus  $C$  increases by 50 % while  $\gamma$  decreases by 60 %. As mentioned previously the identified parameters decrease significantly the force residuals while  $\chi_u$  decreases by 40%. The displacement residuals are about twice the level observed in the elastic identification step.

FIG. 4.26 shows the change of the calculated sum of reaction forces in the two loading direction when the initial and identified parameters are considered. They are compared with the measured load corresponding to each acquired picture. When using Armstrong-Frederick's law the unloading parts of the history is better captured than Johnson-Cook's law. When comparing parameters describing kinematic hardening determined from equibiaxial and uniaxial experiments, differences are noted. This leads us to conclude that uniaxial tests do not necessarily provide kinematic hardening parameters to describe credibly more complex loading regimes.

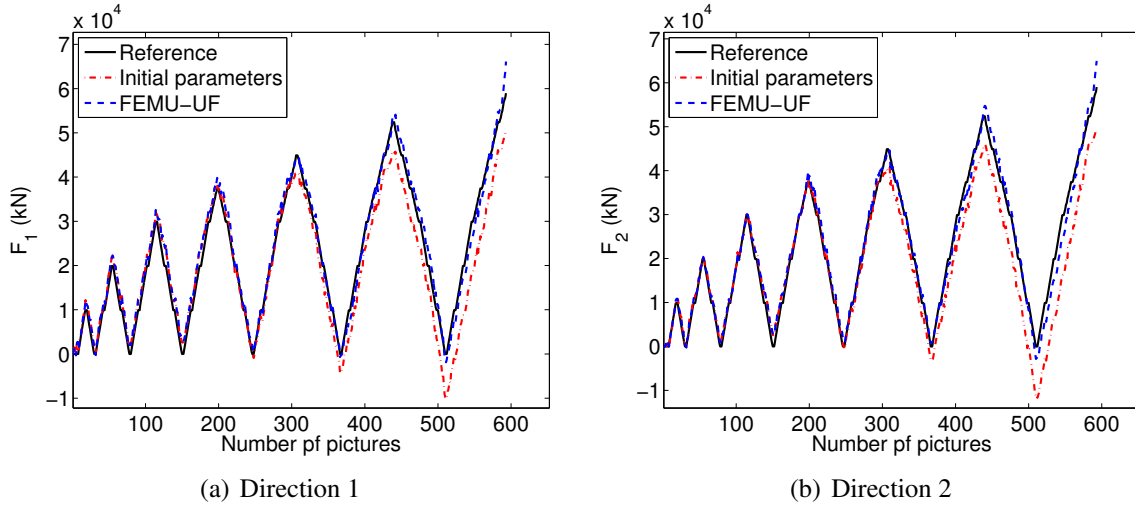


**Figure 4.26:** Comparison of measured force and sum of reaction forces computed with initial and identified parameters for Armstrong-Frederick's constitutive law

## 5 “Snail” loading history

In this section a non-proportional loading regime (*i.e.*, “snail”) is analysed. In the first part results obtained from the two scale pictures are reported. The measured strains in the gauge zones of the cross-shaped sample will be studied and compared with data obtained from the equibiaxial experiment. The goal of the second part is the identification/validation of elasto-plastic laws via the FEMU-UF procedure. Since a more complex loading history is analysed hereafter it is expected that the determined parameters will differ from the previous ones (Section 4 and CHAP. 3). The identification will be carried out on two different “snail” loading histories (see FIG. 4.8(a) and FIG. 4.8(b)).

### 5.1 Two-scale measurements

Displacement fields for the macro- and mesoscales were analysed with RT3-DIC. The regularization lengths applied on the macroscale images is equal to 32 pixels while  $\ell_m = 128$  pixels at the mesoscale. The whole series of images (*i.e.*, 897 pictures) on both scales is considered in order to reveal the strain history with respect to the applied load level from the two sample sides. FIG. 4.27 and FIG. 4.28 show the macro and mesoscale displacement fields in the horizontal and vertical directions for first three loading steps. The maximum applied load for the last cycle corresponds to 30 kN. The specimen was first loaded in the horizontal direction. The measured displacement fields for the first loading step (*i.e.*,  $F_1 = 30$  kN and  $F_2 = 0$  kN) show that the specimen is loaded in tension in the horizontal direction (macro scale - FIG. 4.27(a) and (b), meso scale - FIG. 4.28(a) and (b)) while in the vertical direction compression is noted even though the load is not prescribed. This fact corresponds to Poisson's ratio effect that causes contractions in the



unloaded direction (*i.e.*, vertical).

For the second loading level (*i.e.*,  $F_1 = 30$  kN and  $F_2 = 0.30$  kN) we can note that both directions (macro scale - FIG. 4.27(c) and (d) and meso scale - FIG. 4.28(c) and (d)) are loaded in tension. The range of displacement fluctuations in the two directions is not the same (see FIG. 4.27(d) and FIG. 4.28(d)). This can be explained by the fact that the vertical direction first undergoes contraction ( $F_2 = 0$  kN), and in the second loading step it accumulates less displacement since the starting point of the latter step was negative.

FIG. 5.16(a) illustrates the change of strain components in the loading direction for the first loading cycle of a fatigue test where maximum applied load level was equal to 50 kN. At the end of the second step  $\epsilon_{22}$  reaches levels lower than  $\epsilon_{11}$ . Displacement fields in the the third loading step of the “snail” test (macro scale - FIG. 4.27(e) and (f) and meso scale - FIG. 4.28(e) and (f)) detect tension in the vertical direction while in the horizontal direction contraction is observed.

Results obtained for hybrid “snail” biaxial loading are similar to those determined for a fully load-controlled biaxial experiment. They are reported in Appendix E.

Meso scale displacement fields (FIG. 4.28) show the same material response as the macroscale results. It can be noted that the centre of the specimen is moving due to the control protocol of the experiment. To satisfy the boundary condition (*i.e.*, load difference between two opposite actuators in the horizontal or vertical axis is 0 kN) prescribed in the test rigid body motions occur. The latter are better captured at the mesoscale since a smaller area is observed.

The same DIC strain gauges are considered (see FIG. 4.19). FIG. 4.29 shows the strain history along the two loading axes. In the present case  $\epsilon_{11}$  and  $\epsilon_{22}$  follow completely different paths. When comparing the data obtained on the two sides (*i.e.*, on macro- and mesoscales) a good agreement is observed for the strains measured in the loading axes. Interestingly,  $\epsilon_{12}$  (FIG. 4.29) has higher fluctuations than those recorded for the equibiaxial experiment (FIG. 4.20(c)). This can be explained by the way the experiment is carried out, which may cause small displacement fluctuations of the central part of the sample since the servo-hydraulic machine is load-controlled (FIG. 4.31). In the hybrid “snail” experiment less fluctuations are observed for  $\epsilon_{12}$  (Appendix E) since the displacement was prescribed while the other axis was loaded. This results in a load relaxation along the axis where the displacement is controlled (see FIG. 4.8(b)).

In the previous section when the mean eigen strains were presented (FIG. 4.21) it was noted how they coincided during virtually all the experiment. From FIG. 4.30 it can be noted that this is not the case for non-proportional “snail” loading. From the measured data we can conclude that the material is loaded in a completely different way (*i.e.*, non-proportional). In the sequel elastoplastic parameters will be identified for the “snail” loading regime.

## 5.2 Validation of elastic parameters

In the following, the two “snail” tests will be analysed. The aim is to determine the elastic parameters via FEMU-UF. Before discussing the results, the measurement resolution is

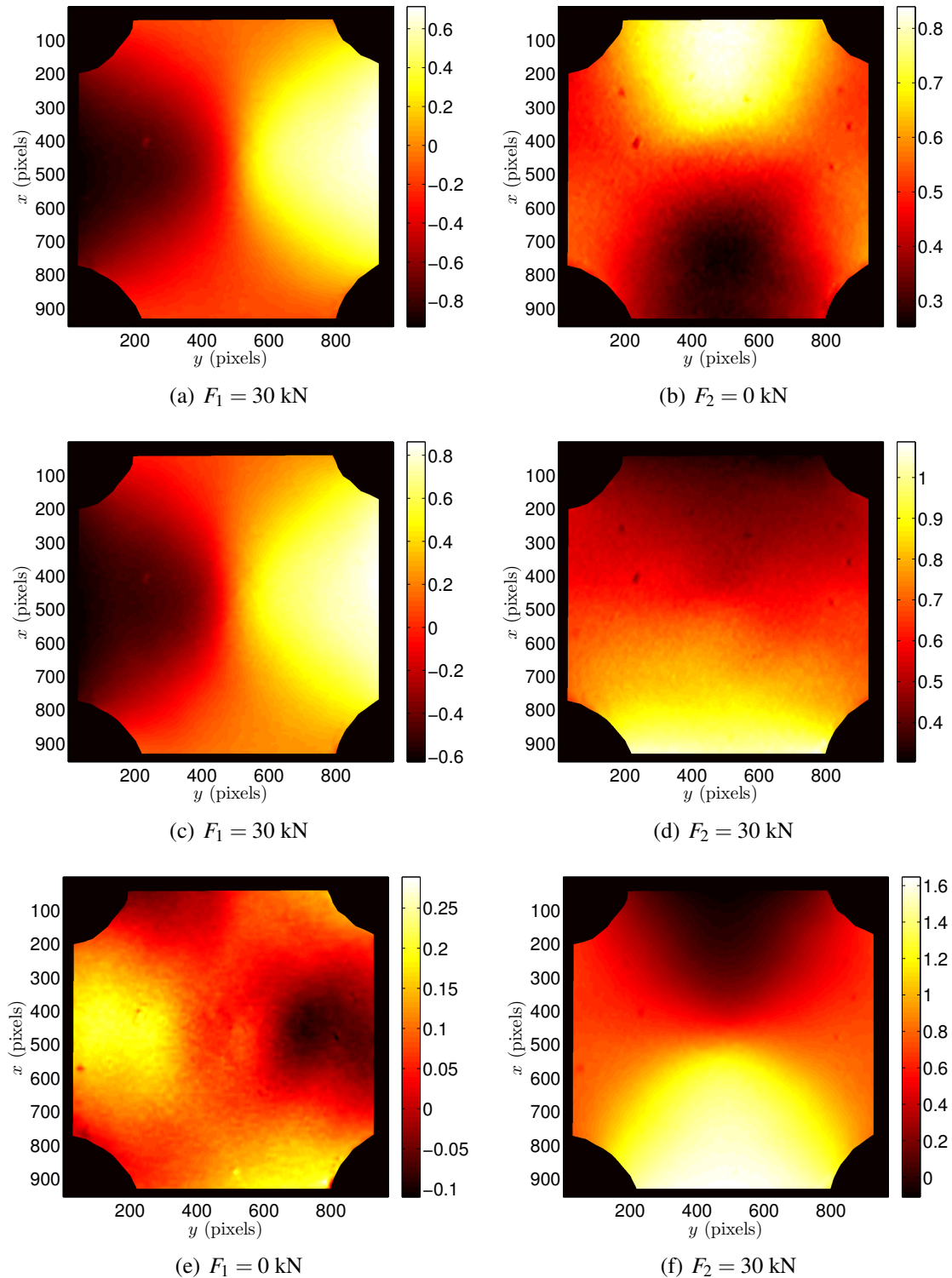


**Figure 4.27:** Measured displacement fields at the macroscale in the horizontal (left) and vertical (right) directions for a maximum loading level of 30 kN. (a) and (b) correspond to loading point 1 (FIG. 4.5(b)), (c) and (d) correspond to loading point 2 (see FIG. 4.5(b)), (e) and (f) correspond to loading point 3 (see FIG. 4.5(b))

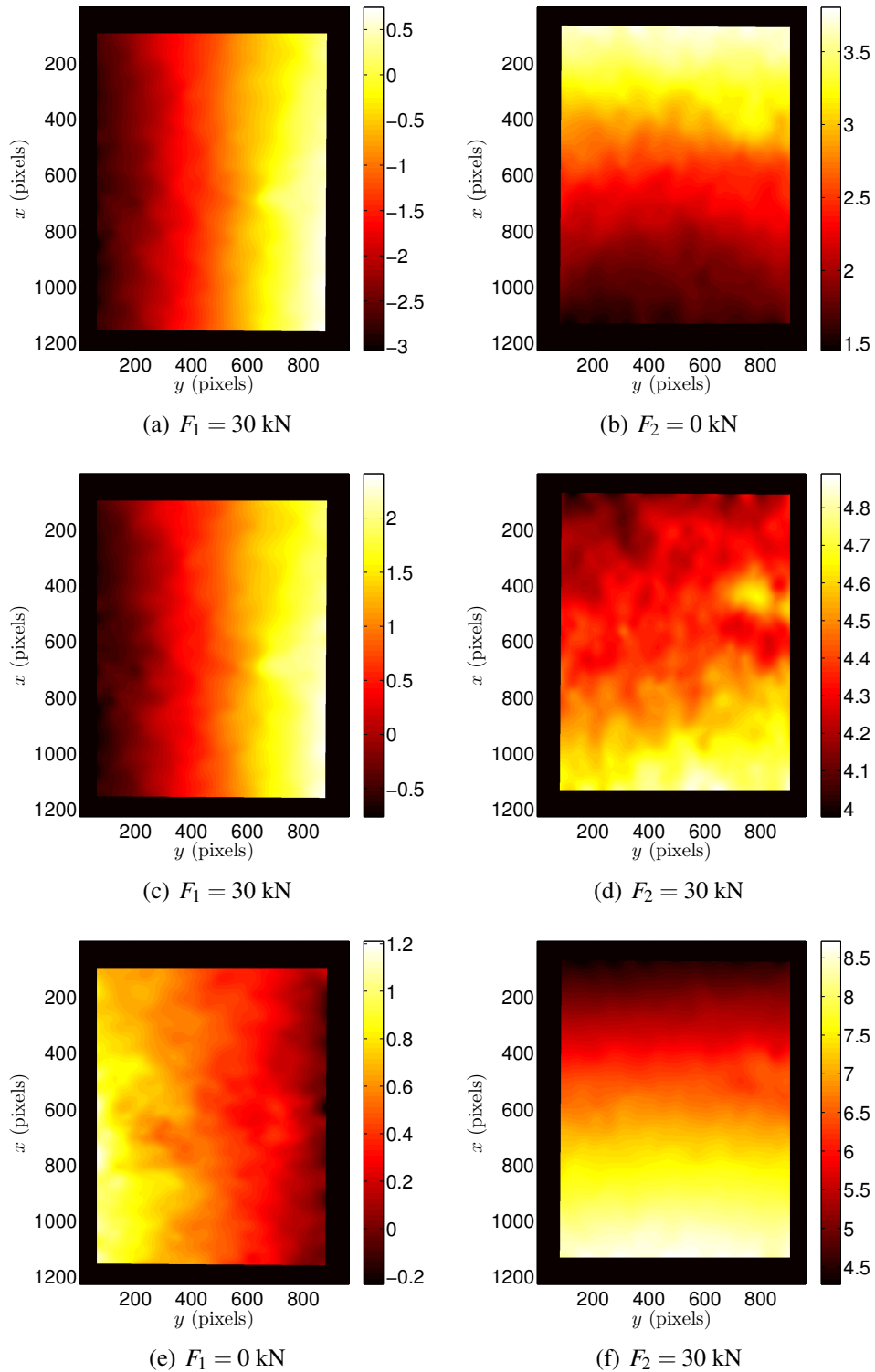


**Figure 4.28:** Measured displacement fields at the mesoscale in the horizontal (left) and vertical (right) directions for a maximum load level of 30 kN. (a) and (b) correspond to loading point 1 (see FIG. 4.5(b)), (c) and (d) correspond to loading point 2 (see FIG. 4.5(b)), (e) and (f) correspond to loading point 3 (see FIG. 4.5(b)).

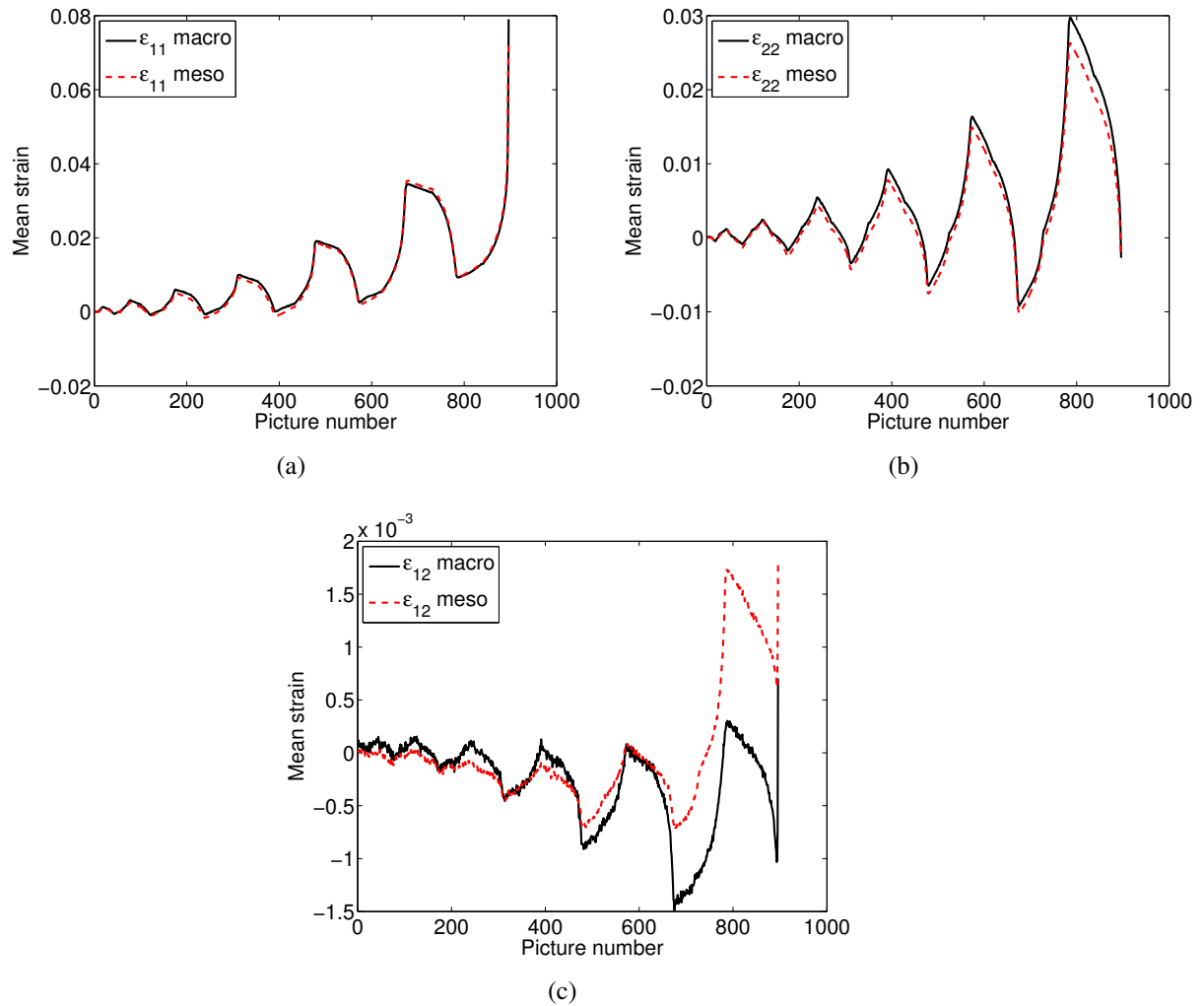


**Figure 4.29:** Change of (a)  $\varepsilon_{11}$ , (b)  $\varepsilon_{22}$ , (c)  $\varepsilon_{12}$  during the fully load-controlled “snail” test at the macro- and mesoscales

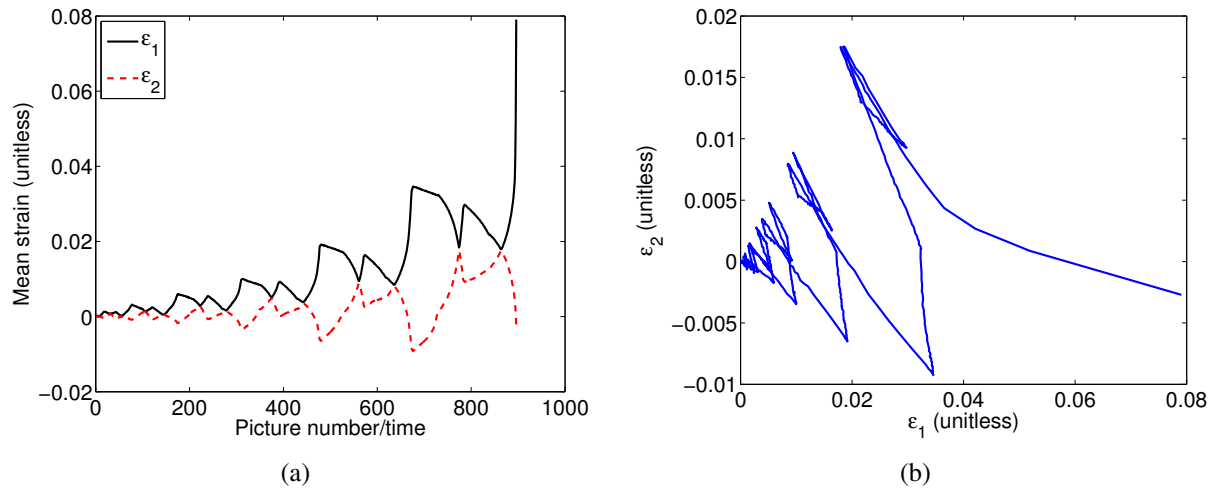


**Figure 4.30:** (a) Change of the mean eigen strains on the macroscale with respect to time. (b) Dependence of mean eigen strains (*i.e.*,  $\epsilon_1$  vs.  $\epsilon_2$ )

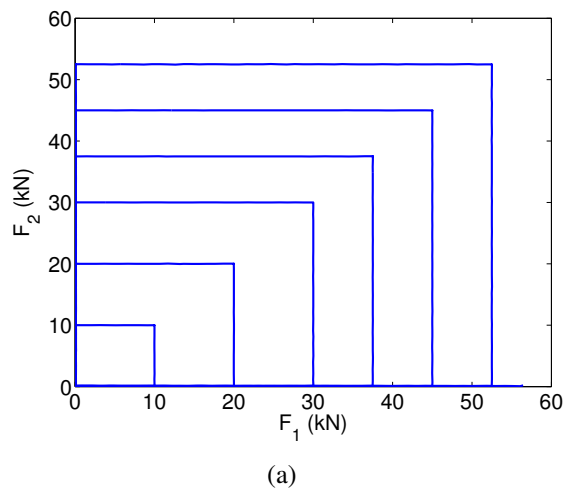


**Figure 4.31:** Measured loading history for the “snail” test

calculated (Equation (3.2) and (3.3)) from 10 images when the loading was not applied. From the standard resolutions (TAB. 4.4) we can note that the displacement resolution for the load controlled test case is 50% lower than for the hybrid one. It is believed that the main difference is due to the texture properties of both tests. The identification of the elastic properties is carried out on the first two cycles. The fully load-controlled test case consisted of 144 pictures while the hybrid one included 101 pictures.

**Table 4.4:** Measurement displacement resolution calculated for fully load-controlled and hybrid “snail” tests

Experiment control	$\gamma_u$ (pixel)	$\gamma_F$ (N)
Load control	0.012	3
Hybrid control	0.020	4

The initial parameters for the FEMU-UF analysis are given in TAB. 4.5. The initial displacement residuals for the load-controlled test are significantly lower (*i.e.*, 4 centipixels) when compared with the hybrid test. This fact results in the inability to identify the Poisson’s ratio for the hybrid test. From the load-controlled experiment, FEMU-UF identifies  $\nu$  (TAB. 4.5) that corresponds to that obtained when using uniaxial test data.

The identification of the Young’s modulus yields for the two cases approximately the same value and induce small decreases of the force residuals. The load-controlled experiment leads to lower values of  $\chi_F$  with respect to the hybrid case. The sum of reaction forces obtained from initial and identified values are shown in FIG. 4.32. For the load-controlled test bigger differences are noted for the second loading axis (FIG. 4.32). Even for the first loading step (*i.e.*,  $F_2 = 0$ ) a linear increase is observed up to 1.5 kN. This phenomenon may be due to damage (*i.e.*, debonding between the matrix and the nodules) since it was detected in early loading stages by tomography (CHAP. 3). The second reason can be caused by modelling errors since the force fluctuations captured on the FE model with the first 10 images are very high (*i.e.*, 0.6 kN). When observing the force response for the hybrid test case the same phenomena occur in direction 1.

**Table 4.5:** Initial and identified elastic parameters for “snail” tests

Parameter	$E$ (GPa)	$\nu$	$\chi_u$ (pixel)	$\chi_F$ (kN)
Load controlled “snail” test				
Reference	160	0.28	0.0142	1.28
FEMU-UF	157.6	0.276	0.0139	1.17
Hybrid “snail” test				
Reference	160	0.28	0.055	1.69
FEMU-UF	155	0.04	0.054	1.56

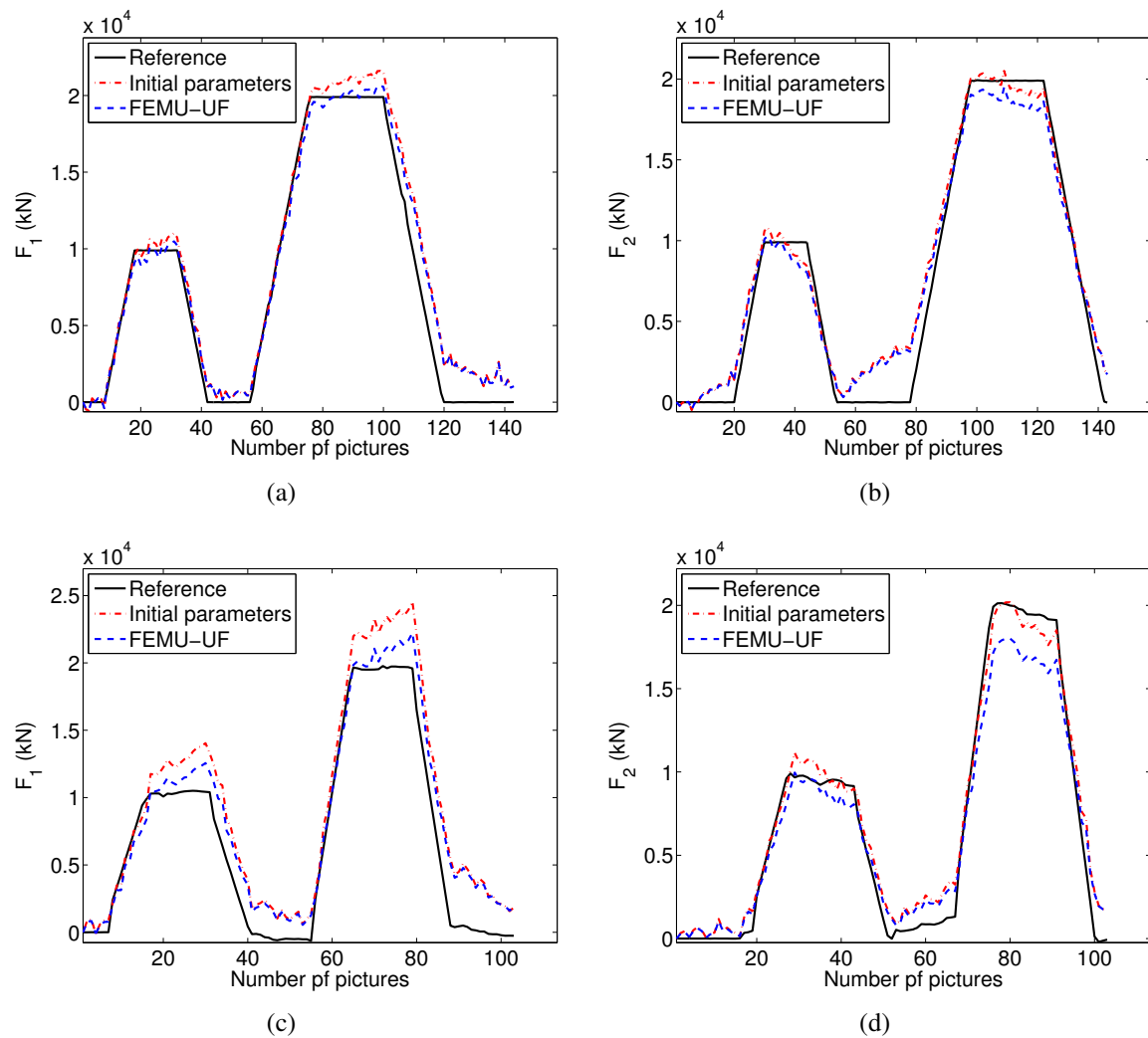


**Figure 4.32:** Comparison of measured force and sum of reaction forces computed with the initial and identified elastic parameters for (a-c) loading direction 1, and (b-d) loading direction 2 of the load-controlled (a-b) and hybrid (c-d) “snail” tests

### 5.3 Identification of plastic parameters

Yielding of the material stressed biaxially is investigated in the sequel. The two material models describing isotropic and kinematic hardening are analysed. The displacement (*i.e.*,  $\chi_u$ ) and force (*i.e.*,  $\chi_F$ ) residuals for the two models provide an information on which law describes best the behaviour of the material under “snail” loading regimes. The load-controlled test case consists of 897 loading steps and the hybrid test of 354 images. The parameters determined from the monotonic uniaxial experiment are introduced as initial parameters for the two material models.

#### 5.3.1 Johnson-Cook’s parameters

The identified parameters ( $\sigma_y$ ,  $K$  and  $n$ ) for the two “snail” tests are reported in TAB. 4.6. For both tests similar values of the parameters are obtained. When compared with the reference parameters it is to be noted that  $\sigma_y$  and  $n$  stay unchanged. The biggest difference is observed for the isotropic hardening modulus  $K$ . For the load-controlled test, it increases by 200 MPa while for hybrid test it increases even more (*i.e.*, 450 MPa). The identified parameters for both experiments slightly change the displacement and load residuals.

FIG. 4.33 shows the sum of reaction forces for the two loading directions when the initial and identified parameters are used to describe Johnson-Cook’s law. For the load-controlled snail test it is noted that the calculated forces in direction 1 (FIG. 4.33(a)) do not properly capture the measured load levels in the unloading parts while in direction 2 (see FIG. 4.33(b)) no agreement is observed in both loading and unloading parts. In the parts of the loading history where the force level should be constant a significant disagreement is observed.

The same trend is obtained for the hybrid test (see FIG. 4.33(c) and (d)). Force residuals decrease more in the latter test but their levels are very high. When compared with the equibiaxial loading the level of  $\chi_F$  is two times higher (see TAB. 4.2). This information leads to the conclusion that more complex cyclic biaxial loading regimes cannot be described in a reasonable way with isotropic hardening laws. Hence kinematic hardening will be investigated. It is noted that the displacement residuals are high when compared to the equibiaxial case (see TAB. 4.2).  $\chi_u$  equals 0.11 pixel for the load-controlled “snail” test, which makes it 2 times higher than the equibiaxial one. An even bigger difference is reported for the hybrid loaded test (*i.e.*, 10 times greater). It is necessary to emphasise that the strains in the “snail” experiments are higher than in the proportional loading regime, which may explain the increase of  $\chi_u$ . Hence, we can conclude that the crack network is more developed. Since the FE model does not capture that phenomenon, it can induce bigger differences between the measured and calculated fields.

#### 5.3.2 Armstrong-Frederick’s parameters

The initial and identified parameters with the corresponding displacement and force residuals are given in TAB. 4.7. The sought parameters ( $\sigma_y$ ,  $C$  and  $\gamma$ ) are determined via FEMU-UF while the elastic ones were fixed. The identified yield stress decreases by



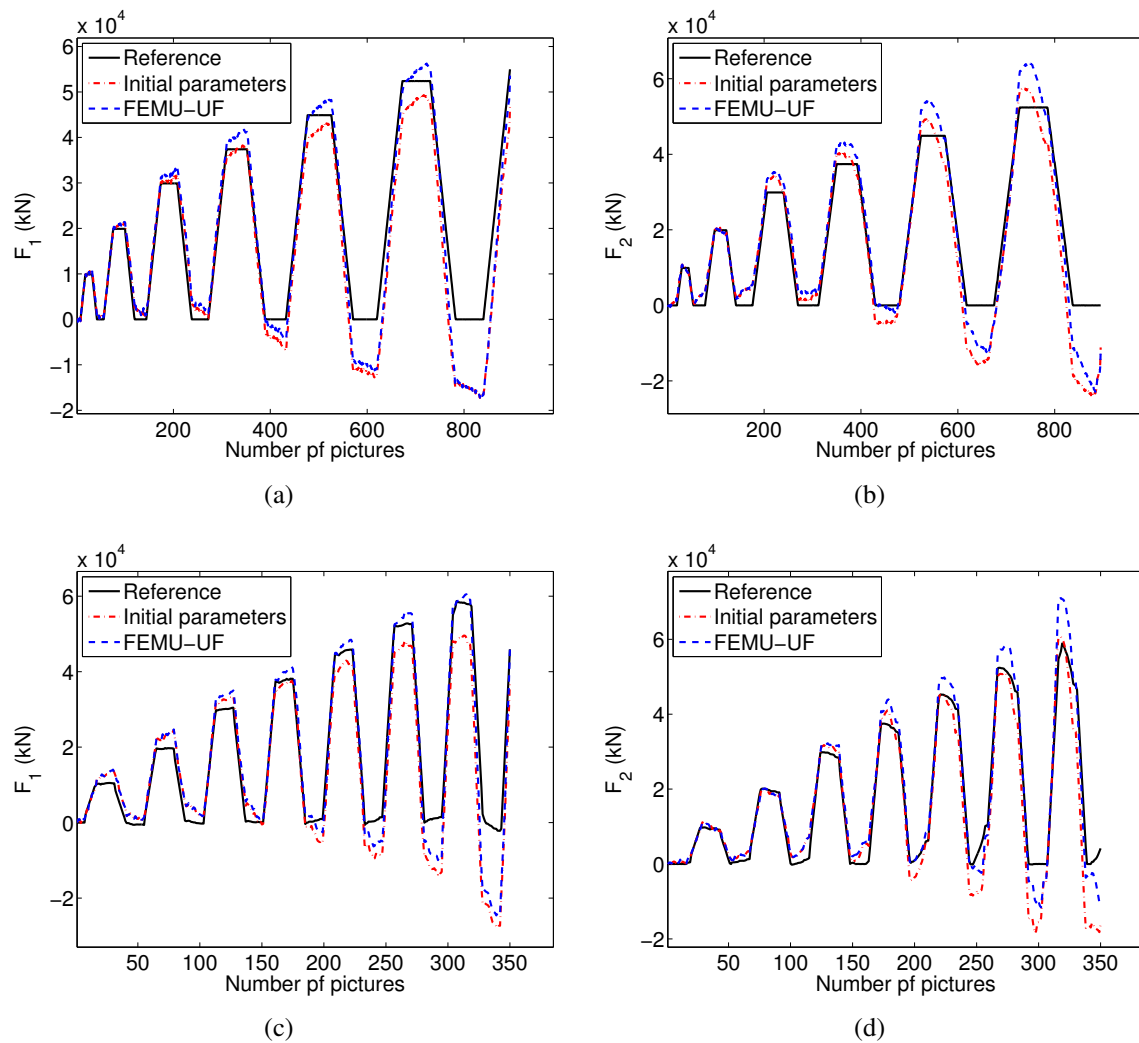


**Figure 4.33:** Comparison of measured force and sum of reaction forces computed with the initial and identified material parameters for Johnson-Cook’s law for (a-c) loading direction 1, and (b-d) loading direction 2 of the load-controlled (a-b) and hybrid (c-d) “snail” tests

**Table 4.6:** Identified Johnson-Cook material parameters on "snail" test cases.

Parameter	$E$ (GPa)	$\nu$	$\sigma_Y$ (MPa)	$K$ (MPa)	$n$	$\chi_u$ (pixel)	$\chi_F$ (kN)
Load controlled "snail" test							
Reference	157.6	0.28	228	850	0.38	0.11	6.6
FEMU-UF	157.6	0.276	225	1027	0.35	0.10	6.3
Hybrid controlled "snail" test							
Reference	155.3	0.28	228	850	0.38	0.471	6.8
FEMU-UF	155.3	0.28	219	1312	0.39	0.468	5.246

30 MPa for the load-controlled test and by 16 MPa for the hybrid test. The other two parameters differ more for the two tests. The fully load-controlled test yields a hardening modulus of 21 GPa in comparison with 30 GPa for the hybrid test. The parameter  $\gamma$  slightly changes for the load-controlled test when compared with the uniaxial experiment (*i.e.*, reference parameters) while for hybrid test it increases by 60 %.

**Table 4.7:** Identified Armstrong-Frederick's parameters for the two "snail" tests

Parameter	$E$ (GPa)	$\nu$	$\sigma_Y$ (MPa)	$C$ (GPa)	$\gamma$	$\chi_u$ (pixel)	$\chi_F$ (kN)
Load-controlled "snail" test							
Reference	158	0.28	289	10	45	0.11	5.3
FEMU-UF	158	0.276	259	21	40	0.06	2.3
Hybrid "snail" test							
Reference	155	0.28	289	10	45	0.48	6.3
FEMU-UF	155	0.28	273	30	74	0.43	2.8

The identified parameters for the two "snail" experiments yield a significant decrease of the force residuals by more than 50 % when compared with the levels induced by the initial parameters. The best fit of the sought parameters is for the load-controlled test, which results in a drop of the displacement residual by 40 % while a lot less for the hybrid experiment (*i.e.*, changes of 4 centipixels are observed in both cases). Similarly, the level of  $\chi_F$  for the load-controlled case is lower with respect to the hybrid test. However, two times less images are used in the hybrid test, which may explain a part of the differences [Robert et al., 2012]. The level of  $\chi_F$  (*i.e.*, 2.3 kN and 2.8 kN) is of the same order of magnitude when compared with the equibiaxial test (*i.e.*, 2 kN). These force residuals are partly attributed to the monitored damage initiations (*i.e.*, debonding between the matrix and graphite nodules (CHAP. 3)) and the subsequently formed crack network (FIG. 4.22).

FIG. 4.34 shows the calculated reaction forces for the two load histories in order to compare the measured and identified load levels. A better agreement is achieved between the measured and identified sum of reaction forces for both cases when compared with

Johnson-Cook’s model. However, there is clear difference with the reference parameters that shows that the identification with a uniaxial test does not describe the “snail” loading regimes in a reliable way.

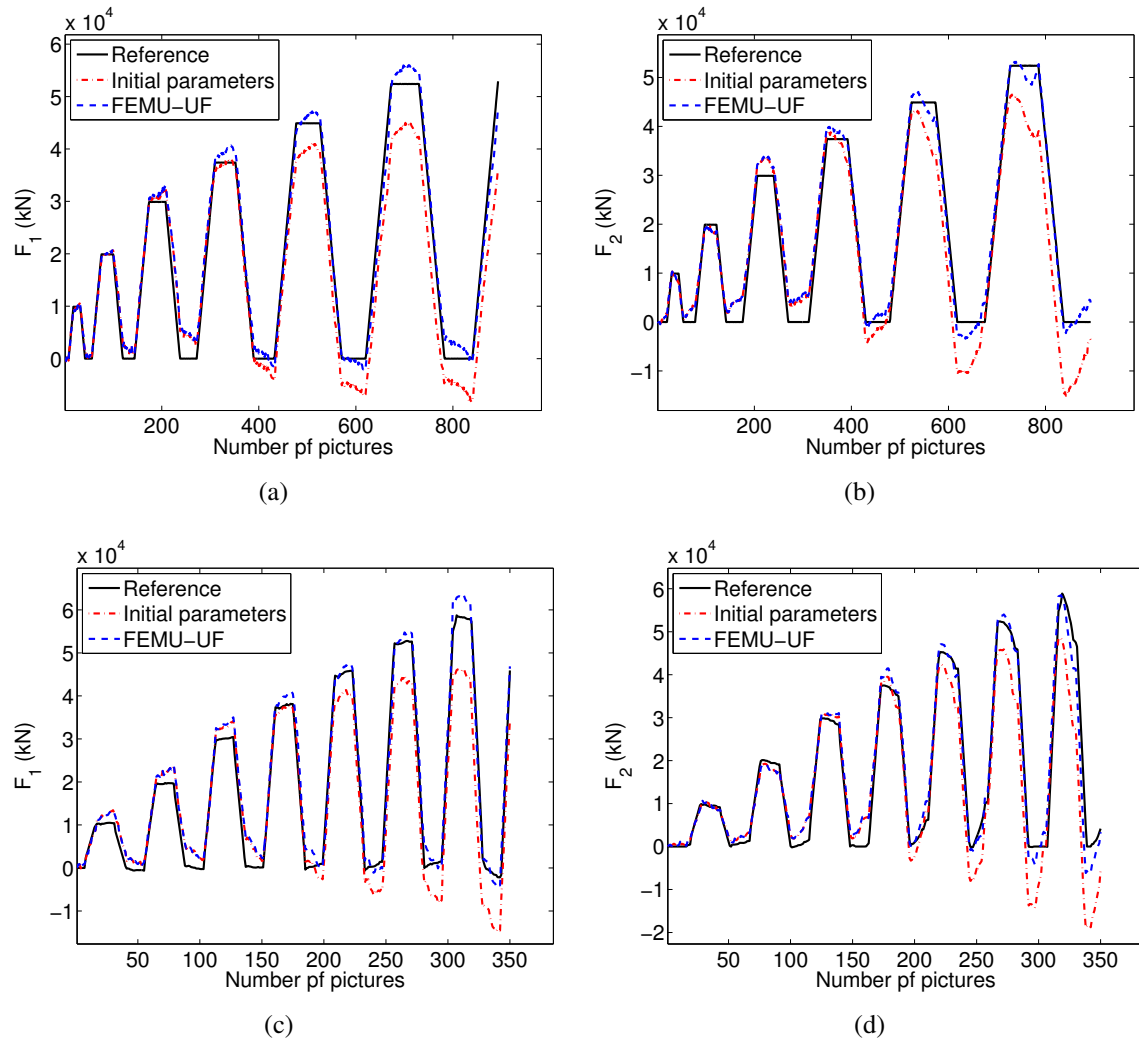


**Figure 4.34:** Comparison of measured force and sum of reaction forces computed with the initial and identified material parameters for Armstrong-Frederick’s law for (a-c) loading direction 1, and (b-d) loading direction 2 of the load-controlled (a-b) and hybrid (c-d) “snail” tests

## 6 Conclusion

The objective of the present chapter was to study the mechanical properties of SG cast iron under biaxial loading configurations. An original setup was used to observe the

experiments on two scales. Both sides of the cross-shaped samples were observed at a macro- and mesoscale. Images captured at the macroscale were dealing with an artificial texture while the images at the meso level used the natural texture of cast iron. The latter was poor and very difficult to handle with classical DIC algorithms (*i.e.*, local and global approaches). The lack of gray level contrast was successfully surpassed by resorting to regularized DIC. The application of the mechanically-regularized methodology showed that even poor image textures could be dealt with successfully.

Two different loading histories were applied in order to study the material behaviour under proportional (*i.e.*, equibiaxial) and non-proportional (*i.e.*, “snail”) loading regimes. First, strain histories were extracted from the measured displacement fields. The results observed on the two scales showed very good agreement even though two opposite sides of the sample were simultaneously analysed. Mesoscale results revealed microcrack network initiation and growth as the sample was more stressed. These phenomena led to a gap of the measured strain fluctuations between the two scales. The two applied loading paths yield completely different strain histories. An equibiaxial loading regime leads to the same strain history for the components measured in the loading direction and the eigen strains. Conversely, “snail” histories are more complex.

Second, the identification of elastoplastic parameters via FEMU has been performed for the two loading histories. Results obtained from uniaxial experiments were used as inputs to the FEMU-UF procedure. Both elastic parameters were only identified on the snail experiment. One of the reasons is related to the fact that the FE model had just four radii treated as traction-free edges while on 90 % of the boundary nodes displacements were prescribed. The lack of free boundary and the feature of the load history leads to an inability of identifying Poisson’s ratio from equibiaxial and hybrid “snail” tests. When identifiable, the value of the Poisson’s ratio is in agreement with that identified from a uniaxial experiment.

The identification of isotropic (*i.e.*, Johnson-Cook model) and kinematic (*i.e.*, Armstrong-Frederick model) hardening parameters was performed on the whole series of images for the three tests. The identified parameters yielded higher force residuals than those observed in uniaxial experiments. This can be explained by early damage inceptions (*i.e.*, in the elastic domain) as detected in CHAP. 3 via X-ray tomography. Another reason is associated with modelling errors as a full 3D FE analysis is run and only 2D-DIC measurements are used. In the biaxial experiments another phenomenon was reported. Crack network formations were observed on the mesoscale, which cause higher values of the force residuals. The results obtained with Armstrong-Frederick’s model are better than those with Johnson-Cook’s isotropic hardening. Higher force residuals obtained in the “snail” experiments when compared with the equibiaxial test provide an information that non-proportional loading regimes are more damaging and complex to analyse, and that more complex models need to be considered.

# Chapter 5

## Biaxial fatigue experiments

*In this chapter two series of fatigue experiments are presented. First, a series of five experiments is performed with an equibiaxial history, and, second, a series of five “snail” loadings. The goal is to evaluate the fatigue lifetime for the two loading paths in order to evaluate the more damaging one. Two-scale DIC is performed to measure displacement fields of both sample sides. From the mesoscale measurements, the crack networks will be detected and quantified with respect to number of cycles. The macroscopic measurements are used in particular to validate the kinematic hardening model identified in the previous chapter.*

### Contents

---

<b>1</b>	<b>Preface</b> . . . . .	<b>155</b>
<b>2</b>	<b>Equibiaxial fatigue experiments</b> . . . . .	<b>156</b>
2.1	Analysis of experiment EBE-1 . . . . .	156
2.2	Microcrack initiation for EBE-5 test . . . . .	164
2.3	Results of equibiaxial fatigue campaign . . . . .	167
<b>3</b>	<b>“Snail” fatigue experiments</b> . . . . .	<b>170</b>
3.1	Validation of the kinematic hardening law . . . . .	170

3.2	Analysis of experiment SBE-2 . . . . .	174
3.3	Microcrack initiation in SBE-5 test . . . . .	180
3.4	Results of “snail” fatigue campaign . . . . .	185
<b>4</b>	<b>Conclusion . . . . .</b>	<b>185</b>

---

# 1 Preface

Wind turbine components such as investigated in the project *The development of methods to increase the reliability of wind turbines* (*i.e.*, wind turbine hub) are subjected to multiaxial load histories. The multiaxial fatigue behavior of materials and structures, which depends on the loading path, is still difficult to describe. Because fatigue data are usually scattered, classical identification techniques of fatigue properties are difficult and require the use of many specimens. This is even more difficult if one wants to study highcycle fatigue (HCF) of materials under multiaxial loadings. The aim of this work is to provide a good understanding of the effect of multiaxial load histories on the fatigue response of SG cast iron. In the present work two-scale DIC measurements are used to evaluate the fatigue response under two different biaxial states of stresses.

A series of biaxial fatigue tests are performed at room temperature to build up an extensive and well-documented database. The testing specimen is a maltese cross thinned in its centre with nonhomogeneous strain/stress fields (see Appendix C). The strains and correlation residuals as well as the crack initiation detection are obtained by the use of Digital Image Correlation (DIC) simultaneously performed on two scales. Ten cruciform specimens made of SG cast iron are loaded by the multiaxial testing machine ASTREE.

Two kinds of loading paths are presented, namely, equibiaxial and non-proportional “snail” (see CHAP. 4). The experimental results (*i.e.*, strain amplitudes) are given for each loading path. For each loading path two different tests will be considered. The first one corresponds to the fact that the crack network initiates during the first cycle. The second one corresponds to crack network initiation after the sample has been cycled. Correlation and mechanical residuals obtained via RT3-DIC analyses will be presented in order to give indications of the crack network behaviour with the number of cycles.

TAB. 5.1 presents the considered loading types. The first and second groups respectively correspond to an equibiaxial loading path (EBE) and a non-proportional “snail” loading path (SBE). The loading definition is given by the maximum and minimum load applied for the proposed proportional and non-proportional histories. This biaxial fatigue campaign presents several interests. Two different loading histories are imposed on the material in the LCF and HCF regimes (*i.e.*, up to  $1.5 \times 10^6$  cycles), with DIC strain gauges and crack initiation detection.

**Table 5.1:** Definition of the equibiaxial and “snail” loading paths. The acronym EBE refers to the *equibiaxial experiment* and SBE to the “*snail*” *biaxial experiment*

	$F_1^{max}$ (kN)	$F_2^{max}$ (kN)	$F_2^{min}$ (kN)	$F_1^{min}$ (kN)
EBE-1 & SBE-1	50	50	0.1	0.1
EBE-2 & SBE-2	40	40	0.1	0.1
EBE-3 & SBE-3	30	30	0.1	0.1
EBE-4 & SBE-4	25	25	0.1	0.1
EBE-5 & SBE-5	20	20	0.1	0.1

## 2 Equibiaxial fatigue experiments

The first series of two-scale fatigue experiments (see FIG.4.3) was conducted in an equibiaxial loading regime. Five different maximum load levels (see TAB. 5.1) are prescribed to investigate the lifetime and crack network formation with respect to the applied number of cycles. When analysing the measured data (*i.e.*, correlation and mechanical residuals, strain histories) two different phenomena are observed considering the initiation of the microcracks. Two tests will be detailed in the sequel. A crack network can be detected at the first cycle (*i.e.*, EBE-1 experiment where the maximum applied force  $F_{max} = 50$  kN). When lower maximum forces are prescribed microcrack initiation starts after a critical number of cycles. Crack detection in this case is more complex and challenging. The EBE-5 test will be illustrated as an example.

### 2.1 Analysis of experiment EBE-1

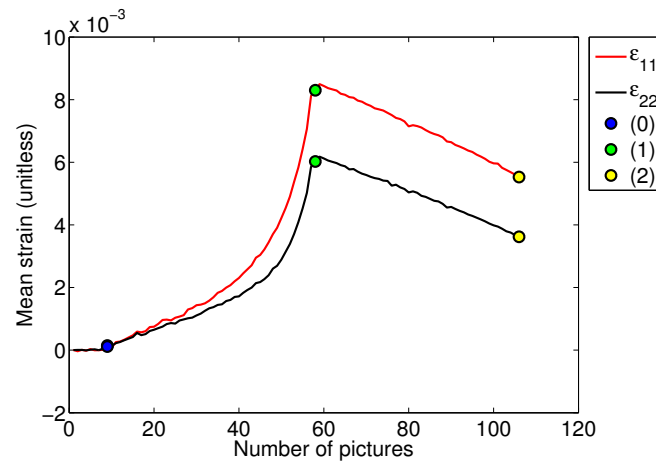
#### 2.1.1 Crack network formation in the first loading cycle

The fatigue behaviour is analysed by performing DIC calculations on the images acquired on two scales. RT3-DIC was performed on all the images in order to reveal the material response to various force amplitudes. For the macro and meso images, an element size of 10 pixels is chosen (FIG. 4.19). From the measured displacement fields, a DIC gauge is considered to evaluate the mean strain histories (FIG. 4.19).

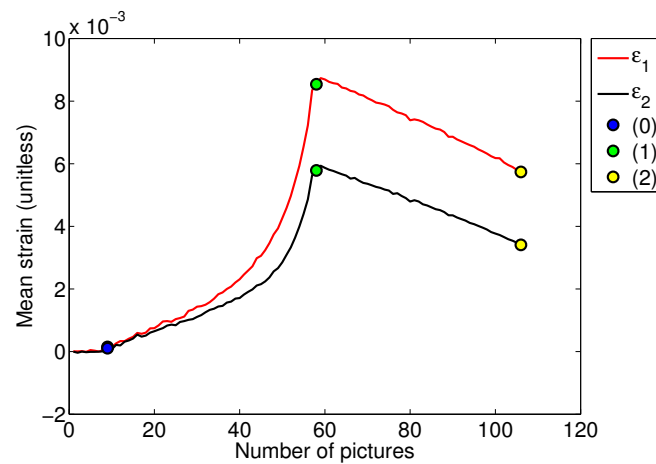
FIG. 5.1(a) shows the strain response to the prescribed load levels at the mesoscale for the first cycle. It is noted that mean eigen strains (FIG. 5.1(b)) correspond to the strain components in the loading direction. The two components (*i.e.*,  $\epsilon_1$  and  $\epsilon_2$ ) follow the same trend (*i.e.*, increase of strain levels with respect to the load level and conversely). However, the strain levels are not equal. Nonlinear strains are detected after 0.2 %. Until 0.2 % of strain a linear response is observed. However, even in this regime the strain levels start to differ. This effect can be explained by crack initiation between the nodules and the matrix in early stages (elasticity). From the reported strain histories for the first cycle it can be concluded that the more damaging direction is 11. The loss of stiffness and plasticity effect is also observed since the strain level corresponding to full unloading does not vanish. The maximum eigen strain is measured in direction 11 and it is equal to 0.85 %, while its corresponding unloading level reaches 0.56 %.

FIG. 5.2 illustrates the gray level residual map obtained from RT3-DIC between the reference configuration and that corresponding to the maximum load level of the first cycle. Higher values of the residuals is an indication of discontinuity or localisation phenomena in the displacement field. The gray level residual map (FIG. 5.2(a)) is shown at the mesoscale. Many cracks branch on the surface of the sample forming a crack network. However, in the left bottom part dominant cracks are observed, which are damaged (*i.e.*, opened) the most. The mechanical residuals (FIG. 5.2(b)) also show similar trends. Most of the crack branches are found in the left part of the map, with the most opened ones in the left bottom corner. It is necessary to emphasise that correlation residuals indi-





(a)



(b)

**Figure 5.1:** Strain histories describing the first cycle of equibiaxial experiment 1 ( $F_{max} = 50$  kN). (a) Normal strains in the loading directions of the sample. (b) Mean eigen strains. Blue, green and yellow circles correspond to the three characteristic points of equibiaxial experiments (see FIG. 4.5(b))

cate more clearly the crack paths since they are obtained pixel-wise while the mechanical residuals are calculated at nodal (*i.e.*, element) level. Until now only the first cycle is analysed. Hence, in order to evaluate fatigue behaviour of the investigated loading path (*i.e.*,  $F_{max} = 50$  kN) the strain evolution and crack network growth will be presented in the following.

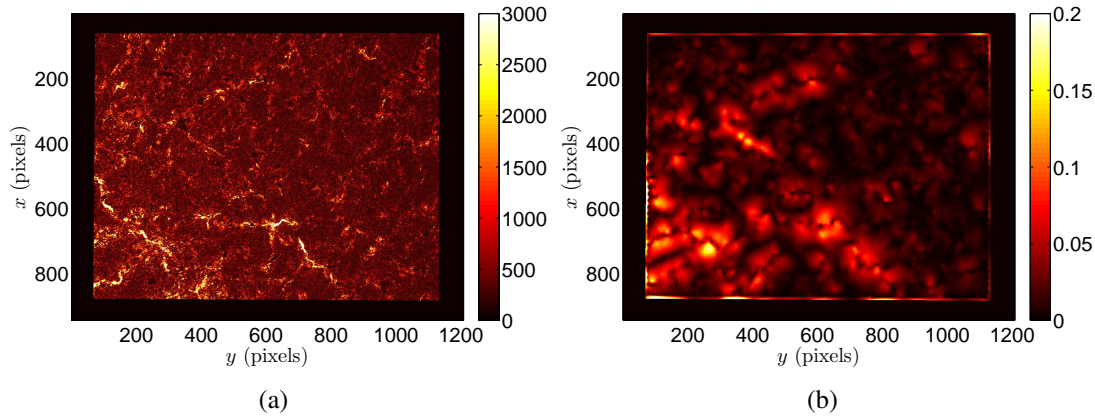


**Figure 5.2:** EBE-1: (a) Displacement and (b) mechanical residual maps corresponding to maximum imposed load level (*i.e.*,  $F_1 = F_2 = 50$  kN) at first cycle.

### 2.1.2 Validation of the kinematic hardening law

In CHAP. 4 the identification of elastoplastic parameters was carried out on with different models, namely, isotropic (*i.e.*, Johnson-Cook) and kinematic (*i.e.*, Armstrong-Frederick) hardening laws were considered in proportional and non-proportional biaxial loading regimes. The results of the equilibrium gap ( $\chi_F$ ) showed that Armstrong-Frederick's law outperforms Johnson-Cook's when the sample is subjected to complex biaxial loadings. Hence, in order to evaluate the stress state in fatigue tests when the sample is loaded with a maximum force of 50 kN, the parameters (see TAB. 4.3) will be validated with the FEMU-UF procedure.

It is necessary to note that for each fatigue experiment (*i.e.*, equibiaxial and “snail” histories) every  $10^n$  cycle, the image acquisition was conducted as in CHAP. 4. However, only the initial cycle is analysed hereafter. The present experiment was load-controlled with a loading rate of 0.5 kN/s. The same protocol was followed to prepare the FEMU-UF procedure as explained in Section 4.2 (CHAP. 4). 110 images were captured during the loading and unloading phases of the first cycle and all of them are used for validation purposes.

The initial and identified parameters are reported in TAB. 5.2. The Young's modulus was identified in a separate analysis and its value is also given (TAB. 5.2). The Poisson's ratio was chosen from the uniaxial test data. The reference parameters lead to a displacement residual of 0.09 pixel with a corresponding force residual equal to 1.75 kN.

The sought plastic parameters (*i.e.*,  $\sigma_y$ ,  $C$  and  $\gamma$ ) are identified in one procedure. The determined parameters (TAB. 5.2) slightly change with respect to the initial ones. The yield stress  $\sigma_y$  decreases by 4 MPa, the hardening modulus  $C$  by 3 GPa and the hardening coefficient  $\gamma$  differs from the initial one by 3. The identified parameters result in slight decreases of the residuals. The displacement error does not change, while the difference between the measured load and sum of the reaction forces on the boundaries is equal to 1.44 kN. It can be noted that displacement residuals are higher by 0.04 pixel when compared with those reported for the cyclic equibiaxial test (see TAB. 4.3). However, the equilibrium gap  $\chi_F$  decreases by 0.5 kN.

**Table 5.2:** Initial and identified Armstrong-Frederick's parameters via FEMU-UF for an equibiaxial loading path

Parameter	$E$ (GPa)	$\nu$	$\sigma_y$ (MPa)	$C$ (GPa)	$\gamma$	$\chi_u$ (pixel)	$\chi_F$ (kN)
Reference	160	0.28	289	23	18	0.089	1.76
FEMU-UF	159	0.28	285	20	15	0.088	1.44

FIG. 5.3 shows the comparison of measured load and sum of reaction forces computed with the initial and identified parameters in the two loading axis. The identified parameters slightly change the history of calculated forces. This leads to the conclusion that the kinematic hardening parameters are validated since just slight adjustments were necessary to better capture the equibiaxial behaviour of the investigated SG cast iron.

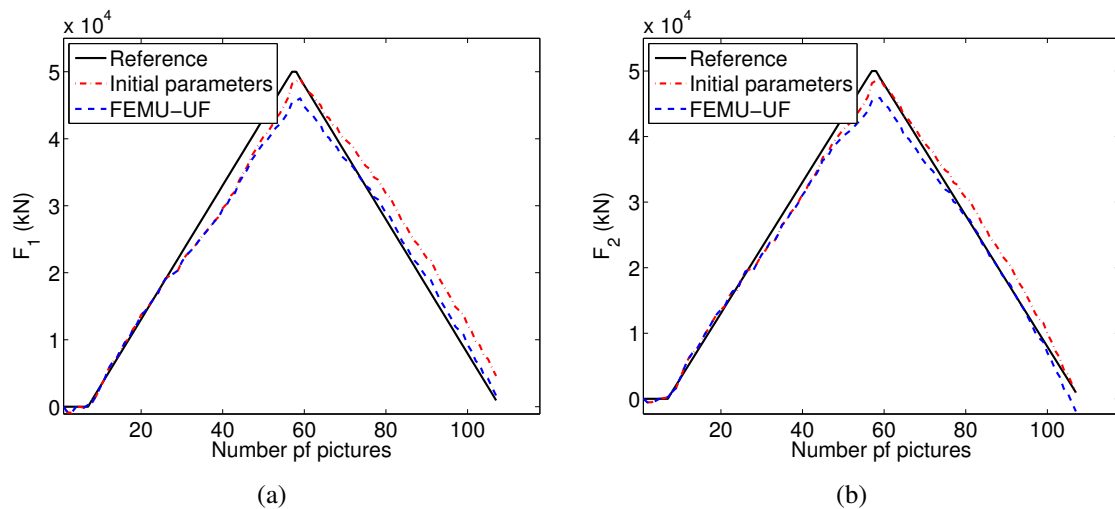


**Figure 5.3:** Comparison of measured force and sum of reaction forces computed with the initial and identified parameters for Armstrong-Frederick's constitutive law

### 2.1.3 Strain history of EBE-1 experiment

With the initiation and propagation of the cracks the strain levels increase and one of the criteria to identify the microcrack growth consists of extracting the strain amplitudes (*i.e.*, difference of maximum and minimum strains over one cycle). The mean strains are calculated via the DIC gauge in order to determine the strain path. FIG. 5.4 shows the material response with the number of cycles. On both strain histories three stairs (*i.e.*, sudden changes of strain level) are detected.

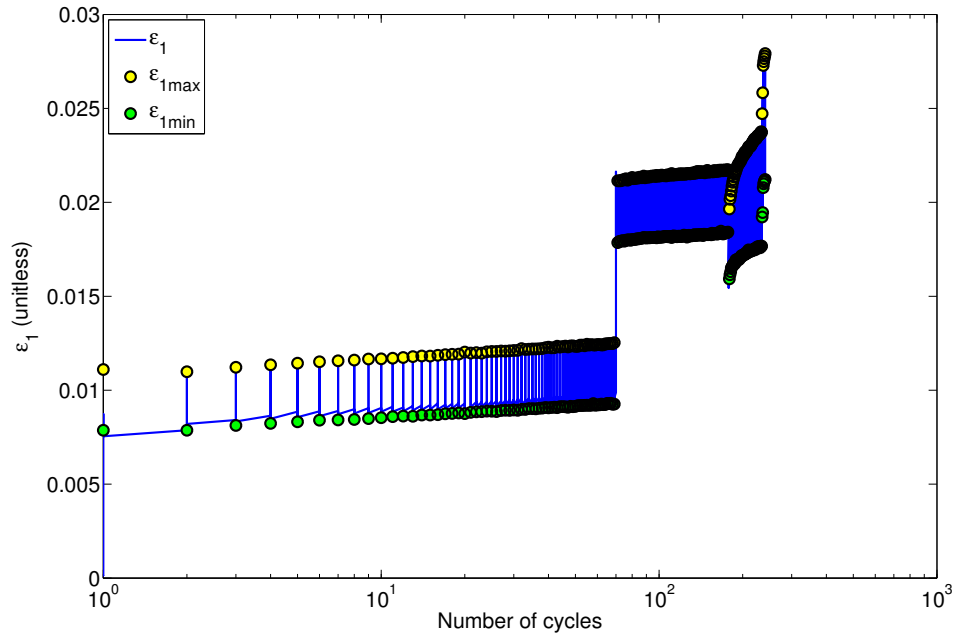
The first increase of  $\varepsilon_1$  and simultaneous decrease of  $\varepsilon_2$  occurs due to the fact that the experiment was interrupted, which caused different values of strains. However, it did not result in a change of the strain amplitudes (see FIG. 5.5). Conversely, the second change (*i.e.*, stair) occurred due to the crack growth. The third stair noted on the strain history is due to the sudden propagation of the crack that becomes dominant (*i.e.*, it caused the failure of the sample). From the residual maps we can observe the crack network growth (FIG. 5.7). To get more information, the strain amplitudes are analysed on the two sides of the sample (see FIG. 5.5).

When comparing the mean strain amplitudes with the number of cycles it is shown how the macroscale observation is more affected by fluctuations than the mesoscale. However, this fact is not surprising since less information is available at the macroscale (*i.e.*, the physical size of the DIC gauge is identical at macro and mesoscales, see FIG. 4.19). The strain amplitude of  $\varepsilon_1$  (FIG. 5.5(a)) show a good agreement when comparing the two observed scales. This is not the case with  $\Delta\varepsilon_2/2$  (FIG. 5.5(b)) where the gap between the two scales is higher. This difference of 0.04% may be an indication of spurious flexure.

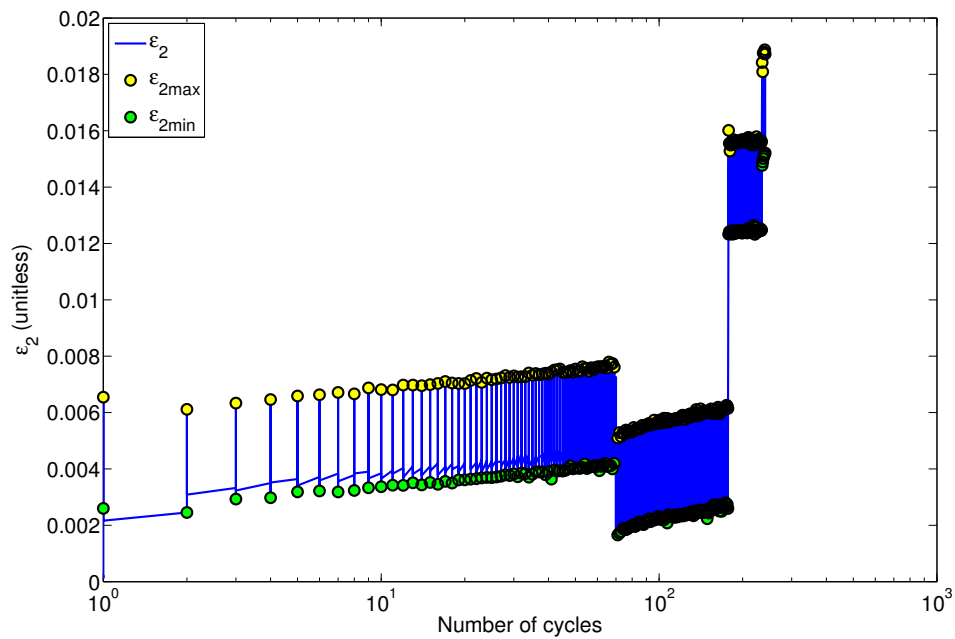
After 10 loading cycles the amplitudes  $\Delta\varepsilon_1/2$  and  $\Delta\varepsilon_2/2$  at the mesoscale gradually increase until the 125th cycle is reached. At this point an increasing gap of  $\Delta\varepsilon_1/2$  is noted (*i.e.*, drop of  $\Delta\varepsilon_2/2$ ). Macroscale observations follow the same trend for the both eigen strains. However, this phenomenon is less clear since the strain fluctuations are higher. It is necessary to emphasise differences between macro and mesoscale strain amplitudes after the drop/increase is reported.  $\Delta\varepsilon_1/2$  at the mesoscale reaches higher values since it better captures the crack network growth. In FIG. 5.4 three stairs were noted. Observing the strain histories the first one is not observed while the second increase/decrease is interpreted as crack growth. The last sudden change of strain history is detected as an increase of the strain amplitude. The formation of a dominant macrocrack has occurred and it caused a fast failure of the sample.

### 2.1.4 Crack network growth

In order to capture the fatigue behaviour (*i.e.*, the crack network growth) mechanical (*i.e.*,  $\tilde{\Phi}_m$ ) and normalized correlation (*i.e.*,  $\hat{\Phi}_c$ ) residuals will be commented. As already discussed cracks initiate at the first loading cycle. Mesoscale observations detect better the initiation and early propagation of the microcracks in the thinned gauge zone of the specimen. Hence, these residuals will be used (see FIG. 5.6(a)). Both residuals exhibit less fluctuation than the mean strains (see FIG. 5.5). The residuals follow the same trend

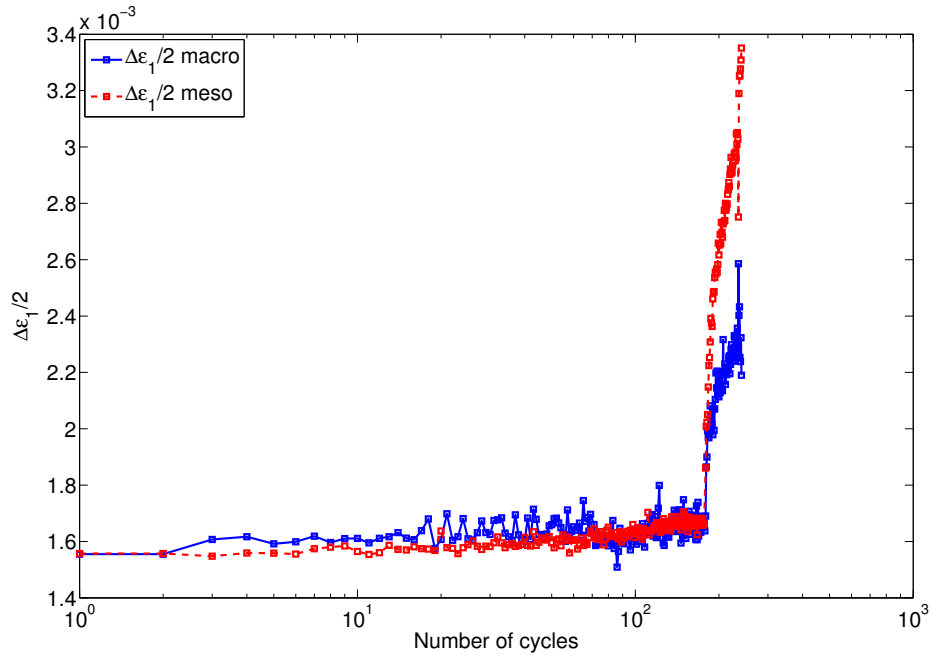


(a)

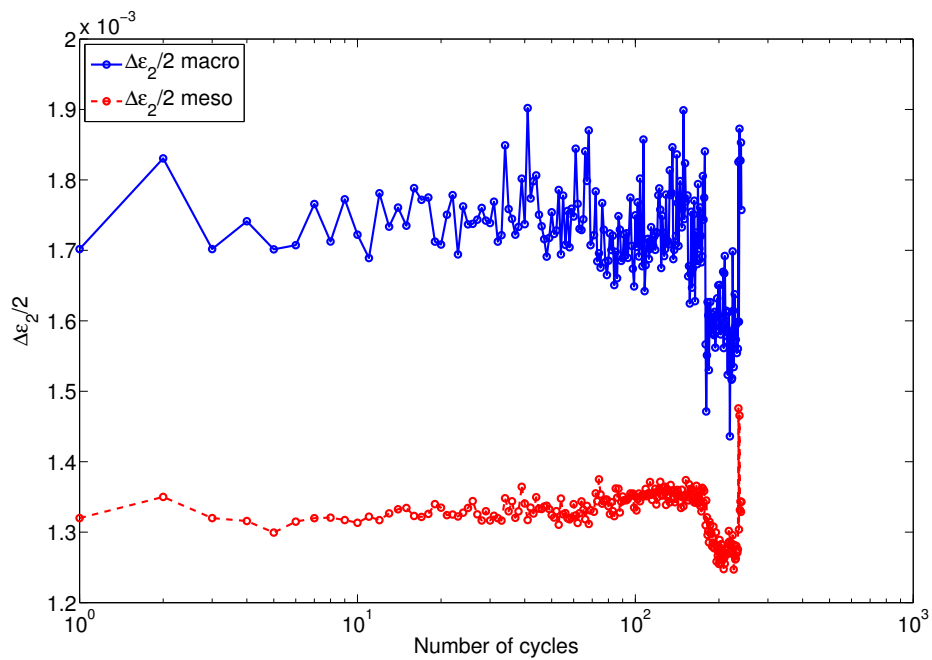


(b)

**Figure 5.4:** Measured (a)  $\epsilon_1$  and (b)  $\epsilon_2$  histories with respect to the number of cycles. The maximum peak values are denoted by yellow circle and minimum with green circles



(a)



(b)

**Figure 5.5:** Measured amplitudes for (a)  $\varepsilon_1$  and (b)  $\varepsilon_2$  at macro and mesoscales

with an increase after the loading first cycle. This leads to the conclusion that cracks start to grow in each loading cycle (*i.e.*, material is more affected by damage). When comparing the two residuals for this case it is observed that  $\hat{\Phi}_c$  is slightly more sensitive to detect changes on the surface of the material.

FIG. 5.6(b) illustrates the two residuals as functions of the maximum eigen strain amplitude measured in the gauge section. It can be noted that variations of the residuals are more sensitive until the 125th cycle (see FIG. 5.5) than the corresponding strain amplitude  $\Delta\varepsilon_2/2$ . In this part of the fatigue experiment strain amplitudes have fluctuations that could be attributed to noise. In the second part (*i.e.*, beyond 125 cycles) the strain variations start to change significantly, which is caused by cracks that growth faster.

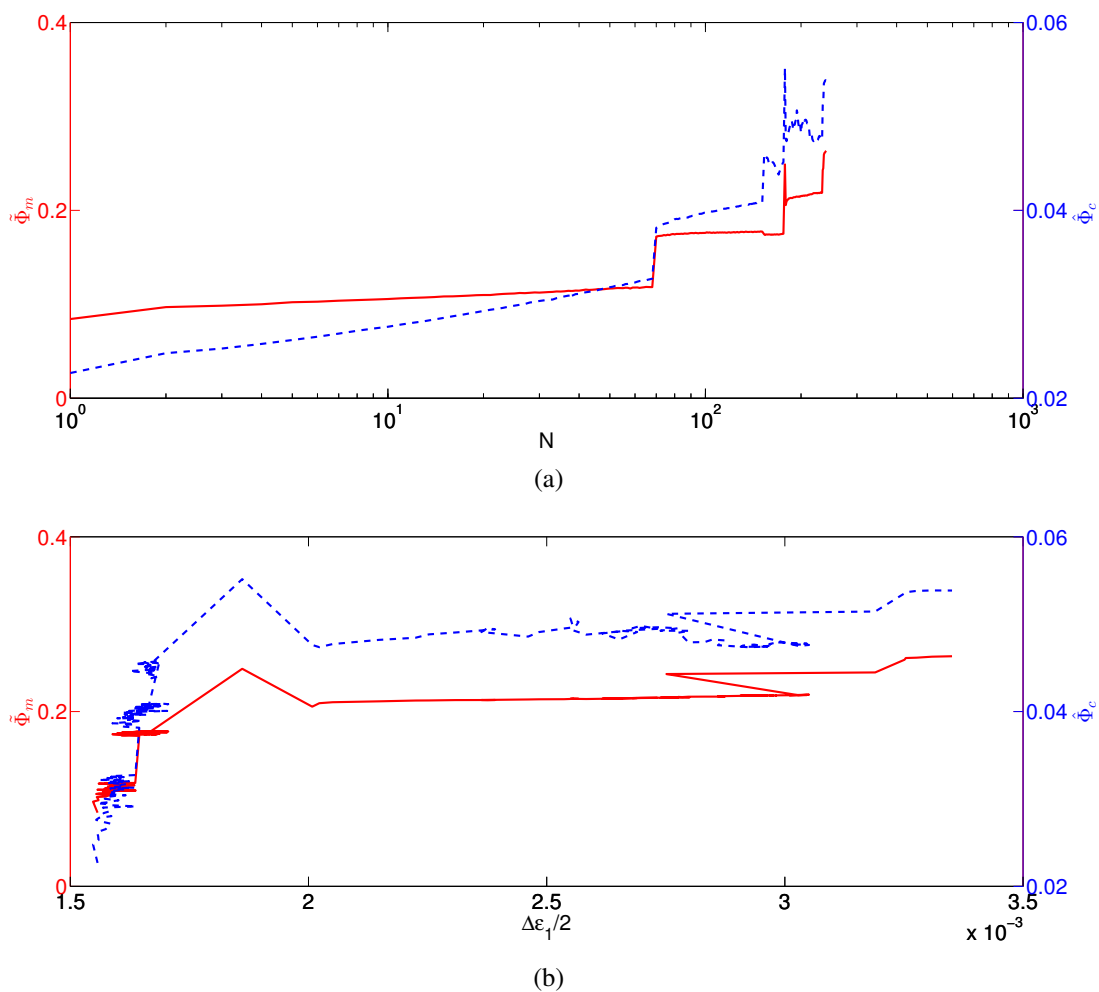


**Figure 5.6:** (a) Change of mesoscale mechanical  $\tilde{\Phi}_m$  and normalized correlation residuals  $\hat{\Phi}_c$  with the number of cycles. (b) Corresponding change of  $\tilde{\Phi}_m$  and  $\hat{\Phi}_c$  with respect to the strain amplitude  $\Delta\varepsilon_1/2$ .

FIG. 5.7 shows the maps of correlation and mechanical residuals for different numbers

of cycles. The cracks captured on the 120th cycle (FIG. 5.7(a) and (b)) are longer than at the first cycle (FIG. 5.17). Between the 120 and 130th cycle, the second “stair” was reported (FIG. 5.4) from which it was assumed that the crack network grew significantly. Residuals corresponding to cycle 230 confirm that fact since from 130 to 230 cycles more cracks initiate than from the first cycle to the 120th cycle (*i.e.*, the correlation residuals shown in FIG. 5.6(a) increases more rapidly after the 125th cycle).

From this presented test it is shown that crack initiation starts at the first cycle, which makes it easier to track with respect to the number of cycles. The correlation and mechanical residuals show even more clearly the change of crack growth regime than the mean strains. The latter ones will play a more important role to observe crack initiation in the following test case.

## 2.2 Microcrack initiation for EBE-5 test

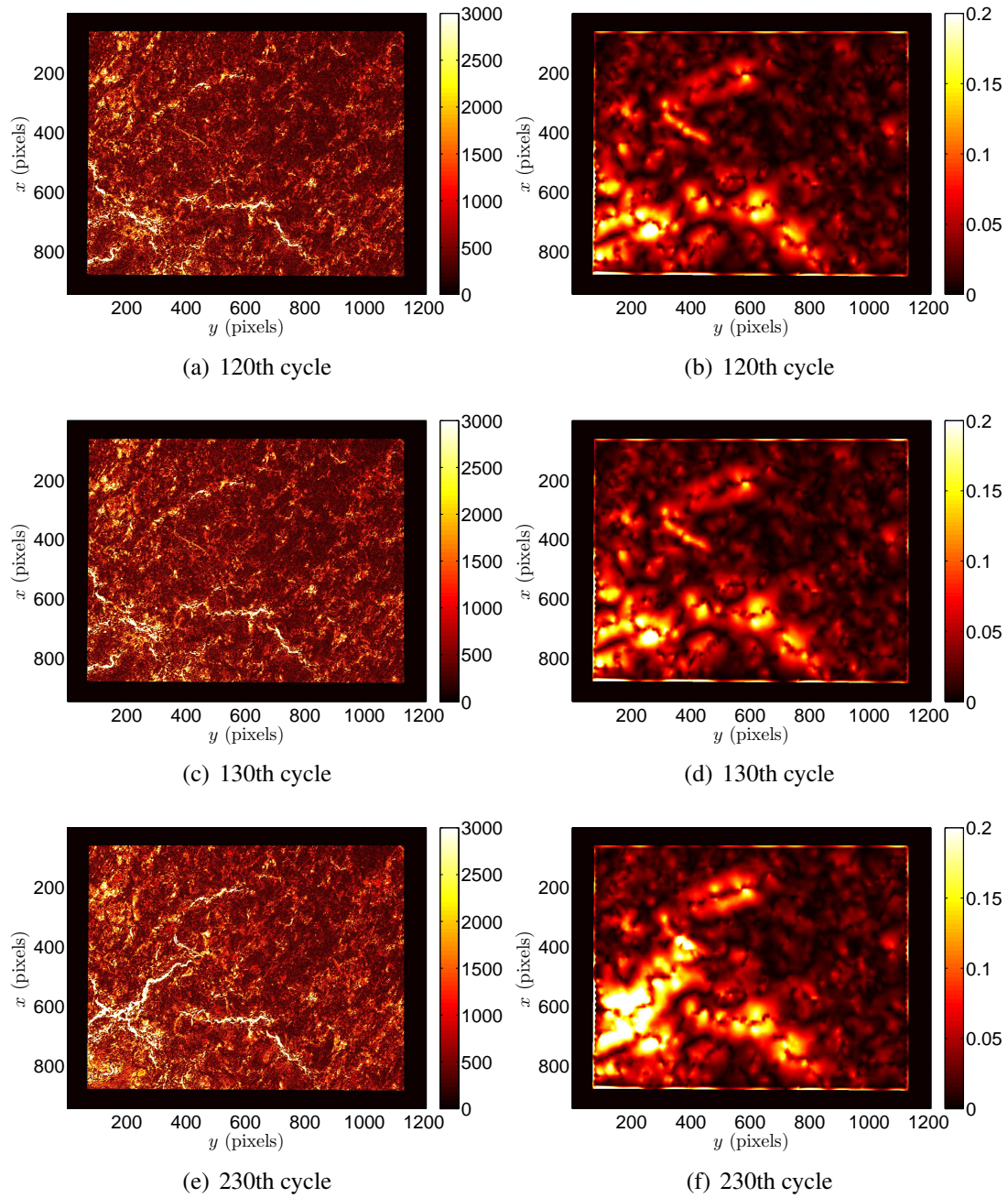
The second equibiaxial fatigue test case corresponds to EBE-5. It was cycled in tension with a maximum load equal to 20 kN. The loading history changed during the experiment. After reaching  $10^6$  cycles, the experiment was stopped and the maximum load level was increased (*i.e.*,  $F_1^{max} = F_2^{max} = 25$  kN). The sample broke for a total number of cycles equal to  $1.5 \times 10^6$ . From a DIC analysis performed on the two scales, the strain variations are evaluated in the thinned gauge zone of the cross-shaped specimen. FIG. 5.8 shows the mean eigen strain histories obtained from DIC gauge at the mesoscale. The maximum strain level equals 0.1 %. When compared with the strain level of the previous test (FIG. 5.1) a linear response is observed. A very good coincidence is noted between the two measured eigen strains. As opposed to the EBE-1 experiment (*i.e.*,  $F_{max} = 50$  kN) the unloading in the first cycle leads to the same level as at the reference point. From this result it can be concluded that the central part of the sample is not as damaged as in the previous case, which makes it more challenging to detect microcracks.

The correlation and mechanical residual maps are shown in FIG. 5.12. For the first loading cycle uniform correlation residuals (FIG. 5.12(a)) are reported. This fact corresponds to a very good match between the reference and corrected deformed image. Mechanical residuals (FIG. 5.12(b)) show rather low fluctuations, which are interpreted as microcracks.

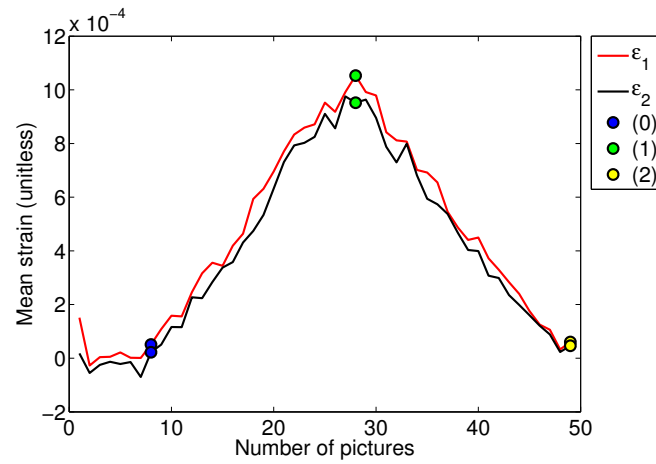
During a fatigue investigation damage may occur. One variant of such phenomena are microcracks that commonly appear when quasi-brittle materials are considered. Since small displacements occur it is a challenge to access to the very beginning of microcrack initiation. There is no defined conventional criterion (*i.e.*, threshold) that can be applied for the definition of the displacement discontinuity. However, the data obtained from regularized correlation (*i.e.*, mechanical residuals ( $\tilde{\Phi}_m$ ) and normalised correlation residuals ( $\hat{\Phi}_c$ )) can be used to give a better estimate of the crack network growth.

Since no cracks were detected for the first cycle correlation and mechanical residuals are extracted for a larger number of applied loads. FIG. 5.10 illustrates the correlation between  $\tilde{\Phi}_m$  and  $\hat{\Phi}_c$  residuals. Over the whole range of  $1.5 \times 10^6$  cycles a correlated increase of both residuals is noted. Both quantities can therefore be used for detection purposes.

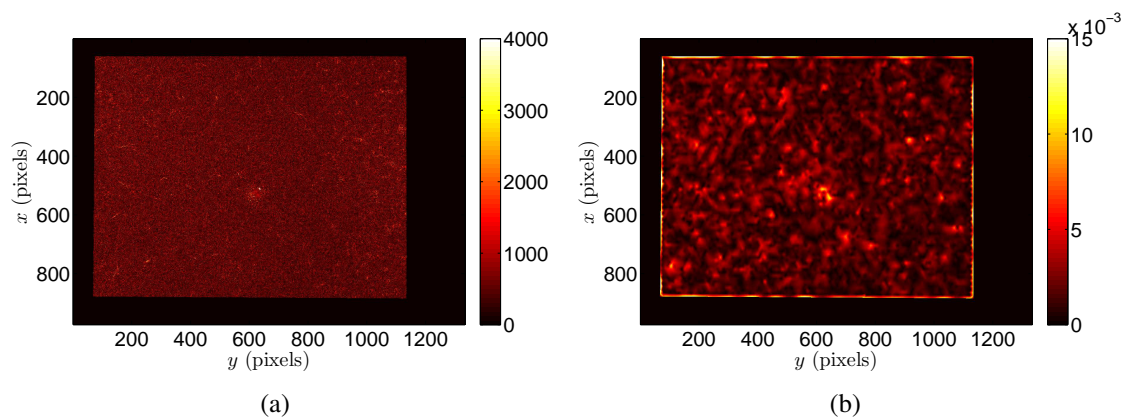




**Figure 5.7:** Mesoscale gray level (left) and mechanical (right) residual maps corresponding to the maximum applied load level

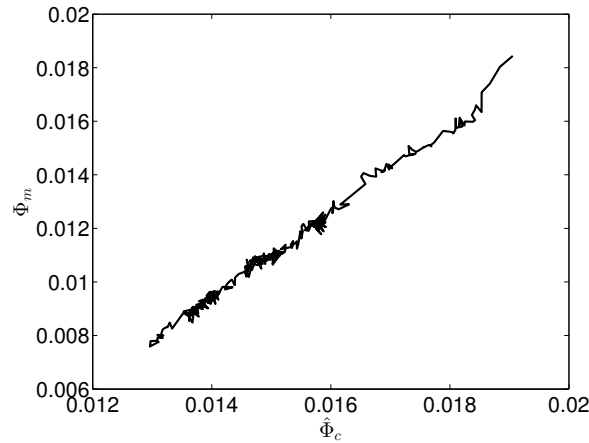


**Figure 5.8:** Mean eigen strains for the first cycle of equibiaxial experiment 5 (*i.e.*,  $F_{max} = 20$  kN). Blue, green and yellow circles correspond to the three characteristic points of the three equibiaxial experiments (FIG. 4.5(a))



**Figure 5.9:** (a) Gray level and (b) mechanical residual maps corresponding to a maximum applied load  $F_1 = F_2 = 20$  kN for the first cycle

The mean eigen strains can also be studied (FIG. 5.11(a)) at macro and mesoscales. In the present case fluctuations of  $\Delta\varepsilon_1/2$  are noted on both scales, they are higher than those observed on the residuals (FIG. 5.11(a)).



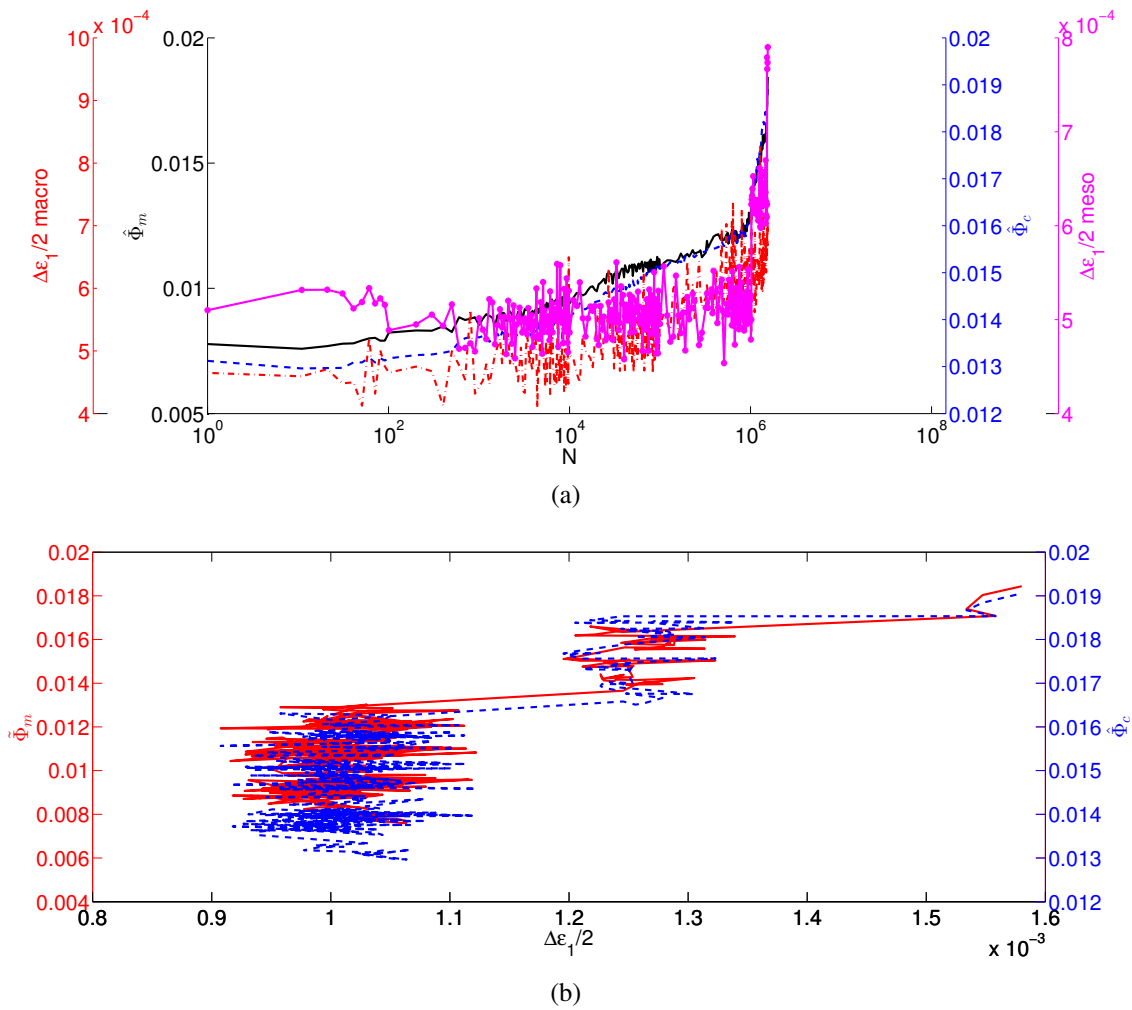
**Figure 5.10:** Correlation between mechanical ( $\tilde{\Phi}_m$ ) and normalised correlation ( $\hat{\Phi}_c$ ) residuals from whole series of images acquired in experiment EBE-5

FIG. 5.11(b) shows the change of correlation and mechanical residuals as functions of the maximum eigen strain amplitude extracted at a mesoscale. For the first  $10^6$  cycles strain fluctuations of the order of 0.02 % are observed. On the contrary correlation and mechanical residuals have a steady increase. From the strain amplitudes it is very difficult to get an information about the presence of a crack network. The strain level increases more significantly as the maximum load increases. Strain fluctuations captured after  $10^6$  cycles correspond to those reported when a maximum load of 20 kN is prescribed. At the very end of the experiment a significant increase of  $\Delta\varepsilon_1/2$  is noted.

FIG. 5.12 shows gray level residual maps. Smaller discontinuities are detected with higher values of the residuals for the 10,000th cycle. As the sample was cycled the microcracks started to grow. A significant increase of discontinuities is reported from 10,000 to 50,000 cycles. When the previous test was analysed one big crack was formed before the specimen broke. In the present test it was not the case. On the image acquired after  $1.55 \times 10^6$  cycles a group of randomly distributed microcracks has initiated. The failure was sudden and without the stable coalescence of a macrocrack.

### 2.3 Results of equibiaxial fatigue campaign

A series of five biaxial experiments with proportional (*i.e.*, equibiaxial) loading histories has been carried out on the multiaxial servo-hydraulic testing machine ASTREE. (TAB. 5.3). In the previous sections two different tests were studied considering the crack network formation. The mean eigen strain amplitudes are compared. As expected decreasing the load level causes an increase of the life time (TAB. 5.3). The lowest number of cycles (*i.e.*, 241) is reported when the maximum load is equal to 50 kN.



**Figure 5.11:** (a) Change of mesoscale mechanical  $\tilde{\Phi}_m$  and normalized correlation residuals  $\hat{\Phi}_c$  with the number of cycles. For comparison purposes  $\Delta\varepsilon_1/2$  are reported at macro and mesoscales. (b) Change of  $\tilde{\Phi}_m$  and  $\hat{\Phi}_c$  with the strain amplitude  $\Delta\varepsilon_1/2$  at the mesoscale

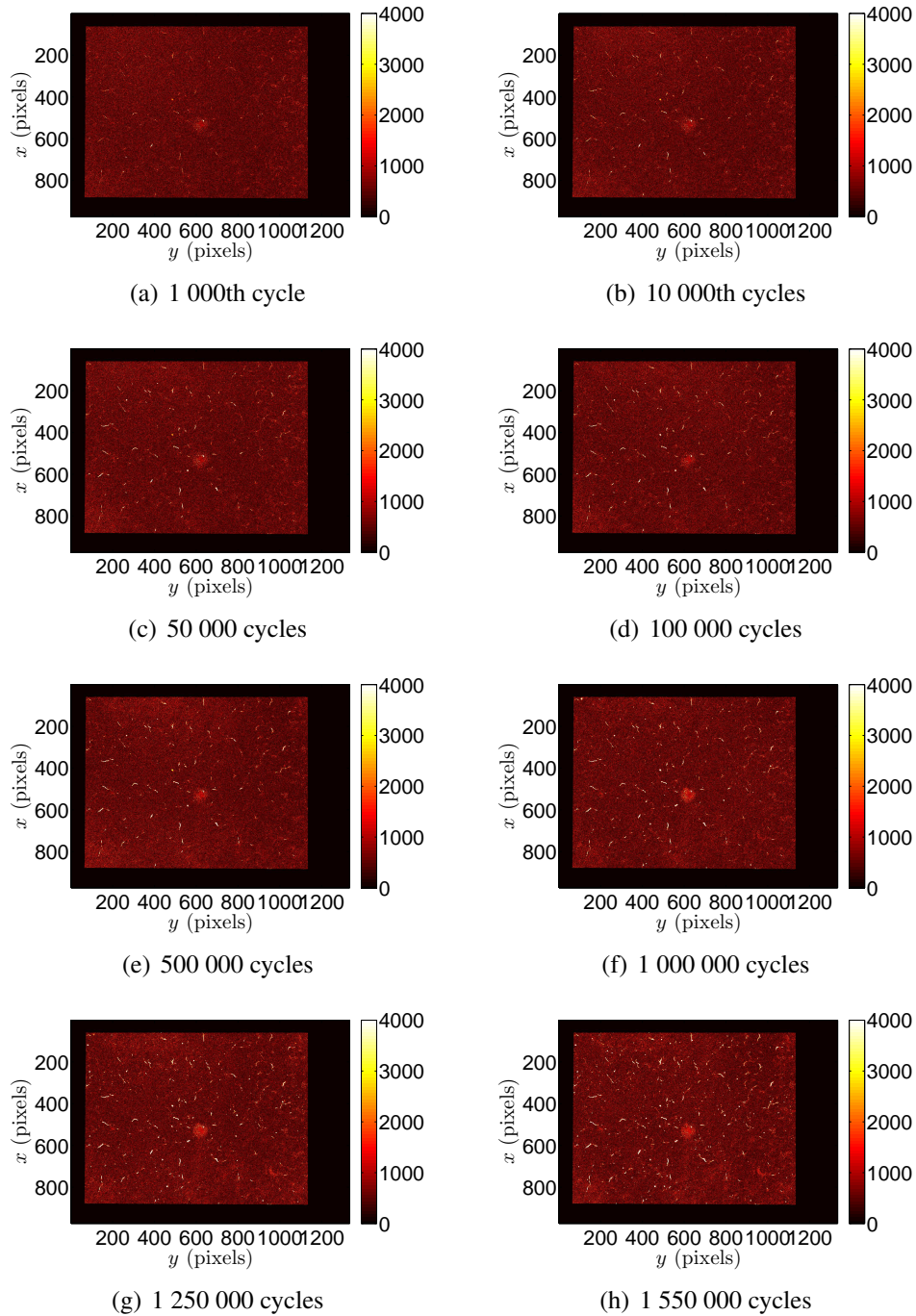


**Figure 5.12:** Correlation residual maps for different cycle number

**Table 5.3:** Number of cycles to failure for the equibiaxial tests

	$F_1^{max}$ (kN)	$F_2^{max}$ (kN)	$F_2^{min}$ (kN)	$F_1^{min}$ (kN)	$N_{failure}$ (cycles)
EBE-1	50	50	0.1	0.1	241
EBE-2	40	40	0.1	0.1	18 224
EBE-3	30	30	0.1	0.1	87 001
EBE-4	25	25	0.1	0.1	370 002
EBE-5	20	20	0.1	0.1	1 550 003

The experimental protocol consisted of two scale DIC analyses where two different sides were used to monitor the material response. FIG. 5.13 and FIG. 5.14 show the strain histories for the equibiaxial loading regime. Higher fluctuations of the strain amplitudes are noted at the macroscale since less elements (and pixels) are used to calculate the displacement and strains. When observing the mesoscale strain amplitudes for  $\epsilon_1$  and  $\epsilon_2$  lower fluctuations are observed.

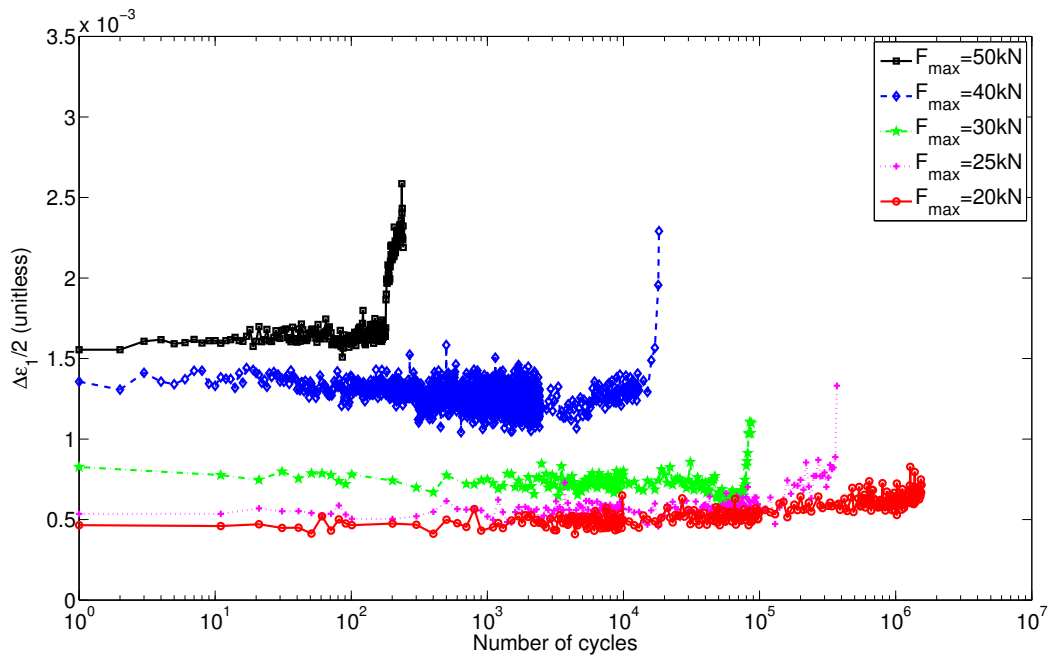
### 3 “Snail” fatigue experiments

The second series of fatigue experiments considers five non-proportional (*i.e.*, “snail”) loading paths. The cyclic experiment presented in CHAP. 4 reported approximately equal load level at which sample was broken for both loading regimes. The aim is to compare the fatigue behaviour for equibiaxial and complex loading cases. For comparison purposes the loading history of the “snail” regime was chosen with the same load levels (TAB. 5.1). The “snail” fatigue experiments are performed in a fully load-controlled mode. Two-scale images are used to monitor the sample surfaces. From the acquired images the mean strain levels are estimated with a DIC gauge. Two different cases (as for the equibiaxial loading regime) are considered to study microcrack initiation. The SBE-2 test is chosen for which microcracks are detected at the first loading cycle while cracks initiated at a later stage for SBE-5 test. The validation of the kinematic hardening model is performed on the SBE-1 test.

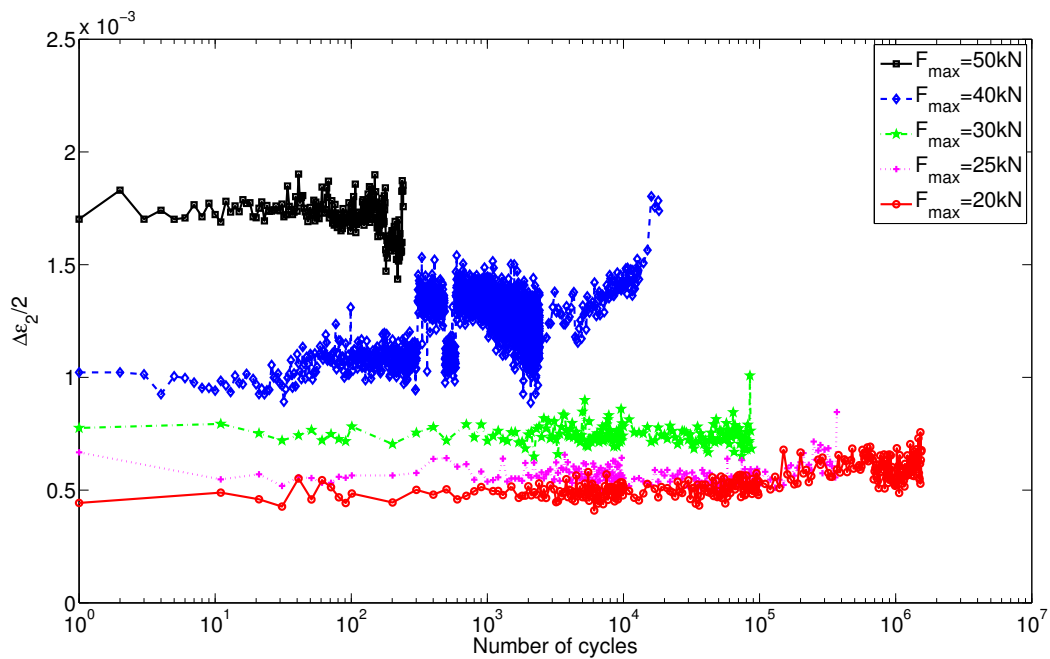
#### 3.1 Validation of the kinematic hardening law

The elastoplastic parameters of the “snail” loading regime were determined in CHAP. 4. Thus, these parameters will be compared with the first cycle of a fatigue “snail” test with the same maximum load level as in Section 2 (*i.e.*,  $F_{1,2}^{max} = 50$  kN). This experiment is chosen since the highest stress level are applied, which yields the highest sensitivities to the sought parameters (*i.e.*,  $\sigma_y$ ,  $C$  and  $\gamma$ ). The analysis of SBE-1 test follows the same experimental and identification protocol as the EBE-1 experiment (see Section 2).

The validation procedure is conducted with the FEMU-UF procedure using 210 load-levels that correspond to the number of acquired images. The Young’s modulus was

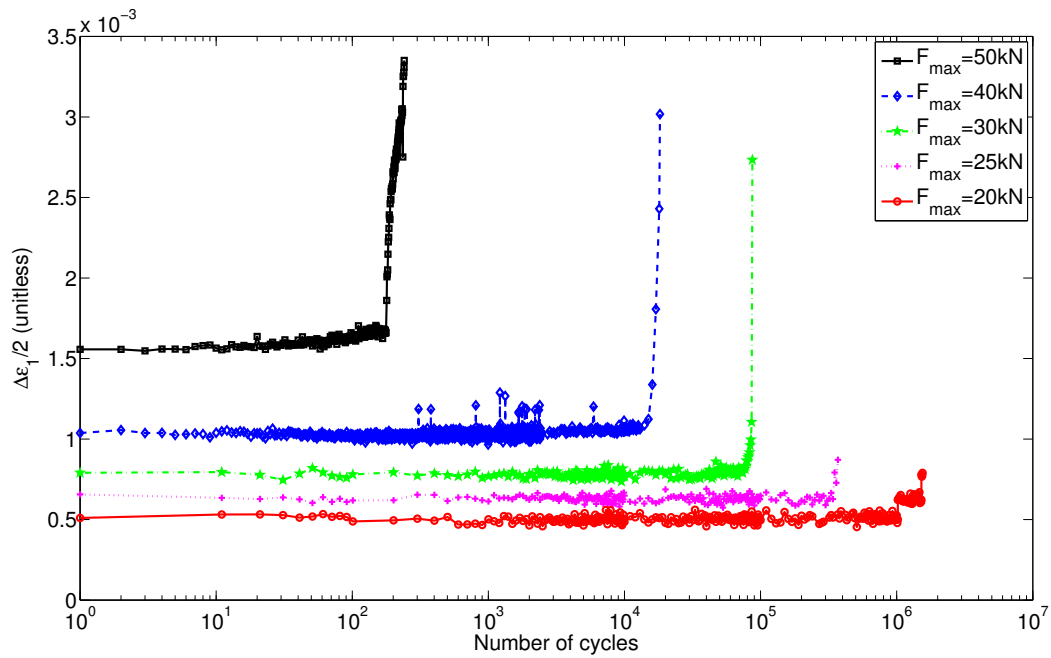


(a)

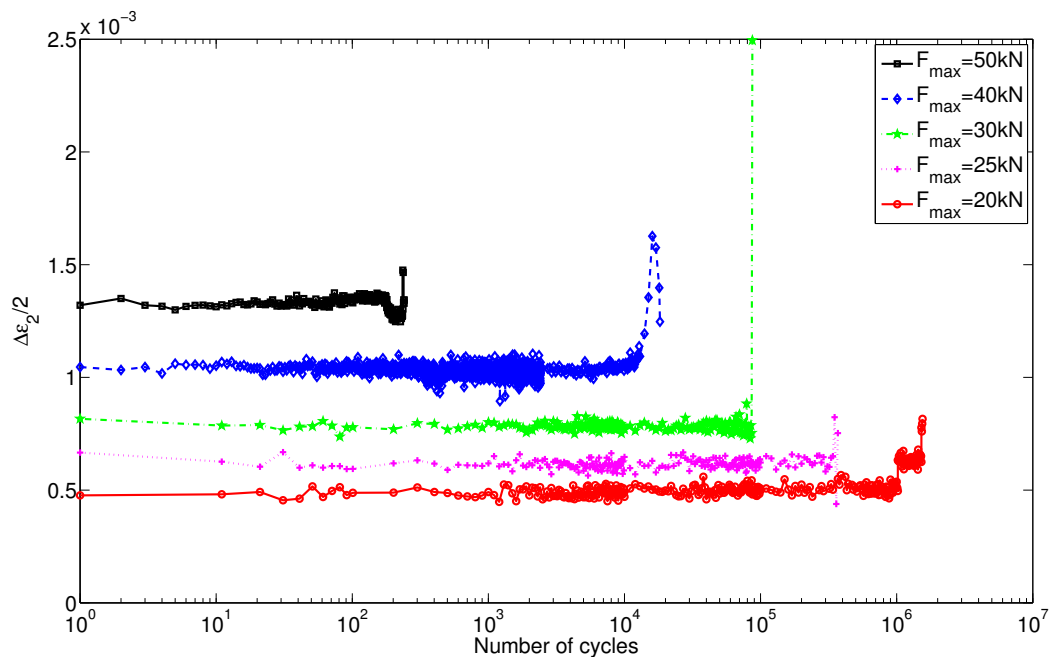


(b)

**Figure 5.13:** History of (a) maximum mean eigen and (b) minimum mean eigen strain amplitudes observed at the macroscale



(a)



(b)

**Figure 5.14:** History of (a) maximum mean eigen and (b) minimum mean eigen strain amplitudes observed at the mesoscale



validated on 27 images, which were taken in the elastic domain (*i.e.*,  $F_1 = 20$  kN and  $F_2=0$  kN). Small changes are noted between the initial and identified Young’s moduli (TAB. 5.4).

The kinematic hardening parameters describing Armstrong-Frederick’s model were taken from previously identified values (TAB. 4.7). The latter yield greater differences in the residuals when compared with the results obtained with the proportional loading path (see Section 2). The displacement error is equal to 0.14 pixel while the equilibrium gap  $\chi_F$  equals 2.23 kN.

FIG. 5.15 shows the comparison between the measured force and sum of reaction forces computed with the reference and identified parameters. Higher force residuals are observed in the loading direction 2 ( $\chi_{F2} = 2.8$  kN and  $\chi_{F1} = 1.2$  kN). It is interesting to note that during the first loading step  $F_2$  starts to increase even though it should be constant (*i.e.*,  $F_2 = 0$ ). This increase starts when the 20-kN level (defined earlier as the elastic limit) is reached in the loading direction 1. The observed phenomenon is presumably related with the damage inception (*i.e.*, debonding between the ferritic matrix and the graphite nodules) in the elastic domain observed by DVC (see CHAP. 3).

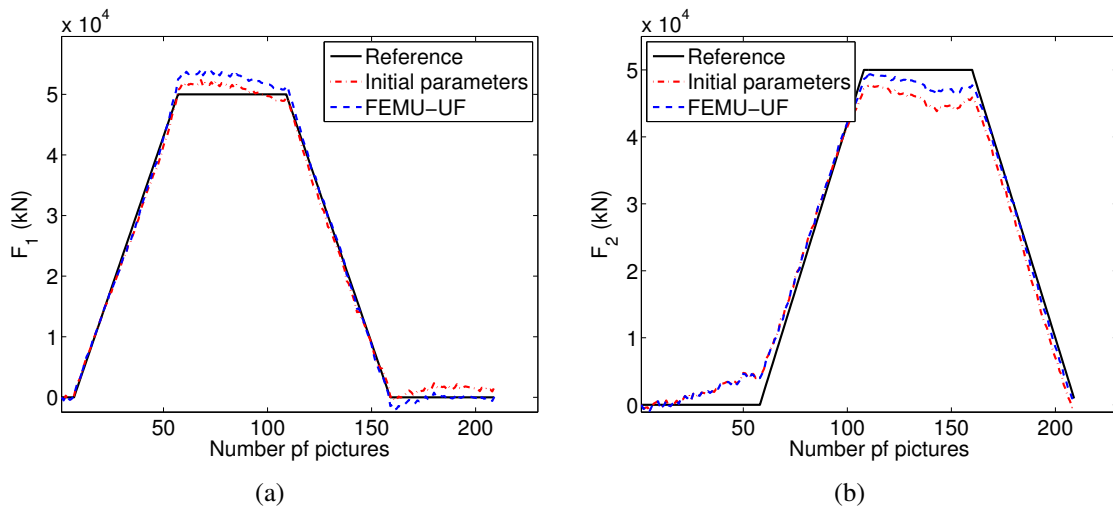


**Figure 5.15:** Comparison of measured force and sum of reaction forces computed with initial and identified parameters for Armstrong-Frederick’ constitutive law

Furthermore, damage initiates in the form of a crack network in the central zone of the cross-shaped sample may also yield higher displacement errors ( $\chi_u$ ). It is important to emphasise that failure occurred on the SBE-1 experiment just after 10 cycles (TAB. 5.5), which leads to the conclusion that the first loading cycle has induced high levels of damage. After 4 cycles a sudden increase of strain amplitude is noted (see FIG. 5.27).

The identified parameters induce a decrease of residuals  $\chi_u$  and  $\chi_F$  when compared with the reference values. Both yield stress  $\sigma_y$  and hardening modulus  $C$  change only slightly in comparison with the hardening parameter (*i.e.*, an increase of 50 % is reported) which yields a decrease of the equilibrium gap  $\chi_F$  of 0.5 kN. The identification/validation

of the parameters carried out on the first cycle of a non-proportional fatigue experiment is in acceptable agreement with the cyclic “snail” experiment (TAB. 5.4).

**Table 5.4:** Initial and identified Armstrong-Frederick’s parameters via FEMU-UF for a snail loading path

Parameter	$E$ (GPa)	$\nu$	$\sigma_Y$ (MPa)	$C$ (GPa)	$\gamma$	$\chi_u$ (pixel)	$\chi_F$ (kN)
Reference	160	0.28	289	21	45	0.14	2.22
FEMU-UF	157	0.28	295	29	91	0.13	1.74

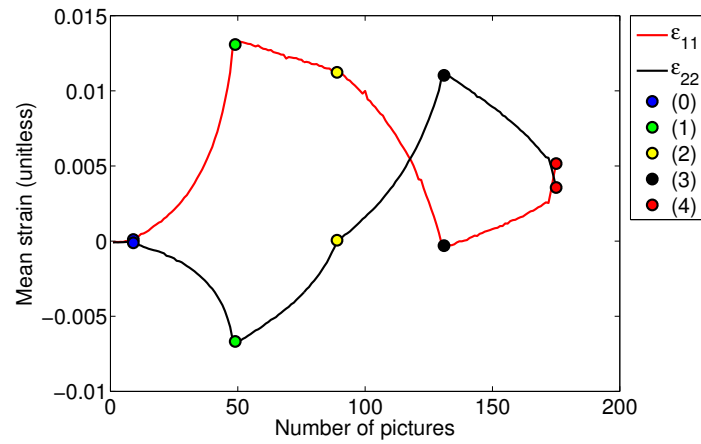
## 3.2 Analysis of experiment SBE-2

### 3.2.1 Crack network formation in the first loading cycle

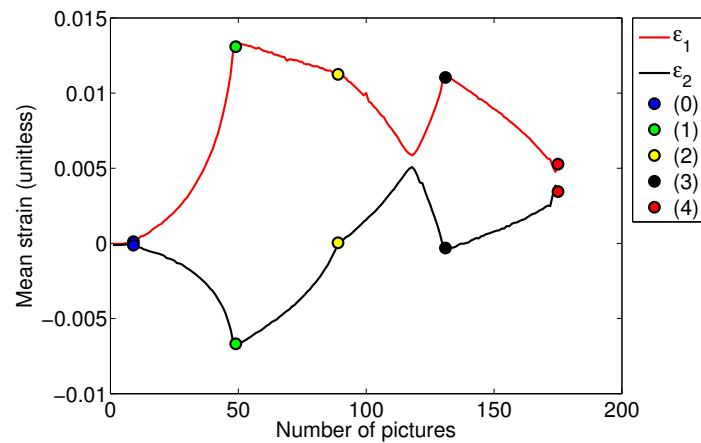
As noted in CHAP. 4 “snail” loading histories lead to more complex material responses as opposed to equibiaxial loadings (see FIG. 4.29 and 4.30). FIG. 5.16 shows the strain response to a snail loading for the first cycle. Four characteristic points are considered. The strain components in the loading direction of the sample (FIG. 5.16(a)) have a more complex response than observed for equibiaxial tests (see FIG. 5.1(a)). When the first axis (*i.e.*, 1-direction) is loaded, the other one has a constant load level (see CHAP. 4) and vice versa. The strain levels reach higher values (*i.e.*, 1.5 %) than those obtained for the equibiaxial history (*i.e.*, 0.86 %). The strain during the unloading phase of the second axis (*i.e.*, unloading in the 2-direction) does not return to the reference point, which can be interpreted as combined effects of plasticity and damage.

The maximum and minimum eigen strains follow different paths than the normal strain in the loading directions of the sample. FIG. 5.16(b) shows how  $\epsilon_1$  and  $\epsilon_2$  change during the loading/unloading sequence. At the beginning of the experiment the maximum eigen strain corresponds to the normal strain along the first loading axis. This is observed until the first axis starts to unload. When  $\epsilon_{22}$  overcomes  $\epsilon_{11}$  the maximum eigen strain changes direction and follows the path of  $\epsilon_{22}$ . In the following the mean eigen strains will be used for calculating the strain amplitude. Even though it can be noted that the biggest difference of eigen strains is reached between the reference and the first loading stage (FIG. 5.16(b)) the strain amplitude will be taken as the difference of the strain level at the first characteristic point (*i.e.*, point 1) and the last one (*i.e.*, point 4).

The test SBE-2 is taken as an example for which the crack network forms at the first loading cycle. FIG. 5.17 shows the correlation and mechanical residuals obtained for the first cycle corresponding to point 1 (FIG. 5.16(b)). The correlation residual map (FIG. 5.17(a)) indicates that the gauge zone of the cross-shaped sample is more affected by damage than EBE-1 (FIG. 5.1(a)). It is necessary to emphasise that more microcracks are detected in the present case even though the maximum load level is lower by 10 kN in comparison with EBE-1. Mechanical residuals (FIG. 5.1(b)) also show more microcracks.



(a)



(b)

**Figure 5.16:** Strain histories describing the first cycle of “snail” experiment 2 ( $F_{max} = 40$  kN). (a) Normal strain for the two loading directions. (b) Mean eigen strains. Blue, green, yellow, black and red circles correspond to five characteristic points of “snail” experiment (see FIG. 4.5(b))

The size of the cracked zone is bigger than for the equibiaxial case. The residual maps confirm the assumption that the “snail” path is more damaging than an equibiaxial one.

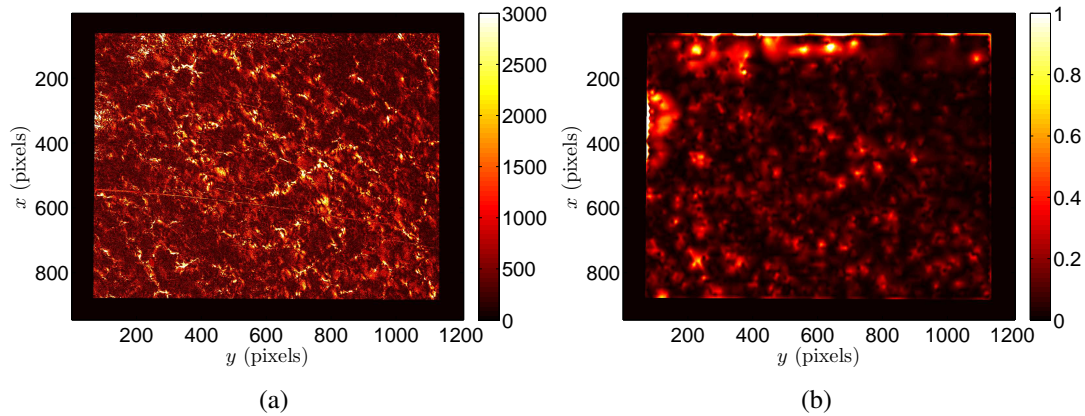


**Figure 5.17:** (a) Gray level and (b) mechanical residual maps corresponding to the maximum applied load level (*i.e.*,  $F_1 = F_2 = 40$  kN)

In the sequel the mean strain data will be analysed in order to study their changes with the number of cycles.

### 3.2.2 Strain history in SBE-2 experiment

From the whole series of images acquired during the SBE-2 experiment displacement fields were measured with RT3-DIC. The mean strain histories are assessed on two scales as explained in previous sections. FIG. 5.18 illustrates the strain histories of the “snail” experiment. From the presented mean eigen strain histories the levels increase until the 100th cycle when the experiment was interrupted.

In order to see how the detected increase of strain levels reflects the material response the strain amplitudes were determined from the peak values of the strain histories (*i.e.*, minimum and maximum strain levels for a given cycle). FIG. 5.19 shows the strain amplitudes evaluated on both scales. Differences between the macro and mesoscales equal 0.05 %. One of the reasons may be spurious flexure, another one may be due to the fact that the crack network is not identical. Since the mesoscale observations better capture the crack network it results in higher strain levels. However, strain amplitudes on both scales follow the same trend. After 10 cycles the strain amplitudes start to increase until the experiment is stopped due to data acquisition problems. This has caused the sudden drop of measured strains (FIG. 5.18) and their amplitudes (FIG. 5.19). The gap is more evident on the  $\epsilon_2$  and  $\Delta\epsilon_2/2$  data. The  $\epsilon_1$  strain history (FIG. 5.18(a)) does not report the stair, which leads to the conclusion that it did not accelerate the crack network growth.

In the following the evolution of the normalised correlation and mechanical residuals are studied to better capture the fatigue behaviour of the investigated material.

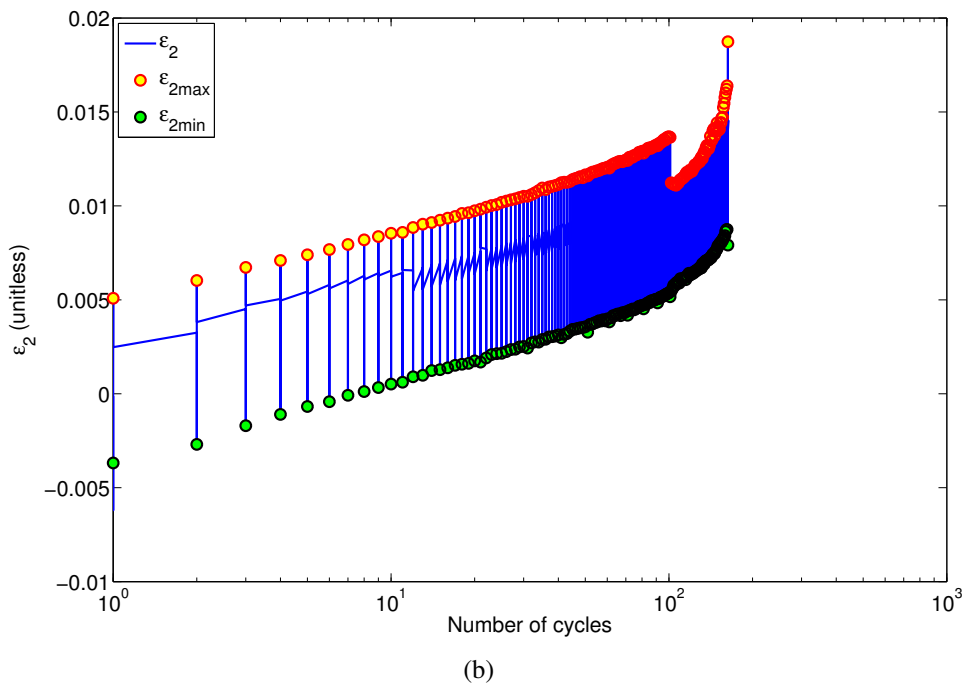
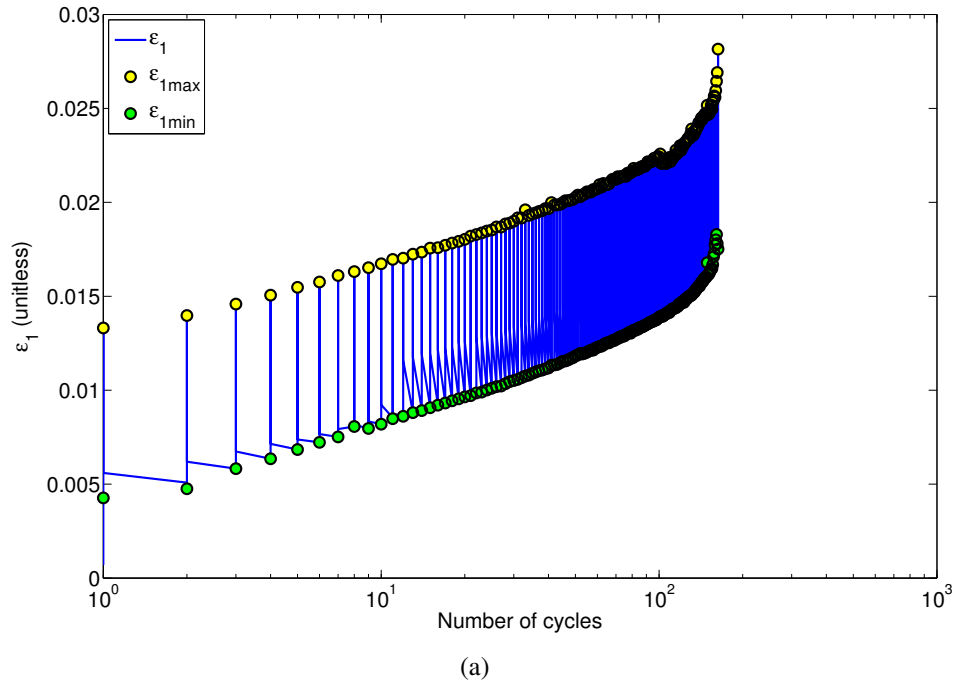
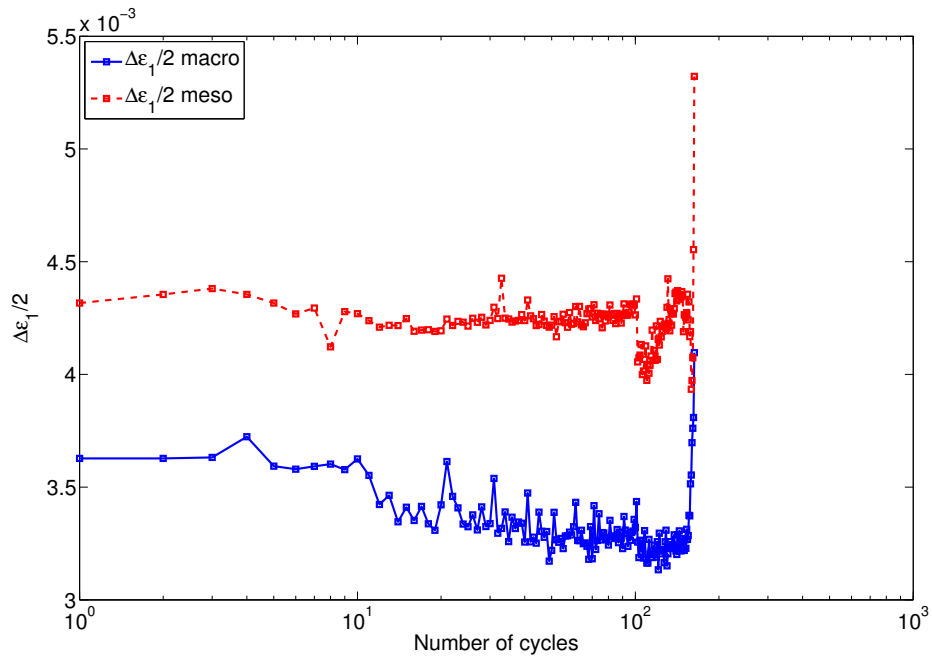
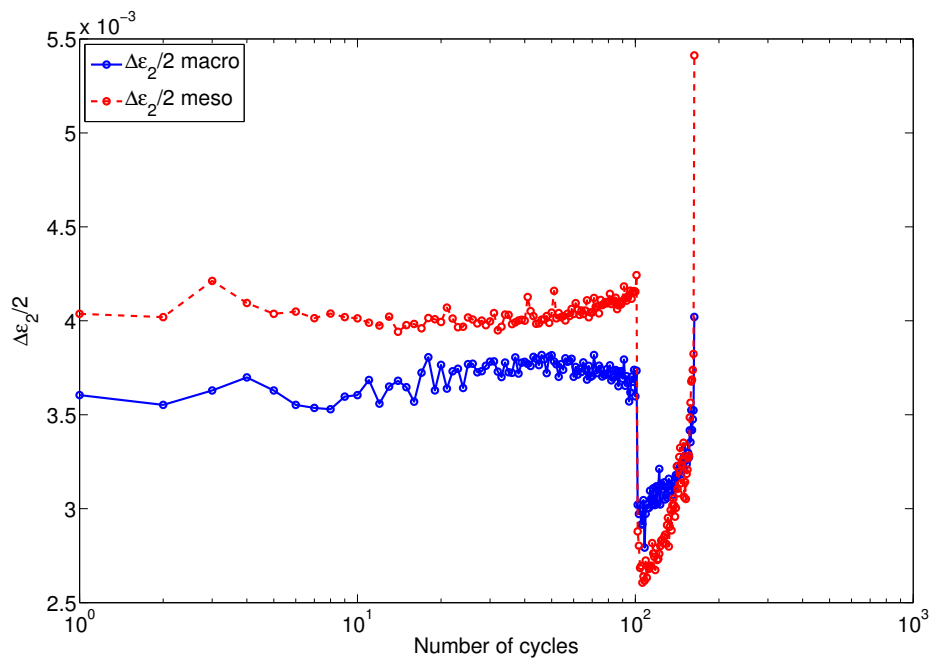


**Figure 5.18:** Measured (a)  $\epsilon_1$  and (b)  $\epsilon_2$  history. The maximum peak values are depicted with yellow circles and minimum with green circles



(a)



(b)

**Figure 5.19:** Measured strain amplitudes (a)  $\varepsilon_1$  and (b)  $\varepsilon_2$  at macro and mesoscales

### 3.2.3 Crack network formation

The normalised correlation and mechanical residuals exhibit less fluctuations than those observed on the strain data. The increase of residuals is easier to detect in order to determine the crack network growth. FIG. 5.20(a) shows the change of  $\hat{\Phi}_c$  and  $\tilde{\Phi}_m$  with respect to the number of cycles. It is noted that until the third cycle a steady state is observed. In the following cycles their levels gradually increases, which indicates that more cracks are formed. After 163 cycles the sample is broken.

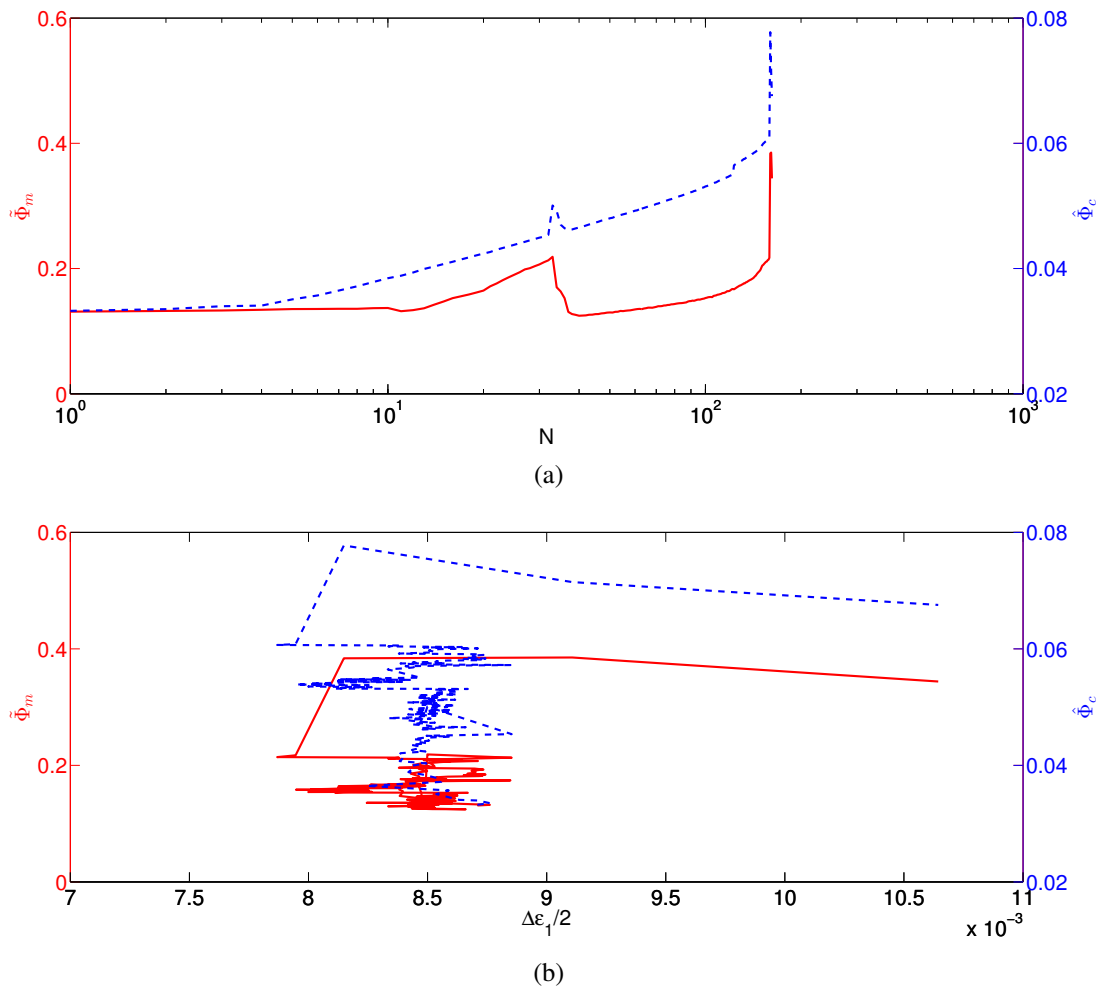


**Figure 5.20:** (a) Change of mechanical  $\tilde{\Phi}_m$  and normalized correlation residuals  $\hat{\Phi}_c$  with the number of cycles. (b) Change of  $\tilde{\Phi}_m$  and  $\hat{\Phi}_c$  with respect to the strain amplitude  $\Delta\varepsilon_1/2$  at the mesoscale

FIG. 5.21 shows the residual maps for different cycles. The crack network grows gradually as the number of cycles increases. Less fluctuations are seen for the first 50 cycles. In the following cycles the crack network formation is better revealed as crack branches are randomly initiated. Higher mechanical residuals were also reached after 100

cycles. In the middle of the figure at the 100th cycle a macrocrack started to be formed (FIG. 5.21(c)) and in the sequel (FIG. 5.21(d)) this crack dominates. The mechanical residual maps are very similar to the correlation residuals.

### 3.3 Microcrack initiation in SBE-5 test

The initiation of microcracks will be investigated for the SBE-5 experiment where the maximum load equals 20 kN. Before studying the mean strains over the whole series of images acquired during the test, the strain response in the first cycle is analysed (FIG. 5.22). For the first two loading steps a linear material response is detected. When the first axis is unloaded (FIG. 5.22, point (2) to (3)) a nonlinear response occurs. This is due to microdamage caused by debonding. The maximum value  $\epsilon_1 = 0.4\%$  is reached at the third loading point. Hence, the strain amplitude of the maximum eigen strain is defined as the difference between the third and fourth loading points of the snail loading path (see FIG. 5.23 and FIG. 4.5(b)).

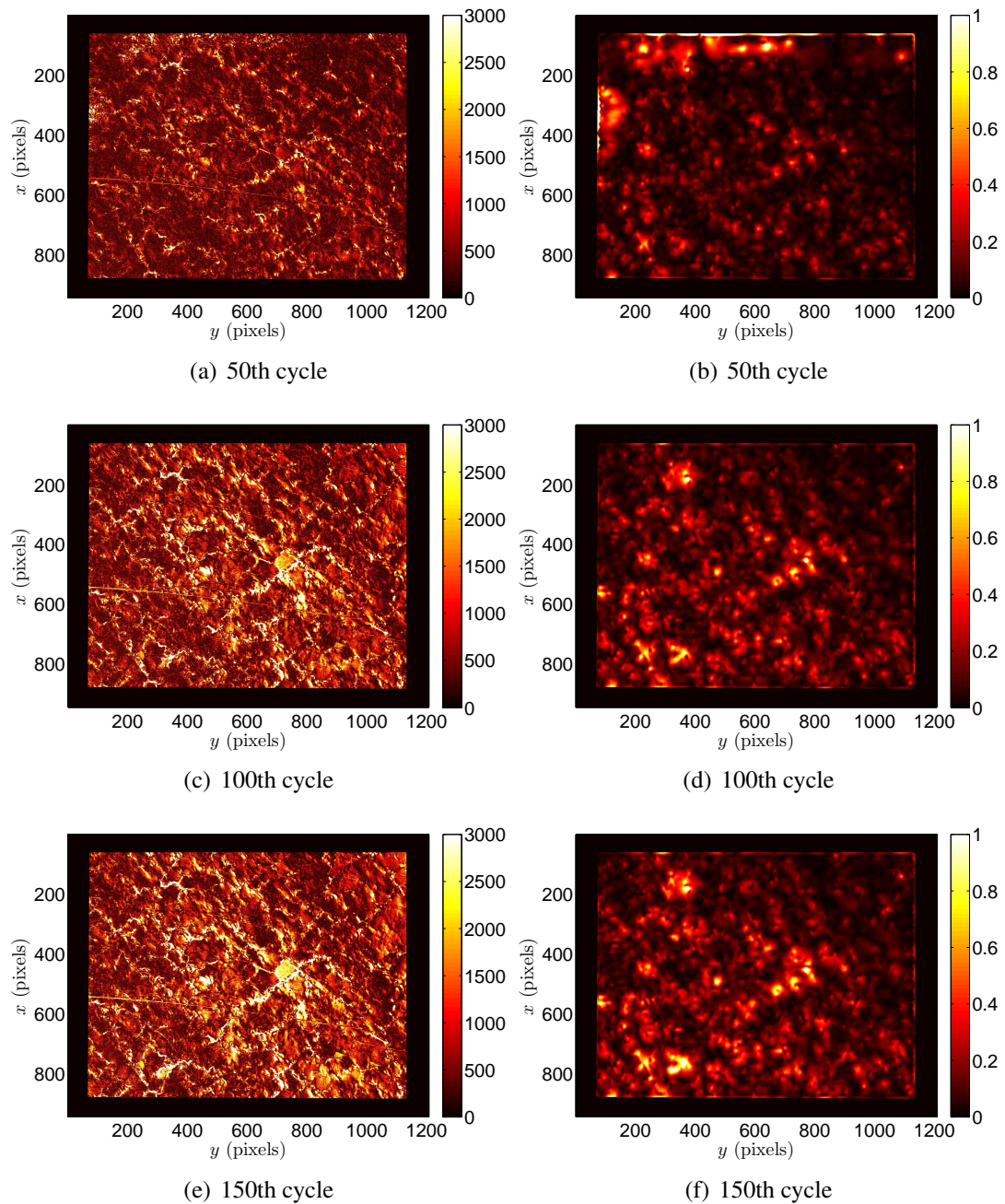
FIG. 5.23 shows the residual maps obtained for the maximum level of  $\epsilon_1$ . In the correlation residuals no area points out a discontinuity even though the strain history has shown a nonlinear response. Mechanical residuals (FIG. 5.23(b)) show more fluctuations but it is not possible to claim that microcracks have initiated in the observed zone.

Since the maps of correlation and mechanical residuals do not capture any discontinuities for the first cycle it can be concluded that the crack network is not formed. In order to evaluate the fatigue behaviour the mean eigen strain amplitudes are assessed on both scales (FIG. 5.24(a)). A very good correspondance is noted between the amplitudes  $\Delta\epsilon_1/2$  on macro and mesoscales where no significant changes occur until 60,000 cycles.

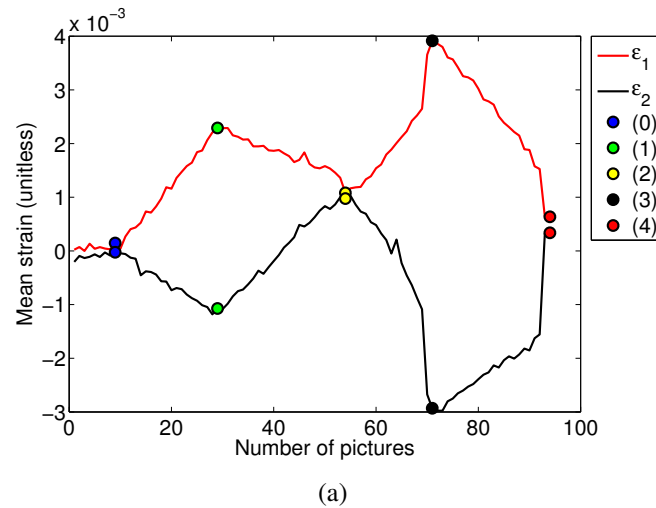
The corresponding correlation residuals are illustrated in FIG. 5.25. The first detected discontinuity (FIG. 5.25(e)) corresponds to 50,000 cycles. For comparison purposes the normalised correlation and mechanical residuals are shown in (FIG. 5.24(a)) as functions of the strain amplitude. No significant change is observed before 60,000 cycles. The maximum eigen strain amplitude analysed on meso scale follows the same trend as the residuals. The macroscopic strain amplitude also increases less since microcracks are captured as easily as on the mesoscale. Comparing the residual maps obtained at 100,000 cycles (FIG. 5.25(f)) with the previous ones, a very significant difference is noted, namely, one dominant macrocrack has formed. Since the crack surface was sliding between 50,000 and 100,000 cycles the metal dust started to appear on the surface of the sample. This leads the residuals to increase in the center of the observed ROI since the conservation of gray levels is violated. As the number of cycles increases more dust is produced (FIG. 5.25(g) and (h)).

FIG. 5.24(b) shows the change of normalised correlation and mechanical residuals as functions of the maximum strain amplitude. The two residuals follow the same trend. At the beginning of the test very small fluctuations are observed. Conversely, when microcracks initiate (after 50,000 cycles) an increase of strain amplitude is noted.





**Figure 5.21:** Gray level (left) and mechanical (right) residual maps corresponding to the maximum applied load level for different cycle numbers



**Figure 5.22:** Mean eigen strains for the first cycle of “snail” experiment 5 ( $F_{max} = 20$  kN). Five characteristic points (FIG. 4.5(b)) of “snail” experiment depicted

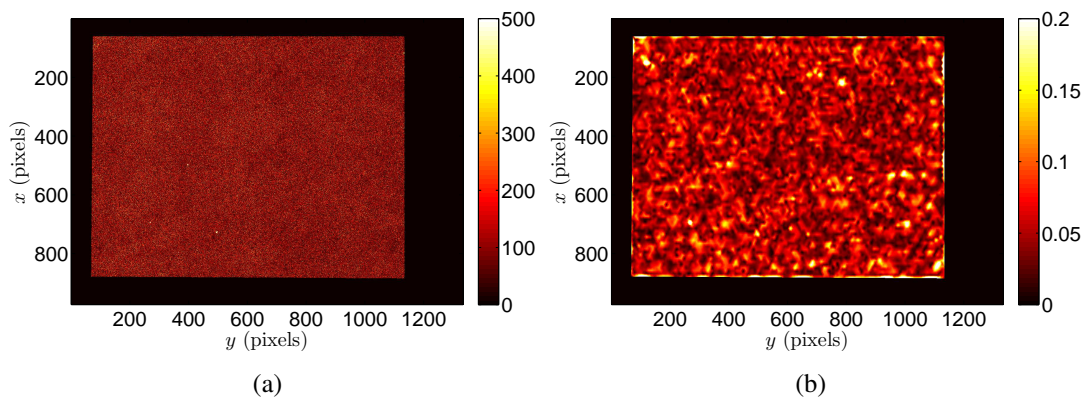


**Figure 5.23:** (a) Gray level and (b) mechanical residual maps corresponding to the load level when the maximum value of  $\epsilon_1$  is reached (*i.e.*,  $F_1 = 0, F_2 = 20$  kN) for the first cycle

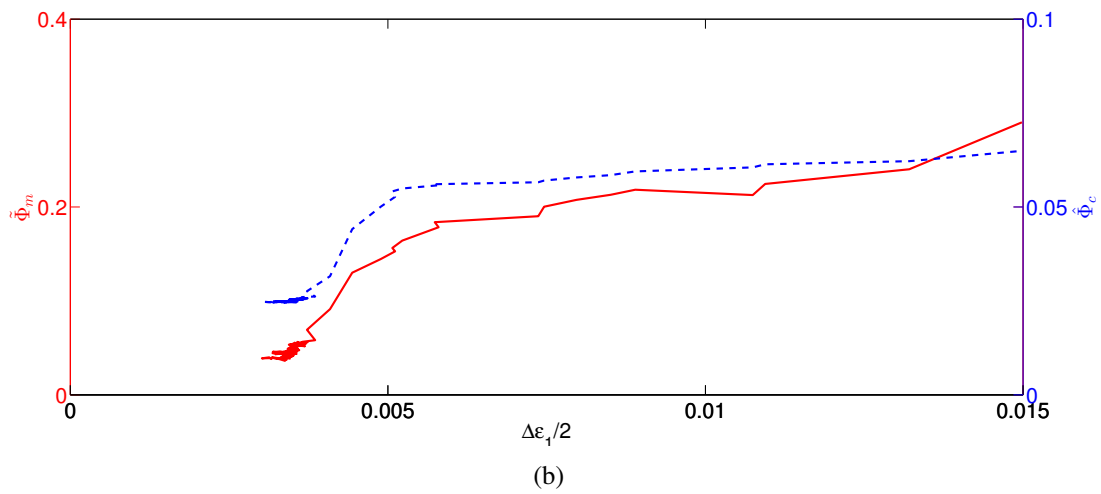
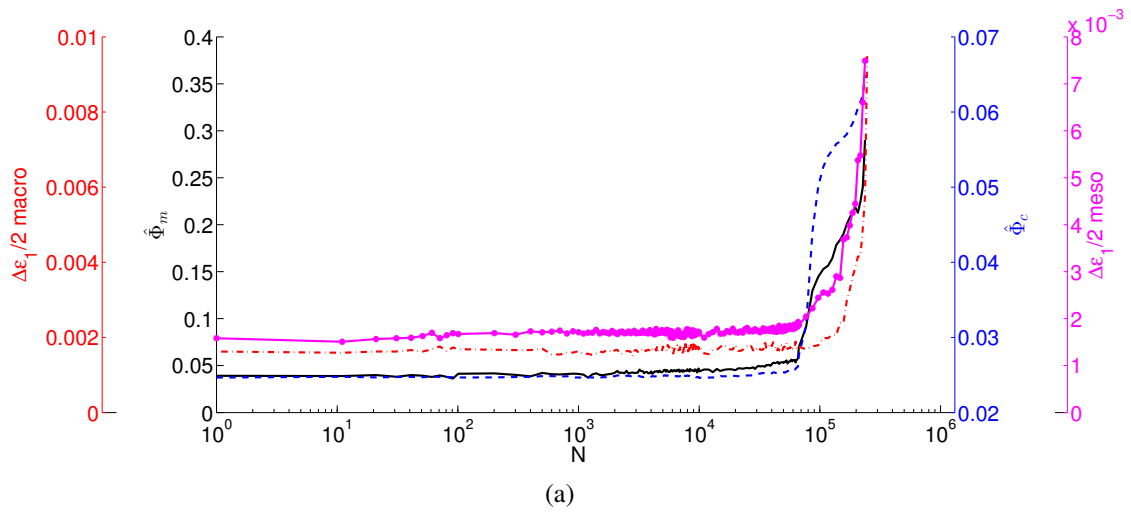


**Figure 5.24:** (a) Change of mesoscale mechanical  $\tilde{\Phi}_m$  and normalized correlation residuals  $\hat{\Phi}_c$  with the number of cycles. For comparison purposes  $\Delta\varepsilon_1/2$  are reported at macro and mesoscales. (b) Change of  $\tilde{\Phi}_m$  and  $\hat{\Phi}_c$  with respect to the strain amplitude  $\Delta\varepsilon_1/2$  at the meso scale

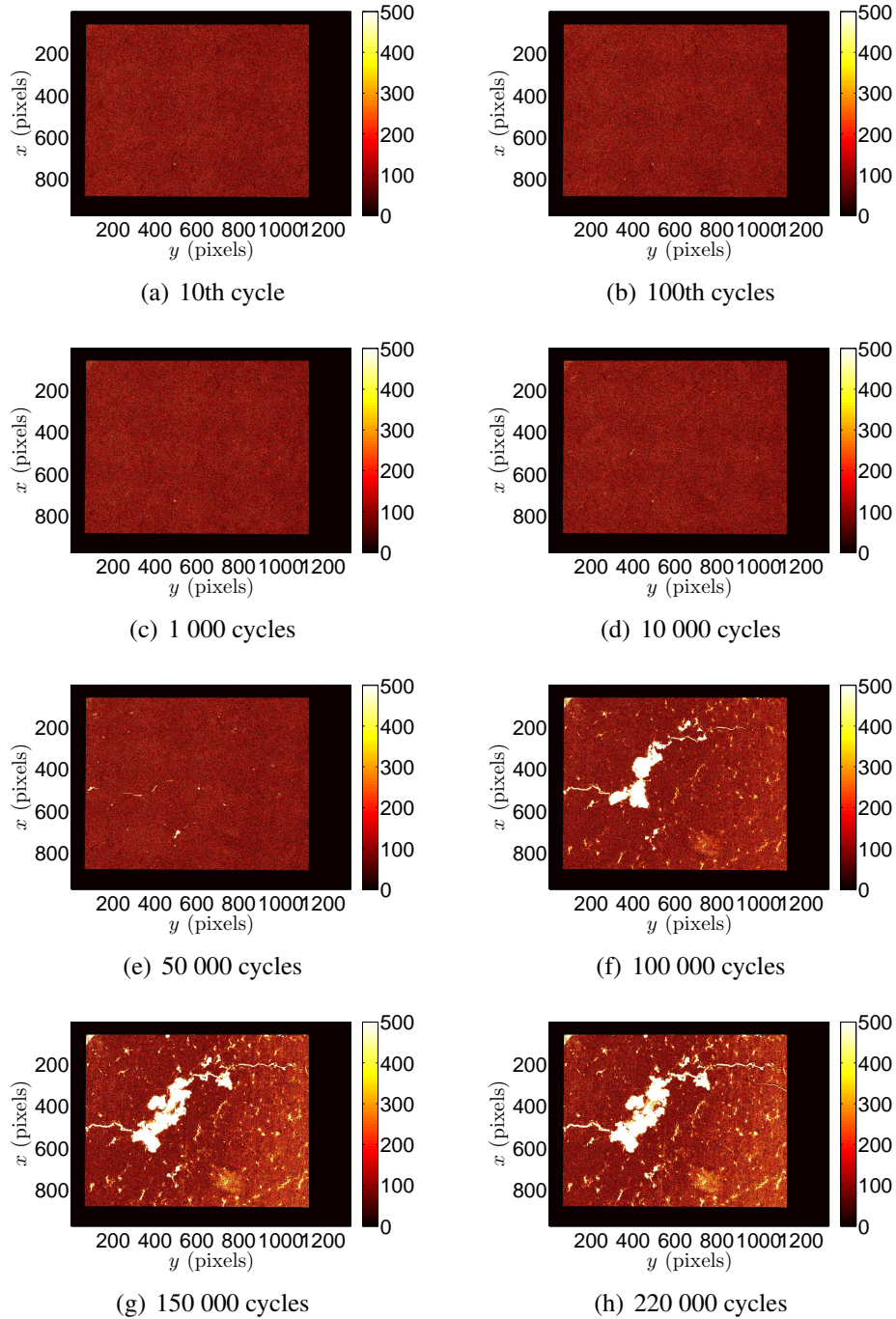


**Figure 5.25:** Correlation residual maps for different cycle number

### 3.4 Results of “snail” fatigue campaign

Five “snail” experiments have been conducted (TAB. 5.5). When comparing the number of cycles to failure for the same maximum applied load as for the equibiaxial experiment it is noted that failure occurs after fewer numbers of cycles in the present case. This leads to the conclusion that the “snail” loading regime is more damaging. Microcracks start to initiate earlier than in equibiaxial test. For the lowest load amplitude (*i.e.*, 20 kN) a nonlinear strain response is observed while the equibiaxial experiment performed with the same maximum level did exhibit such feature. For this load level ( $F_{max} = 20$  kN) the non-proportional experiment leads to a failure after 247,000 cycles whereas the equibiaxial loading did not fail after  $10^6$  cycles.

**Table 5.5:** Number of cycles to failure for the “snail” experiments

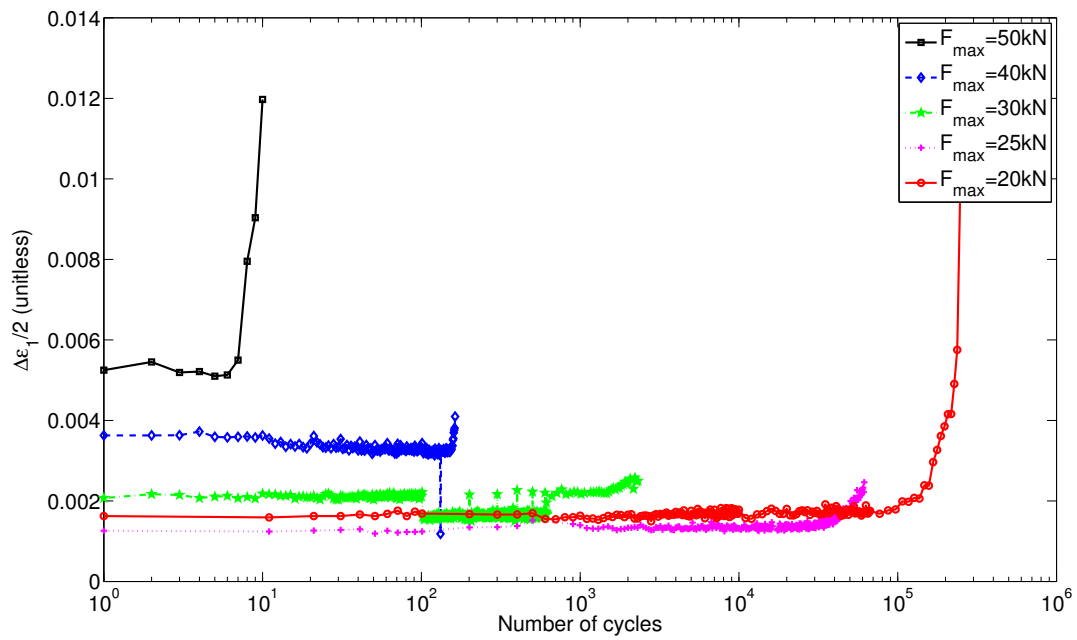
	$F_1^{max}$ (kN)	$F_2^{max}$ (kN)	$F_2^{min}$ (kN)	$F_1^{min}$ (kN)	$N_{failure}$ (cycles)
SBE-1	50	50	0.1	0.1	10
SBE-2	40	40	0.1	0.1	163
SBE-3	30	30	0.1	0.1	2 315
SBE-4	25	25	0.1	0.1	61 501
SBE-5	20	20	0.1	0.1	247 001

FIG. 5.26 and FIG. 5.27 show the strain amplitude histories. As in the previous case more fluctuations are observed on the macroscale. When compared with equibiaxial loading histories higher strain levels are observed (as reported in Section 3.2.1). Three experiments where the lowest load amplitudes are applied (*i.e.*, SBE-3, SBE-4, SBE-5) have approximately the same strain amplitudes.

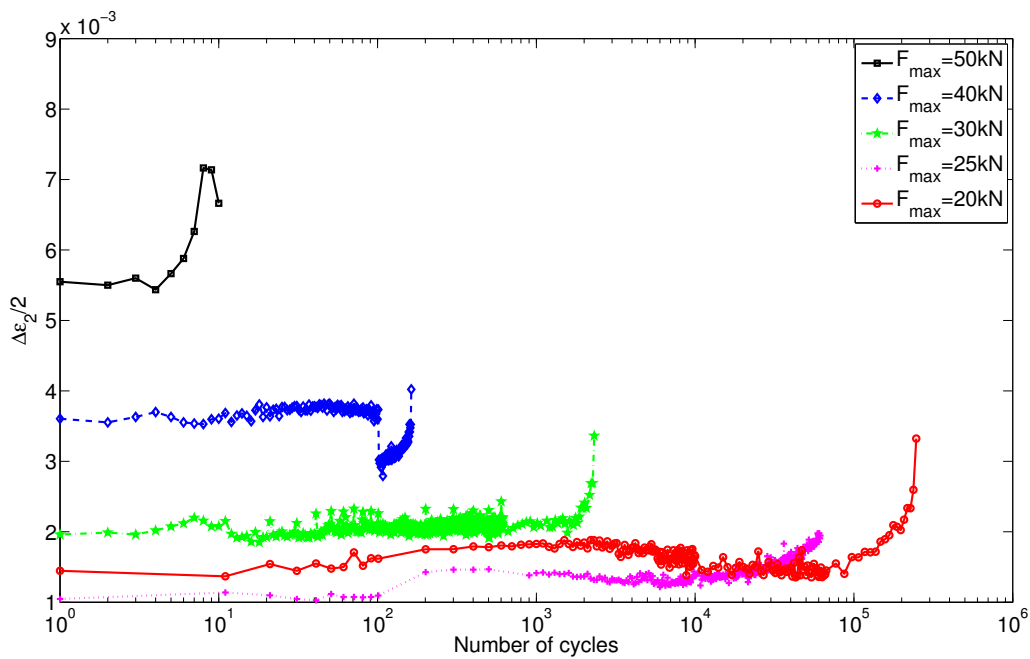
## 4 Conclusion

The goal of the present experimental study was to determine the biaxial fatigue behaviour of the investigated SG cast iron under multiaxial loading conditions. Uniaxial experiments (see CHAP. 3) revealed that the material was quasi-brittle. This feature has also been observed for biaxial loading cases. The experimental setup for fatigue experiments was identical to that used for cyclic biaxial experiments (CHAP. 4). A first camera monitors the whole specimen (*i.e.*, macroscale) with its radii and the second one observes a small zone in the centre of the cross-shaped sample in order to better detect crack initiations. The results have been obtained for two different loading paths (equibiaxial and non-proportional “snail”).

Ten biaxial fatigue tests (five equibiaxial and five “snail” loadings) have been performed up to  $1.5 \times 10^6$  cycles. The strain histories retrieved from the measured displacement fields were obtained on two scales. When comparing the mean strain levels on the two scales a good correspondance was found. The mean strain levels at the macroscale

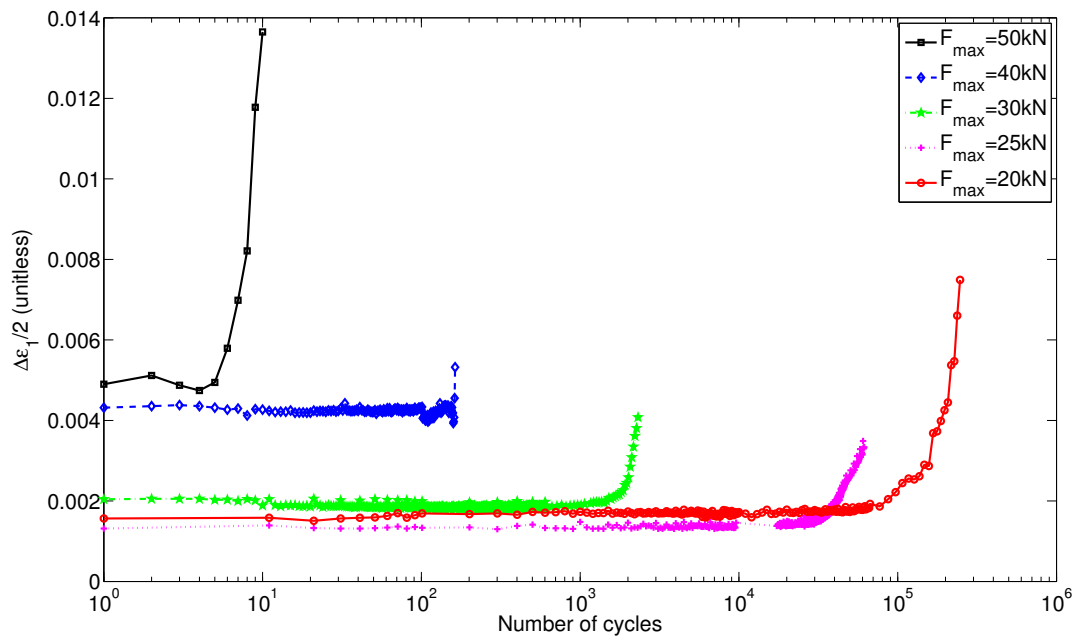


(a)

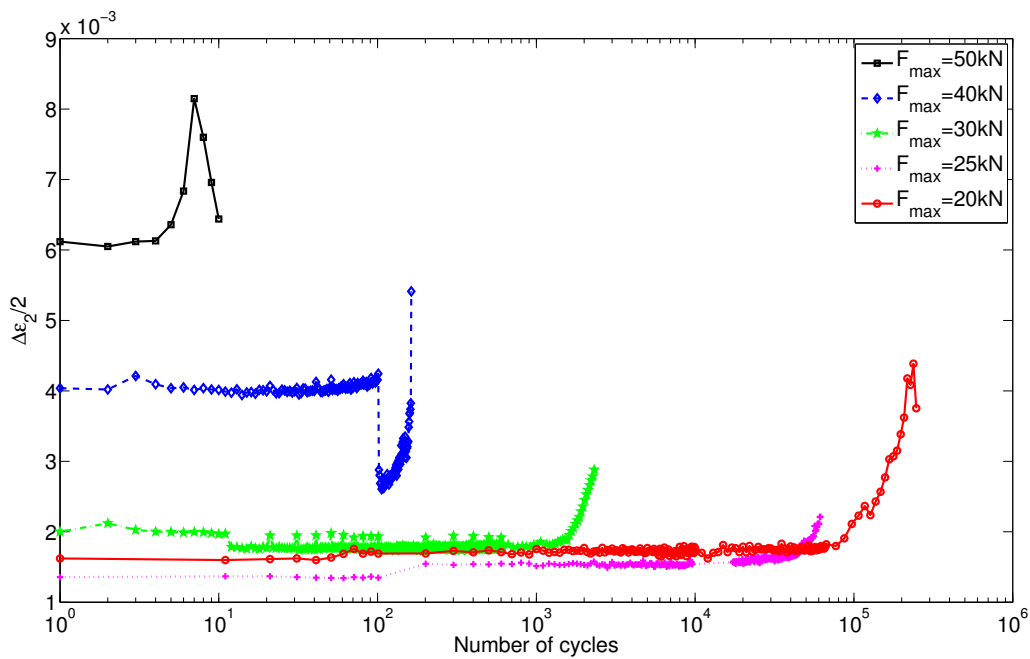


(b)

**Figure 5.26:** History of the (a) maximum mean eigen and (b) minimum mean eigen strain amplitudes on macroscale



(a)



(b)

**Figure 5.27:** History of the (a) maximum mean eigen and (b) minimum mean eigen strain amplitudes on mesoscale

exhibited more fluctuations since less information is available in the DIC gauge (*i.e.*, less pixels). The strain data could not be directly used to assess the crack network formation and growth with the number of cycles. Since minute changes (*i.e.*, microcracks) occur during loading mean strains calculated over a large ROI could not detect the discontinuities very early on. However, correlation and mechanical residuals were used to monitor the crack network initiation and growth. Four tests were presented corresponding to the stage when cracks had initiated. In those cases the crack network formation either started at the very first loading cycle or after some numbers of cycles. In both cases the change of residuals is not fluctuating as much as the strain signals. Crack growth could be monitored on mesoscale observations.

The identification/validation of the kinematic hardening parameters were successfully carried out on the first cycle of the fatigue experiments for the two loading paths. The parameters were determined on tests when the maximum load (*i.e.*, 50 kN) is prescribed because the latter is the most sensitive (*i.e.*, high stress levels occur). The reference parameters were taken from the experiments analysed in CHAP. 4. For the equibiaxial loading regime small differences between initial and identified parameters are noted, while for the “snail” loading path the hardening coefficient  $\gamma$  differs by 50 %. Both tests lead to lower displacement and force residuals.

The goal of two series of biaxial experiments was to investigate the influence of the applied loading path on the fatigue life time. From the analysed results it is concluded that more complex biaxial (*i.e.*, non-proportional “snail”) loading path is more damaging than the proportional loading history. Hence, a lower life time is to be expected from more complex loading histories (FIG. 5.28).



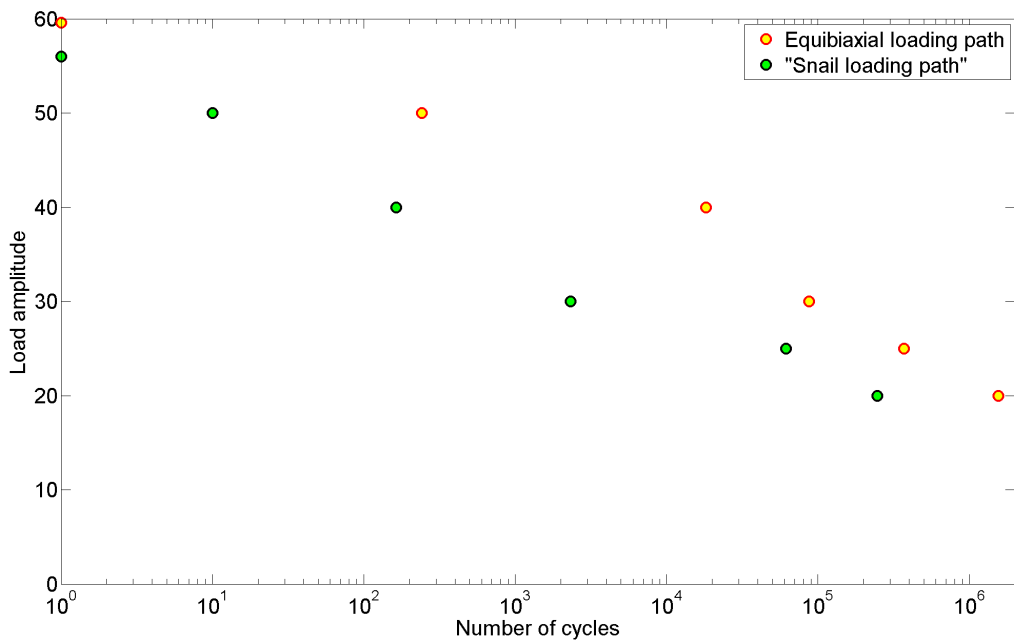


**Figure 5.28:** Comparison of equibiaxial and snail tests. Applied load versus number of cycles to failure. Load levels for first cycle correspond to biaxial experiments presented in CHAP. 4



# Conclusions and perspectives

The general topic of this thesis is the investigation of the mechanical behaviour of nodular graphite cast iron subjected to complex loading histories. Advanced identification procedures allowed us to estimate material parameters for given constitutive laws. This methodology implies a coupling of experimental data and Finite Element simulations in one single framework. It is worth noting that the procedures developed in this work are generic and can be applied to various classes of materials.

The first part introduced the necessary information to address the objectives of this work. Different grades of SG cast iron were introduced. Since the main objective is the investigation of nonlinear phenomena, models accounting for elastoplasticity and damage are proposed. Special emphasis is given to isotropic hardening (*i.e.*, Johnson-Cook constitutive law), kinematic hardening (*i.e.*, Armstrong-Frederick material model) and Lemaitre's damage law. One of the challenges is to assess parameters describing both phenomena (*i.e.*, elastoplasticity and damage) in the same identification scheme. Iterative Finite Element Model Updating was chosen since it couples full-field measurements and FE simulations in a non-intrusive way.

Digital Image Correlation as one of the most commonly applied full-field measurement technique was introduced with two existing approaches. Special emphasis was given to measurement uncertainty as an important criterion to estimate the quality of the measured displacement fields. Local and global DIC approaches were compared and the discussion was extended to regularised and integrated DIC. The R-DIC variant combines grey level conservation and mechanical equilibrium. A decrease of measurement uncertainty was achieved with fine spatial resolutions. It is necessary to emphasise that the algorithm needs to be carefully driven via a relaxation process.

The second part presents and discusses the identification of parameters of linear and nonlinear constitutive laws from simple (*i.e.*, uniaxial) loading regimes. Two tests were considered, namely, monotonic and cyclic loading paths. To identify Young's modulus, a load information is needed (*i.e.*, FEMU-F) and can be supplemented by kinematic data (*i.e.*, FEMU-UF). As opposed to Young's modulus, Poisson's ratio reported high sensitivity to the quality of the measured displacement fields. Isotropic and kinematic hardening parameters identified in both tests differ from the classically fitted ones. For the monotonic test a decrease of residuals was observed, which leads to the conclusion that the identified set of parameters better describes the material response. A cyclic tensile test allows more complex material behaviour to be assessed. The identification residuals confirmed the assumption that kinematic hardening better captures cyclic loadings than

an isotropic model. The lowest residuals were found for a damage model coupled with isotropic hardening. It is believed that the material response could be even more accurately described by coupling a damage model with kinematic hardening (and possibly both hardening regimes).

X-ray tomography allows in-situ mechanical tests to be performed. DVC gives access to 3D volumetric displacements. From a cyclic in-situ test performed on the investigated SG cast iron damage was detected by analysing the grey level residual maps via RC8-DVC. Debonding between the iron matrix and the graphite nodules is observed even in the elastic loading regime. In the future, the identification can be performed with the measured 3D displacement fields via FEMU or even integrated schemes (I-DVC). It is envisioned that the material behaviour (*i.e.*, with damage) could be better captured. This recently applied approach of RC8-DVC measurements will open a new path for assessing more reliable damage models.

In the last part of the manuscript biaxial loading regimes are discussed. First, the identification of elastoplastic properties was considered on two different loading histories, namely, proportional (*i.e.*, equibiaxial) and nonproportional (“snail”) loading paths were prescribed on a cross-shaped specimen with a thinned gauge zone in its center. A two-scale optical setup was implemented, namely, macro and mesoscales were observed.

The objective of the macroscale analysis was to identify the elastoplastic parameters, and the mesoscale data were used to detect microcrack initiations. It is necessary to emphasise that both sides of the sample were observed. The challenge to overcome was measuring displacement fields on poor mesoscale textures in a reliable way since classical DIC approaches had high standard displacement resolutions. R-DIC successfully bypassed these limitations. Since the displacements were measured at both scales, the material response was obtained with DIC gauges. Correlation residuals at the mesoscale were analysed and the crack network formation was captured. This leads to the conclusion that damage is occurring in the thinned gauge zone.

Three loading regimes were considered to identify the elastoplastic parameters (*i.e.*, isotropic and kinematic hardening). The identification residuals obtained with Johnson-Cook’s model are higher when compared with those of Armstrong-Frederick’s model. This trend was found on the three loading histories. A kinematic hardening law outperforms isotropic models when describing cyclic loadings. Equibiaxial loadings resulted in lower residuals than those observed with more complex (*i.e.*, so-called snail) loading regimes.

The fact that there still exist discrepancies can be related to early damage (as observed via in situ test), modelling errors (*i.e.*, a full 3D FE model is run with 2D-DIC measurements). “Snail” loading regimes are more damaging and thus require more complex material models to be chosen. Damage models coupled with plasticity should be considered. Even though it was not presented in this work, cyclic experiments were also carried out with a different optical setup. On one side macroscale monovision while the other side was observed with a stereojig. The displacement fields will be compared for the two setups. The identification will be performed with displacement fields measured with both systems. It is envisioned that more accurate boundary conditions will be available. They

will presumably lead to lower modelling errors.

Moreover, a new series of two scale biaxial experiments could be conducted on cross-shaped sample. In this campaign a new loading path would be introduced, namely, wind-mill histories would be applied. It will be interesting to see whether this more complex loading regime is as even more damaging, and how the various models account for such histories.

The last chapter of this manuscript presents a series of ten fatigue experiments. Five experiments were carried out with an equibiaxial loading history while five of them were subjected to the snail loading path. The objective of this campaign was to study the biaxial fatigue behaviour of the investigated SG cast iron. It is shown that the snail history is more damaging than the equibiaxial loading regime. From the 10 experiments the strain amplitudes were extracted. From their change with the number of cycles it is difficult to detect when and how the crack networks form. Conversely, correlation and mechanical residuals can be used to visualise cracks as they initiate and propagate. Elastoplastic parameters previously identified on cyclic experiments were used for validation purposes. The first loading cycle was analysed for the two histories. Small changes between the reference and identified parameters are observed.

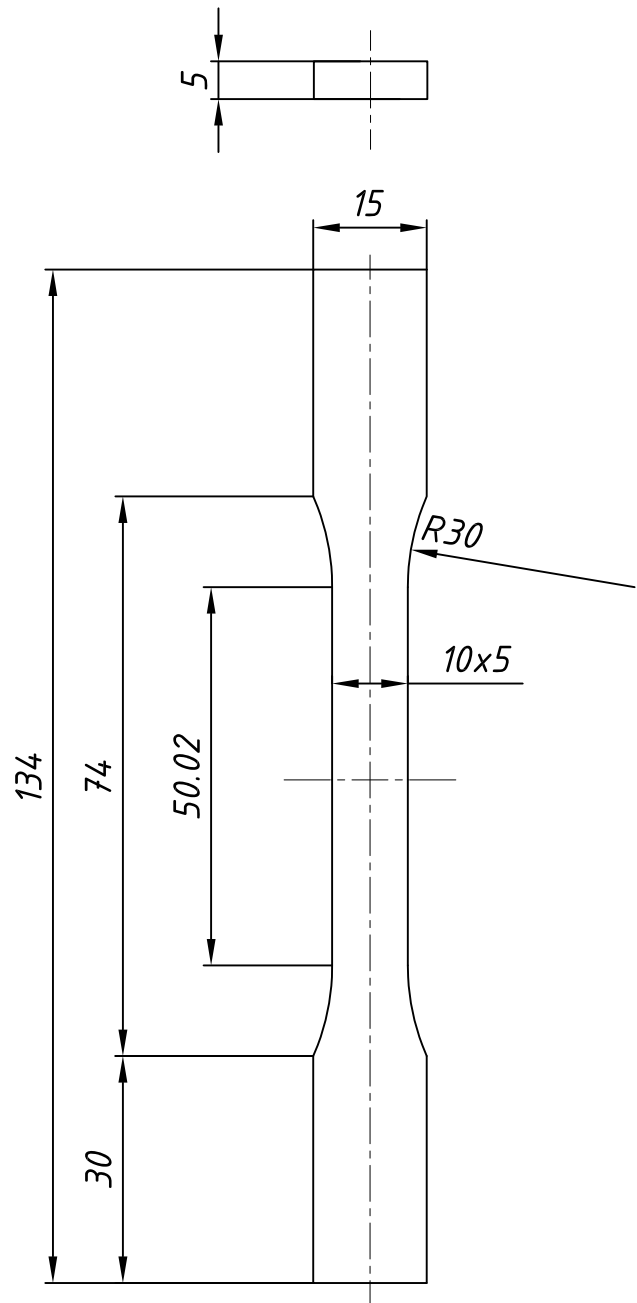
In a future work more attention will be given to the identification/validation of the damage parameters for the fatigue tests. The identified (and validated) kinematic hardening parameters (CHAP. 4) will be used to assess the stress fields in the tested cross-shaped samples. Determining the stress state can be used to describe damage growth. Another path can be followed, namely, the detection and quantification of physical damage (*i.e.*, crack opening displacements in the network) by using mesoscale images. A different regularization can be applied on the damaged material (*i.e.*, microcracks) and the undamaged part of the material [Hild et al., 2014].



# **Appendix A**

## **Design of samples used for standard tensile tests**

*This appendix presents the design of samples used for uniaxial monotonic and cyclic experiments (CHAP. 3). They were machined by water cutting.*

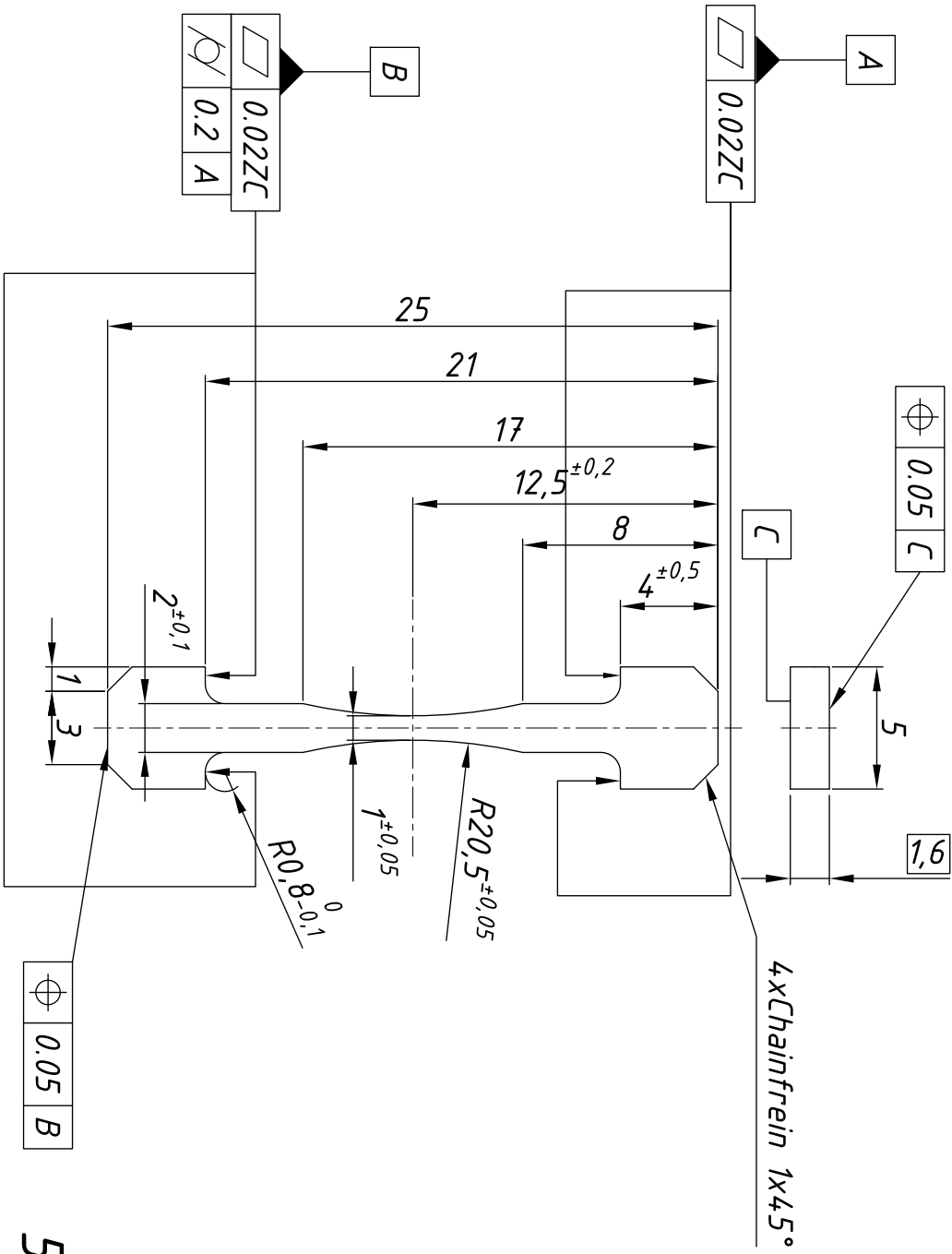




## **Appendix B**

# **Design of uniaxial sample used for in situ tests**

*This appendix presents the design of uniaxial samples used for in situ monotonic and cyclic experiments (see CHAP. 3). The samples are electrodischarge machined from a thin plate.*

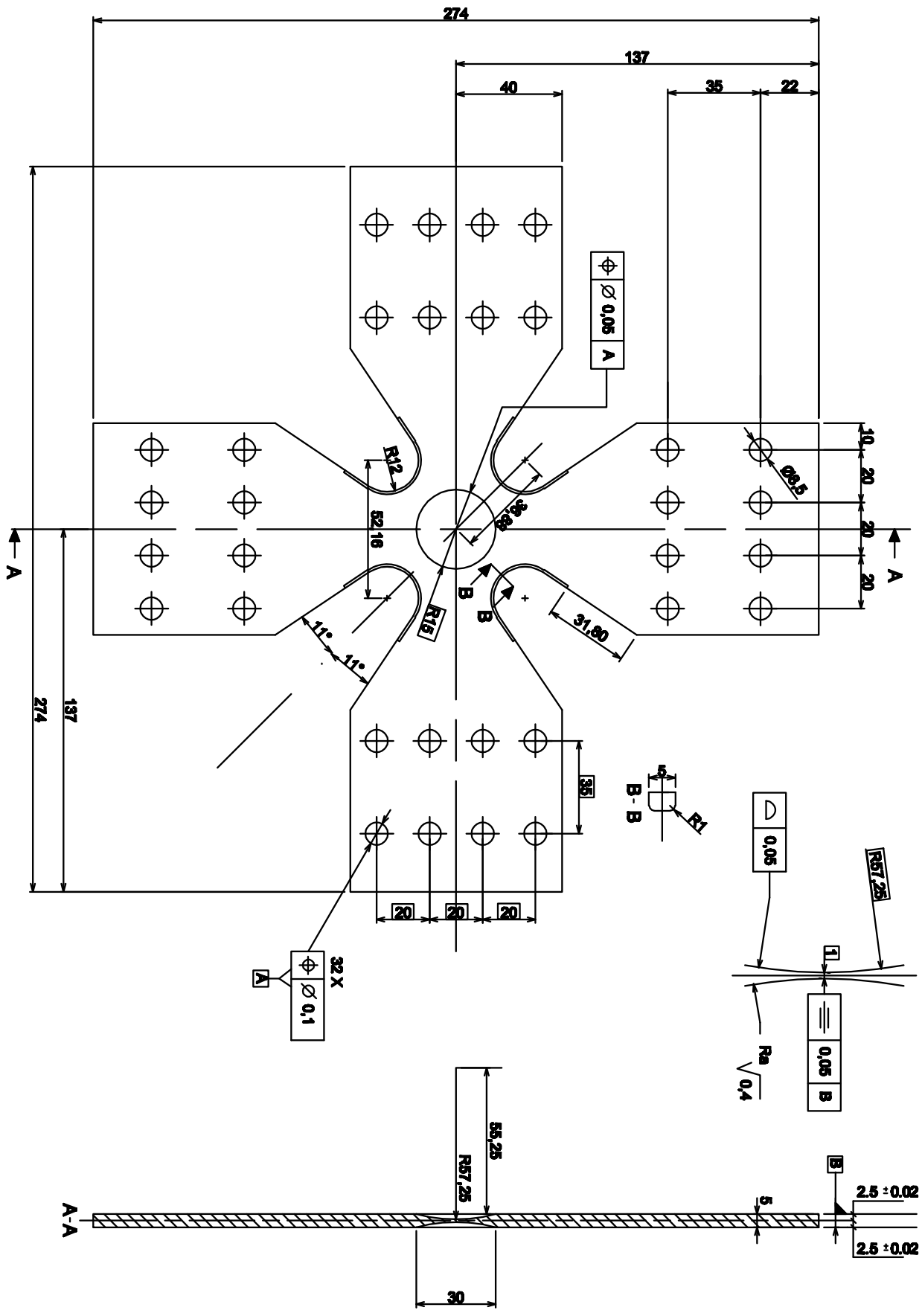


5:1

## Appendix C

# Design of in-plane biaxial specimen

*This appendix presents the design of cross-shaped specimen used for biaxial cyclic (see CHAP. 4) and fatigue (see CHAP. 5) experiments.*



# Appendix D

## Article 1

*This appendix corresponds to the paper entitled:  
'Mechanics-Aided Digital Image Correlation' that appeared  
in 2013 in the Jnl of Strain Analysis for Engineering Design,  
Vol. 48, Pages 330-343. It is co-authored by TOMICEVIC, Z.,  
HILD, F., ROUX, S.*

# Mechanics-aided digital image correlation

*J Strain Analysis*  
48(5) 330–343  
© IMechE 2013  
Reprints and permissions:  
sagepub.co.uk/journalsPermissions.nav  
DOI: 10.1177/0309324713482457  
sdj.sagepub.com  


Zvonimir Tomičević<sup>1,2</sup>, François Hild<sup>2</sup> and Stéphane Roux<sup>2</sup>

## Abstract

By construction, digital image correlation is an ill-posed problem. To circumvent this difficulty, regularization is often performed implicitly through the kinematic basis chosen to express the sought displacement fields. Conversely, a priori information on the mechanical behavior of the studied material is often available. It is proposed to evaluate the gain to be expected from such a mechanical assistance, namely, the measured displacement not only satisfies as best as possible the gray-level conservation but also mechanical admissibility.

## Keywords

Equilibrium gap, full-field measurements, regularization, resolution, T3 elements

Date received: 26 October 2012; accepted: 8 February 2013

## Introduction

One of the limitations of digital image correlation (DIC) comes from its ill-posedness. The limited available information, generally two gray-level images to be registered, impedes the measurement of very rapid fluctuations of the displacement field and hence constitutes a potential barrier to very small-scale displacement resolutions (i.e. the “smallest change in a quantity being measured that causes a perceptible change in the corresponding indication”<sup>1</sup>). Consequently, a compromise has to be found between the standard measurement uncertainty and the spatial resolution.<sup>2,3</sup>

Different strategies have been designed to overcome this limitation. The most classical one is to work with a coarse description of the displacement field based on a discretization scale that is much larger than the pixel scale. This corresponds to the choice made in local (or subset-based) DIC approaches,<sup>4–6</sup> where the size of the zone of interest (ZOI) can be seen as a natural regularization. Apart from this coarse description, no additional assumption is made on the displacement field, which finally has to be interpolated between ZOI centers. In practice, this choice limits the ZOI size to typically 10 pixels or more.<sup>7,8</sup>

To achieve smaller resolutions or spatial resolutions, some additional information has to be provided. One example is to assume that the displacement field be continuous. The latter can be decomposed over a convenient basis of functions that fulfill this constraint. For instance, a finite element (FE) basis can be chosen.<sup>9–11</sup>

The problem to solve no longer consists of a collection of independent correlation computation for each ZOI as was the case for local DIC.<sup>8</sup> When the problem is formulated as a whole and all degrees of freedom determined simultaneously through the solution of a coupled problem, it is referred to as “global DIC”. This coupling involves an overcost in terms of computation time. This extra cost is, however, rewarding in terms of result quality.<sup>12</sup> Furthermore, the postprocessing step of data interpolation and smoothing becomes essentially useless, and hence, a good control of the displacement determination is preserved. In favorable cases, element sizes as small as  $4 \times 4$  pixels can be used.<sup>13</sup>

The spatial resolution can be further decreased (i.e. down to pixel<sup>14</sup> or voxel scales<sup>15,16</sup>) by adding other terms in the minimization of the gray-level conservation.<sup>17</sup> A natural choice stems from the general propositions associated with the regularization of ill-posed problems.<sup>18</sup> It consists in minimizing the fluctuations associated with the Laplacian of the displacement field.<sup>14</sup> This type of filter does work, but it may discard fluctuations that are mechanically admissible.

<sup>1</sup>Department of Engineering Mechanics, University of Zagreb, Zagreb, Croatia

<sup>2</sup>LMT-Cachan, ENS Cachan/CNRS/UPMC/PRES UniverSud Paris, Cachan Cedex, France

## Corresponding author:

François Hild, LMT-Cachan, 61 avenue du Président Wilson, F-94235 Cachan Cedex, France.

Email: hild@lmt.ens-cachan.fr

Another route consists in considering a mechanical filter, namely, the regularization term allows the mechanical admissibility to be enforced in a weak sense. Among the various propositions,<sup>19</sup> the equilibrium gap is chosen<sup>17,20</sup> in the sequel. The advantage of such a regularization will be shown when assessing the resolution and with very difficult textures that are not tractable with classical DIC codes. Furthermore, boundary regularization has not received a lot attention. When comparing experimental and simulated displacement fields for identification or validation purposes, the raw measured boundary conditions are considered<sup>21</sup> or filtered.<sup>22</sup> They can also be parts of the unknowns in an integrated approach to DIC.<sup>23</sup> A new mechanics-based regularization is proposed herein. It acts as a filter in the same spirit as for bulk degrees of freedom. In the following studies, three-noded elements will be considered. They are the simplest in terms of displacement interpolations, even though they are seldom used, if ever, in the framework of global DIC. The other novelty of the developed procedure is that the resolution/spatial resolution (or regularization length) limit can be broken through an *appropriate driving* of the DIC algorithm.

This article is organized as follows. First, the main features associated with global DIC and its regularization are introduced in section “Regularized DIC.” Section “Artificial test cases” is devoted to the analysis of two artificial cases. The first one deals with a sinusoidal displacement field and the second one with a mechanically admissible field. True experimental data are finally studied in section “Analysis of two different textures”. Natural and artificial textures are compared.

## Regularized DIC

### Regularization strategy

The registration of two gray-level pictures in the reference,  $f$ , and deformed,  $g$ , configurations is based upon the conservation of the gray levels

$$f(\mathbf{x}) = g(\mathbf{x} + \mathbf{u}(\mathbf{x})) \quad (1)$$

where  $\mathbf{u}$  is the unknown displacement field to be measured and  $\mathbf{x}$  the pixel location. The sought displacement field minimizes the sum of squared differences  $\Phi_c^2$  over the region of interest (ROI)

$$\Phi_c^2 = \int_{\text{ROI}} \varphi_c^2(\mathbf{x}) d\mathbf{x} \quad (2)$$

where  $\varphi_c(\mathbf{x})$  defines the field of correlation residuals

$$\varphi_c(\mathbf{x}) = |g(\mathbf{x} + \mathbf{u}(\mathbf{x})) - f(\mathbf{x})| \quad (3)$$

The minimization of  $\Phi_c^2$  is a nonlinear and ill-posed problem. If no additional information is available, it is *impossible* to determine the displacement for each pixel independently since there are two unknowns for a given (scalar) gray-level difference. This explains the reason

for choosing a weak formulation in which the displacement field is expressed in a (chosen) basis as

$$\mathbf{u}(\mathbf{x}) = \sum_n u_n \boldsymbol{\psi}_n(\mathbf{x}) \quad (4)$$

where  $\boldsymbol{\psi}_n$  are (chosen) vector fields and  $u_n$  the associated degrees of freedom. The measurement problem then consists in minimizing  $\Phi_c^2$  with respect to the unknowns  $u_n$ . A Newton iterative procedure is followed to circumvent the nonlinear aspect of the minimization problem.<sup>11</sup> The following linear systems are solved iteratively

$$[\mathbf{M}]\{\delta\mathbf{u}\} = \{\mathbf{b}\} \quad (5)$$

where  $[\mathbf{M}]$  is a matrix formed from the dyadic product of fields  $\nabla f \cdot \mathbf{y}_n$ ,<sup>12</sup>  $\{\mathbf{b}\}$  a vector that vanishes when a perfect registration is obtained for each pixel (i.e. Equation (1) is satisfied), and  $\{\delta\mathbf{u}\}$  collects the corrections to the measured degrees of freedom  $u_n$ .

To enforce mechanical admissibility in an FE sense, the equilibrium gap is first introduced.<sup>20</sup> If linear elasticity applies, the equilibrium equations read

$$[\mathbf{K}]\{\mathbf{u}\} = \{\mathbf{f}\} \quad (6)$$

where  $[\mathbf{K}]$  is the stiffness matrix and  $\{\mathbf{f}\}$  the vector of nodal forces. When the displacement vector  $\{\mathbf{u}\}$  is prescribed and if the (unknown) stiffness matrix is not the true one, force residuals  $\{\mathbf{f}_r\}$  will arise

$$\{\mathbf{f}_r\} = [\mathbf{K}]\{\mathbf{u}\} - \{\mathbf{f}\} \quad (7)$$

Similarly, if the displacement field does not satisfy equilibrium, it will induce an equilibrium gap. In the absence of body forces, interior nodes are free from any external load. Consequently, the equilibrium gap method consists of minimizing

$$\Phi_m^2 = \{\mathbf{u}\}^t [\mathbf{K}]^t [\mathbf{K}]\{\mathbf{u}\} \quad (8)$$

where  $t$  is the transposition operator and  $\Phi_m^2$  corresponds to the sum of the squared norm of all equilibrium gaps at *interior nodes only*. Any displacement field prescribed on the boundary gives rise to a displacement field for which  $\Phi_m = 0$ .

This observation requires an additional regularization for boundary nodes. It is proposed to introduce a penalization of short wavelength displacement fluctuations along the edges of the region of interest. The third objective function to be considered has to vanish for *any* rigid body motion

$$\Phi_b^2 = \{\mathbf{u}\}^t [\mathbf{L}]^t [\mathbf{L}]\{\mathbf{u}\} \quad (9)$$

where  $[\mathbf{L}]$  is an operator acting on the ROI boundary.<sup>15</sup> Appendix 2 details the construction of the new operator proposed herein, which has a simple mechanical interpretation.

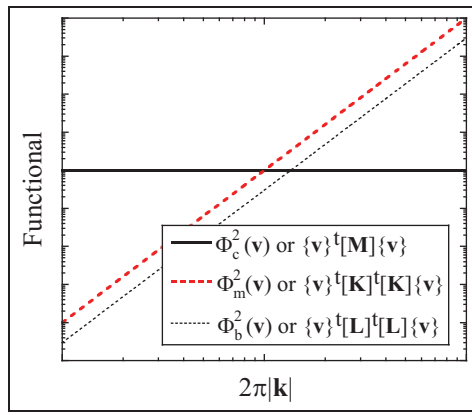


**Figure 1.** Schematic log–log plot of the dependence of the three functionals and the corresponding normalizing terms with the norm of the wave vector  $\mathbf{k}$ . The DIC functional (bold solid line) is wave vector independent. The regularization functionals (dashed lines) are chosen to have a steep slope of 4, so as to define precisely the filtering frequency. Edge regularization is parallel and chosen to be always lower than the bulk one.

**Correlation procedure**

The minimization of correlation residuals ( $\Phi_c^2$ ), equilibrium gap ( $\Phi_m^2$ ), and boundary fluctuations ( $\Phi_b^2$ ) requires the introduction of a total functional  $\Phi_t$

$$(1 + w_m + w_b)\Phi_t^2 = \tilde{\Phi}_c^2 + w_m\tilde{\Phi}_m^2 + w_b\tilde{\Phi}_b^2 \tag{10}$$

where  $w_m$  and  $w_b$  are weights that define length scales associated with  $\tilde{\Phi}_m^2$  and  $\tilde{\Phi}_b^2$  and  $\tilde{\Phi}$  denote *normalized* residuals. To normalize the residuals, let us consider a displacement field in the form of a plane wave  $\mathbf{v}(\mathbf{x}) = \mathbf{v}_0 \exp(i\mathbf{k} \cdot \mathbf{x})$ , where  $\mathbf{v}_0$  is the amplitude and  $\mathbf{k}$  the wave vector. The normalized residuals then become

$$\tilde{\Phi}_c^2 = \frac{\Phi_c^2}{\{\mathbf{v}\}^t[\mathbf{M}]\{\mathbf{v}\}}, \quad \tilde{\Phi}_m^2 = \frac{\Phi_m^2}{\{\mathbf{v}\}^t[\mathbf{K}]^t[\mathbf{K}]\{\mathbf{v}\}},$$

$$\tilde{\Phi}_b^2 = \frac{\Phi_b^2}{\{\mathbf{v}\}^t[\mathbf{L}]^t[\mathbf{L}]\{\mathbf{v}\}} \tag{11}$$

where  $\{\mathbf{v}\}$  collects all the nodal displacements associated with displacement field  $\mathbf{v}$ . The wavelength dependence of  $\{\mathbf{v}\}^t[\mathbf{K}]^t[\mathbf{K}]\{\mathbf{v}\}$  and  $\{\mathbf{v}\}^t[\mathbf{L}]^t[\mathbf{L}]\{\mathbf{v}\}$  is of fourth order, whereas  $\{\mathbf{v}\}^t[\mathbf{M}]\{\mathbf{v}\}$  is wavelength independent<sup>15</sup> (see Figure 1). The equilibrium gap and boundary regularization kernels thus act as fourth-order low-pass filters, damping deviations from mechanical admissibility and edge displacement fluctuations below a given wavelength. Weights  $w_m$  and  $w_b$  are chosen as

$$w_m = (2\pi|\mathbf{k}|\ell_m)^4, \quad w_b = (2\pi|\mathbf{k}|\ell_b)^4 \tag{12}$$

where  $\ell_m$  and  $\ell_b$  denote the regularization lengths for  $\tilde{\Phi}_m^2$  and  $\tilde{\Phi}_b^2$  respectively. With this choice,  $\tilde{\Phi}_c(\mathbf{v}) = \tilde{\Phi}_m(\mathbf{v}) = \tilde{\Phi}_b(\mathbf{v}) = 1$  and  $\Phi_t(\mathbf{v}) = 1$  if  $\ell_m = \ell_b = 1/2\pi|\mathbf{k}|$ .

It is to be emphasized that other forms of regularization kernels could have been chosen. The specific form

of the equilibrium gap comes from the strong penalization of high-frequency oscillations (fourth power of the wave number) and thus also very weak influence on long wavelength modes. The higher  $\ell_m$ , the more weight is put on the equilibrium gap functional  $\tilde{\Phi}_m^2$ ; therefore, the equilibrium residuals have to reach lower levels. Similarly, the edge regularization term is designed to have the same scaling properties as the bulk term. The higher  $\ell_b$ , the more weight is put on the boundary functional  $\tilde{\Phi}_b^2$ ; therefore, the corresponding displacement fluctuations will decrease.

When the material parameters are known, the minimization of  $\Phi_t^2$  with respect to the unknown degrees of freedom can be performed.<sup>15</sup> The above mechanical regularization procedure can be used for an arbitrary supporting mesh, even down to the pixel<sup>14</sup> or voxel<sup>15,16</sup> scales. In the following, the elements will be considered as three-noded triangles (T3) with a linear displacement interpolation.

**Implementation**

A Newton iterative procedure is followed to circumvent the nonlinear aspect of the minimization problem (i.e.  $\Phi_c^2$  is a nonlinear function of the degrees of freedom). Let  $\mathbf{u}^j$  denote the displacement field at iteration  $j$  and  $\{\mathbf{u}\}^j$  the vector collecting all the unknown degrees of freedom. By assuming small increments  $d\mathbf{u} = \mathbf{u}^{j+1} - \mathbf{u}^j$  of the solution,  $\partial\Phi_t^2/\partial\{\mathbf{u}\}^j = \{\mathbf{0}\}$  is recast in a matrix–vector product as

$$([\mathbf{M}] + [\mathbf{N}])\{d\mathbf{u}\} = \{\mathbf{b}\}^j - [\mathbf{N}]\{\mathbf{u}\}^j \tag{13}$$

with

$$[\mathbf{N}] = w_m \frac{\{\mathbf{v}\}^t[\mathbf{M}]\{\mathbf{v}\}}{\{\mathbf{v}\}^t[\mathbf{K}]^t[\mathbf{K}]\{\mathbf{v}\}} [\mathbf{K}]^t[\mathbf{K}]$$

$$+ w_b \frac{\{\mathbf{v}\}^t[\mathbf{M}]\{\mathbf{v}\}}{\{\mathbf{v}\}^t[\mathbf{L}]^t[\mathbf{L}]\{\mathbf{v}\}} [\mathbf{L}]^t[\mathbf{L}] \tag{14}$$

where  $\{\mathbf{b}\}^j$  is updated as the picture in the deformed configuration  $g$  is corrected by using the current estimate of the displacement field  $\mathbf{u}^j$ . In the present case, a cubic gray-level interpolation is considered. Conversely, matrices  $[\mathbf{M}]$  and  $[\mathbf{N}]$  are computed once for all. The iterations stop when the displacement corrections  $\{d\mathbf{u}\}$  reach a small level that is chosen by the user.

In the absence of regularization, the presence of noise leads to secondary minima trapping when small elements are chosen. This is responsible for a degradation of the uncertainty for fine meshes. This secondary minima trapping leads to a multiplicity of stationary solutions of the displacement field. Different solutions are obtained depending on the initial displacement field. Regularization is introduced to mend this problem, at the expense of a priori assumptions on the elastic properties of the considered body. Thus, in the analysis of resolution, a specific pathway consists in first solving the problem with large regularization lengths and



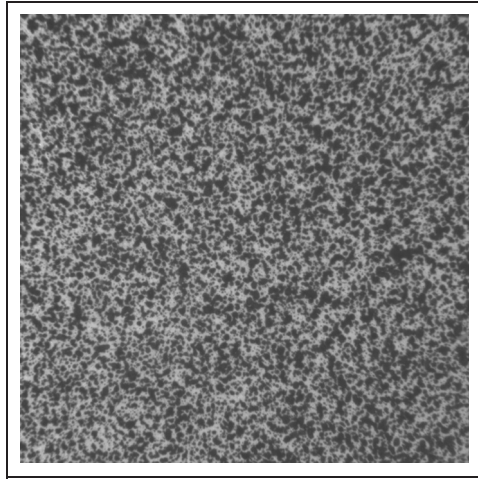


**Figure 2.** Reference picture of the first two test cases.

progressively decreasing the regularization length scales  $\ell_m$  and  $\ell_b$ . Although ending with very low weights given to the regularization, the sought displacement field is driven to a solution where initialization is an “educated guess” based on an elastic interpolation. The final solution will live in an energy landscape where many local minima exist, but the selection of the actual minimum results from a convergence history that is expected to be beneficial.

In the following, series of calculations are generally run with different regularization lengths  $\ell_m$  when  $\ell_b = \ell_m/2$ . Different initial values of  $\ell_m$  are considered and each time a first calculation is run with an initial value of  $\mathbf{u}^0 = \mathbf{0}$ . The next calculation is carried out with the regularization length *divided by 2*. It takes as initial guess  $\mathbf{u}^0$  the displacement field at convergence of the previous calculation, and so on. This procedure will be referred to as relaxation. Finally, the unstructured mesh is composed of triangles whose typical edge is 10-pixel long.

### Artificial test cases

In these first two test cases, a true texture is considered (Figure 2). The picture definition is  $531 \times 531$  pixels with an 8-bit digitization. It corresponds to the central part of a cross-shaped sample analyzed by Claire et al.<sup>20</sup> To create the deformed configuration, two different displacement fields are considered, namely, a first one that is a sine wave and a second one that is mechanically admissible. In both cases, a linear interpolation of the gray levels is used to generate picture  $g$  in the deformed configuration. No noise is included. The same mesh is used in both cases and is made of 2313 inner nodes and 197 edge nodes.

#### Sine wave

The sine wave is an interesting case since it corresponds to one of the standard baseline analyses for optical

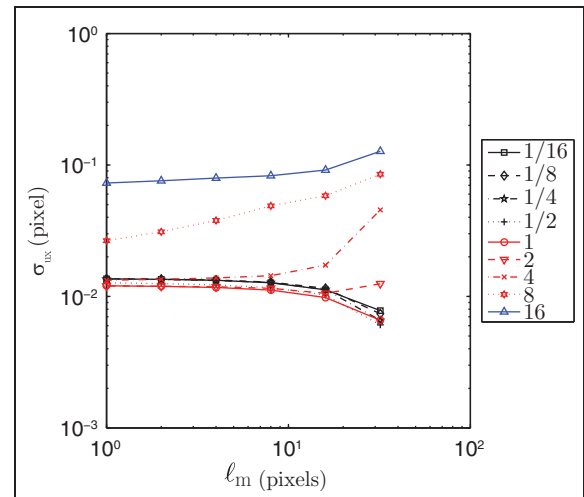


**Figure 3.** Change of the standard displacement error for different regularization lengths and different  $\ell_b/\ell_m$  ratios. For each curve, the relaxation process is to be read from right to left.

systems (in particular in the context of DIC<sup>3</sup>). The choice of the spatial resolution has to be compared with the wavelength of the prescribed displacement. The two components of the latter read

$$u_x(x, y) = 2 \sin(2\pi x/n_x), \quad u_y(x, y) = 2 \sin(2\pi y/n_y) \quad (15)$$

where  $n_x \times n_y$  is the number of pixels in the ROI.

It is worth noting that the normalized correlation residual  $\hat{\Phi}_c^2$  was introduced to evaluate the change in the correlation functional for a perturbation in the displacement field and to compare it to a similar perturbation in the regularization functional. The value of the absolute minimum of  $\Phi_c$  is irrelevant. Thus, only the parabolic expansion of the functional  $\Phi_c^2$  was considered. However, to judge the quality of the image registration itself, it is more relevant to evaluate the norm of  $\varphi_c$ -field. The latter, however, can be affected by a mean change of gray levels between the pictures in the deformed and reference configurations. To cancel out this effect (simply contributing as an offset in gray levels), it is convenient to resort to the standard deviation of  $\varphi$ . A dimensionless estimator consists in comparing this standard deviation to the dynamic range  $\Delta f = \max(f) - \min(f)$  of the reference picture. Thus,  $\hat{\Phi}_c^2 = [\langle \varphi^2 \rangle - \langle \varphi \rangle^2] / (\Delta f)^2$ , where  $\langle \bullet \rangle$  denotes an average of the ROI.  $\hat{\Phi}_c$  will be used in the sequel for estimating the quality of image registration.

Figure 3 shows the change of the standard error between the measured and prescribed displacement fields for the different regularization lengths  $\ell_m$  when  $\ell_b/\ell_m$  is set to different values. The same trends are observed for the two components of the displacement field. Consequently, only one result is reported in Figure 3. When the edge regularization is too large (i.e.  $\ell_b/\ell_m > 1$ ), the error is high. This corresponds to an

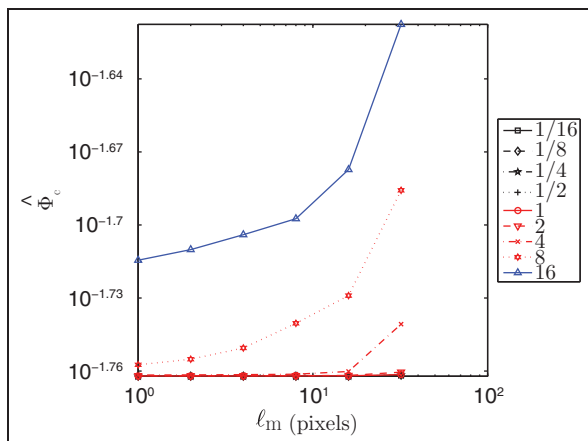


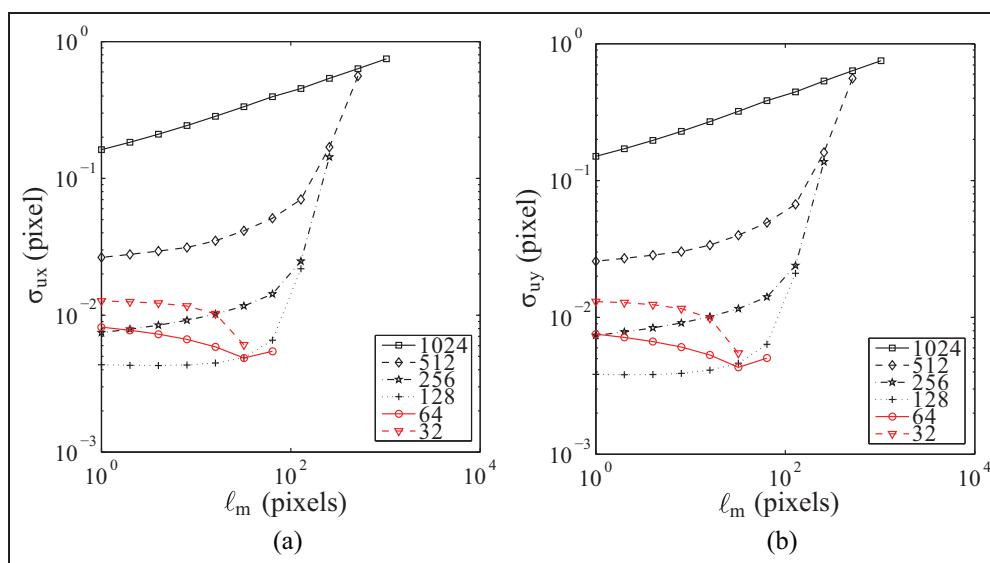
**Figure 4.** Change of the dimensionless correlation residual for different regularization lengths and different  $\ell_b/\ell_m$  ratios. For each curve, the relaxation process is to be read from right to left.

interpolation error since the displacement fluctuations are filtered out. As the edge regularization length decreases, the error decreases too. In the present case,  $\ell_b/\ell_m$  ratios less than 1 lead to very good results even if  $\ell_m$  is relaxed to very small values. This observation justifies the choice of selecting a fixed ratio  $\ell_b/\ell_m = 1/2$  and decreasing both lengths at the same time.

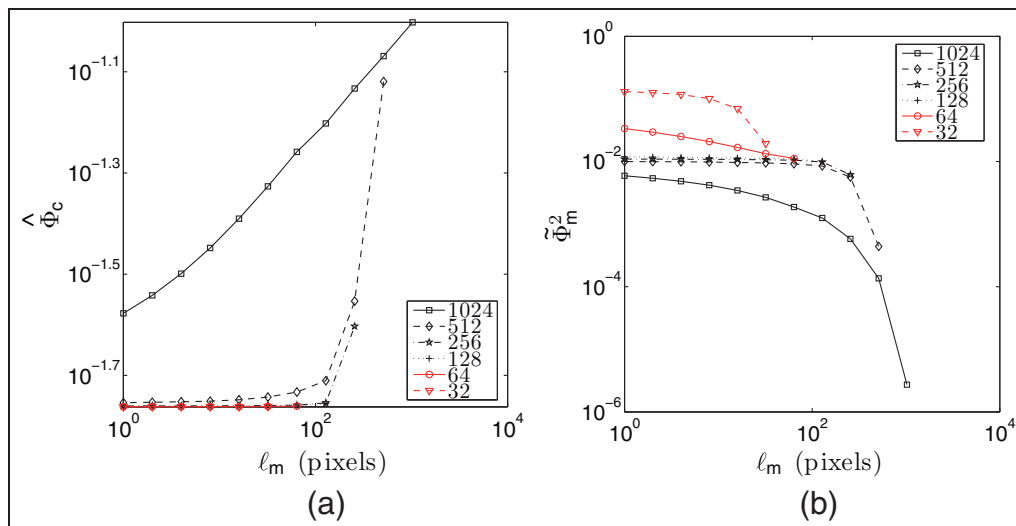
All these trends are confirmed when the mean correlation residuals are analyzed in Figure 4. For a large range of regularization length ratios, the levels of correlation residuals are virtually identical. The image registration is of comparable quality. The only difference is given by the weight put on the mechanical and edge regularizations. This choice is left to the user and its understanding of the underlying behavior of the studied material. The same can be said for the edge regularization, which is related to the boundary conditions of the mechanical analysis when DIC is assisted by mechanics.

Figure 5 shows the change of the standard deviation between the measured and prescribed displacement fields for the different cases when  $\ell_b/\ell_m = 1/2$ . The standard displacement error is virtually identical for the two displacement components (except for very large initial regularization lengths), even though an unstructured mesh is used. No bias is noted due to the fact that the mesh is not regular. Different trends are observed. First, for very large initial regularization lengths (i.e.  $\ell_m > n_x, n_y$ ), the standard error is very high. This is caused by interpolation errors as very large regularization lengths prevent from assessing small displacement fluctuations. When they are relaxed, a smaller but still significant error is observed. Conversely, for small regularization lengths, the standard error remains small but the relaxation increases slightly the error. When an initial value  $\ell_m = 128$  pixels is chosen, the smallest errors are observed. For initial lengths less than  $\ell_m = 128$  pixels, error levels of the order of or less than  $10^{-2}$  pixel are achieved.

For the same series of computations, Figure 6(a) shows the change of the dimensionless correlation residuals  $\hat{\Phi}_c$ . When the initial regularization lengths are such that  $\ell_m < n_x, n_y$ , the correlation residuals reach very similar values, thereby indicating that the results are trustworthy. For the quality of image registration, they indicate that initial regularization lengths  $\ell_m$  less than 256 pixels, the overall registration quality is very close for any initial or subsequent regularization length. This conclusion is in very good agreement with what is observed in Figure 5. For large initial regularization lengths, the mean correlation residuals reach high levels (i.e. almost an order of magnitude higher). This is the consequence of the interpolation error discussed before, as the sought displacement field does not belong to the kernel of the regularization operator. The next choice is then to seek more or less mechanical content in the measured



**Figure 5.** Change of the standard displacement error for different regularization lengths and different initialization lengths  $\ell_m$  (in pixels) indicated in the legend.



**Figure 6.** Change of (a) the dimensionless correlation residuals and (b) equilibrium residuals for different regularization lengths and different initialization lengths  $\ell_m$  (in pixels) indicated in the legend.

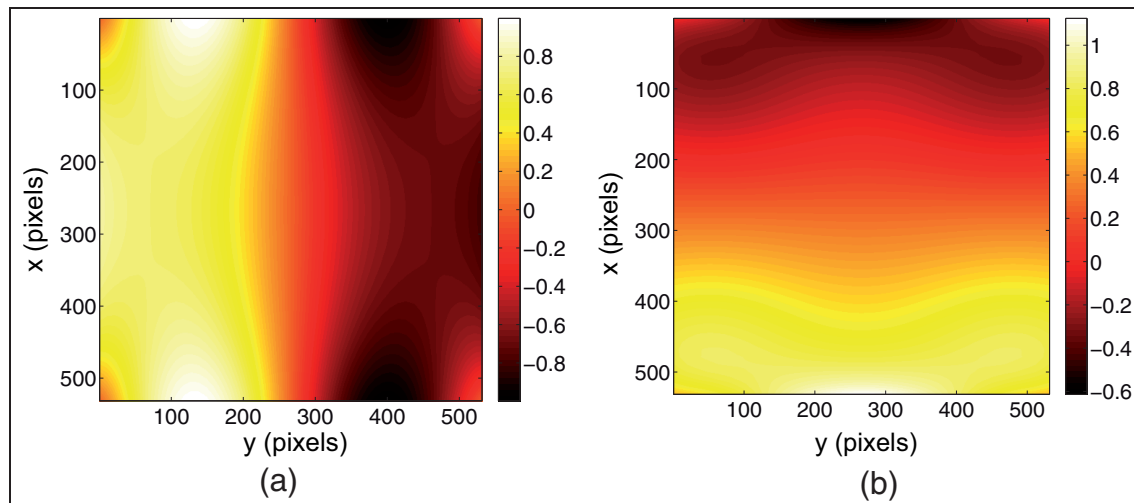


**Figure 7.** Prescribed displacement field in the mechanical test case in (a) the vertical and (b) horizontal directions. The displacements are expressed in pixels.

displacement field. This is characterized by the equilibrium gap whose mean normalized value is shown in Figure 6(b). For larger regularization lengths, the measured field displays less equilibrium gap as its weight in the total functional (10) is increased. There is a whole range of initial values ( $128 < \ell_m < 512$  pixels) for which the equilibrium gap is independent of the initial value of  $\ell_m$ . This zone is the most favorable in the present case.

In all the following analyses, the ratio  $\ell_b/\ell_m$  is set to  $1/2$ . It follows that there is more weight put to the mechanical regularization than the edge regularization. The former will be mainly studied in the remainder of this article.

### Mechanics-based displacement

An elastic calculation (with Poisson's ratio  $\nu = 0.3$ ) is performed on a plate whose size is exactly the same as

the reference picture shown in Figure 2. The boundary of the top part only moves in the horizontal direction, and the boundary of the bottom part has a prescribed displacement that is again a sine wave of unitary amplitude and wavelength equal to the length of the lower edge. A mesh consisting of  $50 \times 50$  Q4 elements is considered. The corresponding displacement is subsequently interpolated at the pixel level by using bilinear shape functions of Q4 elements. Figure 7 shows the displacement components that are used to deform the reference picture of Figure 2. The range of vertical displacement is equal to 2 pixels and that of the horizontal displacements is of the order of 1.7 pixels.

The same type of computation as before is performed in the present case when  $\ell_b/\ell_m = 1/2$ . Figure 8 shows the change of the standard displacement. The same trends are observed when compared to Figure 5 for the same reasons. For initial regularization lengths

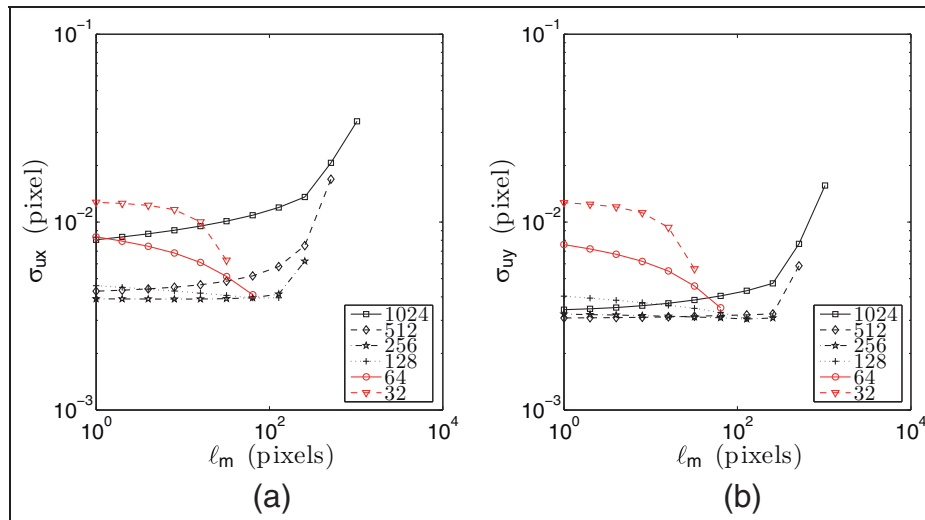


**Figure 8.** Change of the standard displacement error for different regularization lengths and different initialization lengths  $\ell_m$  (in pixels) indicated in the legend.

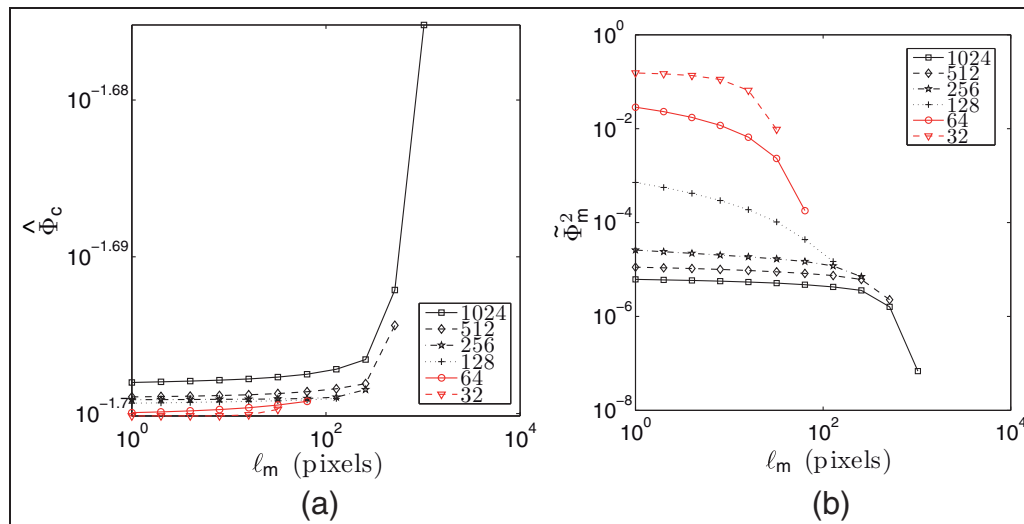


**Figure 9.** Change of (a) the dimensionless correlation residuals and (b) equilibrium residuals for different regularization lengths and different initialization lengths  $\ell_m$  (in pixels) indicated in the legend.

$\ell_m$  ranging from 64 to 512 pixels, the error level is less than  $10^{-2}$  pixel at the end of the relaxation process. It is worth remembering that this error includes the approximations of the reference solution (on a regular Q4 mesh), those of the T3 mesh used in the DIC analysis and the inevitable gray-level interpolation.

The same conclusions can be drawn when the trends observed in terms of correlation residuals (Figure 9(a)) and equilibrium residuals (Figure 9(b)) are compared with those of the previous test case.

There are, however, differences to be noted. First, the correlation residuals do not vary over a large dynamic range when compared to the previous case. It is concluded that even though large regularization lengths are used, they still allow for more fluctuations of the displacement field. Second, the minimum levels of the equilibrium residuals are less than those observed

in the previous case. This is to be expected since the present test case is associated with a mechanically admissible displacement field (in an FE sense).

From the results of the two test cases discussed in this section, it is concluded that the implementation of mechanics-aided DIC (or MA-DIC) is validated. The next section will deal with image pairs obtained during an experimental test.

### Analysis of two different textures

In the following analyses, experimental data are considered. A cross-shaped sample made of nodular graphite cast iron was loaded equibiaxially along two perpendicular directions (i.e.  $F_1 = F_2 = F$ , where  $F_1$  and  $F_2$  are the applied forces along the two directions). One surface of the sample was observed at the macroscale

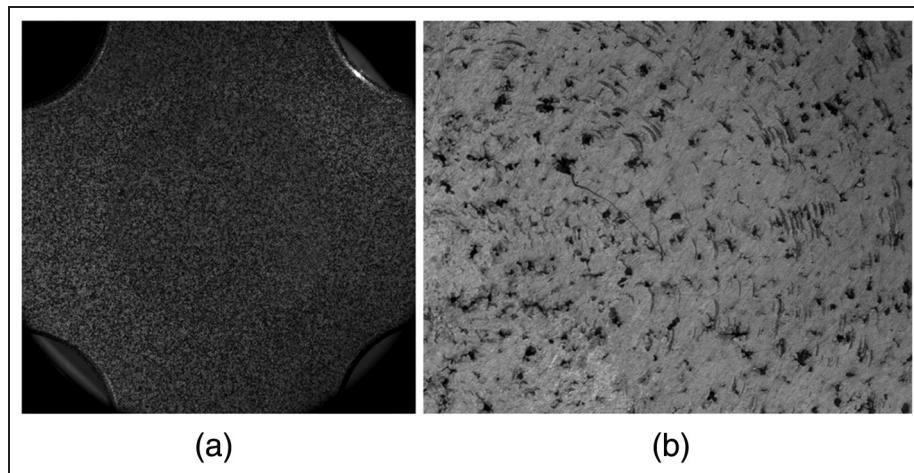


**Figure 10.** Reference pictures at (a) the macroscopic and (b) mesoscopic scales of a cross-shaped sample made of nodular graphite cast iron.

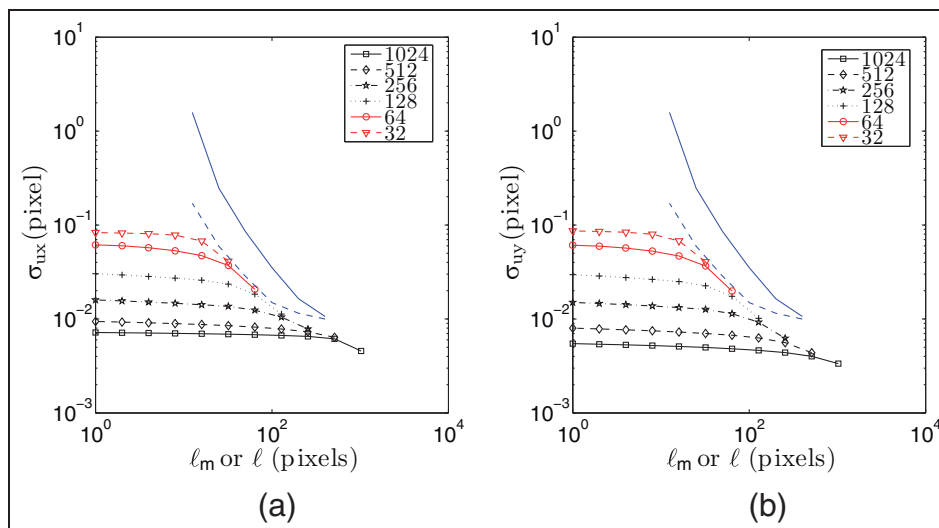


**Figure 11.** Standard displacement resolution in (a) the vertical and (b) horizontal directions for different regularization lengths  $\ell_m$ , ZOI (dashed blue line) or element (solid blue line) sizes  $\ell$  when  $\ell_b/\ell_m = 1/2$ . The legend indicates the initial length  $\ell_m$  (in pixels).

(picture definition:  $1024 \times 1024$  pixels, 12-bit digitization, telecentric lens) and the other one at the mesoscale (picture definition:  $1024 \times 1280$  pixels, 12-bit digitization, telecentric lens) (see Figure 10). The observation of the former required to spray black and white paint to enable DIC analyses. The latter is a natural texture, which is very difficult to analyze with conventional DIC procedures. The physical size of one pixel is  $6.7 \mu\text{m}$  for the mesoscale picture and  $48 \mu\text{m}$  for the macro-scale picture.

### Natural texture

The image pair considered in this section corresponds to two consecutive pictures shot when the sample was already mounted in the testing machine with  $F = 0$ . This analysis is performed to evaluate the resolution of the measurement technique.<sup>1</sup> Figure 11 shows the

standard displacement resolution for the two displacement components of displacement. The larger the regularization length, the smaller the displacement resolution. It is worth noting that any value less than one centipixel is very seldom encountered. This is even more noteworthy that the texture of the pictures is very difficult to analyze. To get all the results reported in Figure 11 (requiring 51 simulations), less than 1 h of CPU time was needed on an Intel Xeon X5660 processor. The mesh consisted of 8749 nodes and therefore involved 17,498 kinematic unknowns.

To compare the present results with more standard approaches, a local and global Q4-DIC analysis is run. It is based on four-noded ZOIs for the local approach and four-noded elements in a global approach. In both cases, a bilinear displacement is considered. The implementation details of both approaches follow very closely those used herein<sup>12</sup> *except* that no regularization

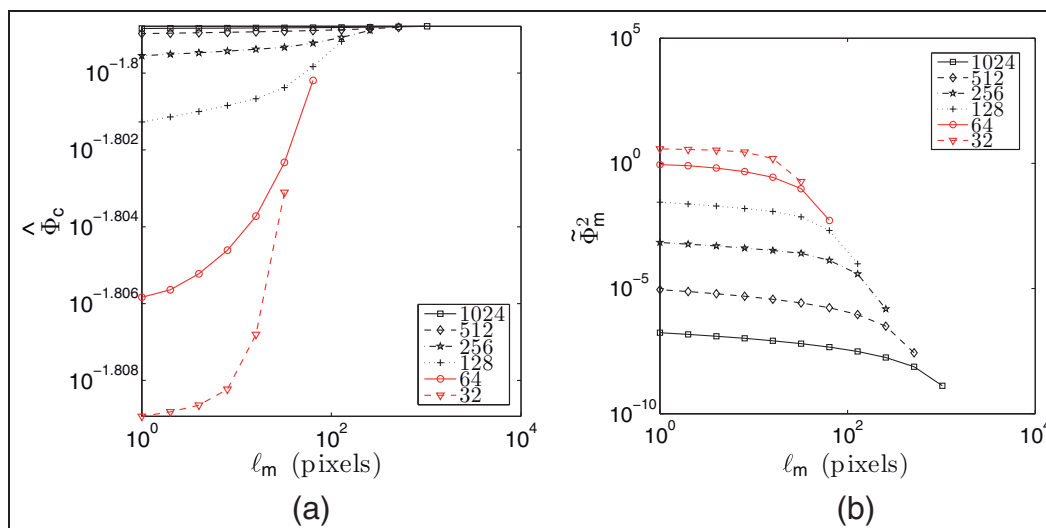


**Figure 12.** Change of (a) the dimensionless correlation residuals and (b) equilibrium residuals for different regularization lengths and different initializations. Note the narrow range of variation of  $\langle \Phi_c \rangle$ .

length is used. The right envelope of the regularized results virtually coincides with those of the global Q4-DIC analysis. The global analysis, as expected when the same ZOI and element size is considered, outperforms the local analysis.<sup>12</sup> With this difficult texture, there is a clear gain to consider global versus local approaches. The regularization proposed herein induces a very significant additional gain as all the nonmechanical fluctuations are filtered out. Finally, the relaxation process of the regularization length leads to very significant reductions of the displacement fluctuations.

Figure 12(a) shows the dimensionless correlation residuals for different initial regularization lengths. Their level remains almost constant and very small for any value of the correlation length. This result indicates that in the present case, it is impossible to discriminate any displacement from the analysis of the correlation residuals alone. However, the equilibrium residuals (Figure 12(b)) vary very strongly with the regularization lengths. In this particular case, the gain provided by the mechanical regularization is spectacular, namely, all the spurious fluctuations are filtered out.

If an estimate of the displacement field is sought with a very light mechanical regularization, the procedure to follow is to run a first correlation with a very large regularization length, say  $\ell_m = 1024$  pixels. At convergence, a second calculation could be run  $\ell_m = 512$  pixels by using an initial guess that is the displacement field at convergence with  $\ell_m = 1024$  pixels. If this path is followed, it can be stopped when  $\ell_m = 1$  pixel. The result given in Figure 11 shows that the displacement resolution is very small and the equilibrium residual remains very small (Figure 12(b)).

The next issue is related to the choice of the variation of the regularization length between two consecutive computations. Figure 13 shows the standard displacement resolution for the two components of displacement when different ratios are applied to the

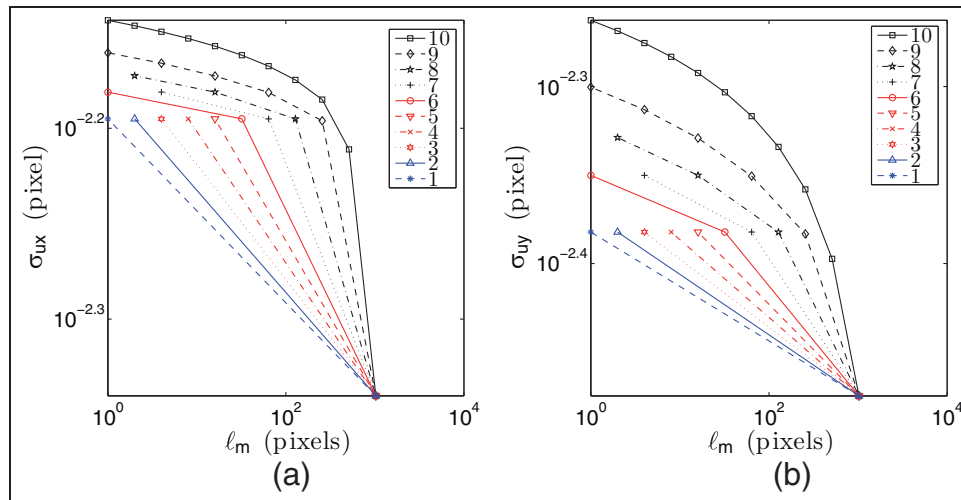
regularization lengths. If a very small regularization is considered and initialized with the result obtained for  $\ell_m = 1024$  pixels, the displacement resolution remains less than when the previous relaxation process is followed. With this route, the displacement resolution becomes even smaller and virtually independent of the final regularization length.

Figure 14(a) shows that the dimensionless correlation residuals are constant for all the computations with this procedure. The equilibrium residuals (Figure 14(b)) vary but not strongly when the regularization length is reduced. This result shows that there is no need to run numerous calculations to relax the regularization. Only a first computation is needed with a large regularization length, say  $\ell_m = 1024$  pixels, followed by a second one for a small length (i.e. values as low as  $\ell_m = 1$  pixel can be considered).

### Artificial texture

The image pair correlated hereafter corresponds to a reference configuration when  $F = 0$ , and a deformed configuration for which  $F = 25$  kN. When this load level is reached, the entire sample still lies within the elastic domain. In the present case, the boundary of the ROI is adapted to the geometry of the sample (Figure 15). No special care was exercised to match the connecting radii to the straight parts. Consequently, the edge regularization discussed previously is still used. Had the geometry been fully match with the external boundary, a traction-free condition could have been used instead.

Figure 16(a) shows the dimensionless correlation residuals for different initial regularization lengths with the same type of computations as before ( $\ell_b/\ell_m = 1/2$ ). Their level remains almost constant for any value of the correlation length and very low. This result indicates that all the evaluations are close. However, the



**Figure 13.** Standard displacement resolution in (a) the vertical and (b) horizontal directions for different regularization lengths and different number of jumps of the regularization length (indicated in the legend).

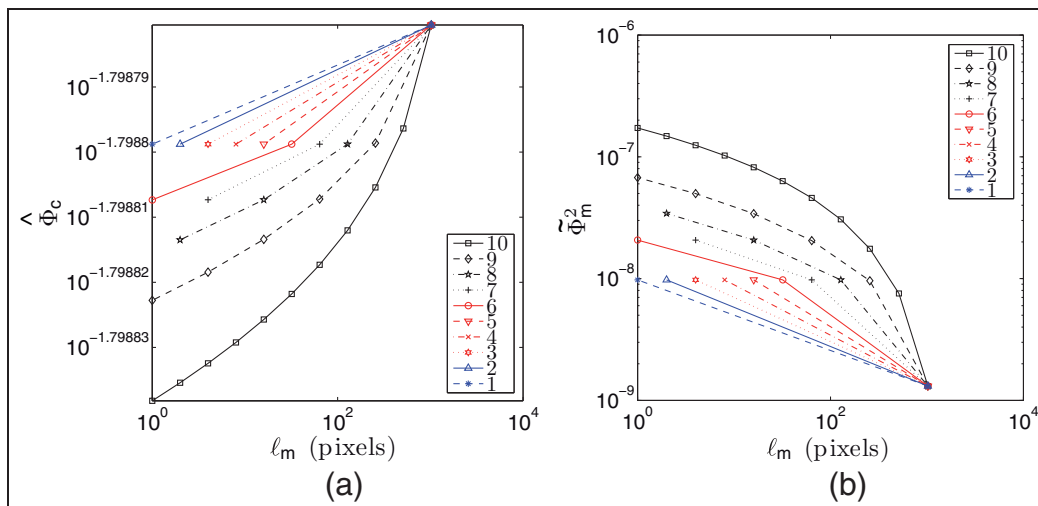


**Figure 14.** Change of (a) the dimensionless correlation residuals and (b) equilibrium residuals for different regularization lengths and different number of jumps (indicated in the legend) to decrease the regularization length. Note the narrow range of variation of  $\hat{\Phi}_c$ .

equilibrium residuals (Figure 16(b)) are the smallest for large initial regularization lengths.

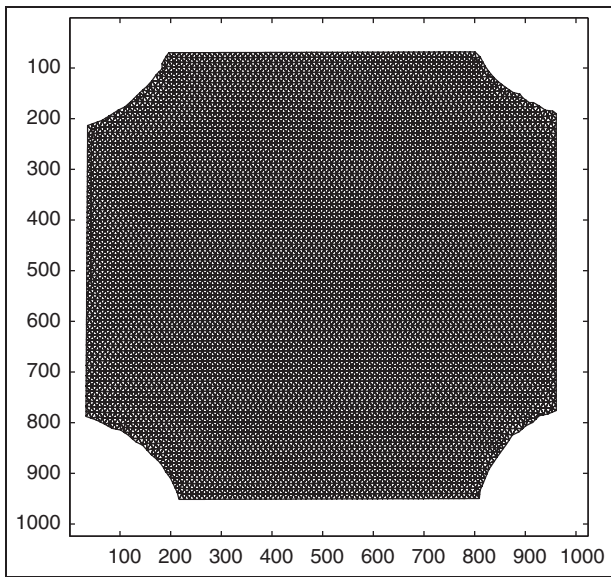
For small initial regularization lengths, the equilibrium residuals are less than those observed in the previous case. This result allows us to fully relax the regularization length (i.e.  $\ell_m = 1$  pixel) and even start with a modest one (e.g.  $\ell_m = 64$  or 32 pixels). This is made possible thanks to the texture quality that is better than that of the previous approach.

Figure 17 shows the displacement components that are measured when  $\ell_m = 1$  pixel with an initial value of 32, 128, and 1024 pixels. The range of vertical displacement is equal to 0.9 pixel and that of the horizontal displacements is about 1 pixel. There is a clear strain concentration in the central part of the sample, where the transverse thickness is reduced (Figure 10(a)). Note that this effect is not taken into account in the

regularization kernel where plane elasticity is assumed to hold. As the initial regularization length increases, the displacement fluctuations of the final results decrease because the relaxation process does not lead to the same solution.

## Summary and perspectives

Introducing a mechanically based regularization in an FE formulation of DIC was shown to lead to a significant reduction of uncertainty levels for artificial nonuniform displacement fields. Application of the same methodology to a real experimental case showed that even poor image textures could be dealt with successfully. In the present analyses, discretizations based upon unstructured meshes made of three-noded triangles (i.e. T3-DIC) were considered in the computations.



**Figure 15.** Mesh made of T3 elements used in the MA-DIC analyses at the macroscopic scale (see Figure 10(a)).

The latter are less demanding than with a pixel-scale DIC approach. However, it is believed that the results presented herein are generic and should apply to pixel-scale DIC procedures.

The fact that a regularization could reduce the uncertainty in the same way as coarsening a spatial discretization has been reported in the past.<sup>15</sup> The novelty of the procedure proposed herein is that the resolution/regularization length limit can be broken through an appropriate driving of the regularized DIC algorithm. The mechanical kernel introduced in the global functional may not provide a genuine picture of the actual displacement field (see the sine wave displacement field as an artificial case study or the last example of a

specimen with a varying thickness). Thus, rather than prescribing a large regularization length scale, the latter can be considered in a transient stage of the algorithm to help dealing with large displacements and/or poor textures (see the picture of spheroidal graphite (SG) cast iron at the mesoscale). This regularization provides only an “educated guess” for the displacement field, where the actual freedom of DIC is very much constrained. However, at convergence, relaxing the regularization length scale to very small values (and hence playing only a negligible role) allows the DIC procedure to inherit from a displacement field that is much closer to the actual displacement field. Hence, spurious pinning of the estimated displacement field in local secondary minima is drastically reduced. However, this reduction is not complete, and if the initial regularization length scale is too small, some amount of random pinning is still present at the initial stage and cannot be relaxed upon further relaxation steps. Figure 17 is an illustration of this property. The existence of history-dependent solutions (i.e. not controlled exclusively by the value of the element size  $\ell$ ) is a clear sign of multiple minima, calling for adapted strategies to avoid (or limit) spurious trapping.

The philosophy of this procedure can be compared with the pyramidal multiscale approach proposed by Besnard et al.<sup>11</sup> There again, kinematic degrees of freedom are reduced and local minima avoided in transient stages of the algorithm. At each scale, the converged field is used as an initialization for the finer scale, and hence, this multiscale driving provided both robustness and lower uncertainties. However, such a multiscale procedure is not easily implemented with a unstructured mesh decomposition, unless the mesh is endowed with a hierarchical structure. In contrast, the mechanical regularization easily complies with an arbitrary discretization.

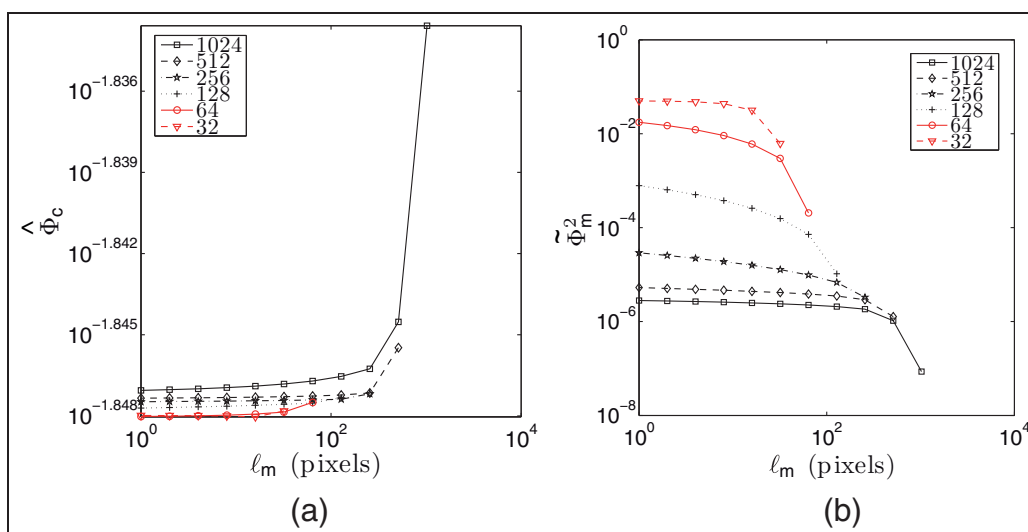


**Figure 16.** Change of (a) the dimensionless correlation residuals and (b) equilibrium residuals for different regularization lengths and different initialization lengths  $\ell_m$  (in pixels) indicated in the legend.



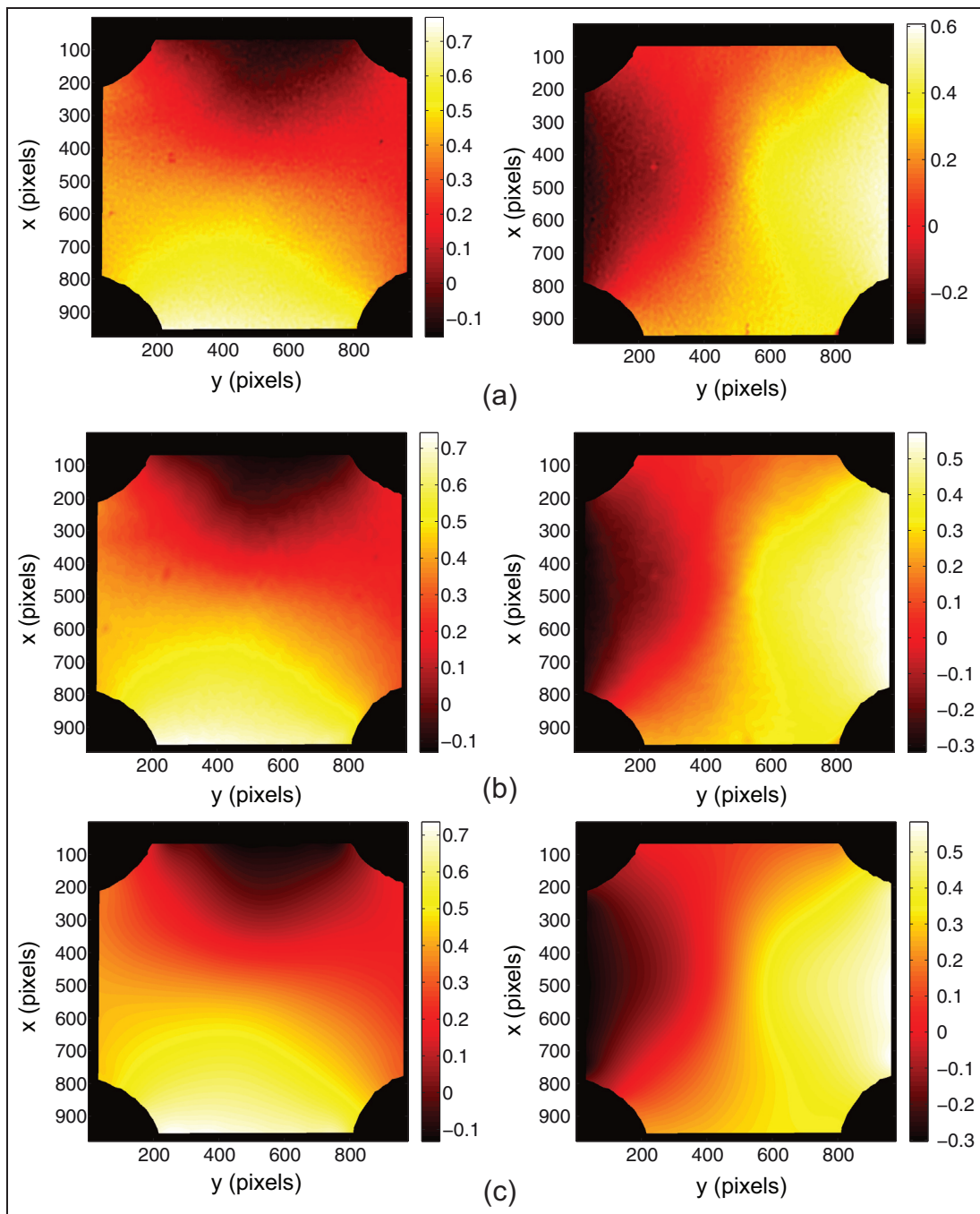


**Figure 17.** Measured displacement field in the biaxial test in the vertical (left) and horizontal (right) directions. Three initial regularization lengths  $\ell_m$  are considered: (a) 32, (b) 128, and (c) 1024 pixels. The final regularization length is identical ( $\ell_m = 1$  pixel). The displacements are expressed in pixels.

### Acknowledgements

Z.T. thanks the International Affairs Bureau of École Normale Supérieure de Cachan for its support during his stay at LMT-Cachan.

### Declaration of conflicting interests

The authors declare that there are no conflicts of interest.

### Funding

This work was partly supported by a grant from Région Île-de-France (plateforme francilienne d'expérimentation mécanique de troisième génération).

### References

1. ISO/IEC Guide 99–12:2007. *International vocabulary of metrology—basic and general concepts and associated*

- terms, *VIM*. Geneva: International Organization for Standardization.
2. Bergonnier S, Hild F and Roux S. Digital image correlation used for mechanical tests on crimped glass wool samples. *J Strain Anal Eng* 2005; 40(2): 185–197.
  3. Bornert M, Brémand F, Doumalin P, et al. Assessment of digital image correlation measurement errors: methodology and results. *Exp Mech* 2009; 49(3): 353–370.
  4. Lucas BD and Kanade T. An iterative image registration technique with an application to stereo vision. In: *Proceedings of the 1981 DARPA image understanding workshop*, April 1981, pp.121–130.
  5. Burt PJ, Yen C and Xu X. Local correlation measures for motion analysis: a comparative study. In: *Proceedings of the IEEE conference on pattern recognition and image processing*, Las Vegas (NV), USA, 14–17 June 1982, pp.269–274. New York (NY), USA: IEEE.
  6. Sutton MA, Wolters WJ, Peters WH, et al. Determination of displacements using an improved digital correlation method. *Image Vision Comput* 1983; 1(3): 133–139.
  7. Sutton MA, McNeill SR, Helm JD, et al. Advances in two-dimensional and three-dimensional computer vision. In: Rastogi PK (ed.) *Photomechanics, topics in applied physics*. Berlin: Springer, 2000, pp.323–372.
  8. Sutton MA, Orteu J-J and Schreier H. *Image correlation for shape, motion and deformation measurements: basic concepts, theory and applications*. New York: Springer, 2009.
  9. Broggiato GB. Adaptive image correlation technique for full-field strain measurement. In: *Proceedings of the 12th international conference on experimental mechanics (ICEM'12)*, Mc Graw-Hill, Milan, Bari, Italy, 29 August–2 September 2004, pp.420–421.
  10. Sun Y, Pang J, Wong C, et al. Finite-element formulation for a digital image correlation method. *Appl Optics* 2005; 44(34): 7357–7363.
  11. Besnard G, Hild F and Roux S. “Finite-element” displacement fields analysis from digital images: application to Portevin-Le Chatelier bands. *Exp Mech* 2006; 46: 789–803.
  12. Hild F and Roux S. Comparison of local and global approaches to digital image correlation. *Exp Mech* 2012; 52: 1503–1519.
  13. Rupil J, Vincent L, Hild F, et al. Probabilistic modeling of mesocrack initiations in 304L stainless steel. *Int J Multiscale Com* 2011; 9(4): 445–458.
  14. Passieux J-C and Périé J-N. High resolution digital image correlation using proper generalized decomposition: PGD-DIC. *Int J Numer Meth Eng* 2012; 92(6): 531–550.
  15. Leclerc H, Périé J-N, Roux S, et al. Voxel-scale digital volume correlation. *Exp Mech* 2011; 51(4): 479–490.
  16. Leclerc H, Périé J-N, Hild F, et al. Digital volume correlation: what are the limits to the spatial resolution? *Mec Ind* 2012; 13: 361–371.
  17. Réthoré J, Roux S and Hild F. An extended and integrated digital image correlation technique applied to the analysis fractured samples. *Eur J Comput Mech* 2009; 18: 285–306.
  18. Tikhonov AN and Arsenin VY. *Solutions of ill-posed problems*. New York: John Wiley & Sons Inc., 1977.
  19. Bonnet M and Constantinescu A. Inverse problems in elasticity. *Inverse Probl* 2005; 21: R1–R50.
  20. Claire D, Hild F and Roux S. A finite element formulation to identify damage fields: the equilibrium gap method. *Int J Numer Meth Eng* 2004; 61(2): 189–208.
  21. Fedele R, Raka B, Hild F, et al. Identification of adhesive properties in GLARE assemblies by digital image correlation. *J Mech Phys Solids* 2009; 57: 1003–1016.
  22. Wei Z, Deng X, Sutton MA, et al. Modeling of mixed-mode crack growth in ductile thin sheets under combined in-plane and out-of-plane loading. *Eng Fract Mech* 2011; 78: 3082–3102.
  23. Leclerc H, Périé J-N, Roux S, et al. Integrated digital image correlation for the identification of mechanical properties. In: *Proceedings of the 4th international conference on computer vision/computer graphics collaboration techniques, MIRAGE'09* (eds A Gagalowicz and W Philips), Rocquencourt, France, 4–6 May 2009, pp.161–171. Berlin: Springer.

## Appendix I

### Notation

$\{\mathbf{b}\}$	correlation vector
$\{\mathbf{b}^n\}$	correlation vector at iteration $n$
$\mathbf{d}\mathbf{u}$	displacement increment vector
$f$	picture in the reference configuration
$\{\mathbf{f}\}$	nodal force vector
$\{\mathbf{f}_r\}$	residual force vector
$F$	applied load level
$g$	picture in the deformed configuration
$i$	imaginary unit
$j$	iteration number
$\mathbf{k}$	wave vector
$[\mathbf{K}]$	stiffness matrix
$\ell_m, \ell_b$	regularization lengths
$[\mathbf{L}]$	edge regularization matrix
$[\mathbf{M}]$	correlation matrix
$[\mathbf{N}]$	global matrix
$n$	index
$n_x, n_y$	number of pixels in the ROI
$t$	transposition operator
$\mathbf{u}$	displacement vector
$\{\mathbf{u}\}$	vector collecting all kinematic degrees of freedom
$u_n$	degree of freedom
$u_x, u_y$	displacement components
$\mathbf{u}^0$	initial displacement vector
$\{\mathbf{u}^j\}$	vector collecting all kinematic degrees of freedom at iteration $j$
$\{\delta\mathbf{u}\}$	correction vector of the measured degrees of freedom
$\mathbf{v}$	trial displacement vector
$v_0$	amplitude of trial displacement
$w_m, w_b$	weights
$\mathbf{x}$	position vector
$x, y$	position component
$\Psi_n$	vector field
$\Phi$	normalized residuals
$\Phi_b^2$	global edge residual
$\Phi_c^2$	correlation residual
$\varphi_c^2$	sum of squared differences
$\hat{\Phi}_c^2$	dimensionless global correlation residual
$\Phi_m^2$	global equilibrium gap residual

$\Phi_t$	total residual
$\nabla$	gradient operator
$\cdot$	scalar product
$\ $	amplitude
$\langle \rangle$	average over the ROI

## Appendix 2

### Edge regularization

In this appendix, the edge regularization is presented. To be consistent with the bulk regularization, a local quadratic form is sought on the nodal displacement that has to be invariant under a rigid body motion. The consequence of this requirement is that such a quadratic form will have a simple mechanical interpretation. Local in the context of a discretized medium means that the edge regularization will only be based on nearest neighbors. Thus, focusing on specific node,  $M_n$ , only the three consecutive nodes located at points  $(M_{n-1}, M_n, M_{n+1})$  will be considered (irrespective of their alignment or not). Because of translational invariance, one may choose  $M_n$  as the origin, so that the geometry is captured through the two vectors  $\mathbf{s}_{-1} = \mathbf{M}_n \mathbf{M}_{n-1}$  and  $\mathbf{s}_1 = \mathbf{M}_n \mathbf{M}_{n+1}$ . It is convenient to introduce the orthogonal vectors of  $\mathbf{s}_{-1}$  and  $\mathbf{s}_1$  rotated by  $\pi/2$ , respectively  $\boldsymbol{\tau}_{-1}$  and  $\boldsymbol{\tau}_1$ .

The displacement vector at those nodes is denoted by  $(\mathbf{u}_{n-1}, \mathbf{u}_n, \mathbf{u}_{n+1})$ . Invariance under translation imposes that the regularization functional should be a quadratic form of  $(\mathbf{v}_{-1}, \mathbf{v}_1) = (\mathbf{u}_{n-1} - \mathbf{u}_n, \mathbf{u}_{n+1} - \mathbf{u}_n)$ . Invariance under rotation imposes that the functional should be invariant under the following change in the displacement field, where  $\boldsymbol{\omega}$  and  $\omega$  denote, respectively, a rotation vector and its magnitude

$$\begin{aligned} \mathbf{v}_{-1} &= \boldsymbol{\omega} \times \mathbf{s}_{-1} = \omega \boldsymbol{\tau}_{-1} \\ \mathbf{v}_1 &= \boldsymbol{\omega} \times \mathbf{s}_1 = \omega \boldsymbol{\tau}_1 \end{aligned} \tag{16}$$

Three scalars  $a_n$  ( $n = 1, 2, 3$ ) can be formed, which are invariant under such a rotation. The first two depend on a pair of neighboring node displacement, namely

$$\begin{aligned} a_1 &= \frac{\mathbf{s}_{-1} \cdot \mathbf{v}_{-1}}{\|\mathbf{s}_{-1}\|^2} \\ a_2 &= \frac{\mathbf{s}_1 \cdot \mathbf{v}_1}{\|\mathbf{s}_1\|^2} \end{aligned} \tag{17}$$

where the normalization has been introduced here for reasons that will become clearer later. The third scalar reads

$$a_3 = \frac{\boldsymbol{\tau}_1 \cdot \mathbf{v}_1}{\|\boldsymbol{\tau}_1\|^2} - \frac{\boldsymbol{\tau}_{-1} \cdot \mathbf{v}_{-1}}{\|\boldsymbol{\tau}_{-1}\|^2} \tag{18}$$

Thus, the most general form for the sought functional is expressed as

$$T_b = \frac{1}{2} \sum_n \alpha_n a_n^2 \tag{19}$$

where  $\alpha_n$  are arbitrary factors. The physical interpretation of those terms is straightforward. The first two correspond to a linear spring connecting nodes  $(M_{n-1}, M_n)$  and  $(M_n, M_{n+1})$ , respectively. Parameters  $\alpha_1$  and  $\alpha_2$  are the stiffnesses of these springs. The last invariant,  $a_3$ , corresponds to the resulting moment of forces at node  $M_n$ , and hence, the last term in the functional would correspond to an angular spring. In the absence of additional information, it is natural to choose all stiffnesses as constant, say equal to unity, and the total magnitude of the functional being set with respect to the other functionals as discussed in the main text.

To make the expression of this functional more explicit, the ‘‘rigidity’’ matrix  $[\mathbf{L}]$  introduced in the main text is obtained by assembling (with respect to all boundary nodes  $i$ ) the local contributions

$$T_b = \frac{1}{2} (\mathbf{v}_1 \quad \mathbf{v}_{-1}) \cdot \begin{pmatrix} \frac{\mathbf{s}_1 \otimes \mathbf{s}_1}{\|\mathbf{s}_1\|^4} + \frac{\boldsymbol{\tau}_1 \otimes \boldsymbol{\tau}_1}{\|\boldsymbol{\tau}_1\|^4} & -\frac{\boldsymbol{\tau}_1 \otimes \boldsymbol{\tau}_{-1}}{\|\boldsymbol{\tau}_1\|^2 \|\boldsymbol{\tau}_{-1}\|^2} \\ -\frac{\boldsymbol{\tau}_{-1} \otimes \boldsymbol{\tau}_1}{\|\boldsymbol{\tau}_{-1}\|^2 \|\boldsymbol{\tau}_1\|^2} & \frac{\mathbf{s}_{-1} \otimes \mathbf{s}_{-1}}{\|\mathbf{s}_{-1}\|^4} + \frac{\boldsymbol{\tau}_{-1} \otimes \boldsymbol{\tau}_{-1}}{\|\boldsymbol{\tau}_{-1}\|^4} \end{pmatrix} \cdot \begin{pmatrix} \mathbf{v}_1 \\ \mathbf{v}_{-1} \end{pmatrix} \tag{20}$$

Noting that  $\|\boldsymbol{\tau}_n\| = \|\mathbf{s}_n\|$  and  $\mathbf{s}_n \otimes \mathbf{s}_n + \boldsymbol{\tau}_n \otimes \boldsymbol{\tau}_n = \|\mathbf{s}_n\|^2 \mathbf{I}$ , the particular choice of ‘‘elastic’’ constants,  $\alpha_n$ , leads to the simplified expression

$$T_b = \frac{1}{2 \|\mathbf{s}_1\|^2 \|\mathbf{s}_{-1}\|^2} (\mathbf{v}_1 \quad \mathbf{v}_{-1}) \cdot \begin{pmatrix} \|\mathbf{s}_{-1}\|^2 \mathbf{I} & -\boldsymbol{\tau}_1 \otimes \boldsymbol{\tau}_{-1} \\ -\boldsymbol{\tau}_{-1} \otimes \boldsymbol{\tau}_1 & \|\mathbf{s}_1\|^2 \mathbf{I} \end{pmatrix} \cdot \begin{pmatrix} \mathbf{v}_1 \\ \mathbf{v}_{-1} \end{pmatrix} \tag{21}$$

To conclude the final expression of the edge regularization matrix, the expression of  $\mathbf{v}$  as a function of the nodal displacement is to be used to convert the above quadratic form into

$$T_b = (\mathbf{u}_{i+1} \quad \mathbf{u}_i \quad \mathbf{u}_{i-1}) \cdot [\mathbf{L}] \cdot \begin{pmatrix} \mathbf{u}_{i+1} \\ \mathbf{u}_i \\ \mathbf{u}_{i-1} \end{pmatrix} \tag{22}$$

with  $[\mathbf{L}] = \frac{1}{2 \|\mathbf{s}_1\|^2 \|\mathbf{s}_{-1}\|^2} [\ell]$

$$\begin{aligned} \ell_{11} &= \|\mathbf{s}_{-1}\|^2 \mathbf{I} \\ \ell_{12} &= -\|\mathbf{s}_{-1}\|^2 \mathbf{I} + \boldsymbol{\tau}_1 \otimes \boldsymbol{\tau}_{-1} \\ \ell_{13} &= -\boldsymbol{\tau}_1 \otimes \boldsymbol{\tau}_{-1} \\ \ell_{21} &= -\|\mathbf{s}_{-1}\|^2 \mathbf{I} + \boldsymbol{\tau}_{-1} \otimes \boldsymbol{\tau}_1 \\ \ell_{22} &= (\|\mathbf{s}_{-1}\|^2 + \|\mathbf{s}_1\|^2) \mathbf{I} - \boldsymbol{\tau}_1 \otimes \boldsymbol{\tau}_{-1} - \boldsymbol{\tau}_{-1} \otimes \boldsymbol{\tau}_1 \\ \ell_{23} &= -\|\mathbf{s}_1\|^2 \mathbf{I} + \boldsymbol{\tau}_1 \otimes \boldsymbol{\tau}_{-1} \\ \ell_{31} &= -\boldsymbol{\tau}_{-1} \otimes \boldsymbol{\tau}_1 \\ \ell_{32} &= \|\mathbf{s}_1\|^2 \mathbf{I} + \boldsymbol{\tau}_{-1} \otimes \boldsymbol{\tau}_1 \\ \ell_{33} &= \|\mathbf{s}_1\|^2 \mathbf{I} \end{aligned} \tag{23}$$



# Appendix E

## Hybrid snail test data

*In this appendix displacement fields of the hybrid snail loading history are reported for macro- (FIG. E.1) and mesoscale (FIG. E.2) DIC analyses. The applied load level corresponds to 30 kN. The change of the mean strains during the experiment is extracted from the DIC gauge. FIG. E.3 shows the strain history in the loading directions while FIG. E.4 reports the mean eigen strains.*

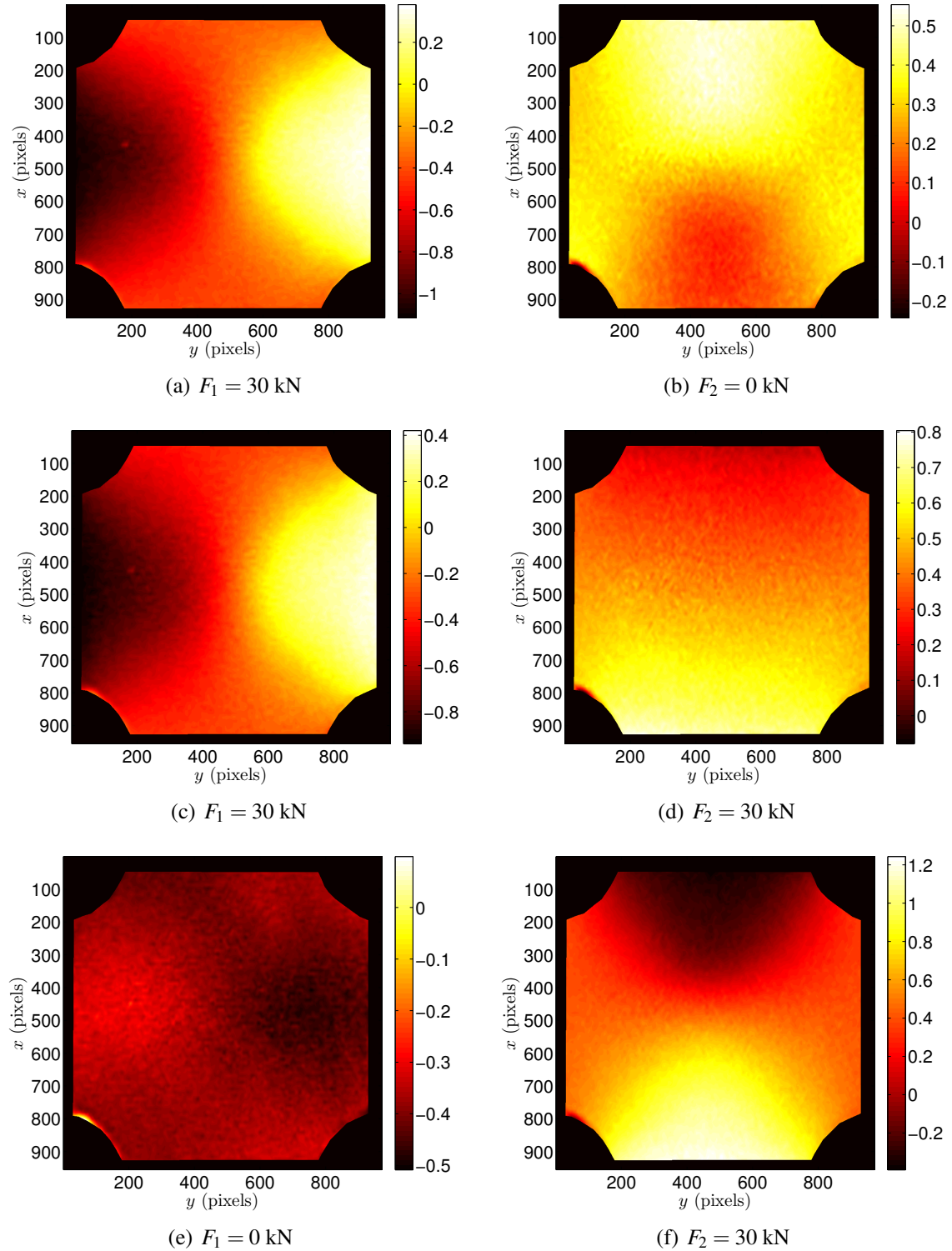


**Figure E.1:** Measured displacement fields at macroscale in the horizontal (left) and vertical (right) directions for the loading step corresponding to 30 kN. (a) and (b) correspond to point 1 (see FIG. 4.5(b)), (c) and (d) correspond to point 2 (see FIG. 4.5(b)), (e) and (f) correspond to point 3 (see FIG. 4.5(b))

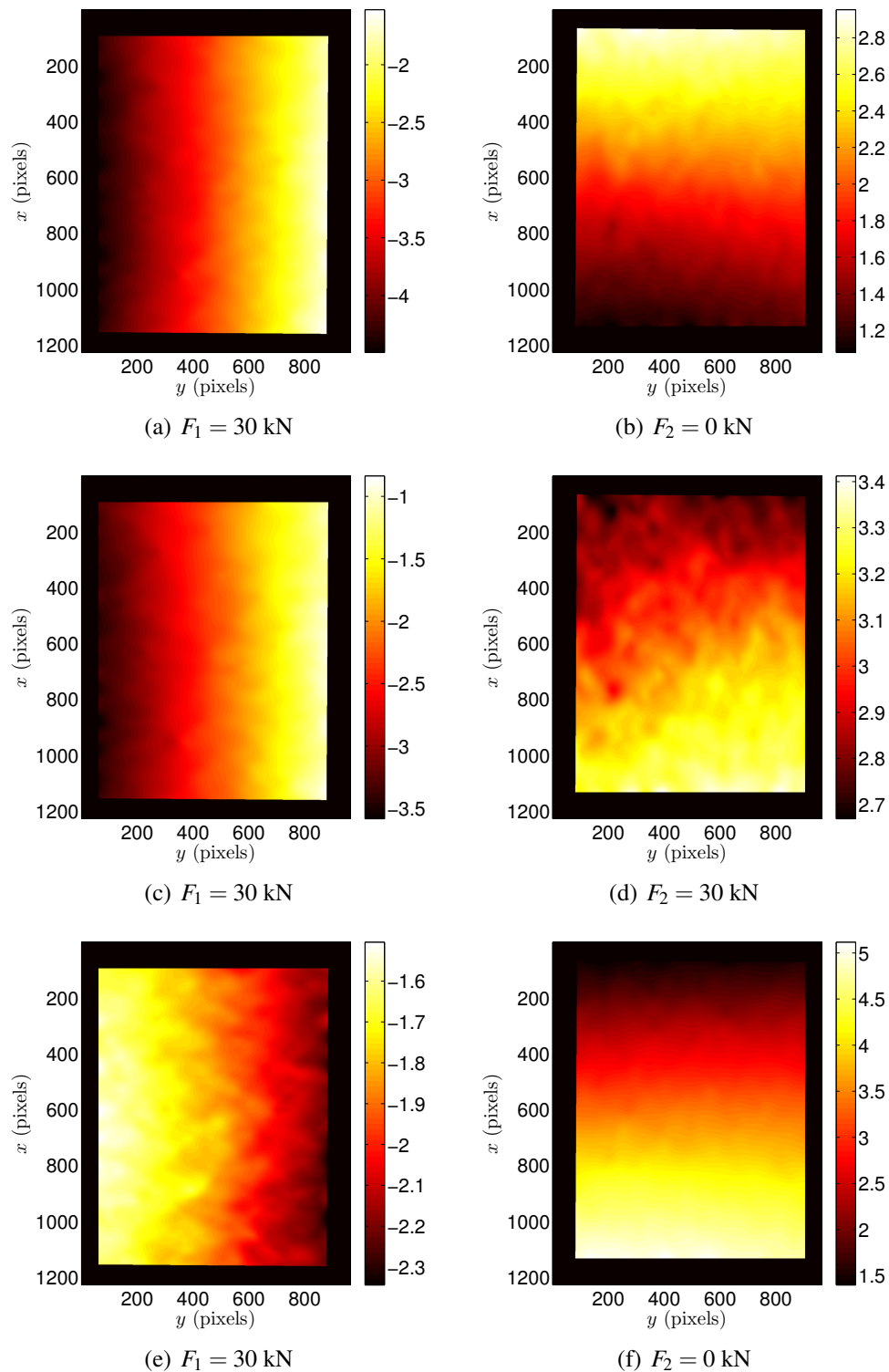
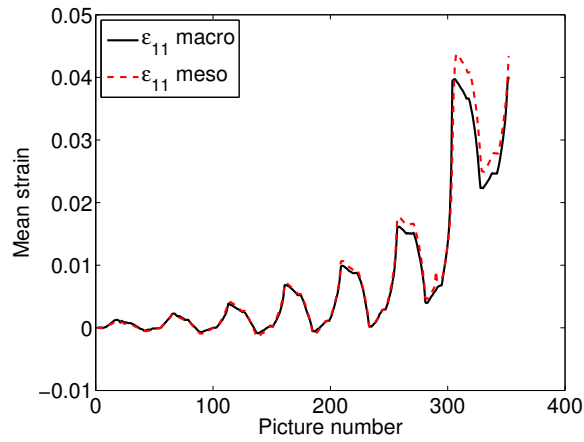
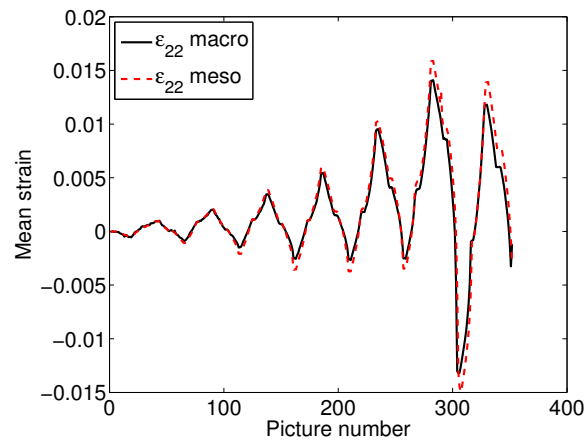


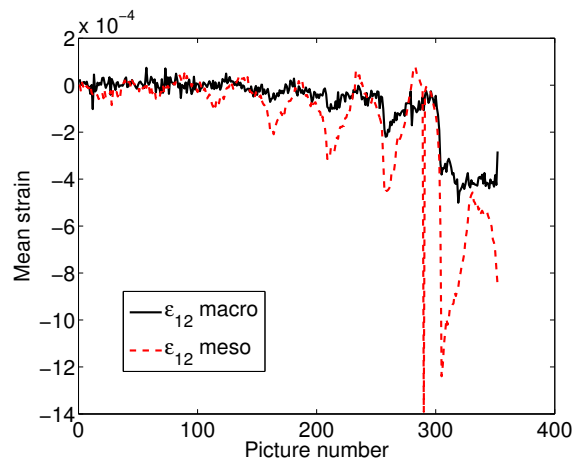
**Figure E.2:** Measured displacement fields at mesoscale in the horizontal (left) and vertical (right) directions for the loading level corresponding to 30 kN. (a) and (b) correspond to point 1 (see FIG. 4.5(b)), (c) and (d) correspond to point 2 (see FIG. 4.5(b)), (e) and (f) correspond to point 3 (see FIG. 4.5(b))



(a)



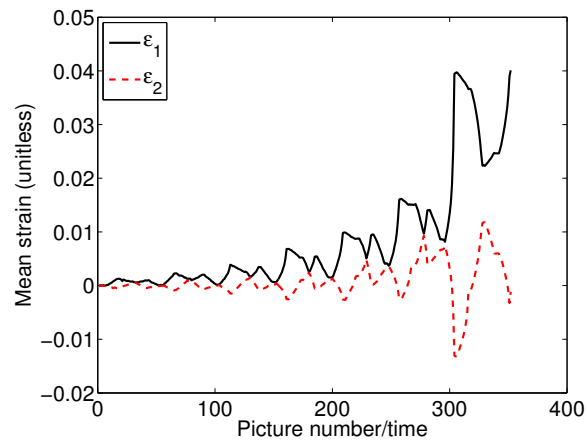
(b)



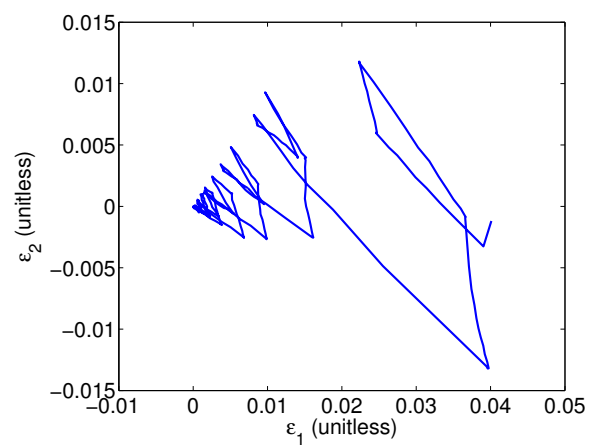
(c)

**Figure E.3:** Changes of (a)  $\epsilon_{11}$ , (b)  $\epsilon_{22}$ , (c)  $\epsilon_{12}$  during the hybrid “snail” loading history on macro and mesoscales



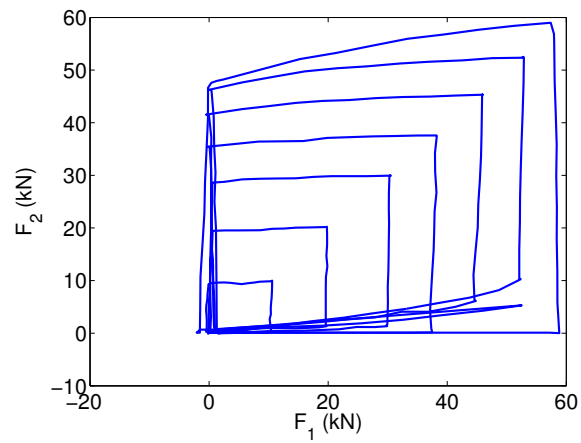


(a)



(b)

**Figure E.4:** (a) Change of mean eigen strains on macroscale with the picture number. (b) Dependence of mean eigen strains (*i.e.*,  $\epsilon_1$  vs.  $\epsilon_2$ )



(a)

**Figure E.5:** Measured loads in the hybrid “snail” path

# Bibliography

- [Abanto-Bueno and Lambros, 2002] Abanto-Bueno, J. and Lambros, J. (2002). Investigation of crack growth in functionally graded materials using digital image correlation. *Engineering Fracture Mechanics*, 69(14-16):695–1711.
- [Adewara and Loper, 1976] Adewara, J. O. T. and Loper, C. R. J. (1976). Effect of pearlite on crack initiation and propagation in ductile iron. *Transactions, American Foundrymen's Society*, 84:513–526.
- [Armstrong and Frederick, 1966] Armstrong, P. and Frederick, C. (1966). A mathematical representation of the multiaxial bauschinger effect. *Report RD/B/N 731, Central Electricity Generating Board*.
- [Avril et al., 2008a] Avril, S., Bonnet, M., Bretelle, A.-S., Grédiac, M., Hild, F., Ienny, P., Latourte, F., Lemosse, D., Pagano, S., Pagnacco, E., and Pierron, F. (2008a). Overview of identification methods of mechanical parameters based on full-field measurements. *Experimental Mechanics*, 48(4):381–402.
- [Avril et al., 2008b] Avril, S., Pierron, F., Sutton, M. A., and J., Y. (2008b). Identification of elasto-visco-plastic parameters and characterization of luders behavior using digital image correlation and the virtual fields method. *Mechanics of Materials*, 40(9):729–742.
- [Babout et al., 2001] Babout, L., Maire, E., Buffière, J., and Fougères, R. (2001). Characterization by x-ray computed tomography of decohesion, porosity growth and coalescence in model metal matrix composites. *Acta Materialia*, 49(11):2055 – 2063.
- [Baruchel et al., 2000] Baruchel, J., Buffière, J.-Y., Maire, E., Merle, P., and Peix, G. (2000). *X-Ray Tomography in Material Sciences*. Hermes Science, Paris France.
- [Batisse et al., 1996] Batisse, R., Fant-Jaekels, H. D., Curie, F., and Virely, J. M. (1996). Biaxial high cycle fatigue tests on a gas transmission pipeline steel. *Fatigue and Fracture of Engineering Materials and Structures*, 19(10):1231–1238.
- [Bauschinger, 1881] Bauschinger, J. (1881). Ueber die veränderung der elasticitätsgrenze und elasticitätsmodul verschiedener. *Metal Civiling N. F.*, 27:289–348.

- [Bay et al., 1999] Bay, B., Smith, T., Fyhrie, D., and Saad, M. (1999). Digital volume correlation: Three-dimensional strain mapping using x-ray tomography. *Experimental Mechanics*, 39(3):217–226.
- [Bayati and Elliott, 1995] Bayati, H. and Elliott, R. (1995). Relationship between structure and mechanical properties in high manganese alloyed ductile iron. *Materials Science and Technology*, 11:284–293.
- [Bergonnier et al., 2005] Bergonnier, S., Hild, F., and Roux, S. (2005). Digital image correlation used for mechanical tests on crimped glass wool samples. *The Journal of Strain Analysis for Engineering Design*, 40(2):185–197.
- [Bernard et al., 2005] Bernard, D., Gendron, D., Heintz, J.-M., Bordère, S., and Ourneau, J. (2005). First direct 3d visualisation of microstructural evolutions during sintering through x-ray computed microtomography. *Acta Materialia*, 53(1):121–128.
- [Besnard et al., 2006] Besnard, G., Hild, F., and Roux, S. (2006). "finite-element" displacement fields analysis from digital images : Application to portevin-le châtelier bands. *Experimental Mechanics*, 46(6):789–804.
- [Bornert et al., 2009] Bornert, M., Brémand, F., Doumalin, P., Dupré, J.-C., Fazzini, M., Grédiac, M., Hild, F., Mistou, S., Molimard, J., Orteu, J.-J., Robert, L., Surrel, Y., Vacher, P., and Wattrisse, B. (2009). Assessment of digital image correlation measurement errors: methodology and results. *Experimental Mechanics*, 49(3):353–370.
- [Bouterf et al., 2015] Bouterf, A., Roux, S., Hild, F., G. Vivier, X. B., Maire, E., and Meille, S. (2015). Damage law identification from full field displacement measurement: Application to four-point bending test for plasterboard. *European Journal of Mechanics A/Solids*, 49:60–66.
- [Brogiato, 2004] Brogiato, G. (2004). Adaptive image correlation technique for full-field strain measurement. *Proceedings 12th Int. Conf. Exp. Mech.*
- [Bruck et al., 1989] Bruck, H., McNeill, S., Sutton, M., and Peters, W. (1989). Digital image correlation using newton-raphson method of partial differential correction. *Experimental Mechanics*, 29:261–267.
- [Buffière et al., 1999] Buffière, J.-Y., Maire, E., Cloetens, P., Lormand, G., and Fougères, R. (1999). Characterization of internal damage in a mmcp using x-ray synchrotron phase contrast microtomography. *Acta Materialia*, 47(5):1613 – 1625.
- [Calloch et al., 2002a] Calloch, S., Bouvet, C., Hild, F., Doudard, C., and LExcellent, C. (2002a). Analysis of mechanical behavior and in-situ observations of cu-al-be sma under biaxial compressive tests by using dic. *SPIE, Third International Conference on Experimental Mechanics*, 4537:83–86.

- [Calloch et al., 2002b] Calloch, S., Dureisseix, D., and Hild, F. (2002b). Identification de modèles de comportement de matériaux solides : utilisation d'essais et de calculs. *Technologies et Formations*, 100:36–41.
- [Chaboche, 1988] Chaboche, J. L. (1988). Continuum damage mechanics: Part i: General concepts, part ii: Damage growth, crack initiation, and crack growth. *Journal of Applied Mechanics*, 55(3):59–71.
- [Chaboche, 1982] Chaboche, L. (1982). The concept of effective stress applied to elasticity and to viscoplasticity in the presence of anisotropic damage. In: *Boehler JP (ed) Mechanical behavior of anisotropic solids*, pages 737–760.
- [Chaboche, 1991] Chaboche, L. (1991). On some modifications of kinematic hardening to improve the description of ratchetting effects. *International Journal of Plasticity*, 7(7):661 – 678.
- [Chalal et al., 2004] Chalal, H., Meraghni, F., Pierron, F., and Grédiac, M. (2004). Direct identification of the damage behaviour of composite materials using the virtual fields method. *Composites: Part A*, 35:841–848.
- [Chantier et al., 2000] Chantier, I., Bobet, V., Billardon, R., and Hild, F. (2000). A probabilistic approach to predict the very high-cycle fatigue behaviour of spheroidal graphite cast iron structures. *Fatigue and Fracture of Engineering Materials and Structures*, 23(2):173–180.
- [Chen et al., 1993] Chen, D., Chiang, F., Tan, Y., and Don, H. (1993). Digital speckle-displacement measurement using a complex spectrum method. *Applied Optics*, 32:1839–1849.
- [Chevalier et al., 2001] Chevalier, L., Calloch, S., Hild, F., and Marco, Y. (2001). Digital image correlation used to analyze the multiaxial behavior of rubber-like materials. *European J. Mechanics A/Solids*, 20:169–187.
- [Chiang et al., 2007] Chiang, K.-T., Chang, F.-P., and Tsai, D.-C. (2007). Modeling and analysis of the rapidly resolidified layer of sg cast iron in the edm process through the response surface methodology. *Journal of Materials Processing Technology*, 182(1-3):525–533.
- [Chow and Lu, 1992] Chow, C. and Lu, T. (1992). An analytical and experimental study of mixed-mode ductile fracture under nonproportional loading. *International Journal of Damage Mechanics*, 1:191–236.
- [Chu et al., 1985] Chu, T., Ranson, W., and Sutton, M. (1985). Applications of digital-image-correlation techniques to experimental mechanics. *Experimental Mechanics*, 25(3):232–244.

- [Claire et al., 2002] Claire, D., Hild, F., and Roux, S. (2002). Identification of damage fields using kinematic measurements. *Comptes-Rendus Mecanique*, 330:729–734.
- [Claire et al., 2004] Claire, D., Hild, F., and Roux, S. (2004). A finite element formulation to identify damage fields: the equilibrium gap method. *International Journal for Numerical Methods in Engineering*, 61(2):189–208.
- [Claire et al., 2007] Claire, D., Hild, F., and Roux, S. (2007). Identification of a damage law by using full-field displacement measurements. *International Journal of Damage Mechanics*, 16(2):179–197.
- [Clément et al., 1984] Clément, P., Angeli, J., and Pineau, A. (1984). Short crack behaviour in nodular cast iron. *Fatigue and Fracture of Engineering Materials and Structures*, 7(4):251–265.
- [Cooreman et al., 2007] Cooreman, S., Lecompte, D., Sol, H., Vantomme, J., and Debruyne, D. (2007). Elasto-plastic material parameter identification by inverse methods: Calculation of the sensitivity matrix. *International Journal of Solids and Structures*, 44(13):4329 – 4341.
- [Cordebois and Sidoroff, 1979] Cordebois, J. and Sidoroff, F. (1979). Damage induced elastic anisotropy. *Coll. Euromech 115*, pages 761–774.
- [Costa et al., 2010] Costa, N., Machado, N., and Silva, F. (2010). A new method for prediction of nodular cast iron fatigue limit. *International Journal of Fatigue*, 32(7):988 – 995.
- [Costa et al., 2008] Costa, N., Machado, N., and Silva, F. S. (2008). Influence of graphite nodules geometrical features on fatigue life of high-strength nodular cast iron. *Journal of Materials Engineering and Performance*, 17(3):352–362.
- [Davison and Stevens, 1973] Davison, L. and Stevens, A. (1973). Thermodynamical constitution of spalling elastic bodies. *Journal of Applied Physics*, 44(2):668.
- [Decreuse et al., 2012] Decreuse, P., Pommier, S., Poncelet, M., and Raka, B. (2012). A novel approach to model mixed mode plasticity at crack tip and crack growth. experimental validations using velocity fields from digital image correlation. *International Journal of Fatigue*, 42:271 – 283.
- [Doudard et al., 2007] Doudard, C., Poncelet, M., Calloch, S., Boue, C., Hild, F., and Galtier, A. (2007). Determination of an {HCF} criterion by thermal measurements under biaxial cyclic loading. *International Journal of Fatigue*, 29(4):748 – 757.
- [Ferro et al., 2012] Ferro, P., Lazzarin, P., and Berto, F. (2012). Fatigue properties of ductile cast iron containing chunky graphite. *Materials Science and Engineering: A*, 554(0):122 – 128.

- [Filetin et al., 2007] Filetin, T., Kovačiček, F., and Indof, J. (2007). *Svojstva i primjena materijala*. Fakultet strojarstva i brodogradnje.
- [Forquin et al., 2004] Forquin, P., Rota, L., Charles, Y., and Hild, F. (2004). A method to determine the macroscopic toughness scatter of brittle materials. *International Journal of Fracture*, 125(1):171–187.
- [Fremy et al., 2014] Fremy, F., Pommier, S., Poncelet, M., Raka, B., Galenne, E., Courtin, S., and Roux, J.-C. L. (2014). Load path effect on fatigue crack propagation in i; ii; iii mixed mode conditions – part 1: Experimental investigations. *International Journal of Fatigue*, 62(0):104 – 112.
- [Fuller, 1977] Fuller, A. (1977). Effect of graphite form on fatigue properties of pearlitic ductile irons. *Transactions, American Foundrymen's Society*, 85:527–536.
- [Gates et al., 2011] Gates, M., Lambros, J., and Heath, M. (2011). Towards high performance digital volume correlation. *Experimental Mechanics*, 51:491–507.
- [Gras et al., 2013] Gras, R., Leclerc, H., Roux, S., Otin, S., Schneider, J., and Périé, J. (2013). Identification of the out-of-plane shear modulus of a 3d woven composite. *Experimental Mechanics*, 53(5):719–730.
- [Grédiac, 1989a] Grédiac, M. (1989a). Principe des travaux virtuels et identification. *C. R. Acad Sci. Paris*, 309(Série II):1–5.
- [Grédiac, 1989b] Grédiac, M. (1989b). Principe des travaux virtuels et identification. *Comptes Rendus de l'Académie des Sciences (in French with abridged English version)*, II(309):1–5.
- [Grédiac and Hild, 2012] Grédiac, M. and Hild, F. (2012). *Full-Field Measurements and Identification in Solid Mechanics*. Wiley-ISTE.
- [Grédiac and Pierron, 2006] Grédiac, M. and Pierron, F. (2006). Applying the virtual fields method to the identification of elasto-plastic constitutive parameters. *International Journal of Plasticity*, 22(4):602–627.
- [Grédiac et al., 2006] Grédiac, M., Pierron, F., Avril, S., and Toussaint, E. (2006). The virtual fields method for extracting constitutive parameters from full-field measurements: a review. *Strain*, 42(4):233–253.
- [Griffith, 1920] Griffith, A. (1920). The phenomena of rupture and flow in solids. *Philosophical Transactions, Series A*, 221:163–198.
- [Grilec et al., 2010] Grilec, K., Jakovljević, S., and Prusac, D. (2010). Erosion of ductile cast iron with quartz particles. *Tehnički vjesnik*, 17(1):17–22.

- [Guillemer-Neel et al., 1999] Guillemer-Neel, C., Bobet, V., and Clavel, M. (1999). Cyclic deformation behaviour and baushinger effect in ductile cast iron. *Materials Science and Engineering: A*, 272(2):431 – 442.
- [Hafiz, 2001] Hafiz, M. (2001). Mechanical properties of sg-iron with different matrix structure. *Journal of Materials Science*, 36(5):1293–1300.
- [Hamam et al., 2007] Hamam, R., Hild, F., and Roux, S. (2007). Stress intensity factor gauging by digital image correlation: Application in cyclic fatigue. *The Journal of Strain Analysis for Engineering Design*, 43:181–192.
- [Hild et al., 2014] Hild, F., Bouterf, A., and Roux, S. (2014). Damage measurements via dic from physical to mechanical damage. *International Journal of Fracture*. *submitted*.
- [Hild and Roux, 2006] Hild, F. and Roux, S. (2006). Digital image correlation: From measurement to identification of elastic properties - a review. *Strain*, 42:69–80.
- [Hild and Roux, 2012] Hild, F. and Roux, S. (2012). Comparison of local and global approaches to digital image correlation. *Experimental Mechanics*, 52(9):1503–1519.
- [Hollomon, 1945] Hollomon, J. H. (1945). Tensile deformation. *Transactions, AIME*, 162:268–290.
- [Hübner et al., 2007] Hübner, P., Schlosser, H., Pusch, G., and Biermann, H. (2007). Load history effects in ductile cast iron for wind turbine components. *International Journal of Fatigue*, 29(9-11):1788–1796.
- [Iacoviello et al., 2008] Iacoviello, F., Bartolomeo, O. D., Cocco, V. D., and Piacente, V. (2008). Damaging micromechanisms in ferritic–pearlitic ductile cast irons. *Materials Science and Engineering: A*, 478(1-2):181–186.
- [ISO/IEC Guide 99–12, 2007] ISO/IEC Guide 99–12 (2007). International vocabulary of metrology—basic and general concepts and associated terms, vim. Standard, International Organization for Standardization, Geneva, CH.
- [Johnson and Cook, 1983] Johnson, G. and Cook, W. (1983). A constitutive model and data for metals subjected to large strains, high strain rates, and high temperatures. *Proceedings. 7th International Symposium Ballistics, Olanda*, pages 541–547.
- [Kachanov, 1958] Kachanov, L. (1958). Rupture time under creep condition. *International Journal of Fracture*, 97(1-4):11–18.
- [Karaman and Cetinarlan, 2010] Karaman, S. and Cetinarlan, C. S. (2010). Manufacturing process of ggg40 nodular cast iron. *International scientific conference Gabrovo*.
- [Krajcinovic, 1989] Krajcinovic, D. (1989). Damage mechanics. *Mechanics of Materials*, 8:117–197.



- [Latourte et al., 2008] Latourte, F., Chrysochoos, A., Pagano, S., and Wattrisse, D. (2008). Elastoplastic behavior identification for heterogeneous loadings and materials. *Experimental Mechanics*, 48(4):435–449.
- [Leclerc et al., 2012] Leclerc, H., Périé, J.-N., Hild, F., and Roux, S. (2012). Digital volume correlation: what are the limits to the spatial resolution? *Mechanics and Industry*, 13:361–371.
- [Leclerc et al., 2009] Leclerc, H., Périé, J.-N., Roux, S., and Hild, F. (2009). Integrated digital image correlation for the identification of mechanical properties. *MIRAGE 2009*, 5496:161–171.
- [Leclerc et al., 2011] Leclerc, H., Périé, J.-N., Roux, S., and Hild, F. (2011). Voxel-scale digital volume correlation. *Experimental Mechanics*, 51(4):479–490.
- [Lemaitre, 1971] Lemaitre, J. (1971). Evaluation and dissipation of damage in metals submitted to dynamic loading. *Proceedings I.C.M.*, 1.
- [Lemaitre, 1984] Lemaitre, J. (1984). How to use damage mechanics. *Nucl. Eng. Design*, 80:233–245.
- [Lemaitre, 1996] Lemaitre, J. (1996). *A Course on Damage Mechanics*. Springer.
- [Lemaitre and Chaboche, 1990] Lemaitre, J. and Chaboche, J. L. (1990). *Mechanics of solids materials*. Cambridge University Press.
- [Lemaitre and Chaboche, 1978] Lemaitre, J. and Chaboche, L. (1978). Aspect phénoménologique de la rupture par endommagement. *Journal de Mécanique Appliqué*, 2:317–365.
- [Lemaitre and Desmorat, 2005] Lemaitre, J. and Desmorat, R. (2005). *Engineering Damage Mechanics: Ductile, Creep, Fatigue and Brittle Failures*. Springer.
- [Lemaitre et al., 1999] Lemaitre, J., Sermage, J.-P., and Desmorat, R. (1999). A two scale damage concept applied to fatigue. *International Journal of Fracture*, 97:67–81.
- [Limodin et al., 2009] Limodin, N., Réthoré, Y., Buffière, J.-Y., Gravouil, A., Hild, F., and Roux, S. (2009). Crack closure and stress intensity factor measurements in nodular graphite cast iron using three-dimensional correlation of laboratory x-ray microtomography images. *Acta Materialia*, 57:4090 – 4101.
- [Limodin et al., 2010] Limodin, N., Réthoré, Y., Buffière, J.-Y., Hild, F., Roux, S., Ludwig, W., Rannou, J., and Gravouil, A. (2010). Influence of closure on the 3d propagation of fatigue cracks in a nodular cast iron investigated by x-ray tomography and 3d volume correlation. *Acta Materialia*, 58(8):2957 – 2967.

- [Lu and Cary, 2000] Lu, H. and Cary, P. (2000). Deformation measurements by digital image correlation: Implementation of a second-order displacement gradient. *Experimental Mechanics*, 40:393–400.
- [Lucas and Kanade, 1981] Lucas, B. D. and Kanade, T. (1981). *DARPA Imaging Understanding Workshop*.
- [Ludwig et al., 2005] Ludwig, O., Dimichiel, M., Salvo, L., Suéry, M., and Falus, P. (2005). In situ three-dimensional microstructural investigation of solidification of an al–cu alloy by ultrafast x-ray microtomography. *Metallurgical and Materials Transactions A*, 36(6):1515–1523.
- [Ludwik, 1909] Ludwik, P. (1909). *Elemente der Technologischen Mechanik*. Verlag von Julius Springer, Berlin.
- [Martin, 2006] Martin, J. (2006). *Materials for Engineering*. Book (Institute of Materials (Great Britain)) Elsevier Science.
- [Mathieu and Fremy, 2012] Mathieu, F. and Fremy, F. (2012). Stress intensity factor extraction in a 3d crack propagation experiment. *SEM XII International Congress and Exposition on Experimental and Applied Mechanics*.
- [Mathieu et al., 2012] Mathieu, F., Hild, F., and Roux, S. (2012). Identification of a crack propagation law by digital image correlation. *International Journal of Fatigue*, 36:146–154.
- [Mathieu et al., 2013] Mathieu, F., Hild, F., and Roux, S. (2013). Image-based identification procedure of a crack propagation law. *Engineering Fracture Mechanics*, 103:48–59.
- [Mathieu et al., 2014] Mathieu, F., Leclerc, H., Hild, F., and Roux, S. (2014). Estimation of elastoplastic parameters via weighted femu and integrated-dic. *Experimental Mechanics*, pages 1–15.
- [McNeill et al., 1987] McNeill, S., Peters, W., and Sutton, M. (1987). Estimation of stress intensity factor by digital image correlation. *Engineering Fracture Mechanics*, 28(1):101–112.
- [Millis et al., 1948] Millis, D., Gagnebin, P., and B.Pilling (1948). Cast ferrous alloy.
- [Mottitschka et al., 2010] Mottitschka, T., Pusch, G., Biermann, H., Zybell, L., and Kuna, M. (2010). Influence of overloads on the fatigue crack growth in nodular cast iron: experiments and numerical simulation. *Procedia Engineering*, 2(1):1557–1567.
- [Murakami, 1988] Murakami, S. (1988). Mechanical modelling of material damage. *Journal of Applied Mechanics*, 55(6):280–286.

- [Murakami and Ohno, 1981] Murakami, S. and Ohno, J. (1981). *A continuum theory of creep and creep damage, in Creep in Structures*. Springer, Berlin.
- [Nadot et al., 1997] Nadot, Y., Ranganathan, N., Mendez, J., and Béranger, A. (1997). A study of natural cracks initiated on casting defects by crack front marking. *Scripta Materialia*, 37(5):549–553.
- [Paris and Erdogan, 1963] Paris, P. and Erdogan, F. (1963). A critical analysis of crack propagation laws. *Journal of Basic Engineering*, 85:528–534.
- [Paris et al., 1961] Paris, P. C., Gomez, M. P., and Anderson, W. P. (1961). A critical analysis of crack propagation laws. *The Trend Engineering*, 13:9–14.
- [Pascual et al., 2009] Pascual, M., Ferrer, C., and Rayón, E. (2009). Weldability of spheroidal graphite ductile cast iron using ni / ni- fe electrodes. *Revista de Metalurgia*, 45(5):334–338.
- [Passieux and Périé, 2012] Passieux, J.-C. . and Périé, J.-N. (2012). High resolution digital image correlation using proper generalized decomposition: Pgd-dic. *International Journal for Numerical Methods in Engineering*, 92(6):531–550.
- [Périé et al., 2002] Périé, J.-N., Calloch, S., Cluzel, C., and Hild, F. (2002). Analysis of a multiaxial test on a c/c composite by using digital image correlation and a damage model. *Experimental Mechanics*, 42(3):318–328.
- [Peters and Ranson, 1982] Peters, W. H. and Ranson, W. F. (1982). Digital imaging techniques in experimental stress analysis. *Optical Engineering*, 21(3):213427.
- [Pierron et al., 2010] Pierron, F., Avril, S., and Tran, V. (2010). Extension of the virtual fields method to elasto-plastic material identification with cyclic loads and kinematic hardening. *International Journal of Solids and Structures*, 47(22–23):2993 – 3010.
- [Plé et al., 2002] Plé, O., Bernier, G., Bayard, E., and Astudillo, O. (2002). Biaxial tensile behaviour of the reactive powder concrete. *ACI Publication SP 209*, 20:369–387.
- [Poncelet et al., 2010] Poncelet, M., Barbier, G., Raka, B., Courtin, S., Desmorat, R., Le-Roux, J., and Vincent, L. (2010). Biaxial high cycle fatigue of a type 304l stainless steel: Cyclic strains and crack initiation detection by digital image correlation. *European Journal of Mechanics - A/Solids*, 29(5):810 – 825.
- [Prager, 1956] Prager, W. (1956). A new method of analysing stress and strain in work hardening plastic solids. *Journal of Applied Mechanics ASME*, 78(493).
- [Promma et al., 2009] Promma, N., Raka, B., Grédiac, M., Toussaint, E., Cam, J. L., Balandraud, X., and Hild, F. (2009). Application of the virtual fields method to mechanical characterization of elastomeric materials. *Int. J. Solids Struct.*, 46(3-4):698–715.

- [Rabotnov, 1969] Rabotnov, J. (1969). Creep problems in structural members.
- [Rabotnov, 1968] Rabotnov, Y. (1968). Creep rupture. *Proceedings of the Twelfth International Congress of Applied Mechanics*, page 342–349.
- [Rannou et al., 2010] Rannou, J., Limodin, N., Réthoré, J., Gravouil, A., Ludwig, W., Baietto-Dubourg, M.-C., Buffière, J.-Y., Combescure, A., Hild, F., and Roux, S. (2010). Three dimensional experimental and numerical multiscale analysis of a fatigue crack. *Computer Methods in Applied Mechanics and Engineering*, 199(21–22):1307 – 1325.
- [Réthoré, 2010] Réthoré, J. (2010). A fully integrated noise robust strategy for the identification of constitutive laws from digital images. *International Journal for Numerical Methods in Engineering*, 84(6):631–660.
- [Réthoré et al., 2007] Réthoré, J., Roux, S., and Hild, F. (2007). From pictures to extended finite elements : extended digital image correlation (x-dic). *International Journal of Solids and Structures*, 335(3):131 – 137.
- [Réthoré et al., 2009] Réthoré, J., Roux, S., and Hild, F. (2009). An extended and integrated digital image correlation technique applied to the analysis fractured samples. *European Journal of Computational Mechanics*, 18:285–306.
- [Robert et al., 2012] Robert, L., Velay, V., Decultot, N., and Ramde, S. (2012). Identification of hardening parameters using finite element models and full-field measurements: some case studies. *The Journal of Strain Analysis for Engineering Design*, 47(1):3–17.
- [Rossi et al., 2006] Rossi, M., Broggiato, G., and Papalini, S. (2006). Identification of ductile damage parameters using digital image processing. *SEM Annual Conference and Exposition on Experimental and Applied Mechanics - Experimental Mechanics - The Building Blocks for Structural Health Management*.
- [Roux and Hild, 2006] Roux, S. and Hild, F. (2006). Stress intensity factor measurements from digital image correlation: post-processing and integrated approaches. *International Journal of Fracture*, 140(1-4):141–157.
- [Roux and Hild, 2008] Roux, S. and Hild, F. (2008). Digital image mechanical identification (dim). *Experimental Mechanics*, 48(4):495–508.
- [Roux et al., 2008] Roux, S., Hild, F., Viot, P., and Bernard, D. (2008). Three-dimensional image correlation from x-ray computed tomography of solid foam. *Composites Part A: Applied Science and Manufacturing*, 39(8):1253–1265.
- [Rupil et al., 2011] Rupil, J., Vincent, L., Hild, F., and Roux, S. (2011). Identification and probabilistic modeling of mesocrack initiations in 304l stainless steel. *International Journal for Multiscale Computational Engineering*, 9(4):445–458.

- [Schreier and Sutton, 2002] Schreier, H. and Sutton, M. (2002). Systematic errors in digital image correlation due to undermatched subset shape functions. *Experimental Mechanics*, 42(3):303–310.
- [Sermage et al., 2000] Sermage, J., Lemaitre, J., and Desmorat, R. (2000). Multiaxial creep-fatigue under anisothermal conditions. *Fatigue & Fracture of Engineering Materials & Structures*, 23:241–252.
- [Simo and Ju, 1987] Simo, J. and Ju, J. (1987). Strain- and stress-based continuum damage models. i - formulation, ii - computational aspects. *International Journal of Solids and Structures*, 23(7):821–869 and 841–869.
- [Sjögren et al., 2011] Sjögren, T., Persson, P., and Vomacka, P. (2011). Analysing the deformation behaviour of compacted graphite cast irons using digital image correlation techniques. *Key Engineering Materials*, 457:470–475.
- [Skrzypek and Ganczarski, 1999] Skrzypek, J. and Ganczarski, A. (1999). *Modeling of Material Damage and Failure of Structures*. Springer.
- [Smith et al., 2002] Smith, T., Bay, B., and Rashid, M. (2002). Digital volume correlation including rotational degrees of freedom during minimization. *Experimental Mechanics*, 42(3):272–278.
- [Sun et al., 2005] Sun, Y., Pang, J., Wong, C., and Su, F. (2005). Finite element formulation for a digital image correlation method. *Applied Optics*, 43(34):7357–7363.
- [Sutton et al., 1986] Sutton, M., Cheng, M., Peters, W., Chao, Y., and McNeill, S. (1986). Application of an optimized digital correlation method to planar deformation analysis. *Image and Vision Computing*, 4(3):143–150.
- [Sutton et al., 2000] Sutton, M., McNeill, S., Helm, J., and Chao, Y. (Berlin: Springer 2000). Advances in two-dimensional and three-dimensional computer vision. in rastogi pk (ed.). *Photomechanics, topics in applied physics*, 77:323–372.
- [Sutton et al., 2009] Sutton, M., Orteu, J.-J., and Schreier, H. (2009). *Image correlation for shape, motion and deformation measurements: basic concepts, theory and applications*. New York: Springer.
- [Sutton et al., 1983] Sutton, M., Wolters, W., Peters, W., Ranson, W., and McNeill, S. (1983). Determination of displacements using an improved digital correlation method. *Image and Vision Computing*, 1(3):133 – 139.
- [Swift, 1952] Swift, H. (1952). Plastic instability under plane stress. *Journal of the Institute of Metals*, 1:1–18.

- [Taillandier-Thomas et al., 2014] Taillandier-Thomas, T., Roux, S., Morgenev, T., and Hild, F. (2014). Localized strain field measurement on laminography data with mechanical regularization. *Nuclear Instruments and Methods in Physics Research Section B: Beam Interactions with Materials and Atoms*, 324(0):70–79.
- [Tikhonov and Arsenin, 1977] Tikhonov, A. and Arsenin, V. (1977). *Solutions of Ill-posed problems*. New York: John Wiley and Sons Inc.
- [Tomičević et al., 2013] Tomičević, Z., Hild, F., and Roux, S. (2013). Mechanics-aided digital image correlation. *The Journal of Strain Analysis for Engineering Design*, 0(0):1–14.
- [Triconnet et al., 2009] Triconnet, K., Derrien, K., Hild, F., and Baptiste, D. (2009). Parameter choice for optimized digital image correlation. *Optics and Lasers in Engineering*, 47:728–737.
- [Unkić et al., 2008] Unkić, F., Glavaš, Z., and Terzić, K. (2008). Utjecaj broja nodula na žilavost feritnog nodularnog lijeva. *Strojarstvo*, 50(4):231–238.
- [Vagnon et al., 2006] Vagnon, A., Lame, O., Bouvard, D., Michiel, M. D., Bellet, D., and Kapelski, G. (2006). Deformation of steel powder compacts during sintering: Correlation between macroscopic measurement and in situ microtomography analysis. *Acta Materialia*, 54(2):513 – 522.
- [Čanžar et al., 2011] Čanžar, P., Tonković, Z., Bakić, A., and Kodvanj, J. (2011). Experimental and numerical investigation of fatigue behaviour of nodular cast iron. *Key Engineering Materials*, 488-489(488-489):182–185.
- [Čanžar et al., 2012] Čanžar, P., Tonković, Z., and Kodvanj, J. (2012). Microstructure influence on fatigue behaviour of nodular cast iron. *Materials Science and Engineering: A*, 556(0):88 – 99.
- [Čanžar et al., 2010] Čanžar, P., Tonković, Z., Kodvanj, J., Bakić, A., and Tomičević, Z. (2010). Modelling of cyclic plasticity and crack propagation. *Key Engineering Materials*, 452-453(452-453):825–828.
- [Verhulp et al., 2004] Verhulp, E., van Rietbergen, B., and Huiskes, R. (2004). A three-dimensional digital image correlation technique for strain measurements in microstructures. *Journal of Biomechanics*, 37(9):1313–1320.
- [Voce, 1948] Voce, E. (1948). The relationship between stress and strain for homogeneous deformations. *Journal of the Institute of Metals*, 74:537–562.
- [Voyiadjis and Basuroychowdhury, 1998] Voyiadjis, G. and Basuroychowdhury, I. (1998). A plasticity model for multiaxial cyclic loading and ratchetting. *Acta Mechanica*, 126(1-4):19–35.

- [Voyiadjis and Kattan, 1991] Voyiadjis, G. and Kattan, P. (1991). Phenomenological evolution equations for the backstress and spin tensors. *Acta Mechanica*, 88:91–111.
- [Voyiadjis and Sivakumar, 1994] Voyiadjis, G. and Sivakumar, S. (1994). A robust kinematic hardening rule with ratchetting effects: Part 2 - application to non-proportional loading cases. *Acta Mechanica*, 107:117–136.
- [Wang and Ohno, 1991] Wang, J. and Ohno, N. (1991). Kinematic hardening rules with critical state dynamic recovery, part ii - application to experiments of ratcheting behavior. *International Journal of Plasticity*, 9(391).
- [Yaacoub-Agha et al., 1998] Yaacoub-Agha, H., Béranger, A.-S., Billardon, R., and Hild, F. (1998). High-cycle fatigue behaviour of spheroidal graphite cast iron. *Fatigue and Fracture of Engineering Materials and Structures*, 21(3):287–296.
- [Yoneyama et al., 2007] Yoneyama, S., Ogawa, T., and Kobayashi, Y. (2007). Evaluating mixed-mode stress intensity factors from full-field displacement fields obtained by optical methods. *Engineering Fracture Mechanics*, 74(9):1399–1412.





# Appendix F

## Životopis

Zvonimir Tomičević rođen je 30. kolovoza 1984. godine u Zagrebu. Osnovnu školu završava 1999. godine u Sesvetama, Zagreb, Opću gimnaziju 2003. godine u Sesvetama, Zagreb, kad upisuje i Fakultet strojarstva i brodogradnje Sveučilišta u Zagrebu. Preddiplomski studij završio je 2007. godine, a diplomski dio studija na smjeru Eksperimentalna mehanika završio je 2008. godine na Fakultetu strojarstva i brodogradnje. Od 2008. godine kao znanstveni novak u suradničkom zvanju asistenta na Zavodu za tehničku mehaniku na Fakultetu strojarstva i brodogradnje u Zagrebu, gdje je pohadao poslijediplomski studij, smjer Teorija konstrukcija. Kao istraživač sudjelovao je na jednom znanstvenom i jednom tehnološkom projektu. Tijekom istraživanja, prvotno je boravio šest mjeseci u Laboratoriju za mehaniku i tehnologiju na Ecole Normale Supérieure de Cachan, Francuska, 2011. g. Početkom 2012. godine upisuje dvojni doktorat između Sveučilišta u Zagrebu i Ecole Normale Supérieure, Cachan, Francuska, te boravi dodatnih 20 mjeseci na Ecole Normale Supérieure u Cachanu, Francuska. Uz istraživački rad, aktivno je sudjelovao u nastavi iz više kolegija dodiplomskog i diplomskog studija. Autor je ukupno 11 znanstvenih radova, od čega je 1 objavljen u CC znanstvenim časopisima. Član je Hrvatskog društva za mehaniku. Služi se engleskim i njemačkim jezikom.



# Appendix G

## Biography

Zvonimir Tomičević was born on August 30, 1984 in Zagreb, Croatia. In 2000 he graduated the Elementary school in Sesvete, Zagreb. After that, he graduated Technical high school in Sesvete, Zagreb, in 2003, when he enrolled the Faculty of Mechanical Engineering and Naval Architecture, University of Zagreb. In 2007 he received the Bachelor degree (BEng Mech) and in 2008 the Master degree (MEng Mech), both at the Faculty of Mechanical Engineering and Naval Architecture, University of Zagreb, course: Experimental mechanics. Since 2009, he has been employed as researcher at the Department of Technical Mechanics at the Faculty of Mechanical Engineering and Naval Architecture, where he enrolled in the postgraduate study in Theory of Structures and Design. He has been working as a research assistant on one scientific and one industrial project. During his research, first he conducted research at the Laboratory of mechanics and technology for 6 months. In 2012 he enrolled in the joint PhD program between University of Zagreb and Ecole Normale Supérieure de Cachan, France and conducts research in Cachan for 20 months. In addition, he has been involved in the teaching activities in a number of courses from the graduate study. He is the author of 11 scientific publications, including 1 contributions published in the CC scientific journals. He is fluent in spoken and written English and German.